# REPORT DOCUMENTATION PAGE

AFRL-SR-BL-TR-01-

0501

| 1. AGENCY USE ONLY *(Leave blank)* | 2. REPORT DATE | 3. REPORT | |
|---|---|---|---|
| | August 2001 | FINAL REPORT 1 Dec 97 - 31 Mar 01 | |

| 4. TITLE AND SUBTITLE | 5. FUNDING NUMBERS |
|---|---|
| MEMS-BASED PROBES FOR VELOCITY AND PRESSURE MEASUREMETNS IN UNSTEADY AND TURBULENT FLOWFIELDS | F49620-98-1-0162 <br><br> 2302/BS |
| **6. AUTHOR(S)** <br> OTHON K. REDINIOTIS | 61102F |

| 7. PERFORMING ORGANIZATION NAME(S) AND ADDRESS(ES) | 8. PERFORMING ORGANIZATION REPORT NUMBER |
|---|---|
| TEXA A&M UNIVERSITY <br> AEROSPACE ENGINEERING DEPARTMENT <br> COLLEGE STATION, TX 77843-3141 | |

| 9. SPONSORING/MONITORING AGENCY NAME(S) AND ADDRESS(ES) | 10. SPONSORING/MONITORING AGENCY REPORT NUMBER |
|---|---|
| AIR FORCE OFFICE OF SCIENTIFIC RESEARCH <br> 801 N. RANDOLPH STREET, ROOM 732 <br> ARLINGTON, VA 22203-1977 | |

**11. SUPPLEMENTARY NOTES**

AIR FORCE OFFICE OF SCIENTIFIC RESEARCH (AFOSR)
NOTICE OF TRANSMITTAL DTIC. THIS TECHNICAL REPORT
HAS BEEN REVIEWED AND IS APPROVED FOR PUBLIC RELEASE
LAW AFR 190-12. DISTRIBUTION IS UNLIMITED.

| 12a. DISTRIBUTION AVAILABILITY STATEMENT | 12b. DISTRIBUTION CODE |
|---|---|
| APPROVED FOR PUBLIC RELEASE, DISTRIBUTION IS UNLIMITED | |

**13. ABSTRACT** *(Maximum 200 words)*

This report presents our work in the development of fast-response, high-accuracy multi-sensor pressure probes of miniature size for velocity and pressure measurement in unsteady and turbulent flowfields, with emphasis on MEMS-based pressure probes. The fabrication and calibration (theoretical and experimental) of miniature (order of 1mm to 2mm in diameter) 5-sensor hemispherical-tip probes, are discussed. The first stages of the development process have been to fabricate a sensitive MEMS pressure sensor and to develop calibration algorithms and environments for fast-response probes.

The work resulted in a prototype MEMS-based 5 sensor probe, several embedded-sensor, fast response 5-sensor probes, and high accuracy steady and unsteady probe calibration and data-reduction algorithms. The work has produced a new type of flow-diagnostics probes that are anticipated to prove valuable to the fluid mechanics community. They are significantly more rugged than hot-wires and much less dependent on repetitive and tedious calibration; provide much larger measurable flow angularity; and although they are not there yet, we soon expect them to be able to match or exceed a hot-wire's spatial resolution capabilities and compete with a hot-wire's frequency response.

| 14. SUBJECT TERMS | | | 15. NUMBER OF PAGES |
|---|---|---|---|
| | | | 209 |
| | | | **16. PRICE CODE** |

| 17. SECURITY CLASSIFICATION OF REPORT | 18. SECURITY CLASSIFICATION OF THIS PAGE | 19. SECURITY CLASSIFICATION OF ABSTRACT | 20. LIMITATION OF ABSTRACT |
|---|---|---|---|
| U | U | U | |

# MEMS-BASED PROBES FOR VELOCITY AND PRESSURE MEASUREMENTS IN UNSTEADY AND TURBULENT FLOWFIELDS

*Final Project Report*

*Submitted by*

**Othon K. Rediniotis**
**Aerospace Engineering Department**
**Texas A&M University**
**College Station, Texas 77843-3141**

*to the*

**Air Force Office of Scientific Research**
**ATTN: NI/DURIP**
**4040 Fairfax Dr., Suite 500**
**Arlington, VA 22203-1613**
**(703) 696-7313**

*Technical Monitor: Dr. Tom Beutner*

# TABLE OF CONTENTS

# 1. ABSTRACT

This report presents our work in the development of fast-response, high-accuracy multi-sensor pressure probes of miniature size for velocity and pressure measurement in unsteady and turbulent flowfields, with emphasis on MEMS-based pressure probes. The fabrication and calibration (theoretical and experimental) of miniature (order of 1mm to 2mm in diameter) 5-sensor hemispherical-tip probes, are discussed. The first stages of the development process have been to fabricate a sensitive MEMS pressure sensor and to develop calibration algorithms and environments for fast-response probes. We fabricated and calibrated several generations of bossed-diaphragm absolute pressure sensors $100\times100$ $\mu m^2$ to $250\times250$ $\mu m^2$ in size. One of the challenges in the pressure sensor development is the design of sensors with sensitivity sufficient for accurate measurements in flow conditions most commonly of interest to the scientific and industrial community. New probe calibration techniques were introduced. Both theoretical and experimental approaches are employed to develop calibration techniques suitable for unsteady and turbulent flow environments with fine time and length scales.

In terms of probe calibration, first new steady calibration algorithm was developed that pushes the envelope of calibration accuracy down to 0.1 degrees in angle prediction and 0.3% in velocity magnitude prediction. Subsequently, unsteady flow effects were theoretically modeled and experimentally validated. Theoretical discussions are coupled with experiments. As aiding tools in the development of the unsteady calibration theory and algorithms, several special experimental facilities and 5-hole probes were developed, including a high-speed unsteady jet facility with velocity fluctuation frequencies as high as 2 KHz.

The work resulted in a prototype MEMS-based 5-sensor probe, several embedded-sensor, fast response 5-sensor probes, and high accuracy steady and unsteady probe calibration and data-reduction algorithms. The majority of our work has already been brought in the market with several companies and universities already using our probes. Several "success stories" are also included in the appendices. The work has produced a new type of flow-diagnostics probes that are anticipated to prove valuable to the fluid mechanics community. They are significantly more rugged than hot-wires and much less dependent on repetitive and tedious calibration; provide much larger measurable flow angularity; and although they are not there yet, we soon expect them to be able to match or exceed a hot-wire's spatial resolution capabilities and compete with a hot-wire's frequency response.

# 2. INTRODUCTION

Multi-hole pressure probes, such as 5-hole and 7-hole probes, have in many cases provided the easiest-to-use and most cost-effective method for steady-state, three-component flow velocity and pressure measurements in research and industry environments. Especially in high-productivity environments, non-intrusive flow measurement techniques such as Laser-Doppler Velocimetry (LDV) and Particle Image Velocimetry (PIV), although powerful, have been traditionally avoided, since they require painstaking efforts toward their successful usage. Costly components, complex setups, troublesome flow "seeding" requirements, lack of flexibility, ruggedness and mobility and ease of misalignment often render such techniques impractical. For steady-state measurements, multi-hole probes are often favored even over Hot-Wire Anemometry, due to the susceptibility of the latter to frequent wire damage and the need for repetitive calibration. However, even after the measurement capabilities of multi-hole probes were expanded in the recent years, in terms of spatial resolution and frequency response, the current state-of-the-art of such probes is still faced with limitations.

Although multi-hole probes have been employed in the measurement of unsteady flowfields (Senoo et al., 1973; Castorph and Raabe, 1974; Kerrebrock et al., 1980; Matsunaga et al., 1980; Ng and Popernack, 1988; Naughton et al., 1993; Rediniotis et al., 1994) they have typically been limited in terms either of frequency response or minimum achievable probe size. For example, although Kerrebrock et al.'s (1980) probe had a decent overall frequency response (30 kHz), it had a rather large size (5mm tip diameter), and, although Matsunaga et al.'s (1980) probe had a relatively small size (2mm tip diameter), it had a limited frequency response (500 Hz). Ng and Popernack (1988) developed a four-sensor probe with a size of 5.2mm and a frequency response of 20 kHz. Naughton et al. (1993) developed a 5-hole probe for supersonic flow measurements. A small tip diameter was maintained (1.1mm) but the frequency response was limited to 50 Hz. Typically, in these efforts the frequency response limitations are caused by the need to have pressure tubing leading from the probe tip to the pressure transducers.

From the above one can infer that the previous state-of-the-art could not simultaneously achieve large measurable bandwidth and good spatial resolution of the fine flow structure when applied to turbulent flow measurements. It should be noted also that in the previous efforts, even in the cases of small tip diameters, the probe bodies immediately downstream of the tips were large in size (10mm and higher) in order to provide the housing for the pressure transducers; in no case were the pressure transducers "micro" in size, the size of currently available Si-diaphragm-type pressure sensors are all in the order of millimeters. Downstream obstructions, such as bulky probe bodies can cause significant flow disruption, especially in flowfields of elliptical nature. For example, they can cause premature vortex breakdown of leading edge vortices (Rediniotis, 1992). To overcome these limitations we are developing MEMS-based, multi-sensor pressure probes that largely eliminate the limitations described above. The new probes combine miniature size with high frequency response and will extend the application regime of multi-sensor probes to unsteady and turbulent flows.

Although probe calibration techniques for steady-state measurements are well established today (Gallington, 1980, Kjelgaard, 1988, Zilliac, 1989, Houtman and Bannink, 1989, Everett et al., 1983, Naughton et al., 1993, Rediniotis et al., 1993, Rediniotis and Chrysanthakopoulos,

4

1995), largely unresolved issues persist pertaining to the calibration of such instruments for measurements in unsteady and turbulent flows. Siddon (1969) used a pressure probe in unsteady flow and examined the error introduced if quasi-steady calibration is used in unsteady flow environments. He concluded that only if the length scale of the unsteadiness is significantly larger than the probe size, the instantaneous unsteady pressures are negligibly different than the quasi-steady pressures. Senoo et al. (1973) employed a three-hole cobra probe to measure 2-D instantaneous flow properties at the exit of a pump impeller. Recognizing the difficulty of calibrating the probe in unsteady flow, they utilized the steady-state calibration of the probe to reduce the unsteady flow data. For their application, arguments were presented as to why the followed approach did not compromise the measurement accuracy, although no quantitatively unequivocal proof was presented.

A theoretical-experimental procedure for calibrating a five-hole probe in unsteady conditions was employed by Matsunaga et al. (1980). This was one of the few attempts to account for unsteady effects in the calibration and part of the approach is adopted herein. However, there, the theoretical part of the algorithm, which consisted of the numerical calculation of the perturbation potential $\phi$ around a hemispherical-tip probe, was not properly corrected to account for fabrication idiosyncrasies and imperfections of the specific probe. Even in steady-state calibration of hemispherical-tip probes, similar methods, utilizing potential flow equations for the flow over a sphere to relate flow angle and velocity to pressure differentials measured by the probe, have been employed (Kjelgaard, 1988). It is now well established in the community that such methods are sensitive to construction defects on the probe, if not properly corrected for the specific probe geometric details. Such correction can only be derived by coupling the theoretical calculations to measurements of the specific probe behavior. This is a demanding task and although necessary if high-quality probe calibrations are desired, especially in unsteady calibration, has been avoided in the past.

If the probe is to be used in turbulent flowfields, to provide velocity and pressure information down to the dissipative length scales and resolve a broad bandwidth of frequencies, the spatial and temporal resolution issues of the calibration are accentuated. The findings of George, Beuther and Arndt (1984) provide good insight into some of these issues. They developed spectral models for turbulent pressure fluctuations by Fourier transforming the solution to the Poisson equation:

$$\frac{1}{\rho} \nabla^2 \tilde{p} = -\frac{\partial \tilde{u}_i}{\partial x_j} \frac{\partial \tilde{u}_j}{\partial x_i} \qquad (2.1)$$

where $\tilde{p}$ is the instantaneous static pressure, $\tilde{u}_i$ is the instantaneous velocity component, i and j=1,2,3 for Cartesian tensor notation and $\rho$ is the density. Homogeneous turbulence and a constant-mean-shear flow were assumed. It was shown there that although the velocity spectrum $E(k)$ drops off as -5/3 in the inertial subrange, the pressure spectrum was dominated by a $k^{-7/3}$ behavior in the same high-wavenumber regime (k is the wavenumber). The fact that the pressure spectrum rolls off faster than the velocity spectra is a potential source of measurement contamination of a pressure-sensitive probe by velocity signals, at high wavenumbers.

5

Fuchs (1972), assuming that Taylor's hypothesis holds, derived expressions for the difference (error) between the static pressure measured by a probe inserted in turbulent flow and the true static pressure of the flow at the same location, if the flow was not disturbed by the presence of the probe. Fuchs further developed conditions that have to be met should this difference (error) be considered negligible. An important such condition is expressed as: $d/\Lambda_x \ll 1$, i.e., the probe diameter should be small compared to the turbulent length scales to be resolved. It is important to realize at this point that these conditions cannot be applied straight to the 5-hole (sensor) probe. The 5-hole probe derives its measurements by disturbing the flow. In a sense, the disturbance it causes to the flow is its principle of operation. An even more important realization of the potential of the five-hole probe as a high-spatial resolution flow measurement instrument should be made. Consider a hot-wire and a high-frequency response multi-sensor pressure probe of the same basic dimensions (1mm effective wire length and probe tip diameter). Also, consider a turbulent eddy with a length scale on the same order (1mm or a fraction of it) being convected over the instrument. A hot wire is incapable of resolving the spatial gradients within the eddy. Its reading is a measure of the spatially averaged heat transfer effect the eddy has on the wire. The multi-sensor pressure probe, however, provides multiple discrete readings at spatially distributed locations within the eddy. The above reasoning serves as an introduction in illustrating the potential of the proposed instrument in resolving spatial gradients of length scales smaller than the probe diameter. Multi-hole probes are traditionally calibrated in uniform freestream and therefore in the absence of shear. However, there are no showstoppers preventing the probe from being calibrated in shear flows and thus being able to operate in and measure shear flows. The instrument's capabilities can be extended to the measurement of shear or spatial gradients with scales smaller than the probe size, especially if an array of pressure sensors is distributed on the probe surface.

In Gossweiler et al. (1994), a 4-hole, fast-response probe was introduced. The probe tip did not have any of the conventional geometries (conical or hemispherical) but was rather formed into a wedge. The tip diameter was 2.5mm and the frequency response was 45 kHz. The probe was used for measurements in turbomachinery related flows, however all data reduction was performed via static probe calibration. The unsteady aerodynamic effects on the probe calibration were not taken into account. The same group (Humm et al., 1994) tested several fast response probes with tip geometries, in order to assess the measurement error made if a static probe calibration is used to reduce probe measurements taken in time-dependent flowfields. Several error sources were identified, the most important of which are: inertial or apparent mass effects (potential flow effects), dynamic boundary layer effects, dynamic stall effects and vortex shedding effects. For a flow oscillation frequency of 5.9 kHz, and depending on probe geometry and size (two probe tip sizes were tested, 4mm and 8mm), errors as high as 100% were identified. The highest errors were observed for wedge-type probe tip geometries, while circular probe tip geometries were found to reduce these errors dramatically (one order of magnitude). This is one of the reasons we have chosen a hemispherical rather than conical tip geometry. Another important result in Humm et al. was the fact that for circular tip geometries the main two sources of errors were inertial (potential flow) effects and spatial velocity gradient effects. Viscosity and circulation related errors were much smaller.

# 3. CONCEPTUAL PROBE DESIGN

Figures 3.1 and 3.2 present our initial design of the MEMS-based probe. In this type of probe, the pressure sensor chip is mounted on the bottom of the hemispherical probe tip. For a hemispherical pressure probe with a diameter of 1 mm, the length of pressure tubing is no longer than the radius of the hemisphere (0.5 mm). The sensor chip is designed to be 0.7 mm on a side in order to be flush mounted on the flat side of the hemispherical tip. As shown in figure 3.1, the chip integrates five sensors, one located at the center of the chip and the other four symmetrically distributed at the corners. Inside the probe, as much area as possible needs to be dedicated to the chip. Therefore, the area dedicated to electrical connections is minimized. A robust, repeatable assembly process is needed for inserting the minute die into the final housing. Finally, the hemispherical dome is hermetically bonded to the pressure sensor chip to complete the probe shown in figure 3.2.
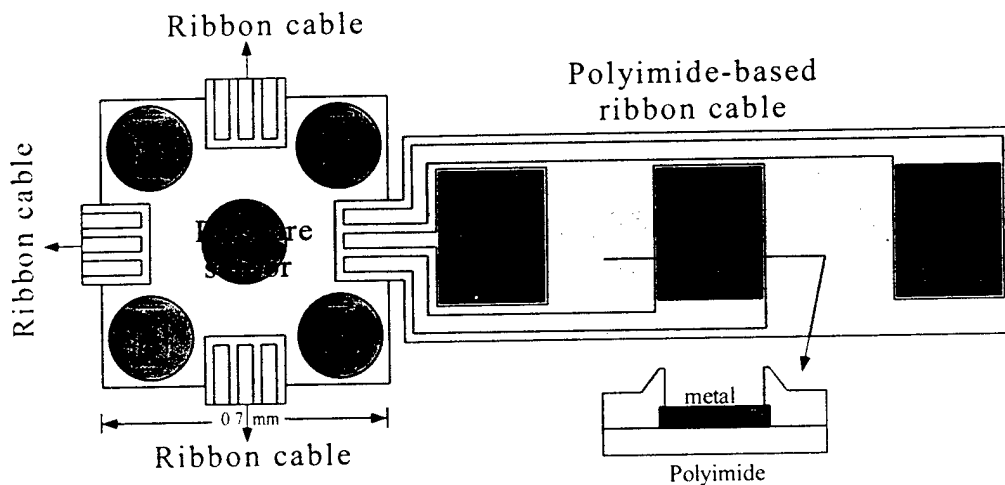
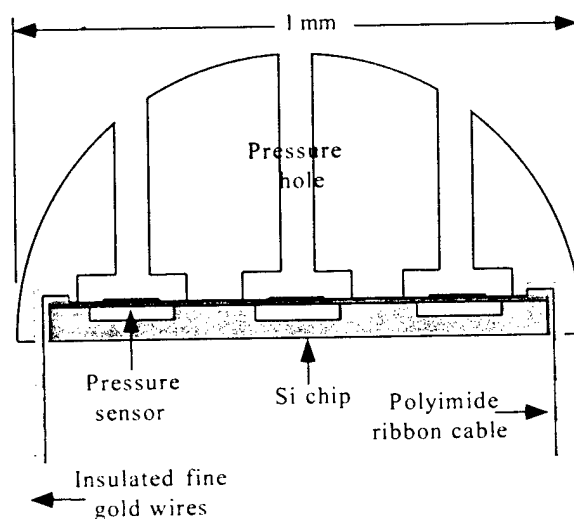Figure 3.1. Layout of diced pressure sensor chip.

Figure 3.2. Packaging of the 5-sensor hemispherical probe.

7

During the project and as our experience with miniature machining and MEMS pressure sensors matured the probe design was updated to facilitate assembly. Figure 3.3 is an exploded view of the updated probe design, schematically showing the various components as they are being assembled, while figure 3.4 schematically presents a cut-away view of the assembled probe. The tip, sealing tubes, and mounting stage are fabricated by the Miniaturization Laboratory, as well as tools to facilitate final assembly. The tip is relatively easy to fabricate, as it consists of simple drilling and counter-boring operations, although great care is taken in producing the hemisphere as accurately as possible. The tubes are off-the-shelf and only require machining to length. The mounting stage is the most difficult piece to fabricate, as it has features requiring the smallest of tools and the highest precision of location. Figure 3.5 shows the stage in detail. The stage is 2 mm diameter brass, approximately 1 mm thick. The pocket is 0.005 inches deep, and is machined with a 0.010" diameter cutter, as are the four slots. The pocket corners are cleared to allow the MEMS array to be accurately positioned relative to the outside diameter of the stage. The slots for the wiring ribbons go completely through the stage, to allow access to the soldering pads on the wires from the MEMS array. The stage plays a crucial role in the assembly of the probe components. The MEMS array, the sealing tubes, and the tip of the probe are placed relative to the outside diameter of the stage, which also serves as the final connection to the probe housing, after the sensor wires are connected. Each of the pressure sensors must be coupled with its corresponding hole in the tip, with no chance of leakage or cross-talk between ports. This is accomplished by sealing all of the tubes to the MEMS array in one epoxy setting, then sealing the tip to the tubes in a separate epoxy setting. A fixture, referred to as the "sealer", is used to accurately position the tubes on the MEMS array, so that epoxy can be placed around the outside diameter of each tube. Pictures of the several fabricated components and the assembled probe are shown and discussed after we first discuss the MEMS pressure array, the relevant fabrication processes and sensor calibration.
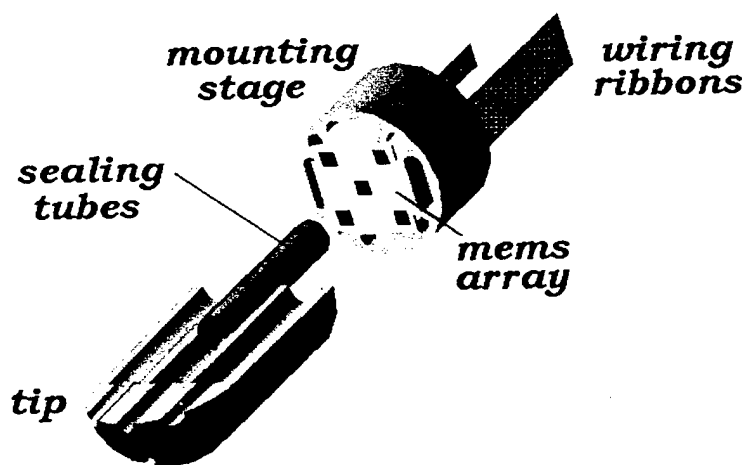


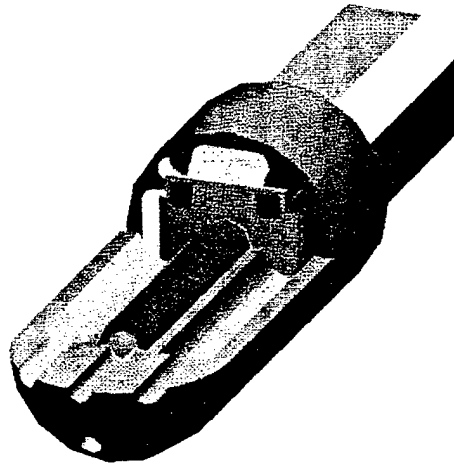**Figure 3.3. Exploded view of the MEMS 5-sensor probe.**

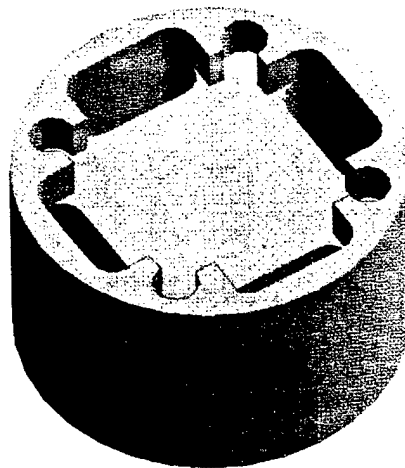**Figure 3.4. Cut-away schematic of assembled probe.**



**Figure 3.5. Schematic of MEMS mounting stage.**

# 4. DEVELOPMENT OF MEMS PRESSURE SENSORS AND SENSOR ARRAY

Most commercial silicon pressure sensors are differential. The advantage is that users can add their own reference pressure to fully utilize the specified pressure range and sensitivity. This is especially important for the low-pressure sensors with a range of only a few psi or less. However, the presence of external plumbing dictates that the sizes of this type of sensors can not be made smaller than 1 mm$^2$. Furthermore, the requirement of having a reference pressure tube on each sensor could become a serious disadvantage in some applications, most notably in arrays. On the other hand, the absolute type pressure sensors with a vacuum reference are convenient to use and can perform equally well if the measured pressure range starts from vacuum, i.e., the full range is utilized. Also, the surface micromachined type can be as small as 100×100 µm$^2$. This small size, combined with the absence of plumbing, make surface micromachined pressure sensors ideal for use in applications where small arrays are needed (i.e. pressure probes). The most significant disadvantage of absolute pressure sensors, however, is the lower sensitivity. Therefore, we have spent most of our design efforts in an attempt to improve the sensitivity.

Though not commercialized, many types of surface micromachined absolute piezoresistive pressure sensors have been developed. Table 4.1 shows the performance comparison for some of these sensors. They use either polysilicon or low stress silicon nitride as the diaphragm and polysilicon resistors as the sensing elements.

| | Diaphragm material | Diaphragm size, (µm$^3$) | Pressure range (psig) | FSO (mV) | Nonlinearity (%) |
|---|---|---|---|---|---|
| Lin | Poly-Si | 2x100x100 | 100 | 75 | 0.2 |
| Kalvesten | Poly-Si | 2x100x100 | 5.8 | 3 | N/A |
| Liu | SiN | 1.5x250x250 | 20 | 25 | 1 |
| Lisec | Poly-Si | 1.7x80x220 | 7.5 | 18 | N/A |
| Jiang | SiN | 1x230x230 | 10/20/30 | 60/95/100 | 0.8 |

**Table 4.1. Comparison of different pressure sensor diaphragms.**

The diaphragm geometry and thickness are all well controlled. Because the gage factor (a measure of change in resistivity as a function of strain) of polysilicon is 3 to 5 times smaller than that of single crystal silicon, these sensors are generally less sensitive than the bulk micromachined silicon pressure sensors. Also, due to the built-in stress of the diaphragm material (especially silicon nitride diaphragms), the linearity is not as good. Therefore, they are not competitive in the individual pressure sensor market. However, potentially they can still be useful in such areas as profiling pressure distributions on a surface where dense sensors are required.

The pressure probe requires high sensitivity in a small pressure range. All of the previous surface micromachined sensors simply used uniform-thickness diaphragms while some of the most sensitive bulk micromachined pressure sensors have more sophisticated bossed structures

on their diaphragms to achieve localized stress concentrations. Therefore, we believed that it would be worthwhile to try the bossed structures on the surface micromachined sensors. As a matter of fact, the bossed structure makes the whole diaphragm stiffer, i.e., less deflection on the center of the diaphragm. This actually could be the most important effect as the maximum center deflection of the surface sensor diaphragm is limited by the sacrificial layer thickness to be 2-3 μm.

Based on the above consideration, we have fabricated a number of different structures. Figure 4.1 shows four of these designs. The first type has the conventional uniform square diaphragm for comparison purposes and the second type has a double-boss square diaphragm, with the sensing resistors located on the thinner part of the diaphragm (near the edges and the center). Because their transverse gage factor is much smaller than its longitudinal one, the polysilicon resistors are oriented toward the center to experience the longitudinal stress. The second type has a thick beam connecting the double bosses and crossing the whole diaphragm, while the polysilicon resistors are placed on the narrow parts of the beam. The third type has two double-bossed beams perpendicular to each other. We initially expected that the stiffness of the diaphragms would increase from type I to type IV. Specific processing details are presented later. Figure 4.2 presents microphotographs of the fabricated type III and IV pressure sensors.
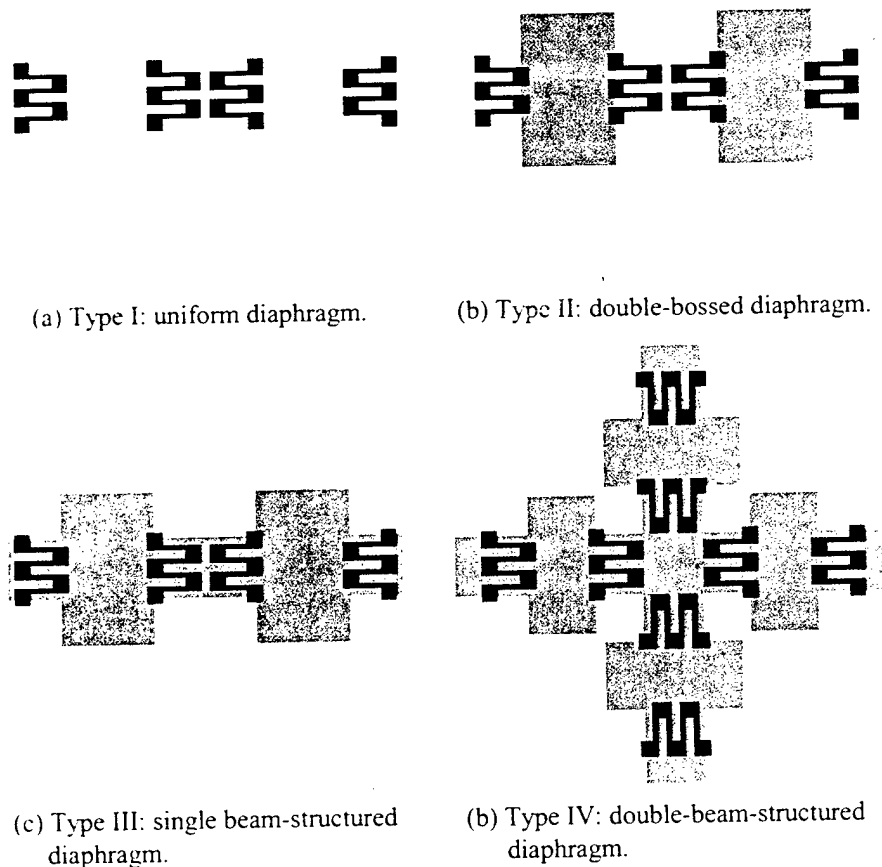


(a) Type I: uniform diaphragm.      (b) Type II: double-bossed diaphragm.

(c) Type III: single beam-structured diaphragm.      (b) Type IV: double-beam-structured diaphragm.

**Figure 4.1. Different structures of pressure sensors.**

We have tested some of the pressure sensors in a pressure chamber. It turned out that for type I sensors, the full-scale output can not exceed 40 mV/5 V for any pressure range below 30 psig. Out of our prediction, type II is worse than type I in every aspect. However, both type III and type IV are satisfactory. For example, type III gives 60 mV/5 V output for a full scale range of 10 psig (figures 4.1.a and 4.3) and type IV generates 95 mV/5 V for a full scale range of 20 psig (figures 4.1.b and 4.4). All these sensitivities are much higher than those of the previously developed surface micromachined pressure sensors. Other characteristics such as optimum power consumption (tradeoff between SNR and possible heat transfer to flow) and temperature sensitivity were also measured.



(a) Type III                    (b) Type IV
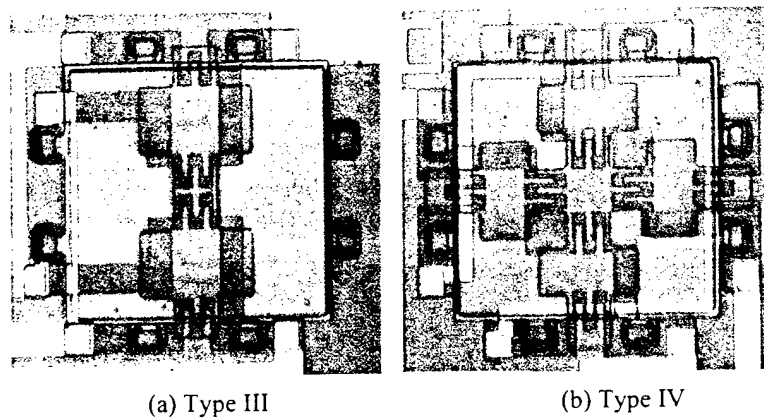
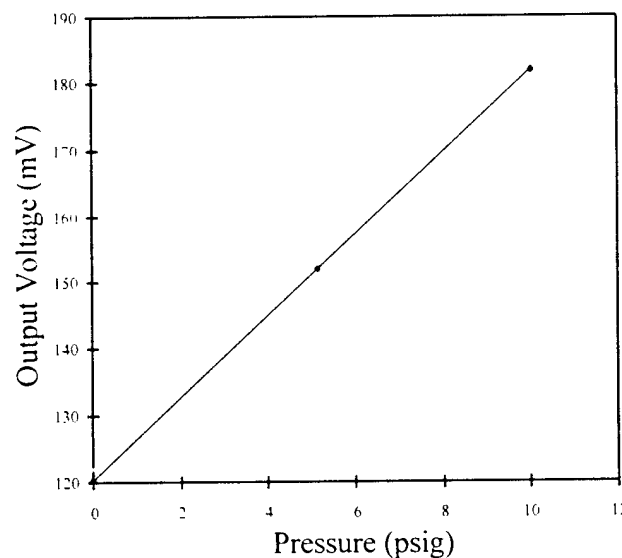**Figure 4.2. Pictures of types III and IV pressure sensors.**



**Figure 4.3. Pressure calibration results for type III sensor. The diaphragm thickness is 1 μm on the thin part and boss thickness is 3 μm. The nonlinearity for all the sensors is less than 1%.**
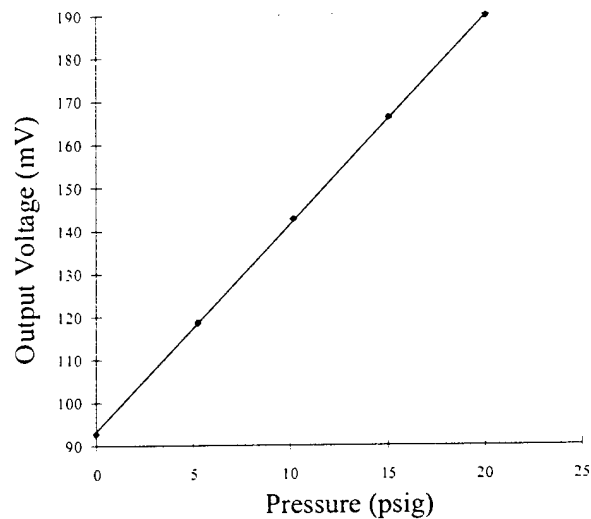
12

**Figure 4.4. Pressure calibration results for type IV sensor. The diaphragm thickness is 1 μm on the thin part and boss thickness is 3 μm. The nonlinearity for all the sensors is less than 1%.**

The knowledge gained from those tests was used to design and fabricate a pressure sensor skin in the shape of a cross. The layout (some layers hidden for the sake of clarity) for the skin is shown in Figure 4.5. The central square is approximately 1.2 mm on a side and contains 5 pressure sensors (shown as white squares). Each sensor sits atop a silicon island, but the arms of the cross are composed entirely of polyamide and metal lines and are completely flexible. We have improved upon our original flexible skin process in the areas of robustness and packaging. The original process (F. Jiang et al., 1997) (simplification shown in Figure 4.6) uses a wet silicon etch such as TMAH or KOH to create the backside cavities. For process compatibility issues, this choice necessitates creating the cavities early in the process, thus implying that a relatively fragile wafer be carefully handled through the rest of the process. The new process (simplification shown in Figure 4.7) uses deep reactive ion etching (DRIE) to create the cavities near the end of the process, after the sensors have been formed. Thus the yield increases significantly, wafer warpage issues are of no concern, and the processing is greatly simplified.

Another important innovation is the fabrication of backside contacts on the flexible skin. In short, the aluminum metalization is sandwiched between top and bottom layers of polyamide. We open up the bottom layer and use electroless gold plating to deposit a composite layer of nickel and gold on top of the aluminum. The top layer of gold is then easily attached to other packaging by means of solder paste, for example. This technology can simplify packaging immensely, as it minimizes hand assembly. A conceptual drawing of this bond is shown in Figure 4.8.
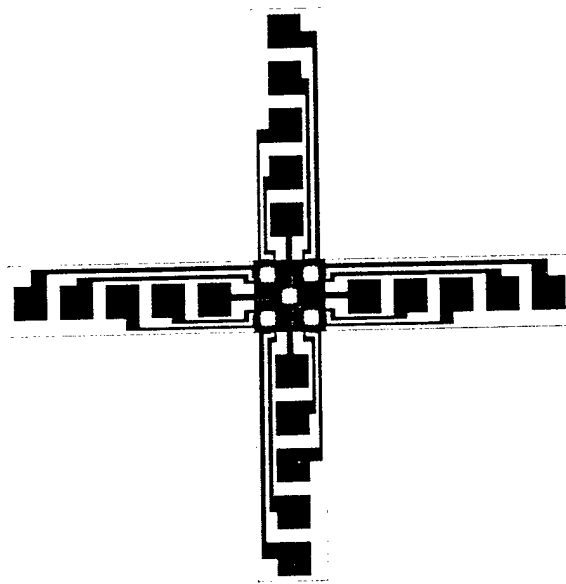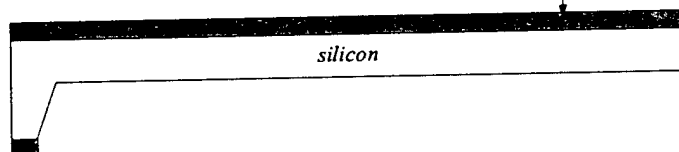
**Figure 4.5. Layout of the pressure sensor array.**
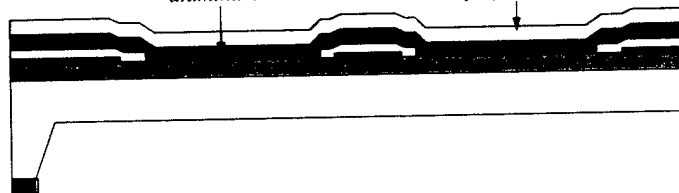
1. TMAH or KOH selectively etches backside.



2. Aluminum/polyimide/aluminum/polyimide processing on frontside.



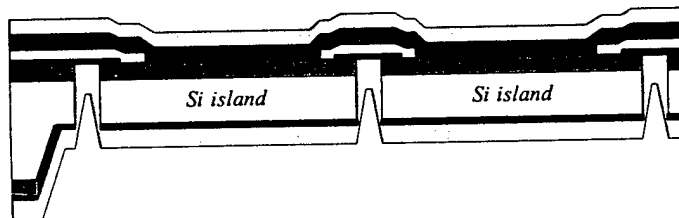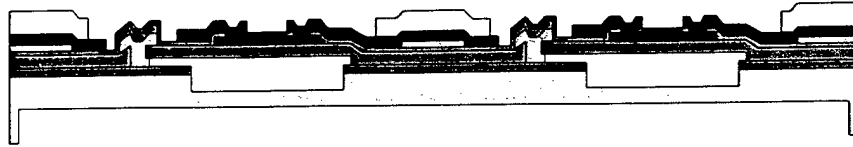3. RIE etches backside using Al mask. Polyimide processing on backside.
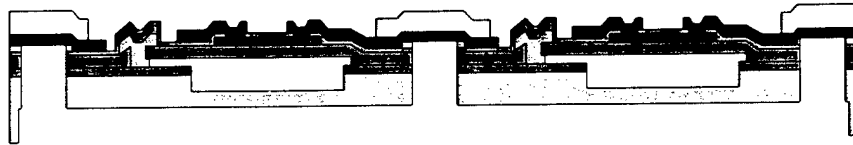


**Figure 4.6. Simplified process flow for original flexible skin.**

12. Pattern backside; RIE etches nitride; DRIE etches Si to 70 μm thick.



13. DRIE etches away silicon between islands; RIE removes nitride;
    Pad etchant removes LTO.



14. Spin, cure and pattern polyimide on the backside. Electroless plate
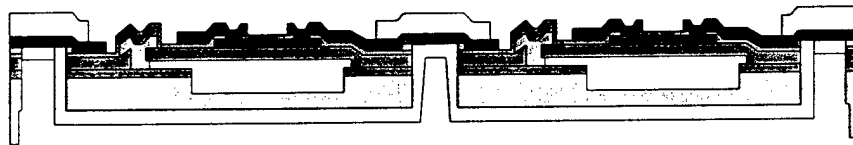    nickel/gold on the backside pads.



**Figure 4.7. Improved process flow using DRIE, backside contacts, and electroless plating.
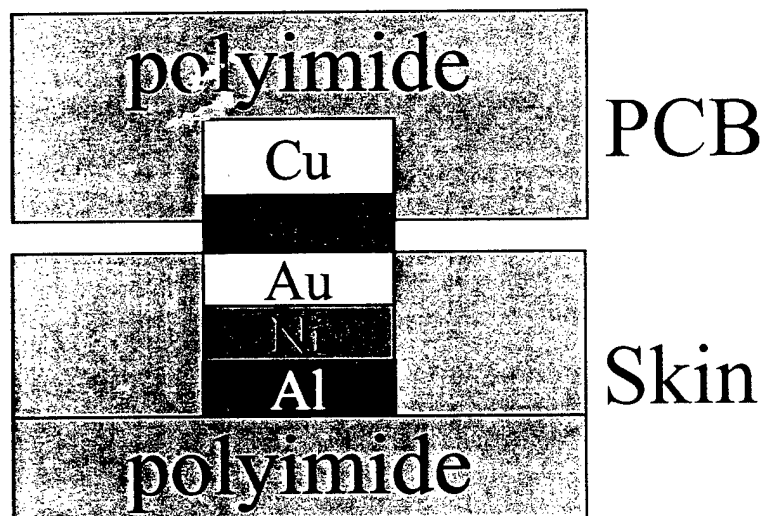Layout of the pressure sensor array.**



**Figure 4.8. Conceptual drawing of new packaging technology.**

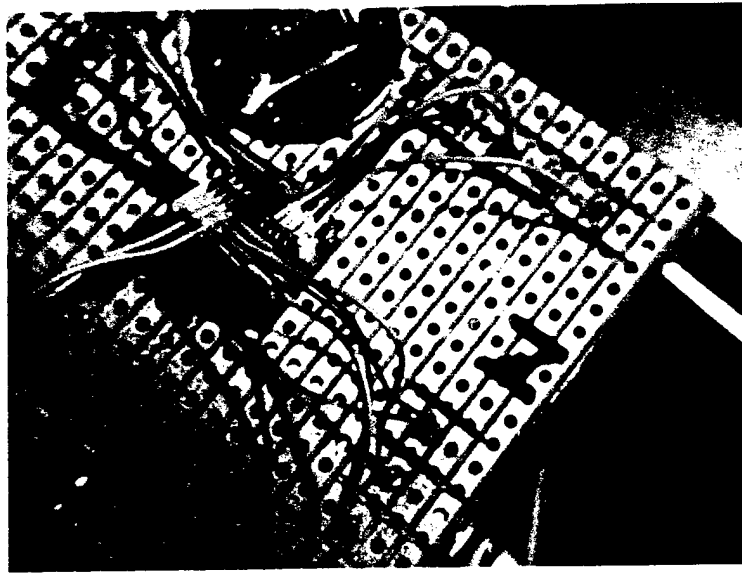**Figure 4.9. MEMS array electrical connector (socket).**
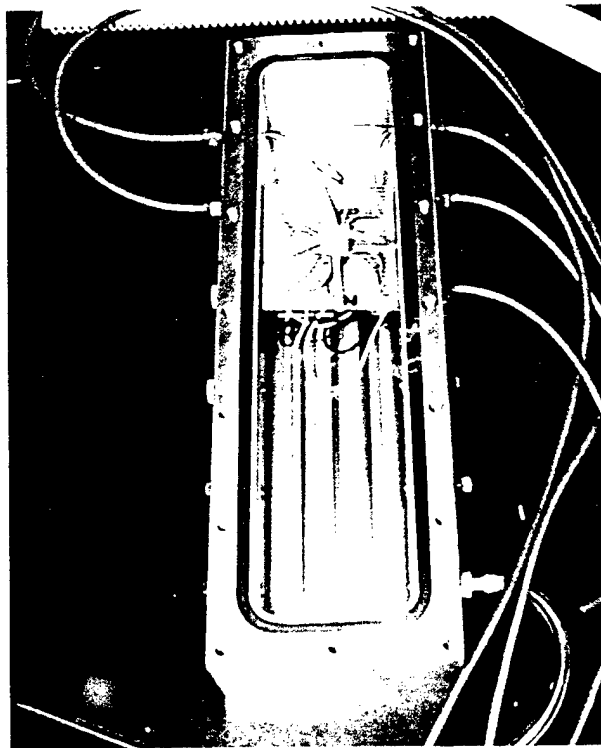


**Figure 4.10. Pressure chamber for calibration of MEMS sensor arrays.**

The socket and MEMS sensor shown in figure 4.9 was subsequently placed inside a pressure chamber (figure 4.10) for sensor array calibration. The chamber is supplied with adjustable and accurately known pressure, while the signal response from all of the sensors are

recorded. A typical MEMS pressure sensor calibration curve is shown in figure 4.11. This curve shows the raw recorded voltage from the MEMS sensor without offset compensation or amplification.



**Figure 4.11. Typical calibration curve for MEMS pressure sensor.**

# 5. PROBE ASSEMBLY

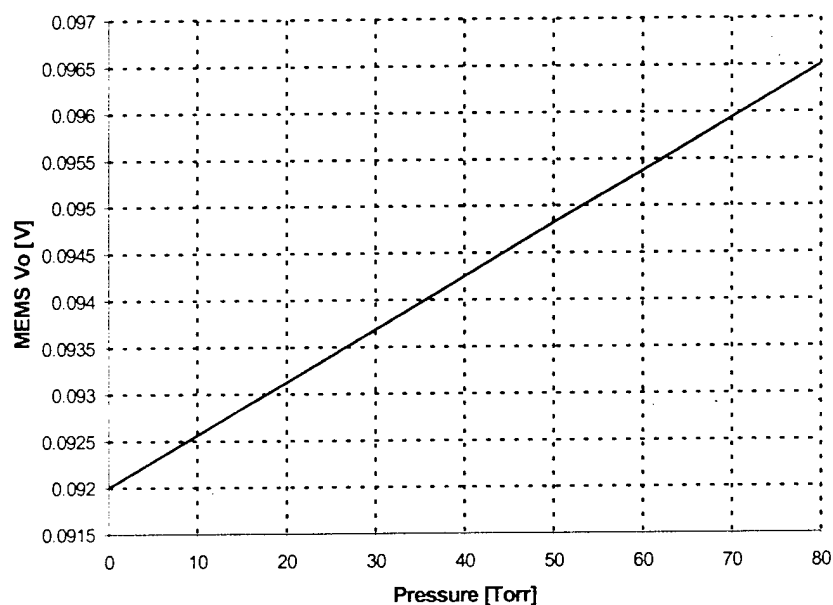This sections discusses the processes involved in the fabrication of the different probe components and the subsequent probe assembly. Figure 5.1 shows the fabricated stage. The stage is 2 mm diameter brass, approximately 1 mm thick. The pocket is 0.005 inches deep, and is machined with a 0.010" diameter cutter, as are the four slots. The pocket corners are cleared to allow the MEMS array to be accurately positioned relative to the outside diameter of the stage. The slots for the wiring ribbons go completely through the stage, to allow access to the soldering pads on the wires from the MEMS array. The "sealer", is used to accurately position the tubes on the MEMS array, so that epoxy can be placed around the outside diameter of each tube. A picture of the first-generation fabricated sealer is shown in figure 5.2 against an adult's fingerprints to illustrate its size. Figure 5.3 shows the MEMS sensor array installed in the stage, while the figure 5.4 shows the assembly after the sealer is installed. The five MEMS pressure sensors can be seen through the openings of the sealer. Finally, in order for the reader to perceive the size of the probe, figure 5.5 presents pictures of the MEMS-probe on a quarter and figure 5.6 shows the probe between an adult's thumb and index fingers. Figure 5.7 shows a typical miniature probe tip.
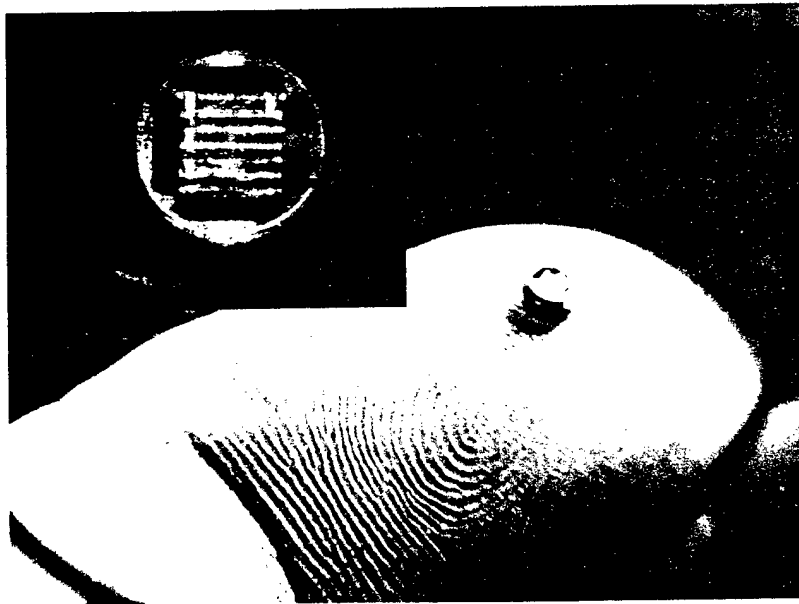


Figure 5.1. Details of the stage inside which the MEMS pressure array is housed.
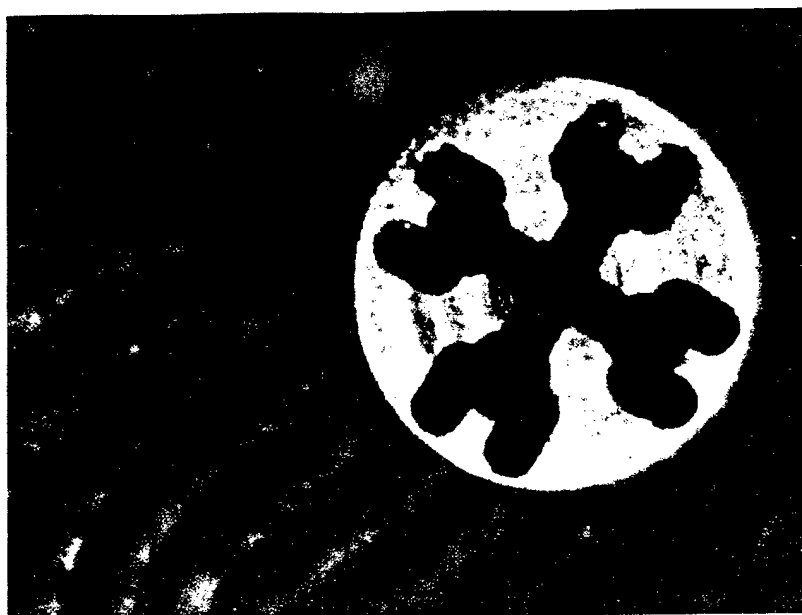
Figure 5.2. Picture of first-generation fabricated sealer shown against an adult's fingerprints.



Figure 5.3. MEMS sensor array installed in the stage.

**Figure 5.4. Picture of assembly after the sealer is installed. The five MEMS pressure sensors can be seen through the openings of the sealer.**



**Figure 5.5. MEMS Sensor housing on a quarter.**

**Figure 5.6. Probe between thumb and index finger.**



**Figure 5.7. Typical probe tip.**

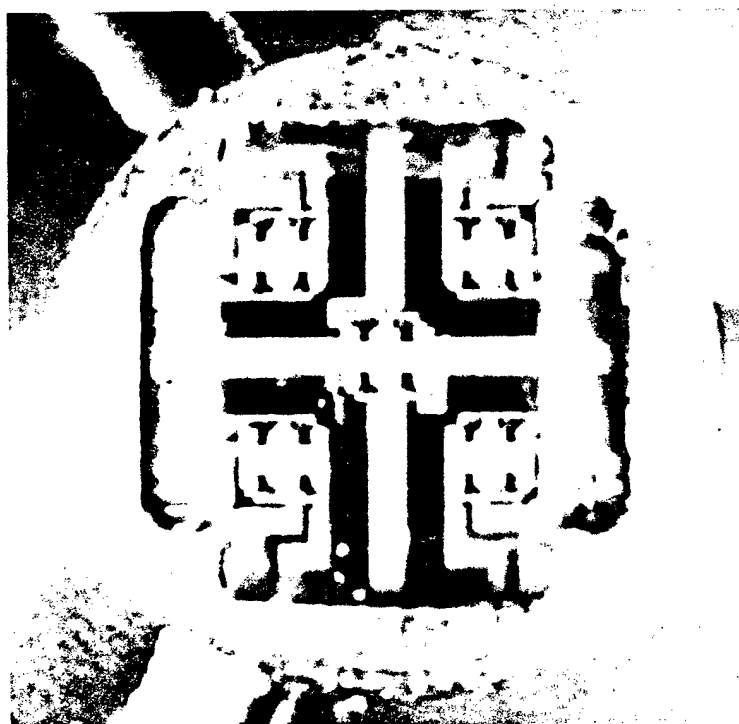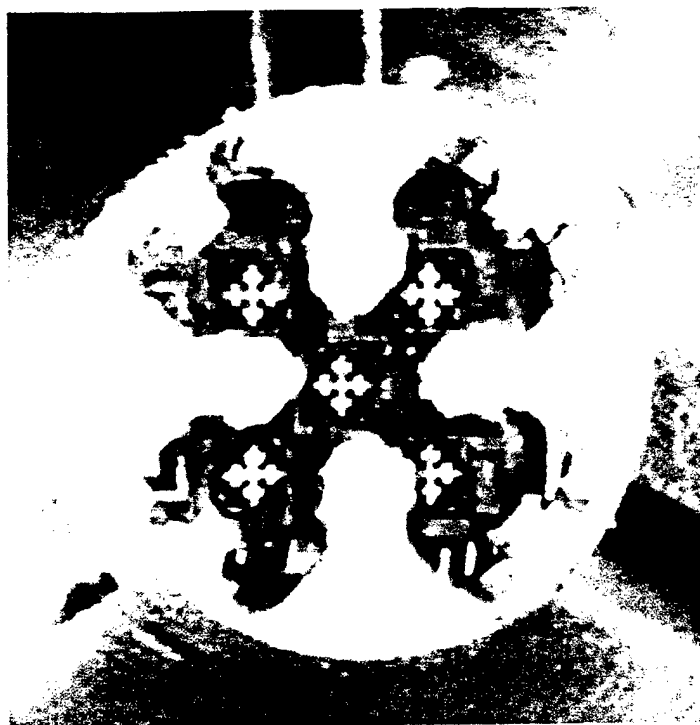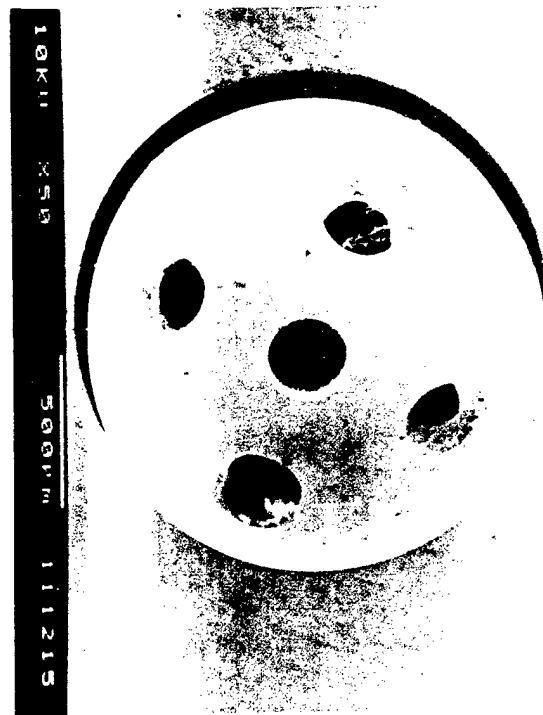In order to appreciate the fabrication and assembly of the probe components, it is necessary to understand the processes involved in miniaturization and the challenges faced by the designer and the technician. We define miniaturization by the size of the cutting tools and part geometry, usually between 0.004" and 0.030". For example, the MEMS probe has an outside diameter of 0.094", but its features require a 0.010" diameter cutting tool, with material thickness as low as 0.004".

The primary challenge in miniaturization arises from scaling down the forces required to machine the material. A miniature tool can only withstand very small forces, so that force must be carefully controlled and spread over the cutting surface. The parameters established in conventional machining usually rely on percentages to calculate depth of cut and feed rate, but these percentages must be adjusted to preserve the miniature tool. For example, the 0.010" cutting tool can cut its full diameter up to .002" deep, feeding at 0.001 inch/second, while spinning at 20,000 rpm (for Brass). The tool pressure and vibration might deflect the tool a full 10% of its diameter, increasing the slot thickness an unpredictable 0.001". While 0.001" is considered precise in conventional machining, it is obviously a large tolerance in miniaturization, where the 0.004" material thickness could be reduced to 0.002" if cuts are made on both sides, a 50% error. This unpredictability is compounded by the lack of instrumentation to accurately measure the result of a machining operation, particularly while the piece is fixed and located in the machine. Optical comparison is the best technique for measuring these small features, but it requires releasing the work-piece and losing its location coordinates. We can measure the end result but we cannot realistically change it if it is incorrect.

A major concern of miniaturization is work-holding and locating. The precision required in locating a miniature work-piece is near the limit of conventional indicators, which can measure 0.0001". Indicators can find the center of round parts accurately, but cannot locate an edge or surface. To do this, a technique called "touch-off" is used, where the spinning cutting tool is actually moved into contact with the work-piece to establish the coordinate. The precision of location or depth of cut is then dependent on the precision of the touch-off, which is limited by the ability of the technician to determine the point of contact. Again, in conventional machining this is considered a very accurate technique, but it is certainly less than optimal in miniaturization.

# 6. INITIAL EVALUATION OF UNSTEADY EFFECTS ON PROBE CALIBRATION

As discussed in the introduction, the inertial effects due to the unsteady flow over the probe tip (hemispherical), are most prominent. In order to first evaluate them and subsequently account for them, we consider the unsteady potential incompressible flow over a sphere of radius a moving in a fluid at rest, with a velocity U(t) along the negative z-axis (figure 6.1).
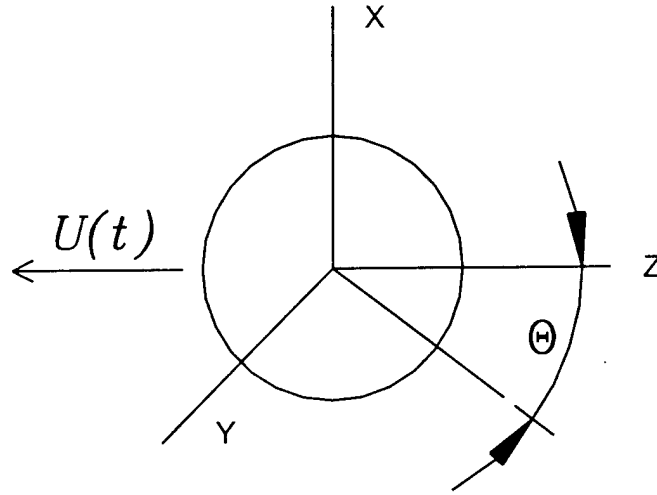


**Figure 6.1. The coordinate system.**

The perturbation potential around the sphere is:

$$\phi(r, \theta, t) = \frac{U(t)a^3 \cos\theta}{2r^2} \qquad (6.1)$$

The pressure over the surface of the sphere is given by the unsteady Bernoulli equation:

$$P(r, \theta, t) = P_r - \rho\left(\frac{\partial\phi}{\partial t} - (\bar{V}_0 + \bar{\Omega} \times \bar{r}) \cdot \bar{V} + \frac{1}{2}\bar{V}^2\right) \qquad (6.2)$$

where:

$$\bar{V}_0 = \left(-U(t)\cos\theta, U(t)\sin\theta, 0\right) \qquad (6.3)$$

is the velocity of the sphere and $\bar{\Omega}(t)$ is the rotation of the sphere. By specifying functions for $U(t)$ and $\bar{\Omega}(t)$, unsteadiness in both velocity magnitude and direction can be accounted for. Since both effects are on the same order of magnitude, here for simplicity, we will set:

$$\bar{\Omega} = 0, \quad \bar{\Omega} \times \bar{r} = 0 \qquad (6.4)$$

The flow velocity is:

$$\bar{V} = \bar{\nabla}\phi = (\frac{\partial\phi}{\partial r}, \frac{1}{r}\frac{\partial\phi}{\partial\theta}, \frac{1}{r\sin\theta}\frac{\partial\phi}{\partial\psi})$$

$$= (-\frac{U(t)\, a^3\cos\theta}{r^3}, \frac{1}{r}\frac{U(t)\, a^3(-\sin\theta)}{2r^2}, 0) \qquad (6.5)$$

$$= (-\frac{U(t)\, a^3\cos\theta}{r^3}, -\frac{U(t)\, a^3\sin\theta}{2r^3}, 0)$$

On the sphere surface (r=a):

$$\bar{V}_0\cdot\bar{\nabla}\phi = (-U(t)\cos\theta, U(t)\sin\theta, 0)$$

$$\cdot(-U(t)\cos\theta, \frac{-U\sin\theta}{2}, 0)$$

$$= U^2(t)\cos^2\theta - \frac{U^2(t)\sin^2\theta}{2} \qquad (6.6)$$

$$\frac{1}{2}(\bar{\nabla}\phi)^2 = \frac{1}{2}(U^2(t)\cos^2\theta + \frac{U^2(t)\sin^2\theta}{4})$$

Also for r=a:

$$\frac{\partial\phi}{\partial t} = \frac{a}{2}\frac{dU(t)}{dt}\cos\theta = \frac{U'(t)\, a}{2}\cos\theta \qquad (6.7)$$

Then by combining the above into equation 5.2 we get:

$$P(r, \theta, t) = P_r - \rho(\frac{\partial\phi}{\partial t} - \bar{V}_0\cdot\bar{V} + \frac{1}{2}\bar{V}^2)$$

$$= P_r + \frac{\rho}{2}(\frac{U^2(t)}{4}(9\cos^2\theta - 5) \qquad (6.8)$$

$$- U'(t)a\cos\theta\,)$$

where

$$\delta P = (P - P_r) = \frac{\rho}{2}(\frac{U^2(t)}{4}(9\cos^2\theta - 5)$$

$$- U'(t)a\cos\theta\,) \qquad (6.9)$$

$$= \delta P_1 + \delta P_2$$

from this

24

$$\delta P_1 = \frac{\rho U^2(t)}{2}(1 - \frac{9}{4}\sin^2\theta) \qquad (6.10)$$

$$\delta P_2 = -\frac{\rho U'(t)a}{2}\cos\theta \qquad (6.11)$$

where $\delta P1$ is the steady pressure term and $\delta P2$ is the unsteady pressure term. If we had considered unsteadiness in the velocity direction as well, the last term would have been:

$$\delta P_2 = -\frac{\rho a}{2}\frac{\partial}{\partial t}[U(t)\cos\theta] \qquad (6.12)$$

By dividing these by $\rho U^2(t)/2$ we arrive at:

$$Cp_{quasi-steady} = \frac{\delta P_1}{\frac{\rho U^2(t)}{2}} = 1 - \frac{9}{4}\sin^2\theta \qquad (6.13)$$

$$Cp_{unsteady} = \frac{\delta P_1 + \delta P_2}{\frac{\rho U^2(t)}{2}}$$
$$= (1 - \frac{9}{4}\sin^2\theta) - \frac{U'(t)a}{U^2(t)}\cos\theta \qquad (6.14)$$

Therefore if we consider quasi-steady probe calibration, i.e. ignore the effects of the unsteady pressure term, we make the following error:

$$\frac{\delta P_2}{\delta P_1 + \delta P_2} = \frac{Cp_{unsteady} - Cp_{quasi-steady}}{Cp_{unsteady}} \qquad (6.15)$$

In order to evaluate this error, let us consider a sinusoidal variation for $U(t)$:

$$U(t) = U_0(1 + A\sin(2\pi f t)) \qquad (6.16)$$

By introducing the non-dimensional frequency

$$K = \frac{2\pi f a}{U_0} \qquad (6.17)$$

the error becomes

$$E = \frac{-AK \cos(\theta) \cos(\phi)}{(1 + A \sin(\phi))^2 \left[1 - \frac{9}{4} \sin^2(\theta)\right] - AK \cos(\theta) \cos(\phi)}$$

(6.18)

where $\phi = 2\pi f t$.

Figures 6.2 and 6.3 present the dependence of error $E$ (its maximum value within one period of oscillation) on the non-dimensional frequency $K$ and the amplitude of the velocity oscillation $A$, for small (figure 6.2) and large (figure 6.3) values of $K$. Figure 6.2 illustrates the point that there is a range of $K$ values, corresponding to practical unsteady flowfields, for which the error made by ignoring unsteady aerodynamic effects is negligible (less than 1%), therefore steady probe calibration would provide accurate measurements. For example consider a flow with a mean velocity $U_0$ of 50m/sec, an amplitude $A$ of 20% of the mean and an oscillation frequency of 250 Hz. That could, for example, correspond to the unsteady flow downstream of a circular cylinder (vortex shedding) 4cm in diameter. For a MEMS probe with a diameter $2a=1.5$ mm, the resulting non-dimensional frequency $K$ is 0.023, which yields (from figure 6.2) an acceptable error of 0.5%. Therefore the development of a steady probe calibration algorithm is important. Many such algorithms have appeared in the literature. As discussed later, the novelty of the steady algorithm developed and presented here resides in its achieved accuracy levels and its breadth of application.



**Figure 6.2. The maximum error in steady vs. unsteady pressure coefficent, E, as a function of the non-dimensional frequency, K at discrete amplitudes, A.**

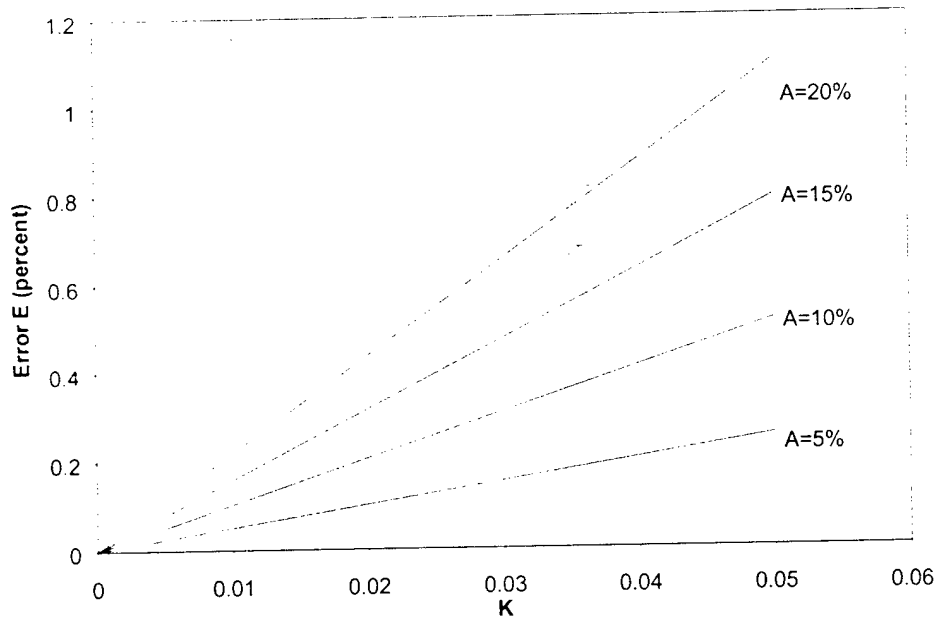**Figure 6.3. The maximum error in steady vs. unsteady pressure coefficent, E, as a function of the non-dimensional frequency, K at discrete amplitudes, A.**

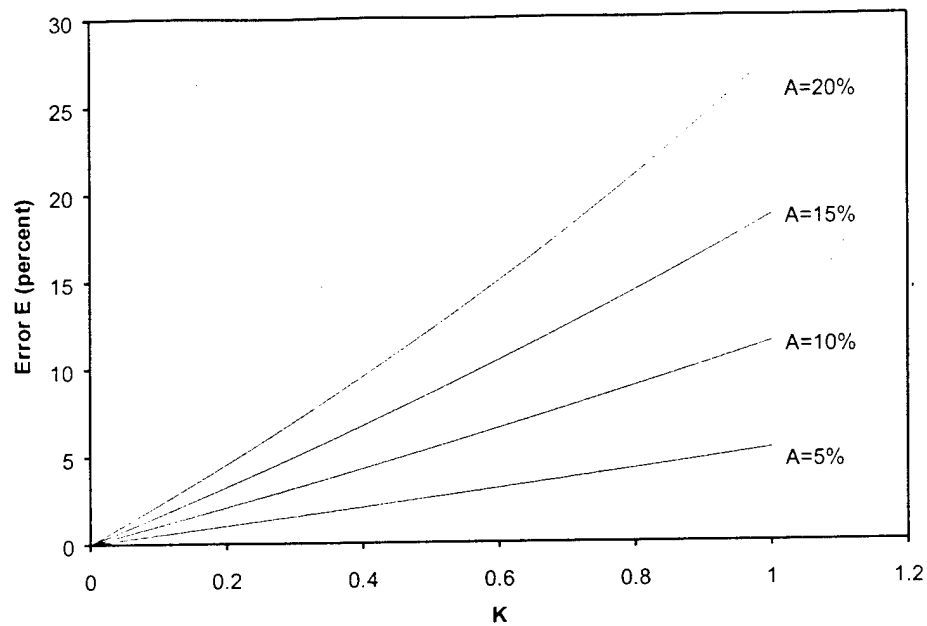With that said, if one considers turbulent flows with fluctuation frequencies on the order of kHz or tens of kHz, the error E becomes non-negligible (figure 6.3), which stresses the need for unsteady probe calibration theory and algorithms as well.

# 7. STEADY PROBE CALIBRATION ALGORITHMS

## 7.1. Local Least-Squares Algorithm

The port pressures recorded from the multi-hole probe in an unknown flow field form a "signature" that is used to determine the flow angularity and magnitude. The analysis of the pressure signature to obtain flow conditions is usually performed with a data reduction algorithm. The topic discussed in this section is the development of a high-accuracy data reduction algorithm for 5-hole (and generally multi-hole) pressure probes.

Historically, a number of different calibration techniques have been utilized for multi-hole probes, all with their own advantages and difficulties. A commonly used method for hemispherical probe tips has been to apply the potential flow equations for a sphere to relate the flow angle velocity magnitude with the pressure differentials measured by the probe. Kjelgaard (1988) used this technique on a hemispherical tipped 5-hole probe. The potential flow calibration method is a direct calculation of properties from a theoretical probe model. This approach is very sensitive to construction defects of the probe tip. When minimizing the probe size manufacturing irregularities are becoming unavoidable and the relative deviation of the physical probe from the theoretical design is increasing. To compensate for the manufacturing defects, each probe has to be calibrated individually using extensive calibration routines.

A method of calibrating multi-hole probes is to insert the probe into a flow field of known magnitude and direction. The probe is then rotated and pitched through a range of known angles, to simulate every possible measurable velocity inclination. For each of the specific angles the pressures from all the pressure ports are recorded and stored in a database. Angle increments are typically 0.5 to 5 degrees yielding a database with several thousand data points, each with a pressure signature that is unique for that angle inclination and velocity magnitude. A calibrated probe can be inserted into an unknown flow field and accurately predict the velocity vector by recording the port pressures and comparing them with the calibration database through a set of non-dimensional coefficients. By interpolation of the recorded angles and pressure coefficients in the calibration database the velocity vector is accurately predicted. Unless the probe is physically damaged the probe will keep its characteristics and only one calibration is required for the lifetime of the probe.

Several methods of comparing the measured pressures with the database have been developed. Bryer and Pankhurst (1971) applied relationships derived from a set of pressure coefficients over the different flow regions of the probe. On a 5-hole probe the measuring regions on the probe were divided into one low angle regime and 4 high angle regimes corresponding to the center port and each of the peripheral ports, respectively. The calibration data was used to derive empirical relationships representing the relative angle inclinations and the magnitude of the velocity vector in terms of the measured pressure coefficients. Using the calibration data points, polynomial curve fits were generated that described the variation of the angle and pressure coefficients throughout the calibration domain. Rediniotis et al. (1993) derived polynomial fits for calibration data for conical 7-hole probes. Further they divided the port specific regions into several sections thus increasing the number of regions for which polynomials were used to describe the calibration coefficients. They created 8 regions describing

the low angle flow (where the center port senses the highest pressure) and 32 high angle regions (where any of the 6 peripheral pressure senses the highest pressure). The method of subdividing the regions increased the agreement of the polynomial fit through the calibration points, but did not necessarily ensure well-behaved calibration surfaces between data points.

The polynomial fit techniques mentioned are global in nature, that is: they generate polynomial fits for relatively large sectors or regions. Though Rediniotis et al. (1993) reduced the region size by subdividing the sectors, the individual regions were still large and could, depending on the density of the calibration data, contain hundreds of data points. Using polynomial fits for large regions can cause the overall prediction accuracy to decline because of the large number of calibration points the fit tries to model. Utilizing a local interpolation scheme instead of a region wide polynomial fit has also been used with multi-hole probe calibration methods. Zilliac (1989) calibrated conical tipped 7-hole probes for use in flow fields with high angularity. For each of the calibration points, the seven port pressures, the total pressure and the known pitch and roll angles were recorded in a database. Sets of non-dimensional angle and pressure coefficients were also stored in the calibration database. For a calibrated probe in an unknown flow field the seven port pressures were recorded and the non-dimensional coefficients calculated. By searching the calibration database for similar coefficient values the approximate flow conditions were identified. Adjacent coefficient values were interpolated to solve for intermediate angles and pressure coefficient values. The accuracy of this technique is dependent on the density of the calibration data.

Applying the two different principles described, the regional polynomial fit and the local data point interpolation, a method is derived to calculate a polynomial interpolation that is local in nature. Using only a few selected data points that have similar angle coefficients as the measured angle coefficients, a low-order polynomial fit is created. The development of a local least-squares (LLS) data reduction algorithm is described in detail in this section.

The flow over a 5-sensor probe can typically be divided into two flow regimes: low-angle (or low-angularity) and high-angle (or high-angularity) regimes. For calibration purposes, all possible velocity vector orientations with respect to the probe are represented by five sectors. Each sector (figure 7.1.1) is identified by a number indicating the port/sensor that senses the highest pressure for all the possible velocity orientations in that sector. For low-angle flow, the highest pressure is registered by port #1 (central hole) while for high-angle flow the highest pressure occurs in one of the peripheral holes 2 through 5.

The local velocity vector at any measurement location can be fully characterized by four variables. For low-angle flow these variables are: pitch angle $\alpha$, yaw angle $\beta$, total pressure coefficient $A_t$ and static pressure coefficient $A_s$. For high-angle (or high-angularity) flow the variables are: cone angle $\theta$, roll angle $\phi$, $A_t$ and $A_s$. These variables need to be determined as functions of the five measured pressures or equivalently, the two non-dimensional pressure coefficients formed from these pressures: $b_\alpha$, $b_\beta$ for low-angle flow and $b_\theta$, $b_\phi$ for high-angle flow (Rediniotis et al., 1993; Everett et al., 1983). The two different systems of angles, (pitch angle $\alpha$, yaw angle $\beta$) and (cone angle $\theta$, roll angle $\phi$), used to describe the velocity vector orientation with respect to the probe, in low angularity and high angularity flow, respectively, are shown in figure 7.1.2.

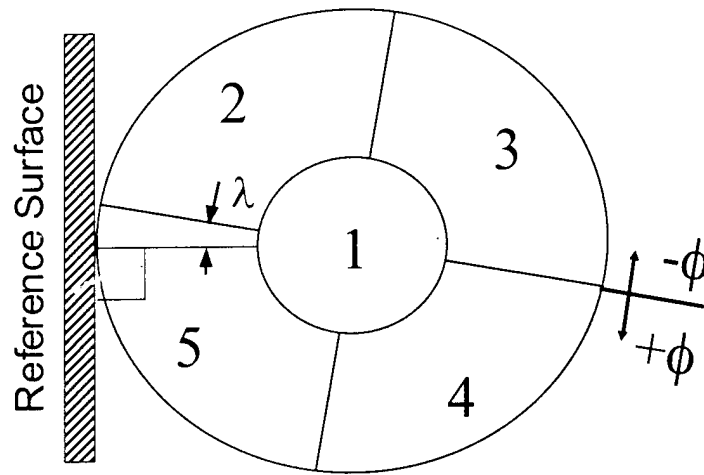**Figure 7.1.1. The 5-sensor probe measurement domain is divided into 5 sectors, each centered on an individual pressure port, labeled 1 through 5.**
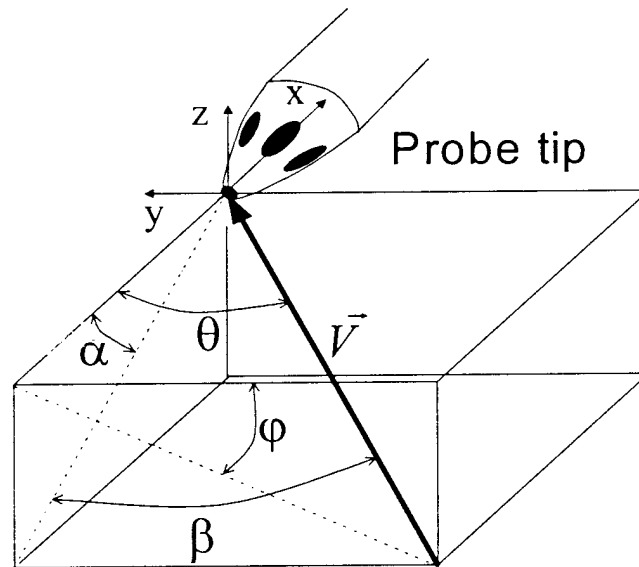


**Figure 7.1.2. Definition of angles used to define the velocity vector orientation with respect to the probe.**

The conversion from the pitch and yaw angles to the cone and roll angles is:

$$\theta = \cos^{-1}(\cos \alpha \cdot \cos \beta) \qquad (7.1.1)$$

$$\phi = \tan^{-1}\left(\frac{\sin\alpha}{\tan\beta}\right) \qquad (7.1.2)$$

For a 5-sensor probe in the low angle flow regime (highest pressure sensed by port 1) the following definitions are used:

$$b_\alpha = \frac{(p_5 + p_4 - p_3 - p_2)}{2 \cdot q} \qquad (7.1.3)$$

$$b_\beta = \frac{(p_4 + p_3 - p_2 - p_5)}{2 \cdot q} \qquad (7.1.4)$$

$$A_t = \frac{(p_1 - p_t)}{q} \qquad (7.1.5)$$

$$A_s = \frac{q}{(p_t - p_s)} \qquad (7.1.6)$$

and the pitch angle, $\alpha$, and yaw angle, $\beta$, as defined in figure 11. The pseudo-dynamic pressure, $q$, is defined as:

$$q = p_1 - \frac{(p_2 + p_3 + p_4 + p_5)}{4} \qquad (7.1.7)$$

For a 5-sensor probe in the high angle flow regime (highest pressure sensed by one of the peripheral ports 2-5) the following definitions are used:

$$b_\theta = \frac{(p_i - p_1)}{q} \qquad (7.1.8)$$

$$b_\phi = \frac{(p^\cdot - p^-)}{q} \qquad (7.1.9)$$

$$A_t = \frac{(p_i - p_t)}{q} \qquad (7.1.10)$$

$$A_s = \frac{(p_i - p_s)}{q} \qquad (7.1.11)$$

and the cone angle, $\theta$, and roll angle, $\phi$, as defined in figure 7.1.2.

31

The pseudo dynamic pressure, q, is defined as:

$$q = p_i - \frac{(p^+ + p^-)}{2} \qquad (7.1.12)$$

In the previous definitions $p_i$ is the highest measured pressure (at the $i^{th}$ port). Looking into the probe tip: $p^+$ and $p^-$ are the pressures measured by the peripheral holes adjacent to port i, in the clockwise and counterclockwise direction respectively. The input coefficients $b_\alpha$, $b_\theta$ will be referred to as b1 and $b_\beta$, $b_\phi$ will be referred to as b2 in the remainder of this text since many of the processes described below use both high and low angle definitions in the same manner.

During probe calibration, a large set of calibration data containing the known velocity vector orientation and magnitude, and the 5 port pressures, is obtained for the desired range of Mach and Reynolds numbers, using a probe calibration setup. Then, in an actual flow-diagnostics experiment, the local flow variables (three velocity components, static and total pressure, Mach and Reynolds number) are calculated as follows: The 5 port pressures are recorded and the non-dimensional pressure coefficients b1 and b2 are calculated. That is $b_\alpha$ and $b_\beta$ for low-angle flow and $b_\theta$ and $b_\phi$ for high-angle flow. The port with maximum pressure is detected and the corresponding low- or high-angle calibration sector is determined. The calibration database is then searched, the calibration points associated with the particular sector are identified and the n closest points to the test point (in terms of proximity in the (b1, b2) plane, as shown in figure 7.1.3) are retained. These closest data points are found in terms of Euclidean distance (in the discussion that follows, subscripts C and T stand for "calibration" and "test", respectively):

$$D_j = \sqrt{\left( \frac{\Delta b2}{\Delta b1} \left( (b1_C)_j - b1_T \right) \right)^2 + \left( (b2_C)_j - b2_T \right)^2} \qquad (7.1.13)$$

where the index j is the calibration point number and $D_j$ is the Euclidean distance, in the (b1, b2) plane, from the tested point (b1$_T$,b2$_T$) to the scaled coefficients of the calibration point (b1$_C$,b2$_C$)$_j$. A global scaling factor, $\Delta b2/\Delta b1$, is introduced to bring the two coefficients b1 and b2 on the same order. This factor is defined using the maximum and minimum values of the coefficients found in the calibration file, and is stored in the calibration database:

$$\frac{\Delta b2}{\Delta b1} = \frac{(b2_C)_{max} - (b2_C)_{min}}{(b1_C)_{max} - (b1_C)_{min}} \qquad (7.1.14)$$

Each of the n selected calibration points is represented by a circle in figure 7.1.3, while the test point is represented by a star. The number n is user defined. Then, a local least-squares interpolation is performed in order to determine the four flow variables, $(A_t, A_s, \alpha, \beta)$ or $(A_t, A_s, \theta, \phi)$, for the test point.

It is necessary that the selected calibration points ($b1_C$, $b2_C$) be uniformly distributed around the test point ($b1_T$, $b2_T$) to obtain a well-behaved polynomial surface and allow for interpolation rather than extrapolation. A procedure checks if the closest calibration points in triplets form triangles around the test point in the b1-b2 plane. The original ranking of the closest points based on Euclidean distance, $D_j$, can be altered to ensure that (if at all possible) combination of the overall closest points forms a triangle around the test point. Typically the algorithm searches for two such triangles.
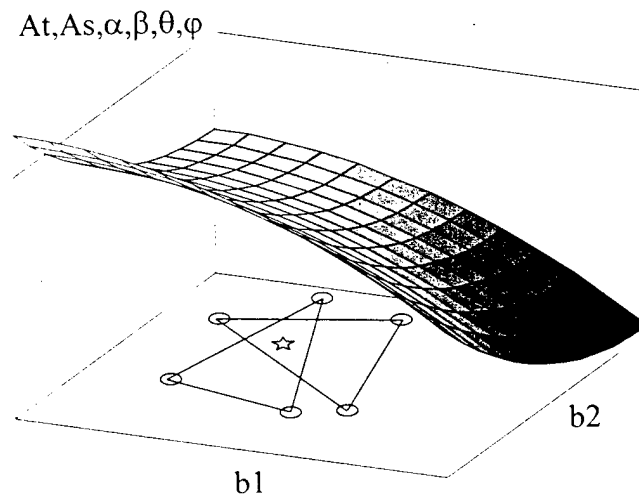


**Figure 7.1.3. A local least-squares interpolation surface with triangulation in the b1-b2 plane.**

In figure 7.1.3 the star indicates the test point ($b1_T$,$b2_T$) and the circles at the corners of the triangles indicate the closest selected calibration points ($b1_C$,$b2_C$) that are also checked for the triangulation requirement. Each triangle is calculated in the following manner (figure 7.1.4):
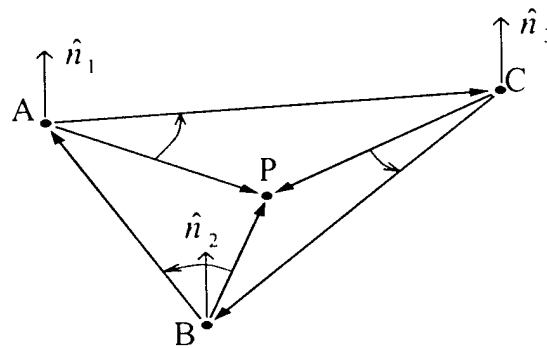


**Figure 7.1.4. The triangulation scheme in the b1-b2 plane.**

$$\hat{n}_1 = \vec{AP} \times \vec{AC} \qquad (7.1.15)$$

$$\hat{n}_2 = \vec{CP} \times \vec{CB} \qquad (7.1.16)$$

$$\hat{n}_3 = \vec{BP} \times \vec{BA} \qquad (7.1.17)$$

where P is the test point $(b1_T, b2_T)$ and A, B, C are three calibration points $(b1_C, b2_C)_j$. $\hat{n}_1$, $\hat{n}_2$ and $\hat{n}_3$ are directional vectors normal to the b1-b2 plane. If all the 3 vectors have the same direction the test point P is within the triangle, otherwise P is outside the triangle.

Calibration points far from the tested point (in the b1-b2 plane) are assumed to have little or no influence on the calculation. Therefore, a local interpolation scheme is used and only calibration points close to the test point are used in the evaluation. A least-squares surface fit technique is used to calculate the two flow angles and the two pressure coefficients as functions of the independent input variables:

$$\alpha = \alpha(b1, b2) \qquad (7.1.18)$$

$$\beta = \beta(b1, b2) \qquad (7.1.19)$$

$$\theta = \theta(b1, b2) \qquad (7.1.20)$$

$$\phi = \phi(b1, b2) \qquad (7.1.21)$$

$$A_t = A_t(b1, b2) \qquad (7.1.22)$$

$$A_s = A_s(b1, b2) \qquad (7.1.23)$$

The selected closest and triangulation-checked calibration points (minimum number determined by the order of the polynomial surface) are used to calculate 4 separate interpolation surfaces. For a linear surface the following polynomial is used to describe the surface:

$$f(b1, b2) = a_0 + a_1 \cdot b1 + a_2 \cdot b2 \qquad (7.1.24)$$

where f can be any of the dependent variables $\alpha$, $\beta$, $\theta$, $\phi$, $A_t$, $A_s$ and $a_0$, $a_1$, $a_2$ are the least-squares polynomial coefficients. After the algorithm determines the polynomial coefficients ($a_0$, $a_1$ and $a_2$), entering the measured input coefficients $(b1_T, b2_T)$ into the calculated function $f(b1, b2)$, interpolated values for $\alpha_T$, $\beta_T$, $\theta_T$, $\phi_T$, $(A_t)_T$ and $(A_s)_T$ are obtained. The angle or pressure coefficient surfaces for the probe are locally smooth and do not exhibit any large gradients or discontinuities. The local least-squares method generates a surface that does not directly go through all the calibration data points, but is rather an average surface. A standard polynomial surface fit can exhibit large fluctuations since the surface is forced to go through all the data

points. The least-squares surface moderates the effect of a badly selected or measured calibration point.

Subsequently, the total pressure and static pressure are calculated from the non-dimensional pressure coefficients $(A_t)_T$, $(A_s)_T$:

$$p_t = p_i - (A_t)_T \cdot q_T \qquad (7.1.25)$$

$$p_s = p_t - \frac{q_T}{(A_s)_T} \qquad (7.1.26)$$

The velocity magnitude and the flow conditions are calculated using adiabatic, perfect gas relationships for air. Mach number from total pressure and static pressure:

$$M = \sqrt{\left(5 \cdot \left(e^{(-2/7 \cdot \ln(p_s/p_t))} - 1\right)\right)} \qquad (7.1.27)$$

Temperature, compressible dynamic pressure and density:

$$T = \frac{T_t}{\left(1 + M^2/5\right)} \qquad (7.1.28)$$

$$q_{compr} = 0.7 \cdot p_s \cdot M^2 \qquad (7.1.29)$$

$$\rho = \frac{p_s}{R \cdot T} \qquad (7.1.30)$$

where R is the universal gas constant ($287[\text{J/kg·K}]$)
The velocity magnitude is calculated by:

$$U = \sqrt{\frac{2 \cdot q_{compr}}{\rho}} \qquad (7.1.31)$$

The Cartesian velocity components for low angle:

$$u = U \cdot \cos \alpha \cdot \cos \beta \qquad (7.1.32)$$
$$v = U \cdot \sin \beta \qquad (7.1.33)$$
$$w = U \cdot \sin \alpha \cdot \cos \beta \qquad (7.1.34)$$

The Cartesian velocity components for high angle:

$$u = U \cdot \cos \theta \qquad (7.1.35)$$

$$v = U \cdot \sin \theta \cdot \cos \phi \qquad (7.1.36)$$

$$w = U \cdot \sin \theta \cdot \sin \phi \qquad (7.1.37)$$

Viscosity derived from Sutherland's law:

$$\mu = \mu_0 \cdot \left( \frac{T}{T_0} \right)^{3/2} \cdot \left( \frac{T_0 + S}{T + S} \right) \qquad (7.1.38)$$

where $S = 111$ K for air. $\mu_0 = 1.1716$E-5 $m^2/s$ and $T_0 = 273$ K for air.
Reynolds number per unit length:

$$\frac{Re}{l} = \frac{U \cdot \rho}{\mu} \qquad (7.1.39)$$

The data reduction procedure described above is repeated for each separate test data point. The data reduction algorithm is designed to handle a wide variety of different probe types (5-sensor or 7-sensor, conical, hemispherical or faceted tip), any Reynolds number and any subsonic Mach number.

**Uncertainty Analysis**

All measured values have errors, all instruments have errors and all calculations using experimental data have errors. Error is defined as the difference between the measured value and the true value. It is often necessary to estimate the error to be able to determine the confidence that the measured or predicted result is within a specified range of the true value. The expected errors from a measurement or prediction will be referred to as the uncertainty and can be estimated in several ways. Example: A calculation, $Z(X,Y)$, depends on two measurements, $X$ and $Y$, that have associated random errors. The maximum values of the two variables due to these uncertainties are Xmax and Ymax respectively. Thus, there is a possibility that the result from the calculation will be $Z(Xmax,Ymax)$, however it is very unlikely that the maximum errors of the two variables will occur at the same time. A more realistic measure for the uncertainty is the most probable error (Moffat, 1982). In statistical calculations the standard deviation can be a measure for the most probable error or uncertainty. The standard deviation is for multiple samples defined as:

$$\sigma = \sqrt{\frac{1}{N} \sum_{i=1}^{N} (x_i - \bar{x})^2} \qquad (7.1.40)$$

where N is the number of samples, $x_i$ is the individual sample estimate, $\bar{x}$ is the average of all the estimates and $\sigma$ is the standard deviation of the data. If the measurement errors have a near

Gaussian distribution, the probability that the measurement is within one standard deviation value $(\bar{x} \pm \sigma)$ is approximately 0.67 or 67 %. This probability will in many cases be too low for an experimenter to have any confidence in the data. By increasing the uncertainty of the error to two times the standard deviation $(\bar{x} \pm 2\sigma)$ a probability of 95 % is achieved. It is important to get a reasonable estimate for the uncertainty, since it can be just as unfortunate to overestimate the uncertainty as it is to underestimate the uncertainty. An underestimation can cause false security, while an overestimation can discard good data as being bad. For many engineering purposes one standard deviation will describe the uncertainty in the data and measurements that fall outside of three standard deviations are considered unacceptable and should be discarded. In multiple-sample theory where a large number of data is recorded under the same conditions, the uncertainty is reported as the mean value ± the standard deviation with given odds or probability. However, in the case of finding the uncertainty of pressure probe data, only one recording is done under a particular set of conditions. The uncertainty of such systems can be estimated using single-sample theory and is reported as the uncertainty with odds only (Moffat, 1982).

*Uncertainty Analysis of Local Least-Squares Algorithm*

To find the uncertainties of the local least-squares data reduction algorithm an extensive analytical and numerical analysis was performed. The procedures to find and determine the uncertainties of the algorithm are shown in table 7.1.

**Table 7.1. Determining the uncertainties of multi-hole pressure probe measurements.**

| *Procedures* |
| --- |
| Investigate all sources of error |
| A combined analytical and numerical analysis of how uncertainties in the pressure measurements propagate through the algorithm |
| Evaluation of the LLS surface fitting procedure |
| Evaluating uncertainty (standard deviation) of the algorithm using data verification test files |

Attention should also be directed to the problem of bias or systematic error, which is error that is roughly constant throughout the sampling of the data. Such errors can be due to errors in the reading of the reference manometer, hysteresis and temperature drift of pressure sensors and probe positioning and measurement. Bias errors are ignored in this analysis because the experimenter should identify them and they can be accounted for. Errors due to non-linearity and the averaged sequential recording of pressures are summed up in an uncertainty in the pressure reading. The errors analyzed are errors due to the data reduction technique and the interpolation routines.

There are two different ways to analyze the uncertainty, the worst-case approach or the constant odds approach. The uncertainty of a function R, that depends on a number of independent variables $x_i$, with associated uncertainty $\delta x_i$, can be described as:
Worst case:

$$\delta R = \left| \frac{\partial R}{\partial x_1} \delta x_1 \right| + \left| \frac{\partial R}{\partial x_2} \delta x_2 \right| + \cdots + \left| \frac{\partial R}{\partial x_n} \delta x_n \right| \qquad (7.1.41)$$

Constant odds:

$$\delta R = \left[ \left( \frac{\partial R}{\partial x_1} \delta x_1 \right)^2 + \left( \frac{\partial R}{\partial x_2} \delta x_2 \right)^2 + \cdots + \left( \frac{\partial R}{\partial x_n} \delta x_n \right)^2 \right]^{1/2} \qquad (7.1.42)$$

The general form for constant odds uncertainty predictions was shown by Kline and McClintock (1953) to estimate the uncertainty in R with good accuracy. The constant odds uncertainty prediction requires that each of the $x_i$'s are independent variables and that they have a Gaussian error distribution.

Each of the coefficients ($R = b_\alpha$, $b_\beta$, $b_\theta$, $b_\phi$, $A_t$ and $A_s$) were differentiated with respect to all the pressure terms ($x_i = p_i$). Eight expressions are derived from the constant odds equation shown above (Wenger and Devenport, 1998). Perturbed values for each of the pressure dependent coefficients are found from (tables 7.2 and 7.3):

**Table 7.2. Low angle perturbed coefficient expressions.**

| Expressions for Low Angle Flow |
| --- |
| $\delta b_\alpha(p_1..p_5, \delta p_1.. \delta p_5, p_{static}, \delta p_{static}, p_{total}, \delta p_{total})$ |
| $\delta b_\beta( p_1..p_5, \delta p_1.. \delta p_5, p_{static}, \delta p_{static}, p_{total}, \delta p_{total})$ |
| $\delta A_{t\ low\ angle}(p_1..p_5, \delta p_1.. \delta p_5, p_{static}, \delta p_{static}, p_{total}, \delta p_{total})$ |
| $\delta A_{s\ low\ angle} (p_1..p_5, \delta p_1.. \delta p_5, p_{static}, \delta p_{static}, p_{total}, \delta p_{total})$ |

**Table 7.3. High angle perturbed coefficient expressions.**

| Expressions for High Angle Flow |
| --- |
| $\delta b_\theta( p_1..p_5, \delta p_1.. \delta p_5, p_{static}, \delta p_{static}, p_{total}, \delta p_{total})$ |
| $\delta b_\phi( p_1..p_5, \delta p_1.. \delta p_5, p_{static}, \delta p_{static}, p_{total}, \delta p_{total})$ |
| $\delta A_{t\ high\ angle}(p_1..p_5, \delta p_1.. \delta p_5, p_{static}, \delta p_{static}, p_{total}, \delta p_{total})$ |
| $\delta A_{s\ high\ angle}(p_1..p_5, \delta p_1.. \delta p_5, p_{static}, \delta p_{static}, p_{total}, \delta p_{total})$ |

It is assumed that the error introduced by the pressure transducer is normally distributed. To simulate perturbed pressure values a random Gaussian distribution of pressure perturbations is created. Using information collected from the ESP user manual, the maximum expected error from the ESP is assumed to be less than 0.07 % of full scale output (FSO). The ESP unit FSO is 10 inches of water and assuming that 0.07 % FSO equals $3\sigma$, the standard deviation of the unit is calculated to 0.0044 Torr. Thus, the perturbation in pressure is assumed to have a standard deviation (uncertainty), $\sigma$=0.005 Torr and being unbiased: $\mu$=0.0 Torr. A data file containing the

perturbation pressures was created and used as random pressure perturbations in the modified data reduction algorithm described above (figure 7.1.5).
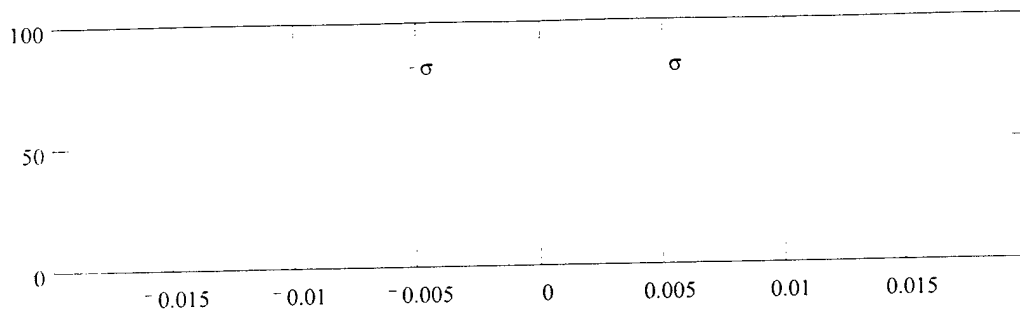


**Figure 7.1.5. Gaussian distribution of perturbation pressures.**

The data reduction algorithm uses six local calibration data points to estimate one test point. The 5 port pressures from each of these points are perturbed using random values from the perturbation file. Also, for each calibration data point the four non-dimensional coefficients: $b_1$, $b_2$, $A_t$ and $A_s$ are calculated. A second set of perturbed coefficients is calculated from the expressions derived above (tables 7.2 and 7.3) using random perturbation pressure values. All the six calibration data points are perturbed in this manner, resulting in randomly perturbed non-dimensional coefficients and interpolation surfaces. The reduction is executed and the results from the perturbed analysis are compared to the results from an unperturbed analysis. The uncertainty is defined as one standard deviation of the difference between the results obtained from the unperturbed surface and the results from the perturbed surface (table 7.4).

**Table 7.4. Calculated standard deviation using the analytical constant odds approach.**

| Data | Standard deviation | Units |
|---|---|---|
| Pitch/Cone | 0.1369 | [deg] |
| Yaw/Roll | 0.1972 | [deg] |
| Velocity | 0.3212 | [%] |

*Surface Fit Evaluation*

An estimation of the errors induced from using a linear least-squares interpolation technique was performed. The surface fitting procedure in many conventional data reduction algorithms is found to be one of the greatest sources of error. A global surface fitting procedure will complicate the structure of the surface because the probe tip surface on a small probe usually contains irregularities that will be reflected in the measured pressures and non-dimensional coefficients. Even smaller sector sized surfaces have these problems when trying to fit an interpolation surface to all calibration points in that sector. A local least-squares approach can be more accurate, because the surface is only covering a small segment of the probe and uses few data points. A linear local least-squares surface can create a very good approximation to the actual data assumed that there is dense grid of calibration data.

A procedure to validate the accuracy of the LLS routine was performed using a known model surface. For each of the separate sectors on a 7-hole probe a surface was created using all the calibration data points belonging to that sector. A second order polynomial surface was created using surface fitting software. The resultant error ($R^2$) of approximating a second order surface over all the calibration data points in each sector was reasonably good. The second order surface will now be regarded as a model surface because it contains similar characteristics as would an actual calibration surface. Because the polynomial expression is known for the surface, a grid of angle coefficients is created with corresponding exact values for the angles. The new grid is created to have similar density and distribution of data points as the actual surface. For the created range of test points the exact values for the pressure coefficients and the angles are known through the four model surface polynomials. The new test file is reduced using a modified version of the LLS algorithm that only reads the test data coefficients and finds the closest (by Euclidean distance) 6 coefficients in the calibration file and interpolates the value for the test data angle. The error is calculated as the difference of the LLS calculated angle and the exact angle calculated by the polynomial expression for the model surface. The data reduction also selects which calibration points to use in the data reduction such that this method can also serve as a measure for the quality of the data point search routine.

As described the surface fit is most probably not a smooth 2nd order polynomial surface over an entire sector and the surface might exhibit larger curvature locally. Several "worst case" examples were analyzed by fitting a higher curvature surface through fewer data points. However, the results from this analysis found that the contributing errors due to the local least-squares surface fit are negligible. Discrepancies between the fitted surface and the model surface were on the order of $10^{-5}$ degrees for angle calculations and $10^{-3}$ percent for velocity calculations.

*Evaluating the LLS Algorithm Using Test Verification Files*

When calibrating multi-hole pressure probes, a common practice is to record a separate test file using non-coinciding data points. The pressures and the angles for the test file are recorded in the same sequence as the calibration data file such that it can be used as a verification of the quality of the calibration and the data reduction algorithm. Several verification files from several different probes calibrated in different facilities were reduced with the developed algorithm, with excellent results. The results for a typical probe are shown in Table 7.5. As seen from tables 7.4 and 7.5 there is good correspondence between the calculated uncertainty and the measurement errors from the data verification files. The quality of the calibration and the data reduction is measured using the discrepancies between the angles and velocity in the verification file and the predicted angles and velocity (figures 7.1.6 to 7.1.9).

**Table 5. Average error standard deviations from a number of experimental test verification files.**

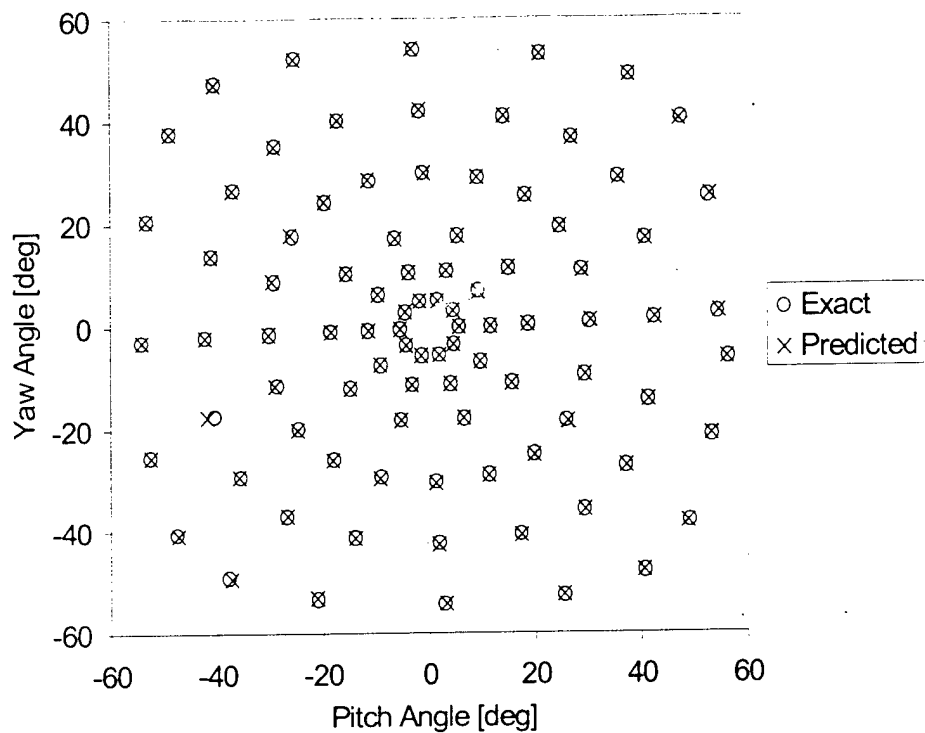| Data | Standard deviation | Units |
|---|---|---|
| Pitch / Cone | 0.1465 | [deg] |
| Yaw / Roll | 0.1855 | [deg] |
| Velocity | 0.3426 | [%] |

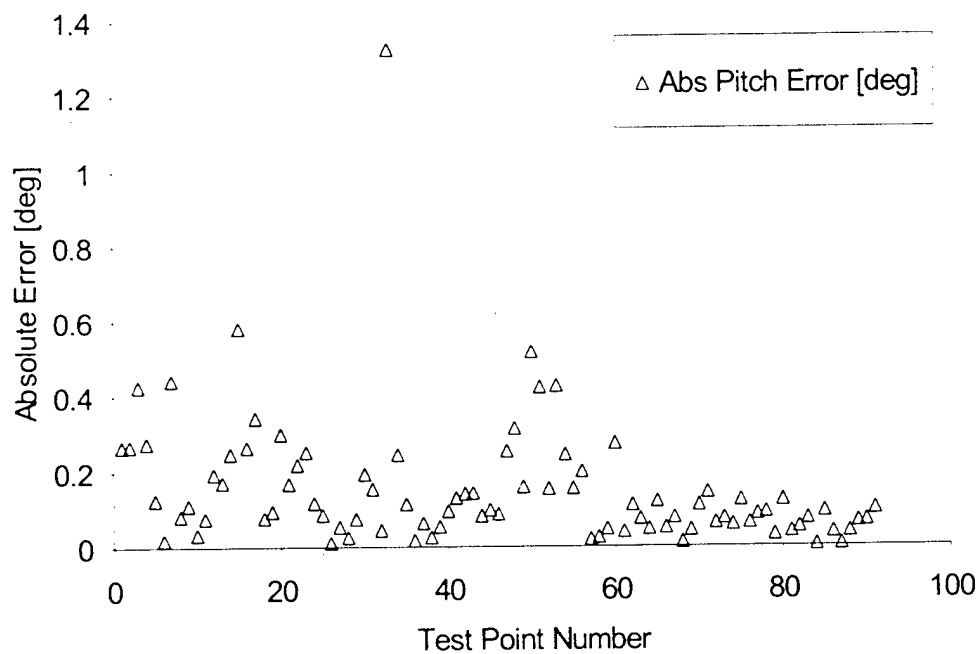**Figure 7.1.6. Exact and predicted pitch and yaw angles for test verification data.**



**Figure 7.1.7. Absolute pitch angle error in degrees. Mean error : 0.151, max error: 1.32, standard deviation: 0.173.**
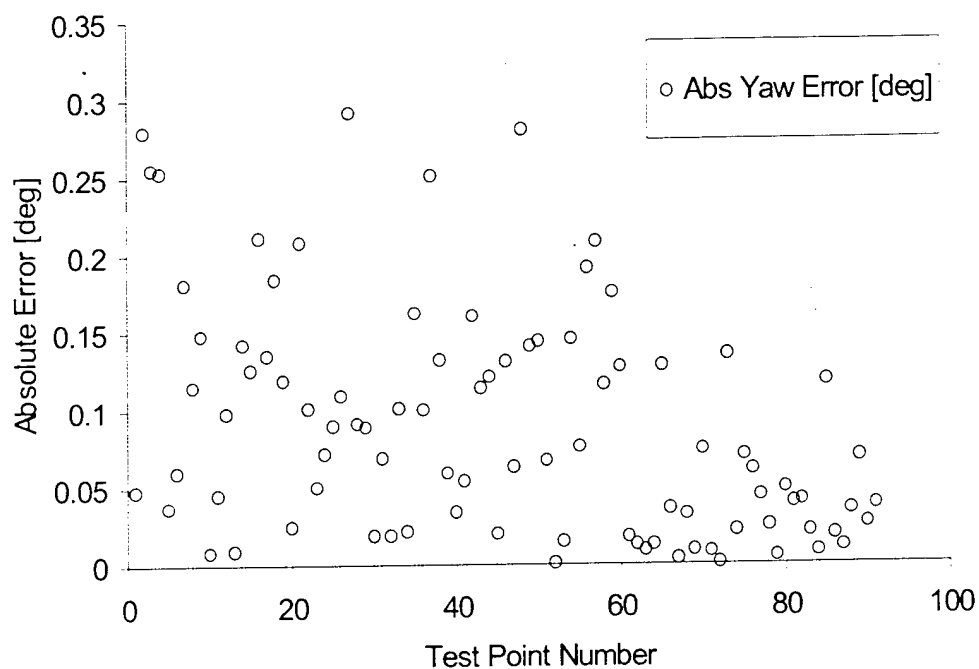
**Figure 7.1.8. Absolute yaw angle error in degrees. Mean error : 0.0888, max error: 0.291, standard deviation: 0.0742.**
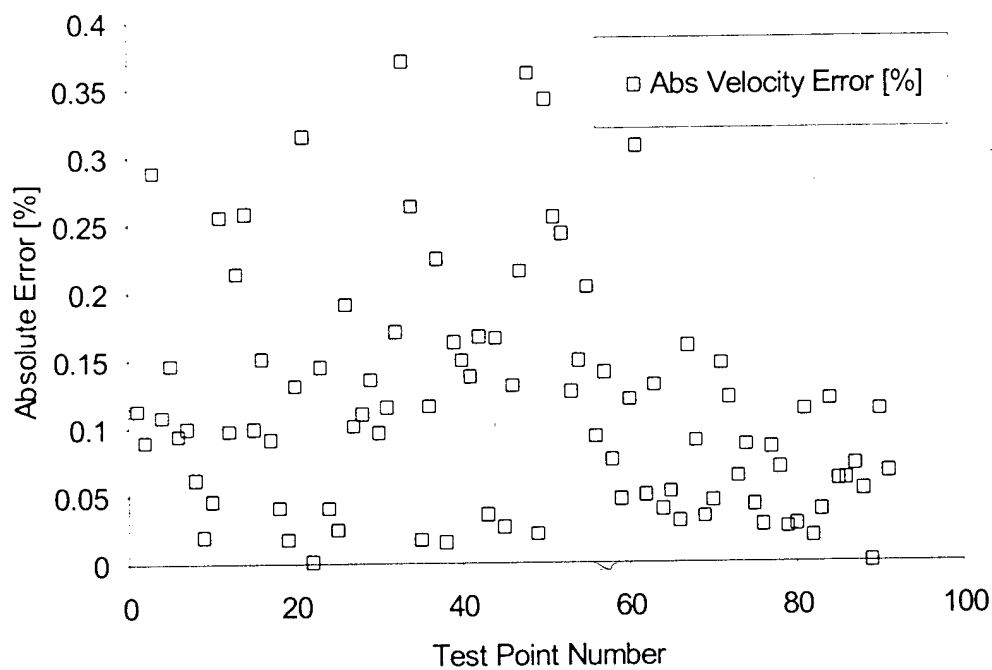


**Figure 7.1.9. Absolute velocity error in percent. Mean error : 0.116, max error: 0.370, standard deviation: 0.0862.**

## 7.2. Neural Network Algorithm

**Nomenclature:**

| | |
|---|---|
| $B_p$ | pitch angle pressure coefficient |
| $B_y$ | yaw angle pressure coefficient |
| $B_c$ | cone angle pressure coefficient |
| $B_r$ | roll angle pressure coefficient |
| $\alpha$ | pitch flow angle |
| $\beta$ | yaw flow angle |
| $\theta$ | cone flow angle |
| $\phi$ | roll flow angle |
| $A_t$ | total pressure coefficient |
| $A_s$ | static pressure coefficient |
| $p_i$ | pressure reading at orifice i of the probe |
| $p^-$ | pressure reading at peripheral port adjacent to port i, in the clockwise direction when looking into the probe tip |
| $p^-$ | pressure reading at peripheral port adjacent to port i, in the counter-clockwise direction when looking into the probe tip |
| $q$ | characteristic of dynamic pressure |
| $\hat{e}$ | sum-squared error |
| $w_{ij}^h$ | weight applied to the connection to node i on layer h from node j on layer h-1 |
| $x_i^h$ | sum of node weighted inputs |
| $f_i^h$ | activation function for node i on layer h |
| $o_i^h$ | output of node i on layer h |
| $\delta_i^h$ | error sensitivity per node |
| $\alpha$ | momentum coefficient |
| $\eta$ | learning rate coefficient |
| $I$ | identity matrix |
| $J$ | error Jacobian matrix |
| $E$ | error vector |
| $C_p$ | generic pressure coefficient; could stand for any of: $B_p$, $B_c$, $B_y$, $B_r$, $A_t$, $A_s$ |
| $\delta C_p$ | uncertainty in the calculation of $C_p$ |
| $\delta p_i$ | uncertainty in the measurement of pressure $p_i$ |

### General

In this section, we present the development of novel neural-network-based steady calibration algorithm for miniature pressure probes. A backpropagation-based neural network calibration algorithm was developed for these probes, with flexibility in network architecture design and network self-optimization capabilities. In the feedforward mode the algorithm yields computational speeds an order of magnitude higher than those typically achieved by similar accuracy interpolation algorithms. The new algorithm has prediction accuracies of 0.28° degrees in the flow angles and 0.35% in the velocity magnitude.

Artificial neural networks have been effectively applied to mechanical and control systems. In aerodynamics, networks have proven their worthiness both as installed components in the aircraft control systems as well as research tools to investigate, model and control fluid flows (Schreck et al., 1993; Schreck and Faller, 1995; Fan et al. X., 1995). Neural networks were coupled with flow measurement tools such as an omni-directional pressure probe to investigate separated and recirculating flows (Kinser and Rediniotis, 1996). In the present work, a novel neural network calibration scheme has been formulated for use in the calibration of multi-hole pressure probes (5-hole or 7-hole). This procedure utilizes a large database of calibration information taken over a large range of flow cone angles (up to 75 degrees). The calibration data is then used to train a multi-layer neural network to predict the flow variables based on calculated pressure coefficients. During the training process, a Network Information file is generated that contains the necessary details of the network weights and biases. Subsequently, test data presented to the network is processed in a feedforward mode to predict the flow direction and magnitude based on the network's knowledge. This versatile technique allows for non-uniform calibration grids, dense calibration grids and updating of the calibration data, provides high prediction accuracy and is very fast in the feedforward mode. Also, the speed in the feedforward mode is independent of the size of the calibration file in contrast to conventional local interpolation algorithms (Kinser and Rediniotis, 1996) of similar accuracy, whose speed is highly dependent on the size of the calibration data file. Moreover, the size of the feedforward code is on the order of a hundred lines, rendering interfacing with existing user codes (such as data-acquisition and data post-processing codes) extremely easy.

Researchers in the flight-test community have used the principles of multi-hole probes to develop flush air data systems (Larson et al., 1987; Larson et al., 1990; Whitmore et al., 1996; Whitmore et al., 1998). In these systems, the nose of the aircraft is instrumented with multiple pressure ports, strategically positioned, and in essence operates as a giant multi-hole probe. In some efforts, neural networks have been successfully used, even in real-time, to extract air data information from the pressure measurements (Rohloff, 1998). These air data systems have a different port arrangement than typical 5 and 7-hole probes, a higher number of ports and are not plagued by calibration issues that emerge as a result of miniaturization. Such an issue for example is the transportability of the calibration from one system to another. For the miniature probes discussed here, calibration transportability, without compromising measurement accuracy, is not an option and each probe has to be calibrated individually. This is due to the fact that the effect of the probe manufacturing defects on the calibration is inversely proportional to the size of the probe.

## Network Architecture

An artificial neural network is composed of processing elements called nodes, with each node having several input branches but only one output branch. Each input connection to a node has a weight associated with it. The input values are multiplied by the associated weights and summed together with a node bias value. An activation function then acts on the summed value producing the output value for the node. An artificial neural network is built of several layers of nodes with the first layer typically having as many nodes as there are input variables. The number of middle or hidden layers is application dependent. Figure 7.2.1 shows a typical network structure, which could be used to train and predict the pitch angle. All the node

44

interconnections are shown. The input layer accepts two input elements. There are two hidden layers and one output layer. The output of each node in a layer serves as input to the nodes of the next layer. In the figure, f1 through f9 are the activation functions applied at each node.

A node's output $o_i^h$ is given by:

$$x_i^h = \sum_j w_{ij}^h \, o_j^{h-1} \quad ; \quad o_i^h = f_i^h (x_i^h) \qquad (7.2.1)$$

where superscript h denotes the layer number, subscript i denotes the node in question, and subscript j denotes the node in the previous (h-1) layer.
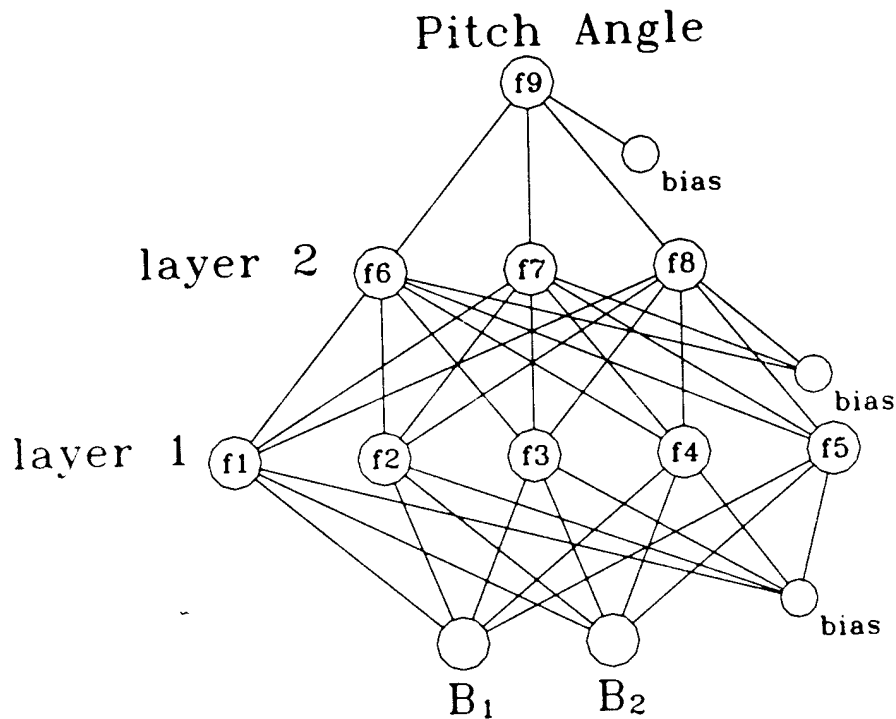


**Figure 7.2.1. A typical network structure that takes a two-element input to train for and predict the pitch angle.**

The artificial neural network algorithm that has been developed utilizes coefficients calculated from probe calibration pressure data for the training of a set of neural networks. For the 7-hole probe, each network utilizes two system inputs - the two pressure coefficients $B_p$ (or $B_c$), $B_y$ (or $B_r$) - and four system outputs - At, As, pitch $\alpha$ (or cone $\theta$) and yaw $\beta$ (or roll $\phi$) angles. A large training set of data containing cone and roll angles and the pressure information is taken using a calibration apparatus. The pressures are reduced to the relevant pressure coefficients. The network uses this information as its training data and, through a training algorithm, adjusts its weights to minimize the resultant error between the predicted and the exact values of the outputs. Once the network is trained, measured pressure data, that may or may not

coincide with the training data, can be input to the network which then predicts the flow variables (velocity and angles) corresponding to the measured pressures.

It was seen that if the high-angle sectors were further split up to improve the description of the measurement domain as shown in figure 7.2.2, higher prediction accuracy could be achieved (although this figure refers to a 7-hole probe, the splitting of the sectors is quite analogous in the case of a 5-hole probe). This was expected from our previous neural network experience in which it became repeatedly obvious that the more complicated the function to be represented and the bigger its definition domain, the harder the task of finding a neural network with high modeling accuracy. So the high-angle sectors were first split into low-high and high-high regimes. The high-high regimes were further split laterally (in roll). For example, sector 2 of figure 3 was replaced by three such subsectors in figure 7.2.2: 2 (low-high), and 13, 14 (high-high). In this way, a 7-hole probe was split up to have as many as 19 sectors. A 5-hole probe would be split into 13 sectors. Care was taken to ensure that there was at least a 5° overlap (in cone and roll) between adjacent sectors. This is done in order to deal with calibration and test points that lie near the borders of adjacent sectors.
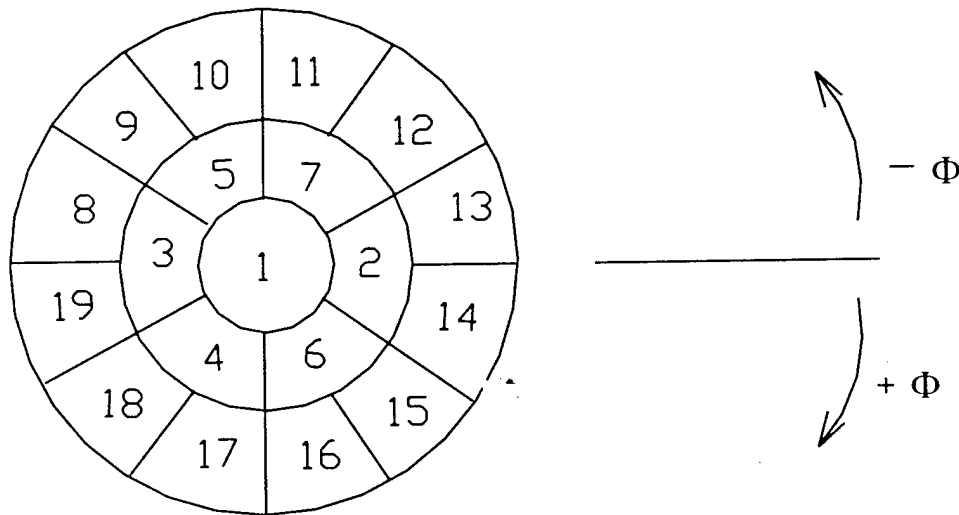


**Figure 7.2.2. The 7-hole domain split up to enhance neural network performance.**

**Artificial Learning**

An artificial neural network learns by adjusting the values of its weights through a training process. The training process consists of giving the neural network sample input-output data pairs and letting the neural network algorithm adjust the weights until it can produce the correct output for each input. This procedure is called supervised learning. Backpropagation is one method of self-correction. During this process, input is applied to the first layer of a neural network and propagated through until an output is generated at the last layer of the neural network. The output obtained through forward propagation is then compared with the desired output to generate an error signal. The error is then distributed back to the nodes of the previous

layer according to their contribution to the error. This process is repeated for all layers, updating the weights. The neural network is iteratively trained with several input-output vector sets until it has all of the training data encoded into it. Once the network has correctly encoded the training data, it can process input data according to the parameters set forth by the training process. It is important to note that the trained neural network will perform only as well as the training data allows. For this reason, care should be taken in selecting the set of training vectors.

Typically, the question of error convergence to a local or global minimum arises. If the backpropagation algorithm converges to a local minimum, learning will then cease and the error of the network output may be unacceptably high. Two simple methods of dealing with this circumstance are to increase the number of hidden layers or to start over the training process with a different set of initial weights. When the backpropagation algorithm does reach an acceptable solution, there is no guarantee that it has reached the global minimum. But as long as the solution is acceptable from an error standpoint, convergence to a local minimum is irrelevant. To avoid the situation of the algorithm converging to a local minimum without reaching a desired minimum error, momentum learning was implemented in the code. Momentum learning allows the network to respond, not only to the local gradient of the error surface, but also to recent trends in the error surface. The algorithm is thus less likely to get trapped in local minima. To speed up convergence, adaptive learning was also implemented. Adaptive learning allows the learning rate to vary depending on the output error. This allows the network to adapt the learning rate to the local terrain of the error surface. When a larger rate is possible for stable learning, the rate is increased. When smaller learning rate is required, the rate is automatically decreased.

The training algorithm accepts as its input a raw pressure data file containing the calibration data for the probe. This data file is then converted to training vector files for every sector of the probe. The training vector files are used to train the neural networks by backpropagation. Weight initialization is performed either by generating random weights or by using existing weights files from previously trained similar networks. During training, the weight matrices are updated using a steepest descent technique to progress towards the minimum error. The error is calculated at each node on the output layer as the difference in the predicted and known outputs:

$$\delta_k^H = \frac{df_k^H(x_k^H)}{dx_k^H}(o_k^H - known) \qquad (7.2.2)$$

where $\delta_k^H$ is the error sensitivity for node k on the output layer H. The error is backpropagated through the network by the following recurrence relation (Freeman and Skapura, 1992; Fausett, 1994; Hagan et al., 1996; Hassoun, 1997):

$$\delta_i^{h-1} = \frac{df_i^{h-1}(x_i^{h-1})}{dx_i^{h-1}}\sum_k w_{ki}^h \delta_k^h \; ; \qquad h = 2...H \qquad (7.2.3)$$

For each of the nodes in the hidden layers, $\delta_i^h$ represents the contribution of error to the network output. The weight changes at each node are then calculated by the following learning rule:

$$\Delta w_{ij}^{h}(t+1) = \alpha \Delta w_{ij}^{h}(t) + (1-\alpha)\eta \delta_i^h o_j^{h-1} \qquad (7.2.4)$$

where $\Delta w_{ij}^{h}(t)$ is the change in weights for layer h at iteration t, $o_j^{h-1}$ is the output of node j on layer h-1, and $\delta_i^h o_j^{h-1}$ is the estimated error gradient calculated for each weight, which can be expressed as:

$$\frac{\partial e}{\partial w_{ij}^{h}} = \delta_i^h o_j^{h-1} \qquad (7.2.5)$$

As previously mentioned, to aid in convergence, a momentum term $\alpha$ is used to dampen the oscillations in the convergence and the adaptive learning rate term, $\eta$ is used as a type of dynamic over- and under-relaxation for updating the weight matrices. The learning rate is increased and the weights are updated after each iteration that reduces the sum-squared error $e$ of the network. After each unsuccessful iteration the learning rate is decreased and the weight changes are discarded.

To further improve the convergence rate, the Levenberg-Marquardt optimization method was implemented (Demuth et al, 199):

$$\Delta \mathbf{W} = (\mathbf{J}^T \mathbf{J} + k\mathbf{I})^{-1} \mathbf{J}^T \mathbf{E} \qquad (7.2.5)$$

Here $\mathbf{J}$ is the error Jacobian matrix consisting of the partial derivatives of the error terms with respect to the node weights, k is a scalar, $\mathbf{I}$ is the identity matrix and $\mathbf{E}$ is the error vector determined from the known vector output and the network calculated values. When k is large, the expression is approximately the gradient descent method. When k is small, the expression approximates the Newton method. Since the second method is faster but tends to be less accurate when near an error minima, the scalar k is adjusted like the adaptive learning rate. As long as the error decreases, k is made larger. If the error increases, k is made smaller. Further, residual monitoring and active perturbation of the weight matrices are additional methods used by the algorithm to insure satisfactory convergence and to stimulate learning.

## Network Optimization

Different network architectures will obviously produce different levels of prediction accuracy. Procedures to find the optimum network structure for specific problems have so far been primarily based on trial and error. Ideally, the neural network code should develop its own intelligence and experience in deciding on the optimum architecture rather than the user being tied to hours of tedious, manual interrogation. In the present code, although the user can at any time override the code's decisions, an expandable heuristic rule base is incorporated that guides the algorithm in the optimal network selection. The main function of these rules is to associate a certain problem or a certain class of problems to certain optimal network architecture or a range of optimal architectures. The main function of the code's optimizer is to generate and train different network architectures and, by comparing their relative performance for a specific problem, conclude on a set of optimal architectures. It can generate optimal network

architectures for 5-hole probes, 7-hole probes, conical, hemispherical and faceted tip geometries and spherical omni-probes. For the probes calibrated here, the typical optimal architecture consisted of one input layer, two hidden layers and one output layer, and the number of nodes per hidden layer were typically 8 and 4 for the first and second hidden layer, respectively. The activation functions that worked the best were: linear, sine, cosine, hyperbolic tangent and sigmoid.

## Calibration Hardware and Setup

Pressure data-acquisition during probe calibration and use was performed with a 32-transducer Electronic Pressure Scanner (ESP) from PSI, Inc. with a pressure range of $\pm 10$ inH$_2$O. The ESP pressure scanner was interfaced to a laboratory computer and was calibrated on-line. The calibration was performed using the apparatus described in Kinser and Rediniotis (1996). A 16-bit A/D board from ComputerBoards was used to perform data-acquisition. A dual-axis stepper-motor assembly, which is computer controlled, can vary the cone and roll angles $(\theta, \phi)$ in the ranges $(0°, 180°)$ and $(-180°, 180°)$ respectively. The positioning resolution for the calibration assembly is $0.32°$ in cone and $0.9°$ in roll. To be able to assess the accuracy of the calibration technique, test data were also collected which involved positioning of the probe at several known orientations, $(\alpha_{test}, \beta_{test})$, or $(\theta_{test}, \phi_{test})$, none of them coincident with any of the orientations used for calibration, $(\alpha_{cal}, \beta_{cal})$ or $(\theta_{cal}, \phi_{cal})$, and collection of the pressures. These pressures were fed into the calibration routines and a predicted pair $(\alpha_{pred}, \beta_{pred})$ or $(\theta_{pred}, \phi_{pred})$ was calculated. The difference between the two pairs $(\alpha_{test}, \beta_{test})$ and $(\alpha_{pred}, \beta_{pred})$ or $(\theta_{test}, \phi_{test})$ and $(\theta_{pred}, \phi_{pred})$ is a measure of the calibration accuracy, although some bias errors are not included (for example due to tunnel flow angularity, as seen later in section 6).

Calibration and data acquisition were performed in the Texas A&M 3'x 4' Aerospace Engineering Wind Tunnel. This is a closed circuit tunnel with a test section equipped with a breather so that the static freestream pressure is equal to the control room pressure. The clear Plexiglas test section is 4 ft. wide, 3 ft. tall and 6 ft. long. The contraction ratio is 9:1. The maximum speed achieved in the tunnel is about 150 ft/sec with freestream turbulence less than 0.16%. To avoid temperature fluctuations over time, there is an active cooling system to keep the freestream temperature at 60°F during testing.

## Discussion of Results and Error Analysis

One of the salient features of the calibration algorithm developed is the range of available control over the network architecture. Typical commercial codes allow for an input layer, a few hidden layers (limited number) each one with a specific activation function for the entire layer, and an output layer with its activation function. The code developed here allows the user to specify different activation functions at each node. The activation functions f1 through f9 in figure 7.2.1 can be selected from a database of functions or can be user-defined. These functions include constant, linear, quadratic, cubic, logsig, tansig, cosine, sine and exponential functions. These functions can be customized and the user can define new activation functions.

To assess the effect of using multiple activation function within a layer, two types of network architectures were trained on data from analytical polynomials and actual probe calibration data. The first architecture had one type of activation function per layer while the second employed multiple functions within a layer. Both network architectures were optimized through the algorithm's optimizer. In the first network architecture the network with the best performance was found to have the following structure: four layers, 3 hidden layers, each with a single activation function: linear, quadratic, and cubic respectively. The optimal network of the second type was a simpler two-layer network. Its single hidden layer utilized 3 different node types: linear, quadratic, and cubic. Both architecture have the ability to model a cubic polynomial selected for this test. However, the multi-function network requires only 2 layers, 4 nodes, and 10 weights to achieve better results than the 4 layer, 10 node, 34 weight single-function/layer network. The convergence rate for the multi-function network is markedly better as figure 7.2.3 illustrates. Of the two architectures, multi-function layer networks have been consistently found to have higher convergence rates and converge to lower error levels.
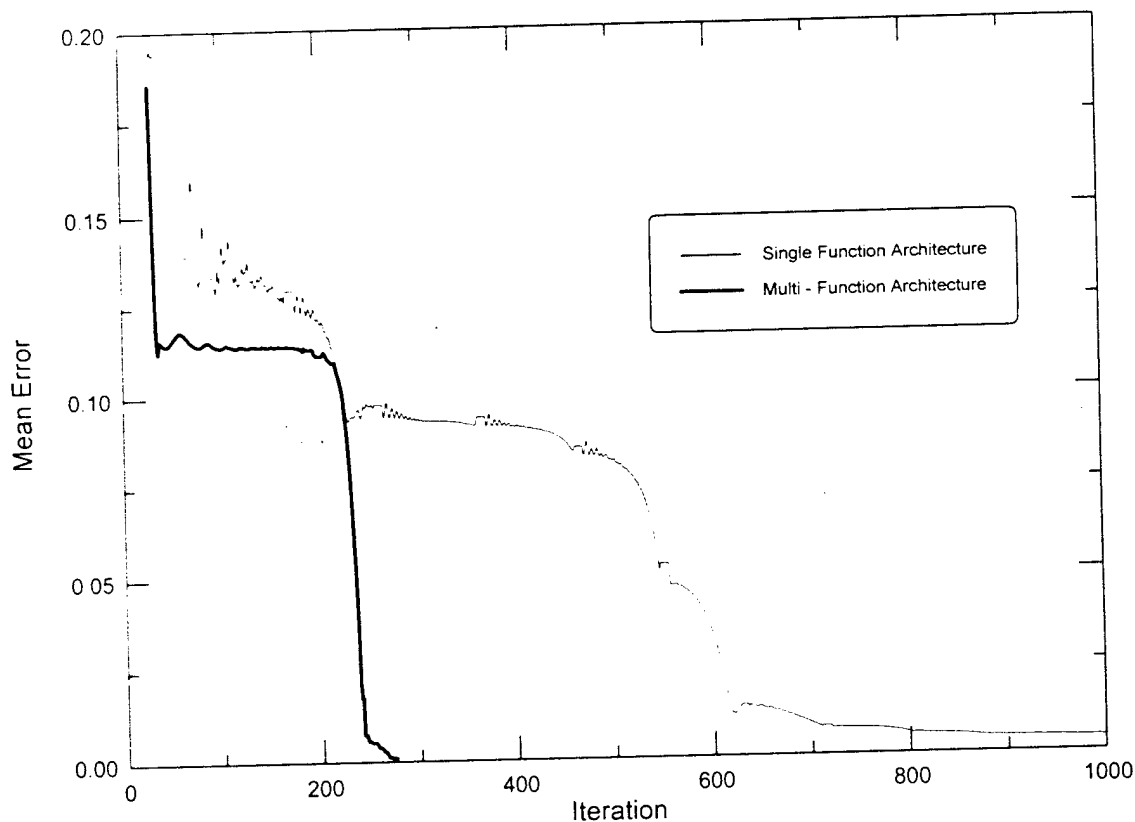


**Figure 7.2.3. Convergence history for single and multiple activation function architectures.**

Once the network has been trained to a satisfactory level of convergence, an output binary file is then created which contains all the trained network information. This binary file is used by the feedforward procedure for reducing any new pressure data acquired with the calibrated probe, to the velocity components and the orientation angles. This feedforward mode

50

is exceptionally fast as compared to similar accuracy local least squares interpolation techniques and is not dependent on the size of the calibration data file. Typically, the neural network code can reduce a test data file that contains 100 test points in just about 5 seconds whereas the same test file may take about a minute to be processed by the local least squares interpolation technique. As mentioned in the introduction, this increased data reduction rate of the neural network algorithm makes it suitable for applications like air-data systems, where several readings per second are required.

A miniature 5-hole probe, 0.063" (1/16") in diameter was calibrated at a free-steam velocity of 70ft/sec. The high angle sectors were split up as described above to enhance the performance of the networks. Figure 7.2.4 shows the predictions for the flow angles both in low-angle and high-angle sectors. Typical calibration performance results are shown in figures 7.2.5 in the form of error histograms. The error is represented along the horizontal axis, while the vertical axis (labeled "frequency") represents the number of points in a specific error bin. The error band of a specific bin is indicated by the width of the corresponding vertical bar. From these histograms the following error statistics can be calculated:

pitch angle: average absolute error = $0.22°$ , standard deviation of error = $0.26°$
yaw angle: average absolute error = $0.28°$, standard deviation of error = $0.34°$
cone angle: average absolute error = $0.15°$, standard deviation of error = $0.18°$
roll angle: average absolute error = $0.17°$, standard deviation of error = $0.21°$
velocity magnitude: average absolute error = $0.35\%$, standard deviation of error = $0.52\%$.

The higher error levels in the pitch and yaw angle prediction (low-angle sector), as compared to the error levels in the cone and roll angle prediction (high-angle sectors) are due to the fact that, as previously discussed, each of the high-angle sectors was further split up to several sub-sectors, and each sub-sector was calibrated individually, while no such sub-division was applied to the low-angle sector.

The uncertainty analysis presented below is based on the techniques discussed in Moffat, (1982) and their application to the multi-hole probe problem follows the procedures discussed in Zilliac (1993). First, the uncertainty of the pressure measurement hardware is estimated. The pressure scanner used was calibrated during calibration of the probe, on-line, every one hour. A five-point calibration was performed which accounted for transducer nonlinearities. The reference manometer used for calibration had an uncertainty of 0.005 Torr for the range of pressures used here (+/- 6 Torr). The above combination along with a one-count A/D conversion uncertainty of the 16-bit A/D board, yielded a pressure measurement "worst case" error of 0.015 Torr or 0.009 inH₂O. Errors in angular positioning were negligible. The resolution of the cone and roll positioning stepper motors ($0.32°$ and $0.9°$) should not be confused with their positioning precision which is on the order of arc seconds. "Slipping" of the stepper motors could of course compromise the accuracy, especially since no angular positioning encoders were employed. However, strong evidence (although not absolute proof) that no "slipping" occurred was the fact that at the end of a calibration session the stepper motors returned the probe, as instructed, to the exact orientation that it started from at the beginning of the session. If any "slipping" had occurred it should have happened in a fashion such that all "slipping" occurrences canceled themselves out, which is a very unlikely event. Bias errors due to probe sting deflection were also negligible at the speeds of calibration and for the specific structural design of the sting.

Uncertainty in the tunnel flow angularity will cause a bias error if the probe is tested or used in a different facility. However, for the calibration test processes followed in this work, as described earlier, flow angularity does not have an effect, for the following reason. Both calibration and test data were taken in the same facility and free-stream velocity, and the calibration apparatus was designed such that it maintained the probe tip always at the same location, regardless of probe orientation.
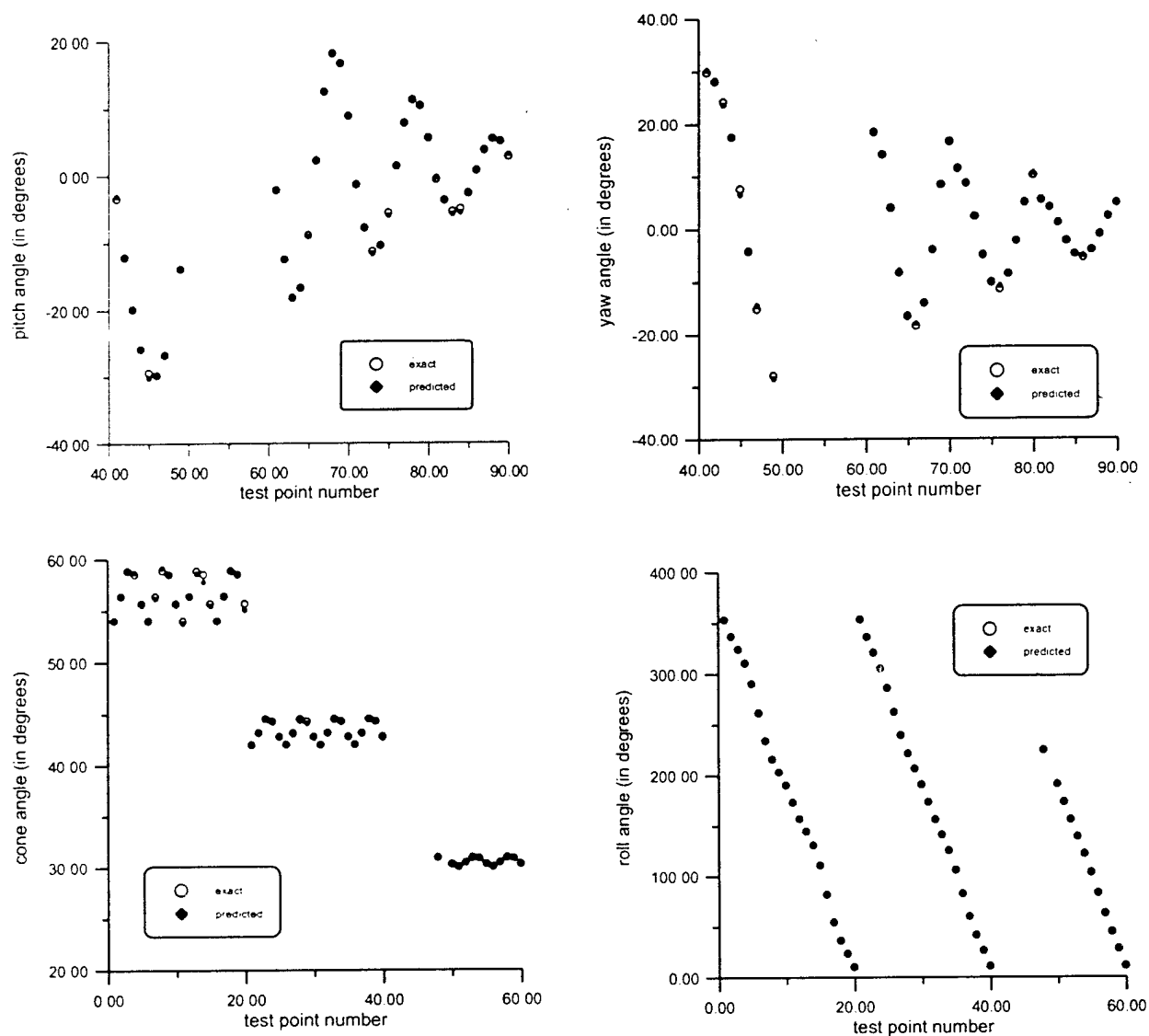


**Figure 7.2.4. Neural network prediction results for: pitch angle, yaw angle, cone angle, roll angle.**

52
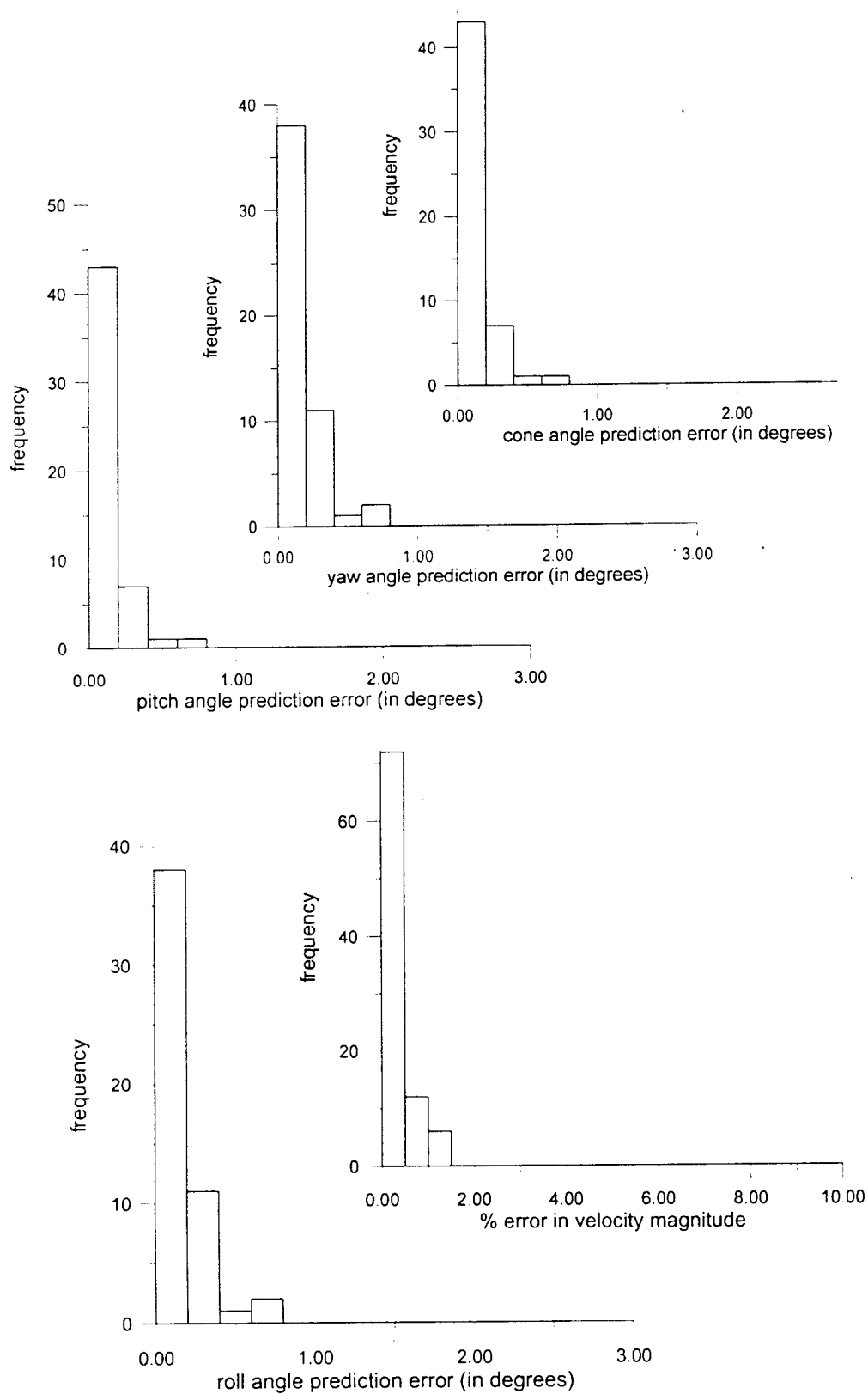
**Figure 7.2.5. Prediction error histograms for pitch, yaw, cone and roll angle and velocity magnitude.**

The uncertainty in the evaluation of the pressure coefficients $B_p$, $B_y$, $B_c$, $B_r$, $A_t$, $A_s$ was calculated using their definition formulas and constant-odds combination given by:

$$\delta\ C_p = \sqrt{\sum_i (\frac{\partial\ C_p}{\partial\ p_i} \delta p_i)^2} \qquad (7.2.6)$$

where $C_p$ is any of the pressure coefficients and $\delta p_i$ is the uncertainty in the measurement of pressure $p_i$. Subsequently, and in order to see how the uncertainty in the calculation of the pressure coefficients propagates through the neural network technique, a "jitter" approach was followed. The estimates of the $\delta p_i$'s were obtained from a Gaussian distribution with zero mean and a standard deviation of 0.005 Torr. This was chosen so that the "worst case" error in pressure measurement, i.e. 0.015 Torr, corresponds to three standard deviations from the mean, which in turn corresponds to a 99.5% probability that the pressure measurement error is smaller or equal to 0.015 Torr. The above allowed the estimation of uncertainty in $B_p$ (or $B_c$), $B_y$ (or $B_r$), $A_t$ and $A_s$ for every calibration and test point, through equation (7.2.6). The obtained $\delta B_p$ (or $\delta B_c$), $\delta B_y$ (or $\delta B_r$), $\delta A_t$ and $\delta A_s$ were used to perturb the original values of these coefficients for the calibration points, and the perturbed values were subsequently used as the inputs to train the neural networks. Once the networks were trained, they were used to reduce the test data that were also perturbed in the manner explained above. The predictions obtained in this process were compared to those obtained from the unperturbed networks and test points, and the standard deviation of the differences between these two yielded estimates for the overall uncertainty. The results are listed below:

Standard deviation in cone angle errors: $0.24^\circ$
Standard deviation in roll angle errors: $0.37^\circ$
Standard deviation in velocity magnitude error: 0.72 %

Figure 7.2.6 shows the histograms of these errors. The statistical properties of these histograms are very similar to the ones obtained from the actual calibration tests (figure 7.2.5). As seen above, the error levels obtained from the actual test are within those predicted from the uncertainty analysis. It should be pointed out here that the uncertainty analysis presented here applies strictly to "steady-state" flows. The issues of probe calibration and measurement accuracy in unsteady flow environments are addressed in a different section.

In summary, a neural network based probe calibration algorithm was developed. The algorithm's features include flexibility in network architecture design and network self-optimization capabilities. The introduction of multiple activation function architectures had a significant positive impact on the network training convergence rates and levels. In the feedforward mode the algorithm yields computational speeds an order of magnitude higher than those typically achieved by similar accuracy interpolation algorithms. Moreover, the small size of the feedforward code facilitates its formulation into a subroutine and enhances its easy of interfacing with other software. A miniature 5-hole probe was calibrated and tested in the wind tunnel. The new algorithm combined with precision probe calibration hardware and procedures yielded prediction accuracies of $0.28^\circ$ degrees in the angle prediction and 0.35% in the velocity magnitude prediction. Finally, an error analysis was performed on the calibration procedures

and algorithm and yielded uncertainty levels compatible with those produced by the actual probe test.
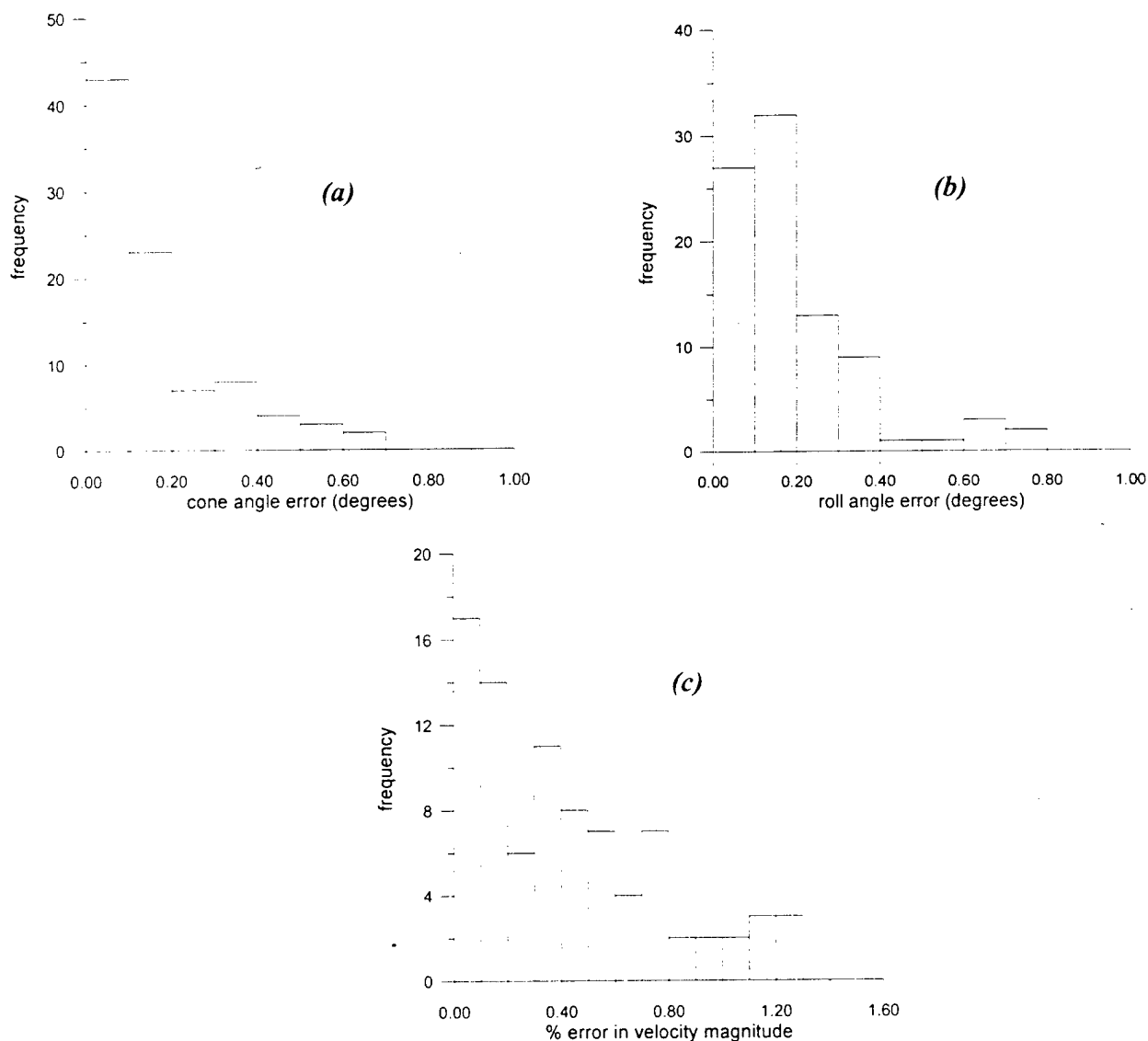


Figure 7.2.6. Error histograms derived from uncertainty analysis: (a) cone angle error, (b) roll angle error, (c) velocity magnitude error.

# 8. UNSTEADY PROBE CALIBRATION–THEORETICAL FORMULATION

## Theory and Background

As it has already been discussed, the unsteady calibration of the probe will have to deal with the modeling of the flow inertial effects. The inertial effects come from the probe-fluid interaction in an accelerated flowfield. If a sphere is translating in steady motion through an inviscid fluid at rest the drag is zero (d'Alembert's paradox). The absence of drag is due to the equal and opposite pressure forces on the windward and the leeward side of the sphere. This result is naturally not observed in experiments due to the viscous effects that are particularly dominant on the leeward side of the sphere. For the same sphere in accelerated translation through a fluid at rest, the pressures on the windward and leeward sides no longer balance and there is a resulting force acting in the direction opposite to that of the acceleration. The implications of this phenomenon for a multi-hole probe in an unsteady (accelerated) flowfield is that the measured pressure on the surface of the probe no longer depends only on the total pressure and tip geometry alone, but also on an additional term that depends on the rate of change of the velocity of the fluid. This section describes a theoretical method to quantify and then correct these inertial effects such that a multi-hole probe can be successfully used in unsteady flowfields.

In incompressible, irrotational flows the relationship between pressure and velocity for steady fluid flow is governed by the steady Bernoulli equation:

$$p_t = p_s + \frac{1}{2}\rho U^2 + \rho g h \tag{8.1}$$

where $p_t$ is the total pressure and $p_s$ is the static pressure. For airflows the hydrostatic pressure term $\rho g h$ is negligible and typically disregarded, however for water flow this term can contribute a significant portion of the total measured pressure. The following discussion of inertial effects will assume negligible hydrostatic pressure contribution. In an isentropic stagnation of a jet of air onto a solid surface (such as the tip of a probe) the local static pressure will increase to equal the total pressure of the flow (since at the stagnation point U=0). If now one considers a sphere moving in an infinite fluid at rest at a time dependent velocity, the Bernoulli equation can, for a body-fixed reference frame, be written as:

$$p(\vec{r},t) = p_s - \rho\left[\frac{\partial \phi}{\partial t} - \overline{U(t)}\cdot\bar{\nabla}\phi + \frac{1}{2}\left(\bar{\nabla}\phi\right)^2\right] \tag{8.2}$$

This equation describes the pressure in the fluid in terms of the position vector $\vec{r}$ and time t. For the sphere, the flowfield is axisymmetric such that the position vector can be described in terms of only two components in a spherical coordinate system, namely its r and θ components (fig. 8.1).
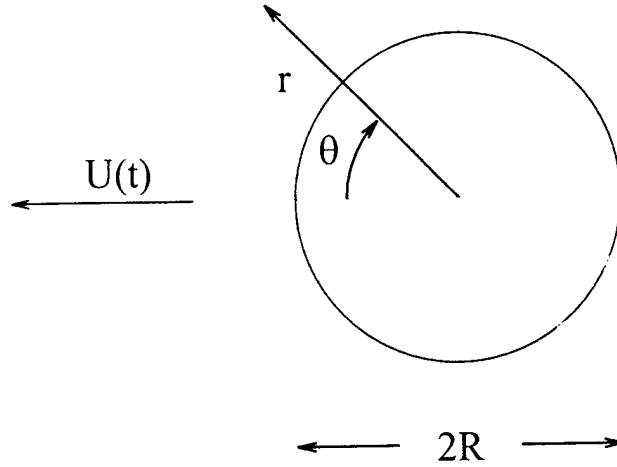
**Fig. 8.1. Definition of parameters for the sphere moving in an infinite fluid at rest.**

The velocity potential $\phi$ is a scalar describing the 3-dimensional velocity vector and is defined by:

$$\bar{U} = \vec{\nabla}\phi \tag{8.3}$$

The sphere velocity $\overline{U(t)}$ is given as:

$$\overline{U(t)} = U(t)\cos(\theta)\hat{r} - U(t)\sin(\theta)\hat{\theta} \tag{8.4}$$

For a sphere the velocity potential can found by setting up the appropriate boundary conditions using a method of separation of variables and assuming axisymmetric flow:

$$\phi(\theta,t) = -\frac{1}{2}U(t)\frac{R^3}{r^2}\cos(\theta) \tag{8.5}$$

Where the radius of the sphere is given by R and U(t) is the velocity of the sphere. It is desired to find the pressure distribution on the sphere surface as a function of the velocity and the angle $\theta$, by calculating each of the terms in the unsteady Bernoulli equation:

Time derivative of the perturbation potential: $\dfrac{\partial \phi}{\partial t} = -\frac{1}{2}R\dfrac{dU(t)}{dt}\cos(\theta)\Big|_{r=R}$

Gradient of the potential: $\vec{\nabla}\phi = \dfrac{\partial \phi}{\partial r}\hat{r} + \dfrac{1}{r}\dfrac{\partial \phi}{\partial \theta}\hat{\theta} = U(t)\dfrac{R^3}{r^3}\cos(\theta)\hat{r} + \frac{1}{2}U(t)\dfrac{R^3}{r^3}\sin(\theta)\hat{\theta}$

Scalar product of the disturbance velocity and the disturbance potential:

$$\overline{U(t)} \cdot \overline{\nabla} \phi = [U(t)\cos(\theta), -U(t)\sin(\theta)] \cdot \left[ U(t)\frac{R^3}{r^3}\cos(\theta), \frac{1}{2}U(t)\frac{R^3}{r^3}\sin(\theta) \right]$$

$$= U(t)^2 \cos^2(\theta) - \frac{1}{2}U(t)^2 \sin^2(\theta)\Big|_{r=R}$$

The square of the disturbance potential:

$$\frac{1}{2}\left(\overline{\nabla}\phi\right)^2 = \left[ U(t)\frac{R^3}{r^3}\cos(\theta), \frac{1}{2}U(t)\frac{R^3}{r^3}\sin(\theta) \right]^2 = \frac{1}{2}U(t)^2 \cos^2(\theta) + \frac{1}{8}U(t)^2 \sin^2(\theta)\Big|_{r=R}$$

Substitution of the above equations into the unsteady Bernoulli equation for the translating sphere gives the following expression for the pressure distribution on the sphere surface:

$$p(\theta, U, t) = p_s + \underbrace{\frac{1}{2}\rho U(t)^2 \left( \frac{9}{4}\cos^2(\theta) - \frac{5}{4} \right)}_{I} + \underbrace{\frac{1}{2}\rho R \frac{dU(t)}{dt}\cos(\theta)}_{II} \qquad (8.6)$$

This is the pressure distribution on the surface of the sphere moving at velocity U(t) in a fluid at rest. The same pressure distribution would also be seen if the sphere is fixed and the flowfield is moving with velocity U(t).

The term dφ/dt term is known as the inertial or apparent mass term. For steady flow the inertial term vanishes and the pressure distribution on the sphere is given by the term I in equation 8.6. However for unsteady flows the inertial term will be non-zero and therefore, in the case of a multi-hole probe, corrections must be made to accurately resolve the velocity magnitude from the measured port pressures. Term I in equation 8.6 is the steady contribution to the pressure distribution on the sphere and it scales with the dynamic pressure and a geometric parameter. Term II is only present in time dependent flowfields, is the unsteady contribution to the pressure distribution and scales with the fluid density, the velocity rate of change and a geometric parameter, different than that in the steady term.

$$p(\theta, U, t) = \underbrace{\frac{1}{2}\rho U(t)^2 \left( \frac{1}{4}\left(9\cos(\theta)^2 - 5\right) \right)}_{I} + \frac{1}{2}\rho R \frac{dU(t)}{dt}\underbrace{\cos(\theta)}_{II} \qquad (8.7)$$

Equation 8.7 is basically equation 8.6 re-written to identify the steady and unsteady geometric parameters, while the static pressure term $p_s$ has been dropped, leaving the surface pressure to be described as a differential quantity i.e. with respect to the static pressure. The geometric parameters are described by I and II (and also R) in equation 8.7 and it will be assumed that the general form of this equation is valid even for non-spherical shapes, such as hemispheres or approximate hemispheres. The only terms expected to change are the geometric terms I and II. Thus we shall adapt this general form to describe the pressure on the surface of the probe:

$$p(\alpha,\beta,U,t) = \frac{1}{2}\rho U(t)^2 Cp_{steady}(\alpha,\beta) + \frac{1}{2}\rho R \frac{dU(t)}{dt} Cp_{unsteady}(\alpha,\beta) \tag{8.8}$$

Where $\alpha$ and $\beta$ are the flow pitch and yaw angles relative to the probe tip. For a sphere, $Cp_{steady}$ is identical to term I and $Cp_{unsteady}$ is identical to term II in equation 8.7:

$$Cp_{steady} = \frac{1}{4}\left(9\cos(\theta)^2 - 5\right) \qquad Cp_{unsteady} = \cos(\theta) \tag{8.9}$$

Equations 8.9 are plotted versus cone angle in fig. 8.2. Notice the asymmetry of the unsteady pressure coefficient, which is the factor that contributes, even for an ideal inviscid flow, to a drag on the sphere, and is also known as the apparent mass or inertial contribution.
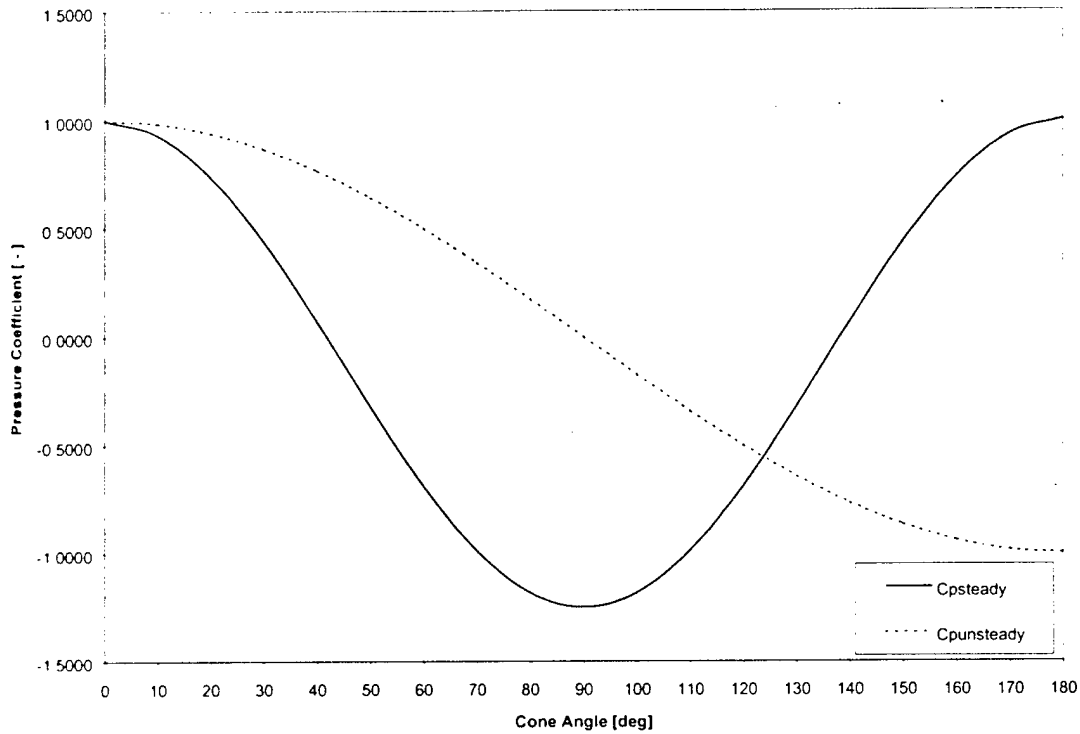


Fig. 8.2. Theoretical $Cp_{steady}$ (solid line) and $Cp_{unsteady}$ (dotted line) for a sphere.

For the sphere the inertial contribution has now been identified and the pressure anywhere on its surface can be calculated for a steady or accelerated flowfield. The magnitude of the inertial contribution compared to the steady contribution of the pressure on the sphere surface depends on the flow velocity, rate-of-change of velocity and the sphere size. To demonstrate the effects of the inertial term, consider a 2 mm sphere in a sinusoidally oscillating air stream with a mean velocity of 60 m/s, 30% amplitude and frequency 20 kHz. The true dynamic pressure of the flow (as in the absence of the sphere) is given directly by:

$$P_{dyn} = \frac{1}{2}\rho U(t)^2 \qquad (8.10)$$

The pressure that would exist at the forward stagnation point on the sphere surface is given by equation 8.7 (for $\theta=0$). Plotting these two pressures versus time reveals that the sphere pressure is larger in amplitude and leads the flow dynamic pressure in phase (fig. 8.3). It is also seen that the sphere pressure crosses the true dynamic pressure at the peaks and in the valleys, where the velocity derivative is zero.
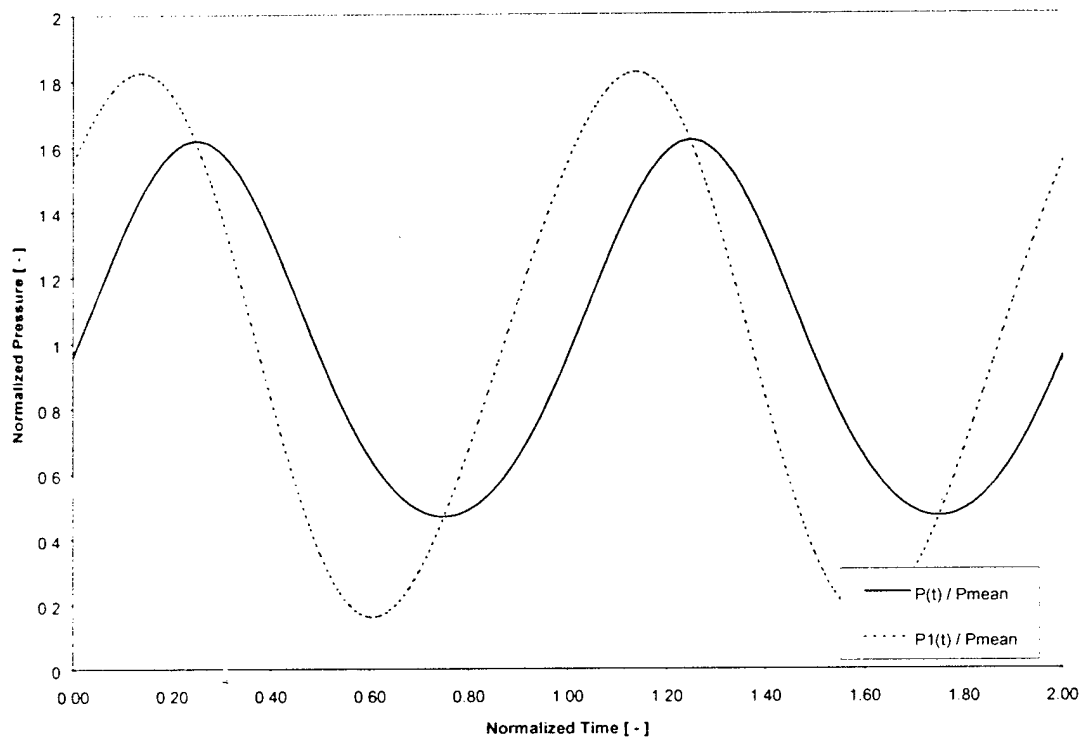


**Fig. 8.3. The pressure at the forward stagnation point (dotted line) versus the true total pressure of the fluid in the absence of the probe (solid line).**

In the above example the surface pressure on the sphere was calculated for a known flowfield, however the purpose of a multi-hole probe is to treat the flowfield as unknown and resolve the angularity and velocity magnitude from the measured port pressures. Before all of the information required to resolve such an unknown flowfield can be processed, it is necessary to study the probe surface pressure behavior in a known flowfield.

*Comparison of Theoretical and Real Probe*

A multi-hole probe typically has a central pressure port and 4 or 6 peripheral pressure ports. Equation 8.8. can be modified such that each of the pressure ports has an associated expression that relates the flow velocity and angularity with the measured port pressure. Note

that the pitch and yaw angles ($\alpha$, $\beta$) are global, i.e. with respect to the probe, not local, i.e. with respect to the individual ports:

$$p_i(\alpha,\beta,U,t) = \frac{1}{2}\rho\,U(t)^2\,Cp_{steady_i}(\alpha,\beta) + \frac{1}{2}\rho\,R\,\frac{dU(t)}{dt}\,Cp_{unsteady_i}(\alpha,\beta) \qquad (8.11)$$

where i indicates the ith port of the multi-hole probe. A theoretical multi-hole probe can be modeled as a sphere with ports at known angular locations. If this theoretical probe is placed in a flowfield with given incidence angle, velocity and rate-of-change of velocity the corresponding port pressures can be found by modifying equation 8.11 to account for the angular offset in port locations. Denoting pressure port i with P, the forward center port with C and the stagnation point with X, the problem reduces to finding $\theta_{xp}$ from fig. 8.4.
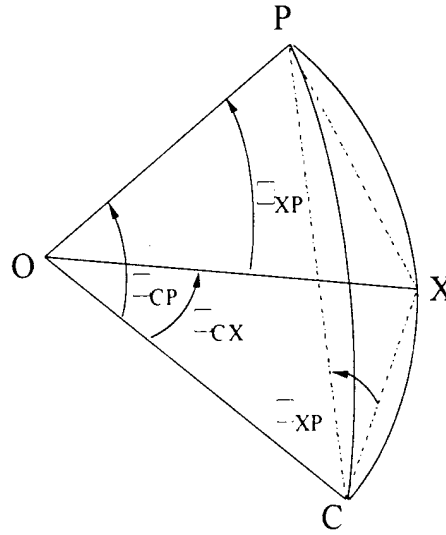


**Fig. 8.4. Finding the individual port pressures as a function of incidence angle.**

In figure 8.4, "O" denotes the center of the sphere and all lengths OC, OP and OX are equal to the radius of the sphere, R. From geometry, angle $\theta_{XP}$ is given by:

$$\theta_{xp} = 2\sin^{-1}\left[\left(\sin\left(\frac{\theta_P}{2}\right)^2 + \sin\left(\frac{\theta_X}{2}\right)^2 - 2\sin\left(\frac{\theta_P}{2}\right)\sin\left(\frac{\theta_X}{2}\right)\cos(\phi_{xp})\right)^{-\frac{1}{2}}\right] \qquad (8.12)$$

where $\theta_P$ and $\theta_X$ is the cone angle position of the pressure port and the stagnation point, respectively. $\phi_{XP}$ is the difference between the roll angles of the port location and the stagnation point. To investigate the assumption that a multi-hole probe behaves in a manner similar to a sphere, a theoretical 5-hole probe based on a sphere was created. This theoretical probe had a center port at $\theta = 0$ deg., and 4 peripheral ports located at a fixed cone angle, $\theta = 33$ deg. and roll angles of 0, 90, 180 and 270 deg. (Fig. 8.5).
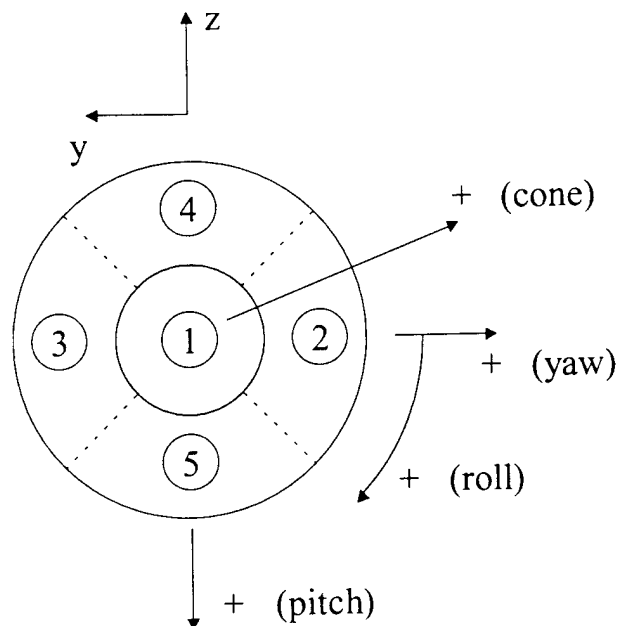
**Fig. 8.5. Port numbering and definition of angle system for theoretical 5-hole probe.**

The steady pressures on the surface of this probe were then compared with the calibration file for a real 3.2 mm hemispherical tipped probe with port numbering identical to that of fig.8.5 and pressure port diameter of 0.3 mm. The probe is hemispherical within the fabrication limitations, i.e. its shape deviates from a perfect hemisphere and each pressure ports is not a point, but rather spans a finite range of angles (due to the port diameter which is about $1/11^{th}$ of the probe diameter), with the port center approximately located at a cone angle of $\theta = 33$ deg. This probe was calibrated in a wind tunnel at 30 m/s using a cone and roll angle system. The theoretical model was used to calculate the 5 port pressures for the same angle combinations as in the actual calibration file. In figs. 8.6 to 8.8 the calculated and experimental pressures for the center port and ports 2 and 3, are compared directly. Very reasonable agreement is seen for all pressures. Bearing in mind that for such a small probe tip the shape is only nearly hemispherical and that the pressure ports are not points, but rather span a finite angle, the agreement is quite good.

Only modifications in the steady Cp coefficient for the sphere given in equation 8.9 are necessary to identically match the steady results for a perfect hemisphere. However, for a real probe, calibration is necessary to create a Cp curve that accounts for all of the manufacturing idiosyncrasies. The following discussion will assume a probe with a tip that behaves like a sphere (thus known steady and unsteady Cp) to derive a data reduction procedure to resolve the flow angle and velocity in an unknown unsteady flowfield. In a later section the calibration necessary to find the steady and unsteady Cp for a real probe will be discussed.
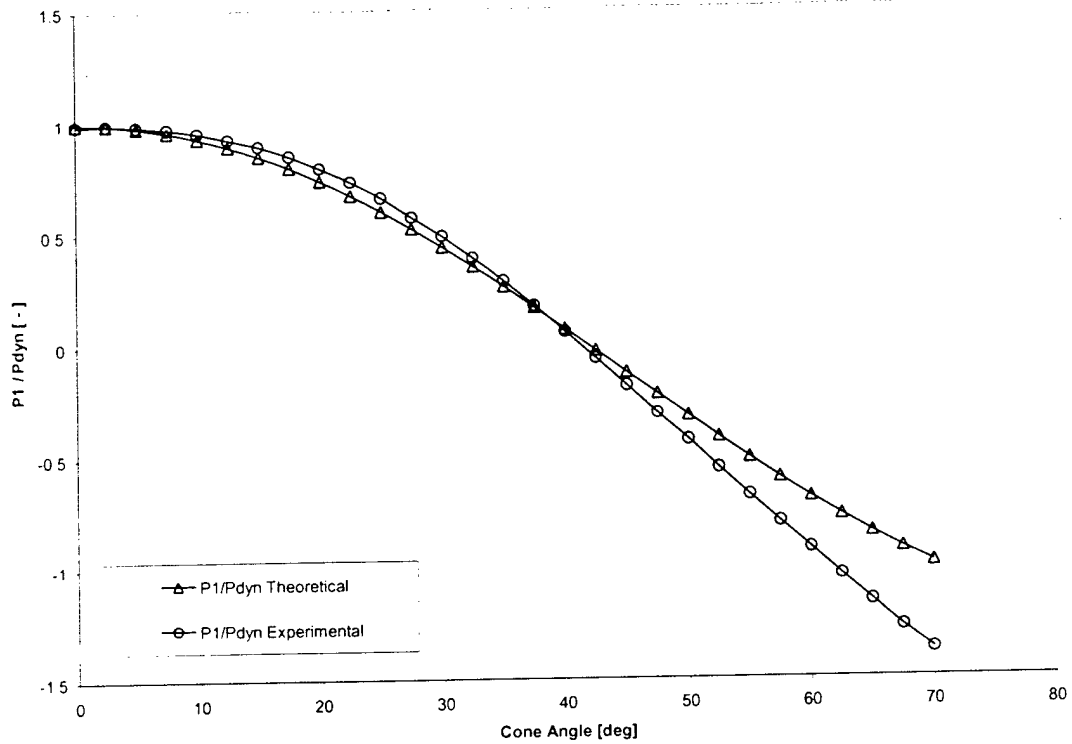
Fig. 8.6. Theoretical and experimental center port pressure for roll angle of zero degrees.
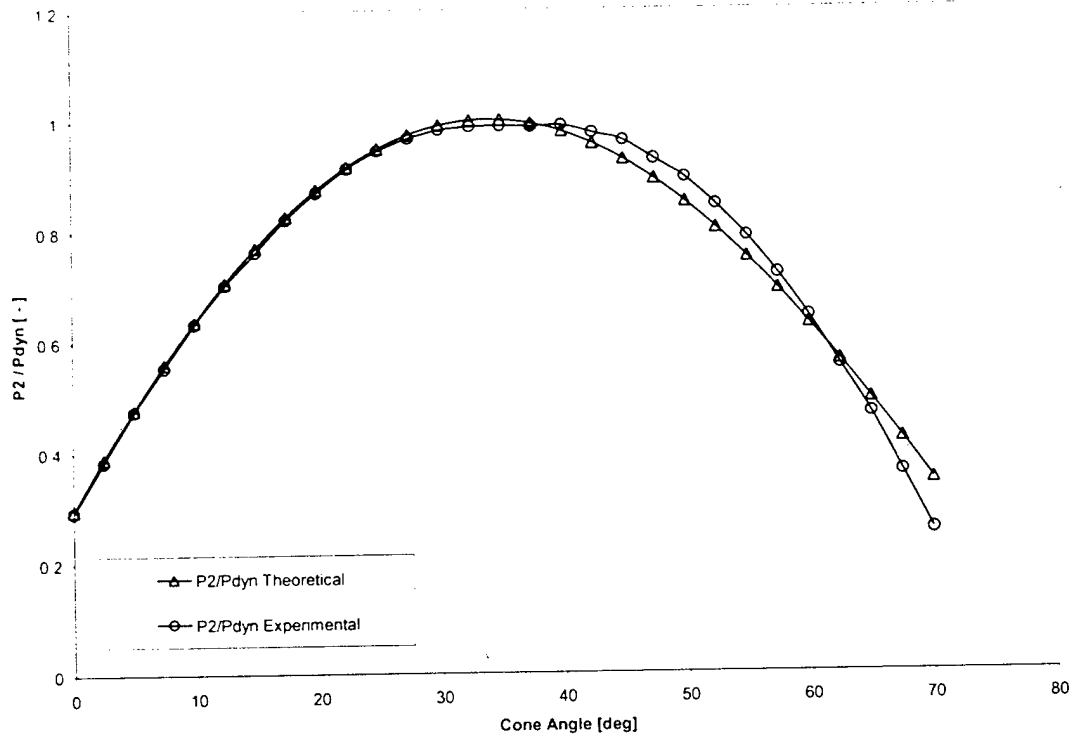


Fig. 8.7. Theoretical and experimental port 2 pressure for roll angle of zero degrees.
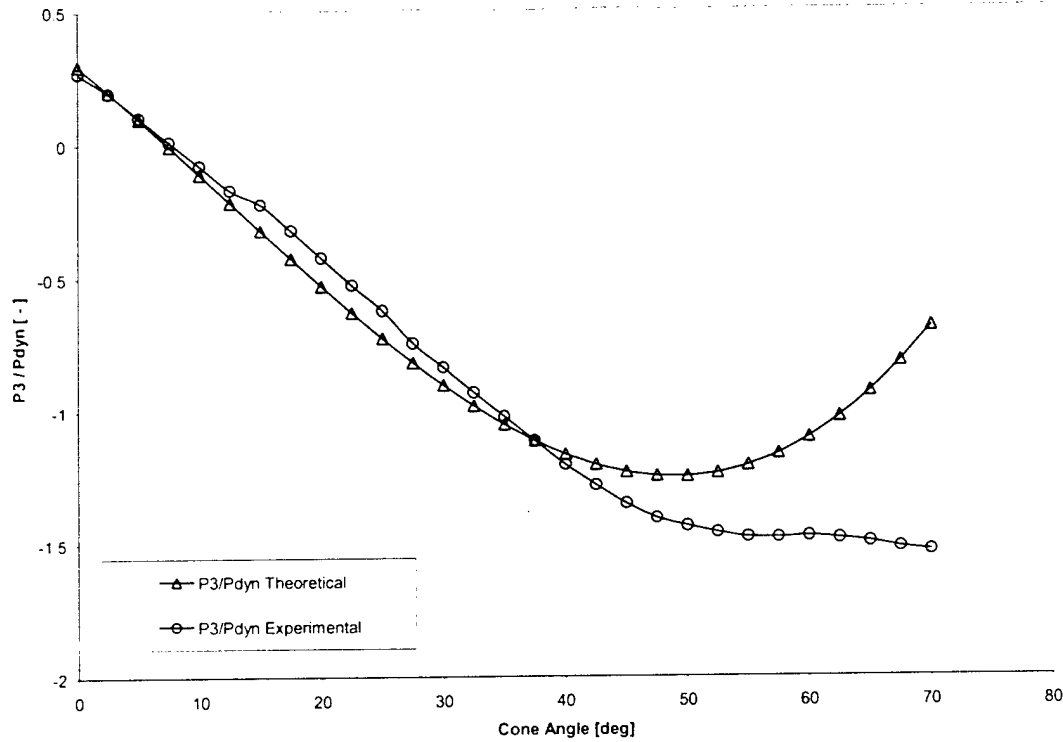
**Fig. 8.8. Theoretical and experimental port 3 pressure for roll angle of zero degrees.**

## Parameters of Unsteady Flowfields

Some assumptions must be made at this point to ensure the validity of the above equations. We assume that there are no spatial freestream velocity gradients over the probe diameter. This leads to the restriction that the wave length of the oscillations in the oncoming fluid must be much larger than the size of the probe (Kovasznay et al., 1982):

$$kR << 1 \tag{8.13}$$

where k is the wave number of the traveling disturbance/wave and R is the radius of the probe. Furthermore it shall be assumed that the flow oscillations are purely axial, i.e. there are no angular oscillations in the flowfield. There are no inertial effects caused by angular oscillations. Moreover, in an aerodynamic design study of probe geometries, Humm and Gossweiler found that for cylinders there is negligible circulation induced forces from angular oscillations. Assuming that these results are also valid for a sphere or a hemisphere, the probe will be able to resolve flows in which angular oscillations are present, assuming again that there are no significant gradients over the probe diameter. To characterize unsteady flows, a non-dimensional frequency, $\omega^*$ (similar to Strouhal number) has traditionally been used:

$$\omega^* = \frac{2R\omega}{\overline{U}} \tag{8.14}$$

64

However for a more general, non-periodic flow, a rate-of-change parameter K is better suited to non-dimensionalize equation 8.8:

$$K = \frac{\frac{dU}{dt}R}{U^2}$$

(8.15)

With this, equation 8.8 reduces to:

$$Cp(\alpha,\beta,K) = \frac{p(\alpha,\beta,U,t)}{\frac{1}{2}\rho U^2} = Cp_{steady}(\alpha,\beta) + KCp_{unsteady}(\alpha,\beta)$$

(8.16)

where again for a sphere, $Cp_{steady}$ and $Cp_{unsteady}$ are given by equations 8.9. The K parameter is descriptive of the magnitude of the unsteady or inertial effects seen by the probe. The K parameter for a periodic flow will also be periodic hence it is not a constant like the non-dimensional frequency, $\omega^*$.

Figure 8.9 shows the steady and unsteady pressure contributions for a given K value. For a K value of 0.1 the measured pressure at the forward stagnation point is 10 % higher than the true dynamic pressure (in the absence of the probe). From the expression in equation 8.8 the error made in the estimate of the pressure coefficient, by ignoring the inertial term, is linearly proportional to the probe size and the rate-of-change of velocity and inversely proportional to the square of the velocity. To further demonstrate the point, consider a typical fast response probe with a hemispherical tip (will be considered spherical for this example). The probe has a tip diameter of 2 mm and is placed in a oscillating air stream at zero incidence angle. The velocity signal is sinusoidal at 2 kHz, with a mean of 60 m/s and 30% amplitude. Figs. 8.10 and 8.11 shows the true velocity signal and the calculated K-coefficient for the time history. Fig. 8.12 shows the true dynamic pressure of the flow and also the pressure that would be measured at the forward stagnation point. If the inertial effects are ignored, the error made in the magnitude of the pressure is equal to the value of the rate-of-change coefficient. For example, fig. 8.11 shows a maximum K-value of 0.075, which means that for the 2 mm probe in the described flowfield a measurement error in the port pressure of 7.5% is expected if the inertial effects are not accounted for. If the same probe is placed in a flowfield oscillating at 20 kHz the effect is shown in figs. 8.13 to 8.15 and one can see an increase in the error from 7.5% to 75%.

In light of these plots one must realize that both steady and unsteady probe calibrations are valuable, depending on the application. For a range of applications where the K value is sufficiently small a quasi-steady data reduction can be used with a high degree of accuracy. As the K value increases, the need for unsteady calibration becomes more and more obvious.
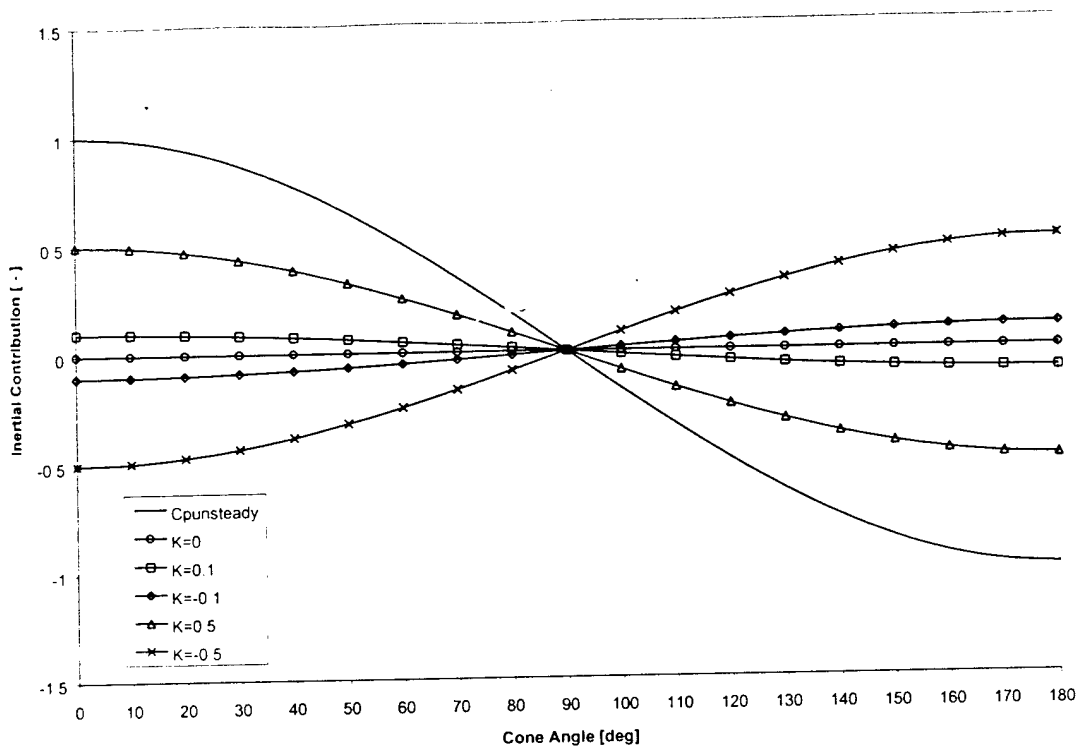
**Fig. 8.9.** The steady and unsteady contributions to the pressure coefficient Cp, vs. angle from the forward stagnation point (θ), and with the rate-of-change coefficient, K, as parameter.
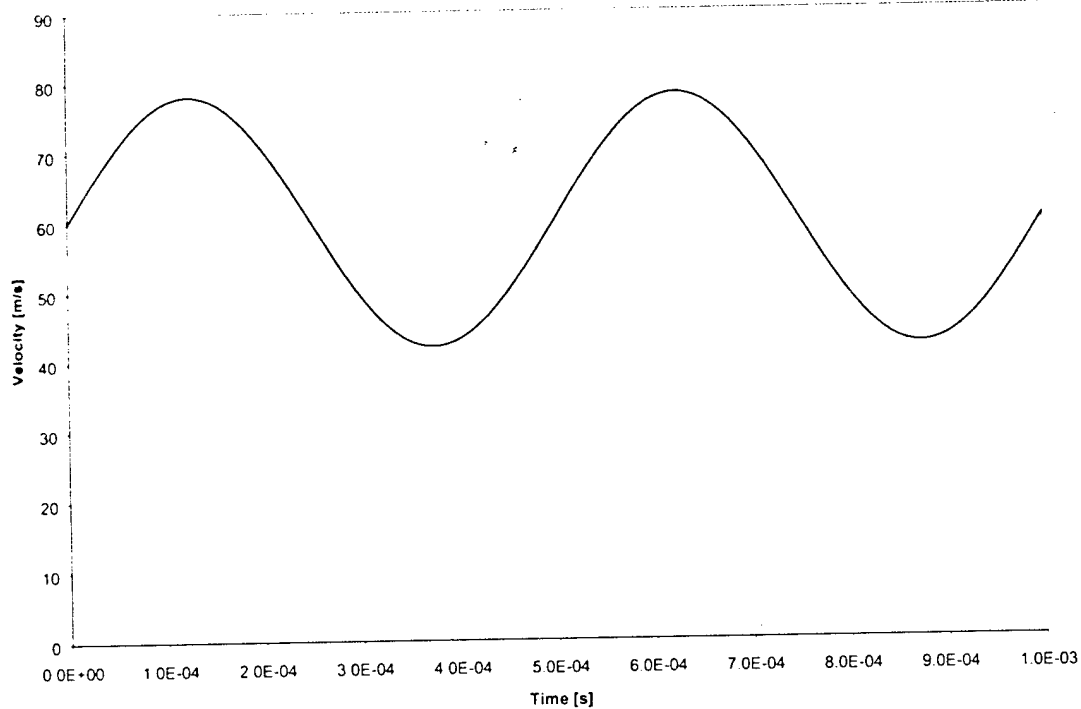


**Fig. 8.10.** Flow velocity with mean 60 m/s, amplitude 30% and frequency 2 kHz.
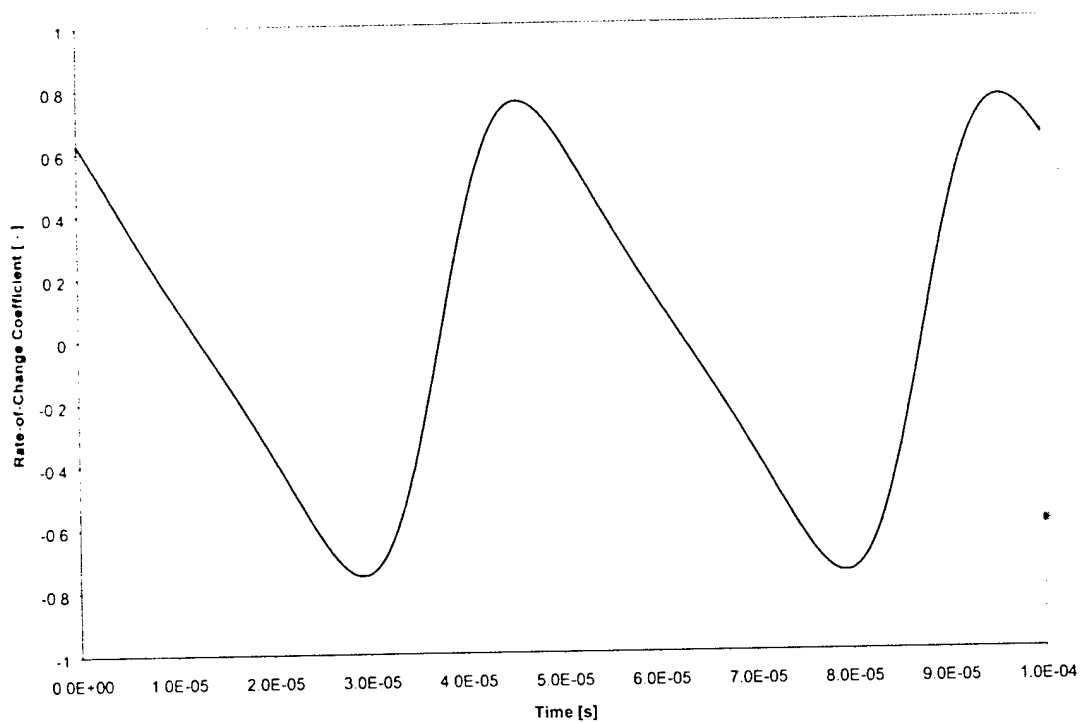
66
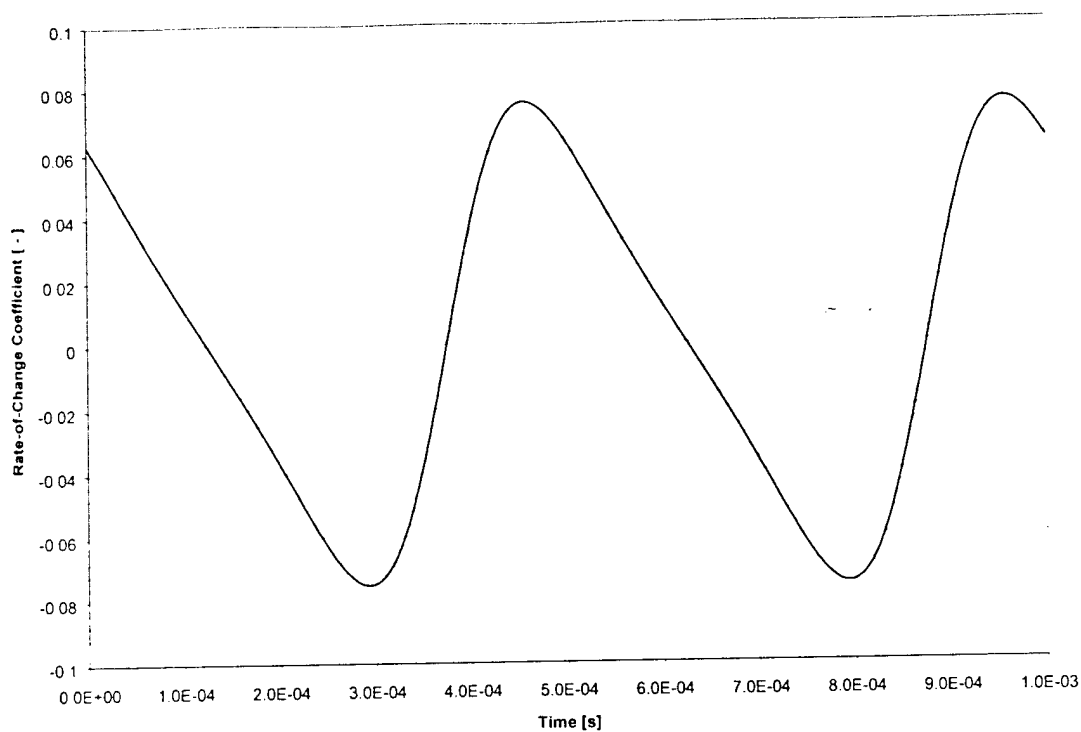
**Fig. 8.11. Rate-of-change coefficient, K.**
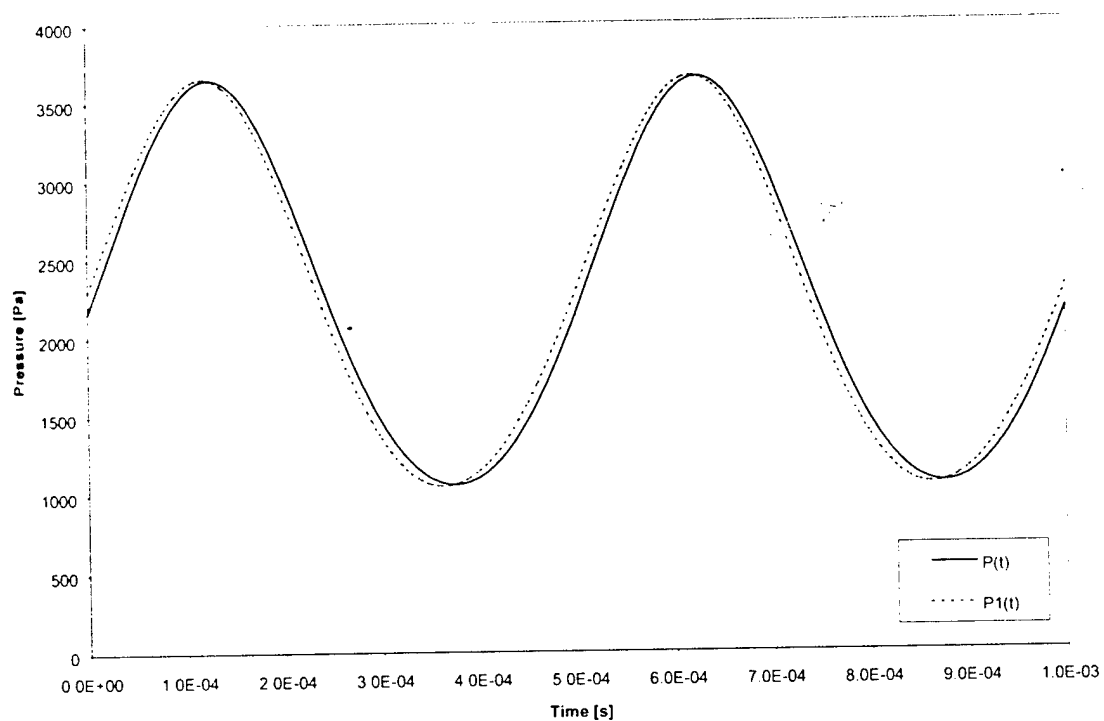


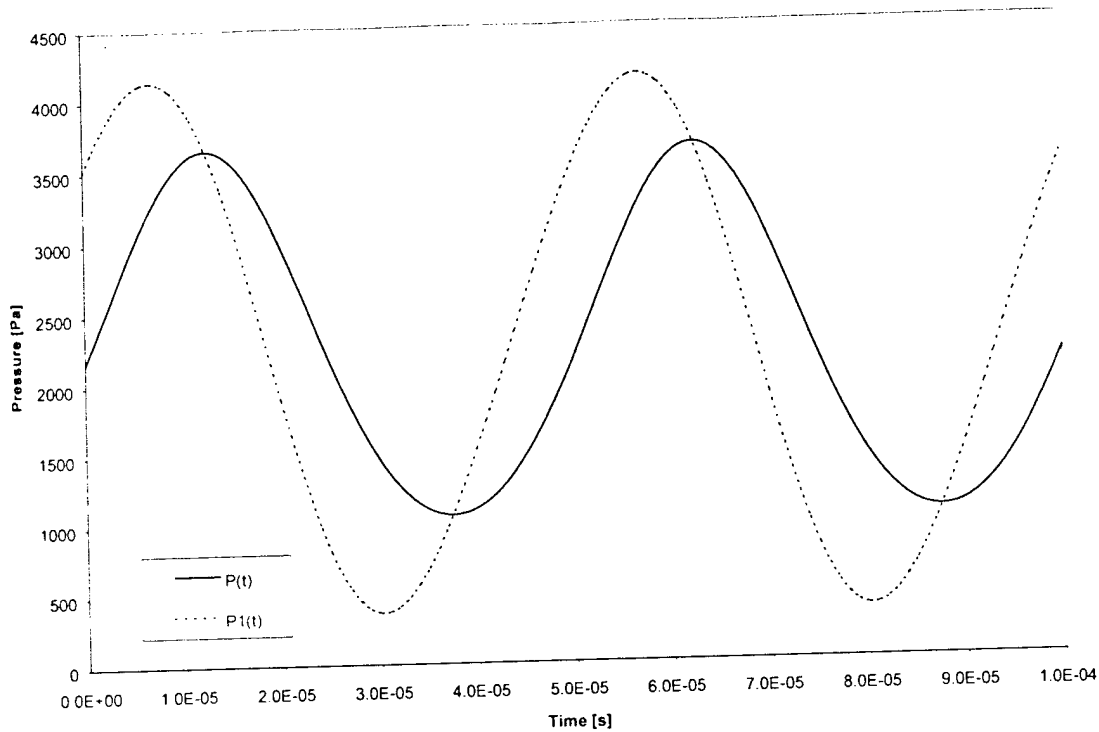**Fig. 8.12. True dynamic pressure and pressure that would be measured at the forward stagnation point on the probe.**

67
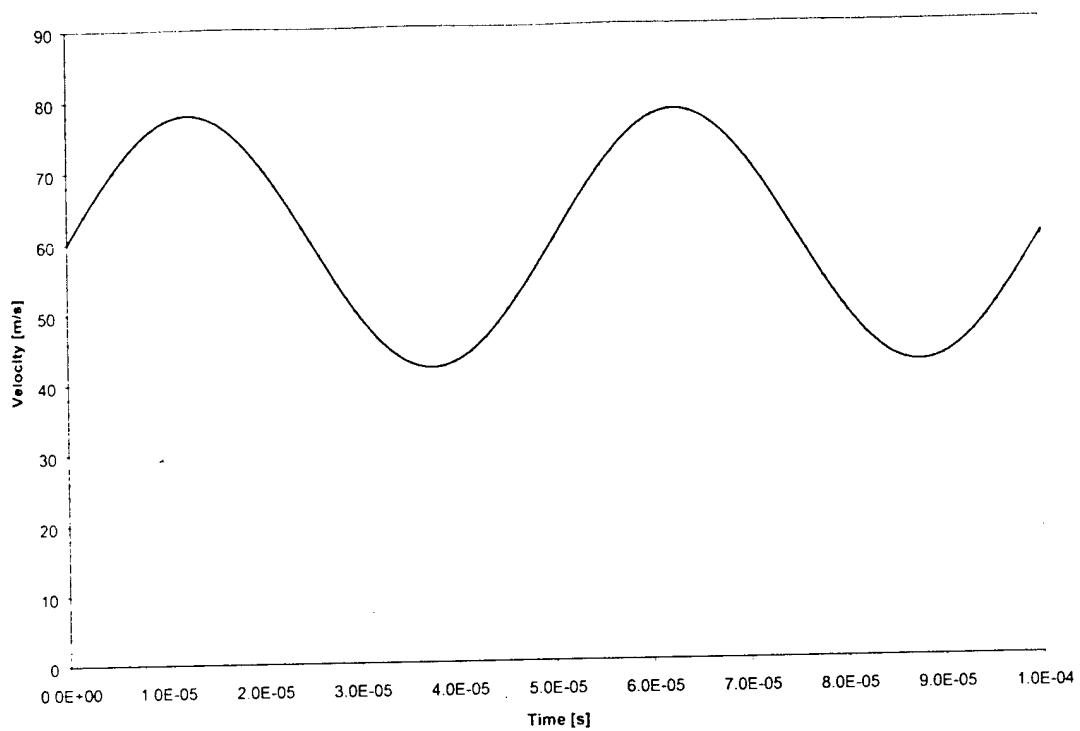
**Fig. 8.13. Flow velocity with mean 60 m/s, amplitude 30% and frequency 20 kHz.**



**Fig. 8.14. Rate-of-change coefficient, K.**

**Fig. 8.15. True dynamic pressure and pressure that would be measured at the forward stagnation point on the probe.**

## Calculation of Flow Angle

Steady probe calibration (see section 7) is performed to determine the relationship between the port pressures and the flow incidence angle. Two non-dimensional pressure coefficients ($B_\alpha$ and $B_\beta$) are used to describe this relationship and are found from experimental calibration of the probe in a steady flowfield with known total and static pressures. The probe is pitched and yawed through a range of angles to simulate all possible angle inclinations and for each such angle the port pressures are recorded and the coefficients calculated. Polynomial surface fits are created that relate the incidence angle ($\alpha$ or $\beta$) to the independent pressure coefficients ($B_\alpha$ and $B_\beta$). For steady data reduction of an unknown flowfield the independent pressure coefficients $B_\alpha$ and $B_\beta$ are calculated from the measured port pressures and the pitch and yaw angles of the flow are given directly by their individual polynomial expressions. This procedure is well established for steady probe calibration and data reduction, but in an unsteady or accelerated flowfield the individual pressures that compose these coefficients also contain inertial effects (eq. 8.11). The contribution of the inertial term in the measured pressure can be significant (fig. 8.15) and the effect this has on the independent coefficients must thus be analyzed. For the port numbering in fig. 8.5 the definitions of $B_\alpha$ and $B_\beta$ are given as (from section 7):

$$B_\alpha = \frac{p_5 - p_4}{p_1 - \frac{1}{4}(p_2 + p_3 + p_4 + p_5)}$$
(8.17)

$$B_\beta = \frac{p_2 - p_3}{p_1 - \frac{1}{4}(p_2 + p_3 + p_4 + p_5)}$$
(8.18)

As discussed in section 7 an additional set of independent pressure coefficients can be defined for high angle flows, however the present discussion will be limited to low angle flows (i.e. where the central pressure port sees the highest pressure). The functions in eqns. 8.17 and 8.18 when plotted against the pitch and yaw angle for the steady theoretical model reveal that $B_\alpha$ depends mostly on the pitch angle and is nearly independent of the yaw angle. Similarly, $B_\beta$ depends mostly on the yaw angle and is nearly independent of the pitch angle. This is a result of geometric symmetry and potential flow. For a well-made probe the coefficients are also very nearly independent. Figs. 8.16 and 8.17 show the steady theoretical surfaces for a sphere:
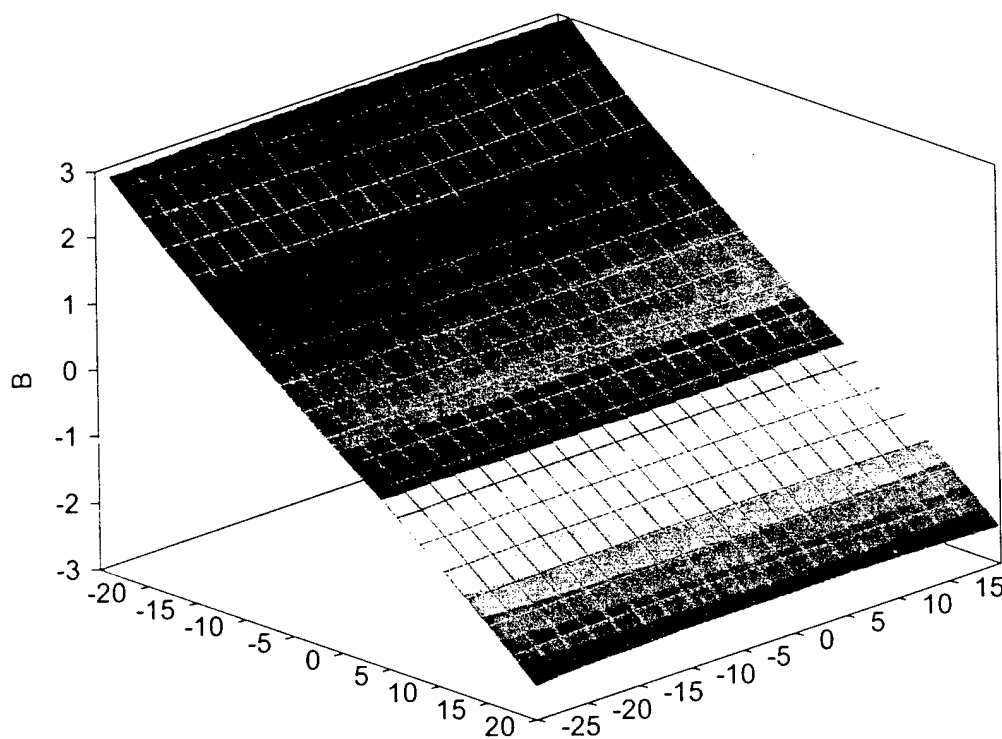


Fig. 8.16. $B_\alpha$ surface vs pitch ($\alpha$) and yaw ($\beta$) angles for a theoretical 5-hole probe based on a sphere.
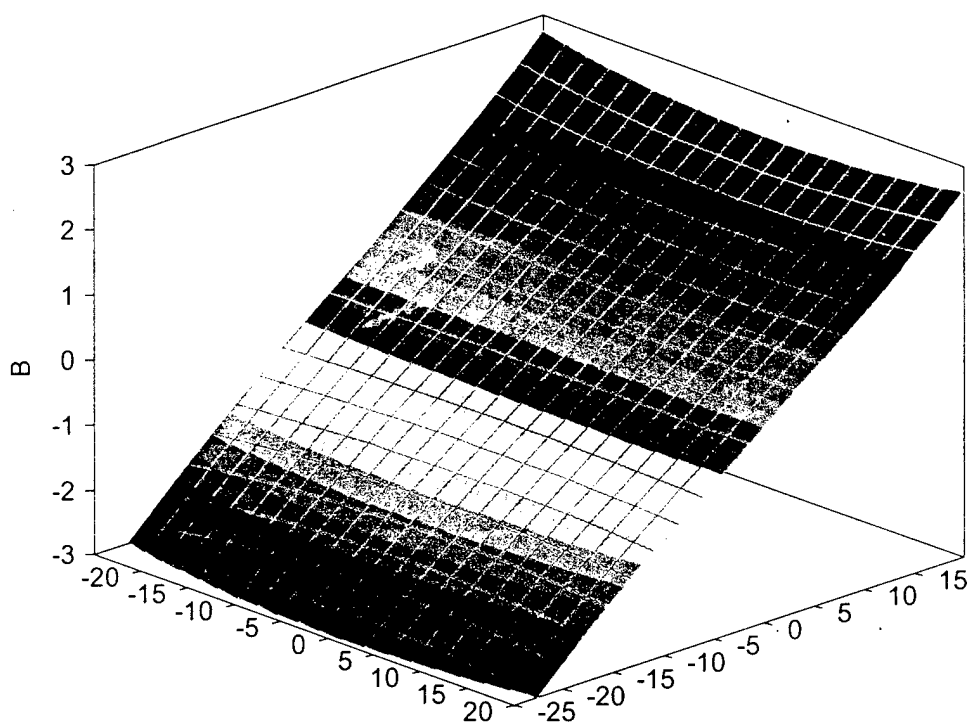
Fig. 8.17. $B_\beta$ surface vs pitch ($\alpha$) and yaw ($\beta$) angles for a theoretical 5-hole probe based on a sphere.
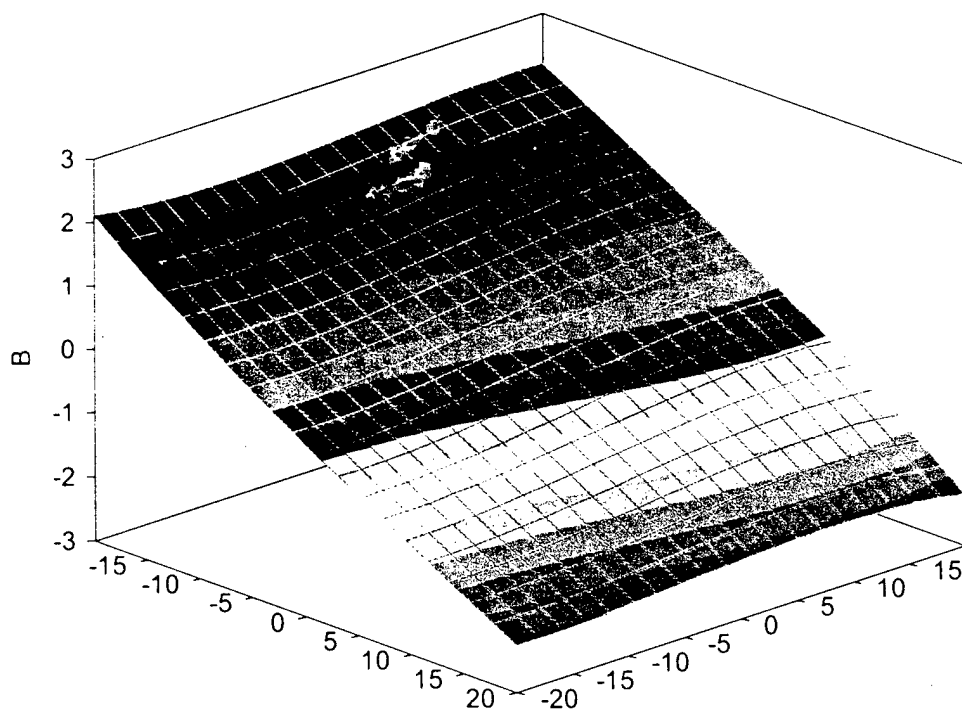


Fig. 8.18. $B_\alpha$ surface vs pitch ($\alpha$) and yaw ($\beta$) angles for a real hemispherical 5-hole probe.
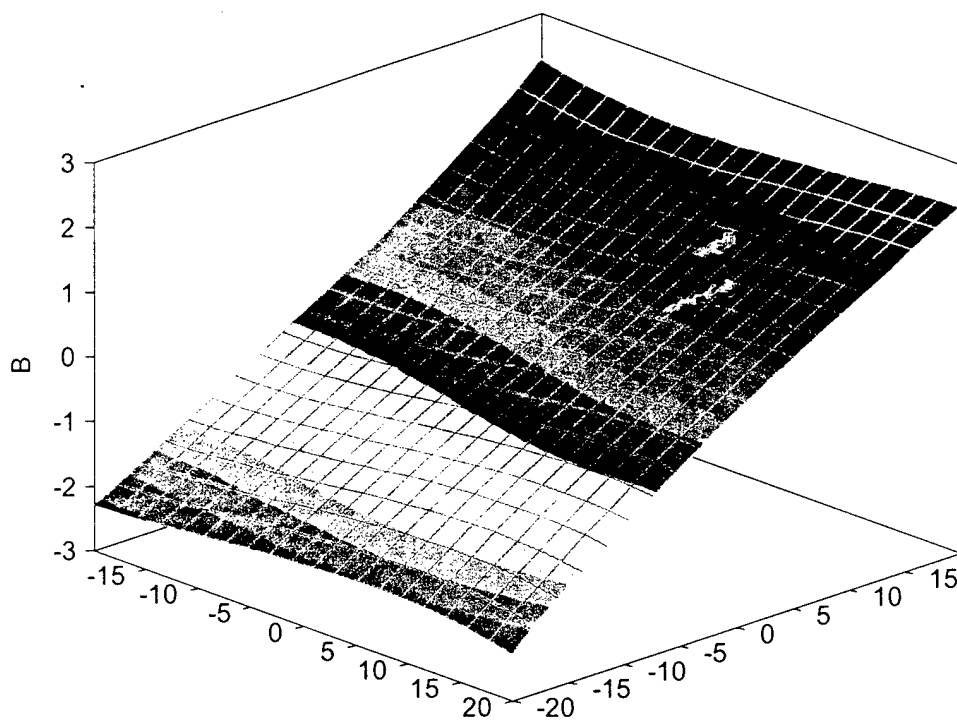
Fig. 8.19. $B_\beta$ surface vs pitch ($\alpha$) and yaw ($\beta$) angles for a real hemispherical 5-hole probe.
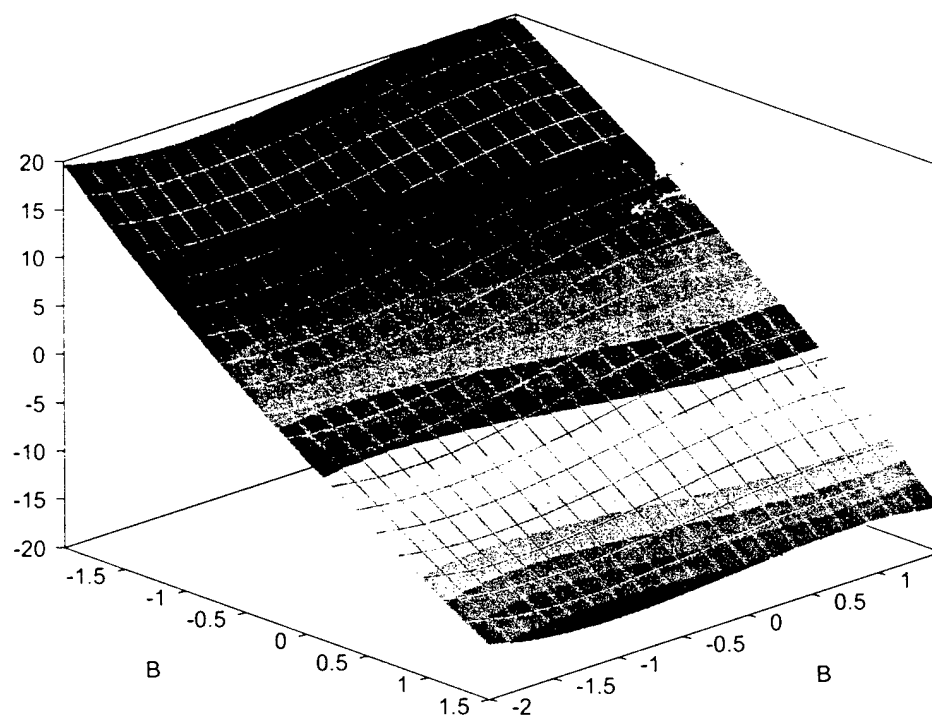


Fig. 8.20. Pitch ($\alpha$) surface vs $B_\alpha$ and $B_\beta$ for a real hemispherical 5-hole probe.
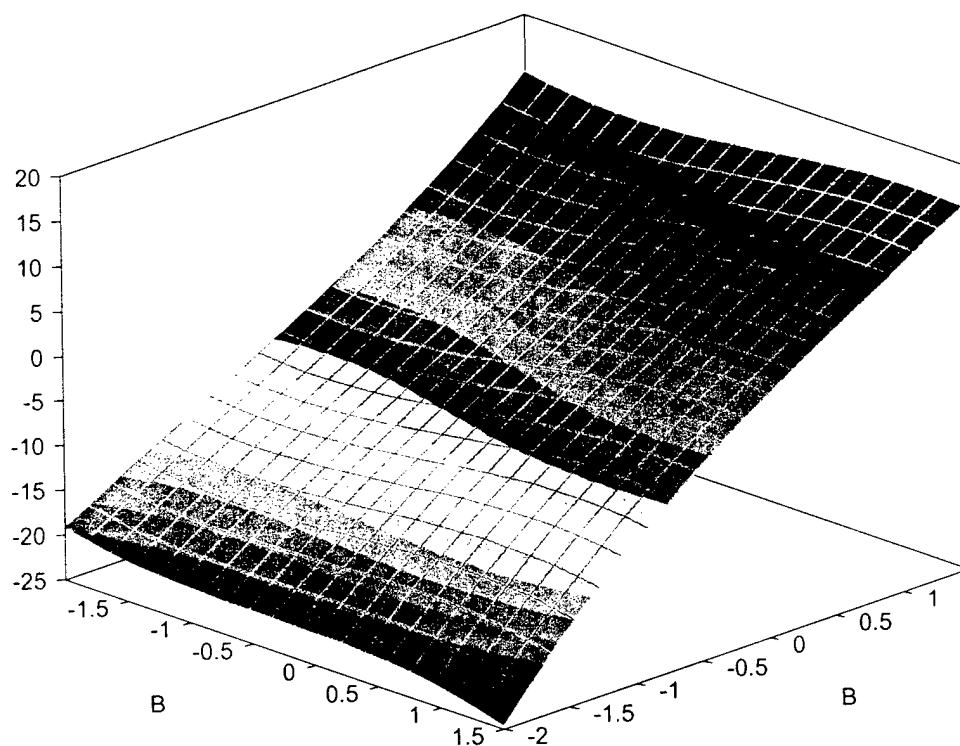
**Fig. 8.21. Yaw (β) surface vs $B_\alpha$ and $B_\beta$ for a real hemispherical 5-hole probe.**

Figs. 8.18 and 8.19 show the independent pressure coefficients for a real hemispherical tipped 5-hole probe. Comparing figs. 8.18 and 8.19 with figs. 8.16 and 8.17 the same trends are seen, however, for a real probe, there is a slight correlation between the two coefficients. Similarly, the angles can be plotted versus the $B_\alpha$ and $B_\beta$ coefficients, indicating how well these surfaces behave and their suitability for polynomial surface fitting (figs. 8.20 and 8.21).

The independent pressure coefficients $B_\alpha$ and $B_\beta$ are defined in terms of the port pressures $p_i$. Using the same expressions and dividing throughout with the dynamic pressure ($1/2\rho U^2$) the coefficients can be described in terms of pressure coefficients according to equation 8.16. The theoretical sphere-based probe is used to generate two sets of independent pressure coefficients: a steady set is identical to what is seen in figs. 8.16 and 8.17, the other includes the inertial term with its magnitude given by the rate-of-change parameter, K. For a K-value of zero the steady and unsteady definitions are identical, but for increasing K-values at large yaw angles the steady and unsteady values diverge (fig. 8.22).

The results in fig. 8.22 are quite remarkable. The $B_\beta$ coefficient show very little dependence on the inertial term for yaw angle up to about 30 degrees even for very large values of K. As mentioned earlier the low angle definition of $B_\beta$ is never used for angles larger than about half the cone angle to the peripheral ports. In fig. 8.23, the data of fig. 8.22 is plotted again as the difference between the steady and unsteady coefficients as a percentage of the range of $B_\beta$ for a limited range of yaw angles.
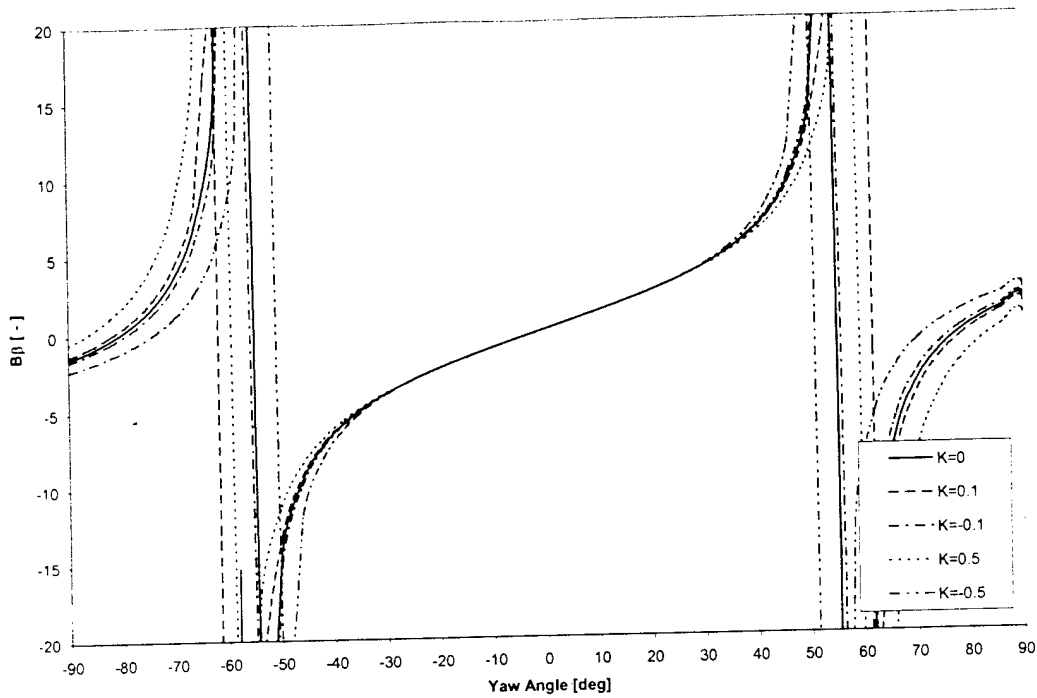
Fig. 8.22. The steady and unsteady definitions of simplified Bbeta vs. yaw angle for a simulated 5-hole probe with rate-of-change, K as parameter.
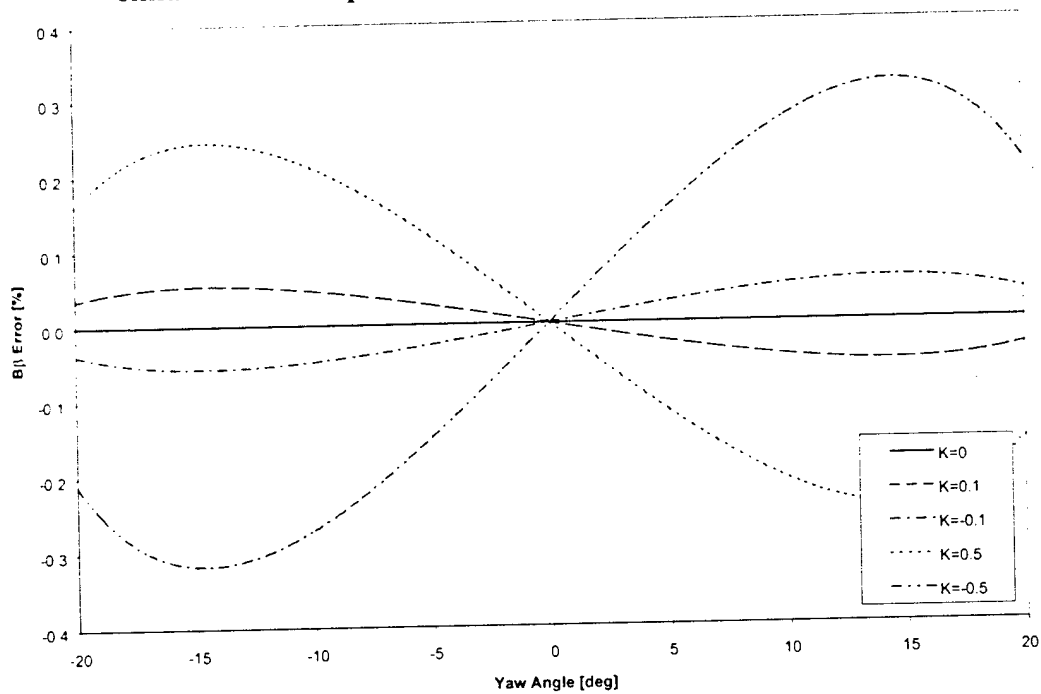


Fig. 8.23. The difference between the steady and unsteady definitions of simplified the $B_\beta$ vs. yaw angle for a simulated 5-hole probe. The error is given as a percentage of the range of the $B_\beta$ coefficient.

Fig. 8.23 shows the error in $B_\beta$ as a percentage of the range of $B_\beta$ for yaw angle from -20 to 20 degrees at zero degrees pitch angle. The remarkable result from this is that for the theoretical model the inertial effects do not alter the $B_\beta$ appreciably and hence the steady calibration data can be used to calculate the angles from the unsteady port pressures that contain significant inertial effects. The process is: the probe is first calibrated in a steady flowfield creating polynomial surface fits for the flow incidence angles $\alpha$ and $\beta$ versus the steady $B_\alpha$ and $B_\beta$. Then, in the data reduction procedure for an unknown unsteady or accelerated flowfield, the port pressures, which may contain significant inertial effects individually, can be used to calculate the independent pressure coefficients directly from eqns. 8.17 and 8.18. These independent coefficients can be used to find the flow angles from the polynomial surface fits from the steady calibration directly. Hence, no inertial correction is necessary to find the flow angles using this procedure.

$$\alpha = f(B_\alpha, B_\beta)\big|_{unsteady} \approx f(B_\alpha, B_\beta)\big|_{steady} \tag{8.19}$$

$$\beta = f(B_\alpha, B_\beta)\big|_{unsteady} \approx f(B_\alpha, B_\beta)\big|_{steady} \tag{8.20}$$

The fact that the inertial contribution is negligible is remarkable and simplifies the task of resolving the flowfield considerably. For a range of pitch and yaw angles the error in the independent coefficients behave as in figs. 8.24 and 8.25.
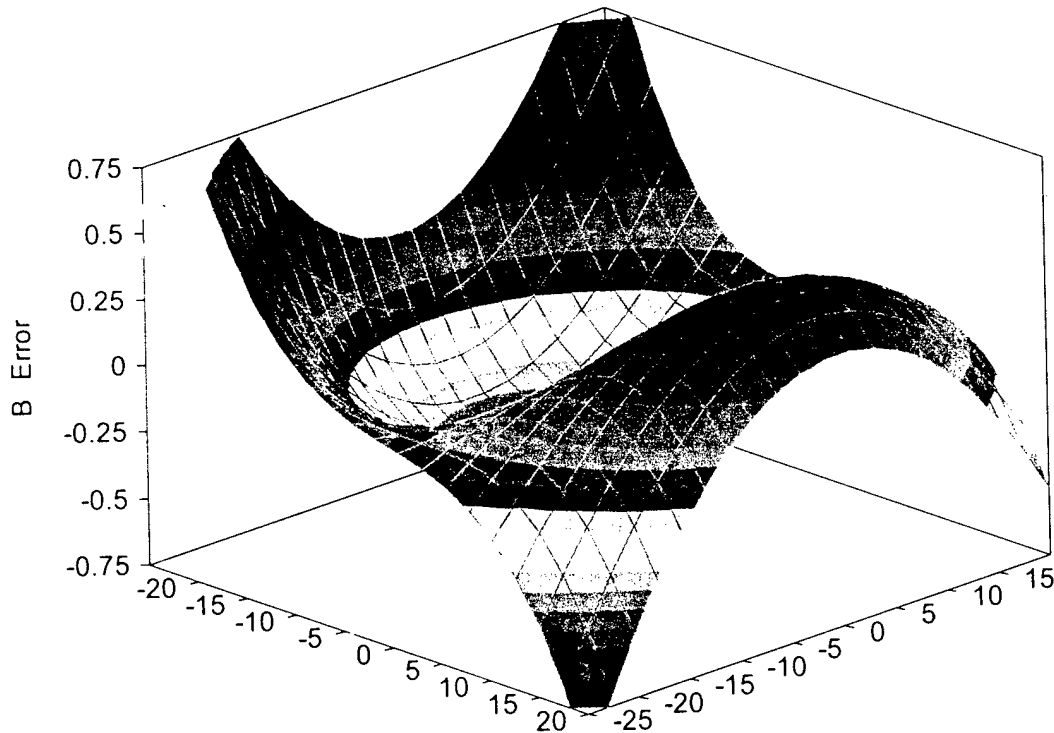


Fig. 8.24. Comparison of steady and unsteady definitions of $B_\alpha$ for a K value of 1.0 vs. pitch and yaw angle. The error is given as a percentage of the range of $B_\alpha$.
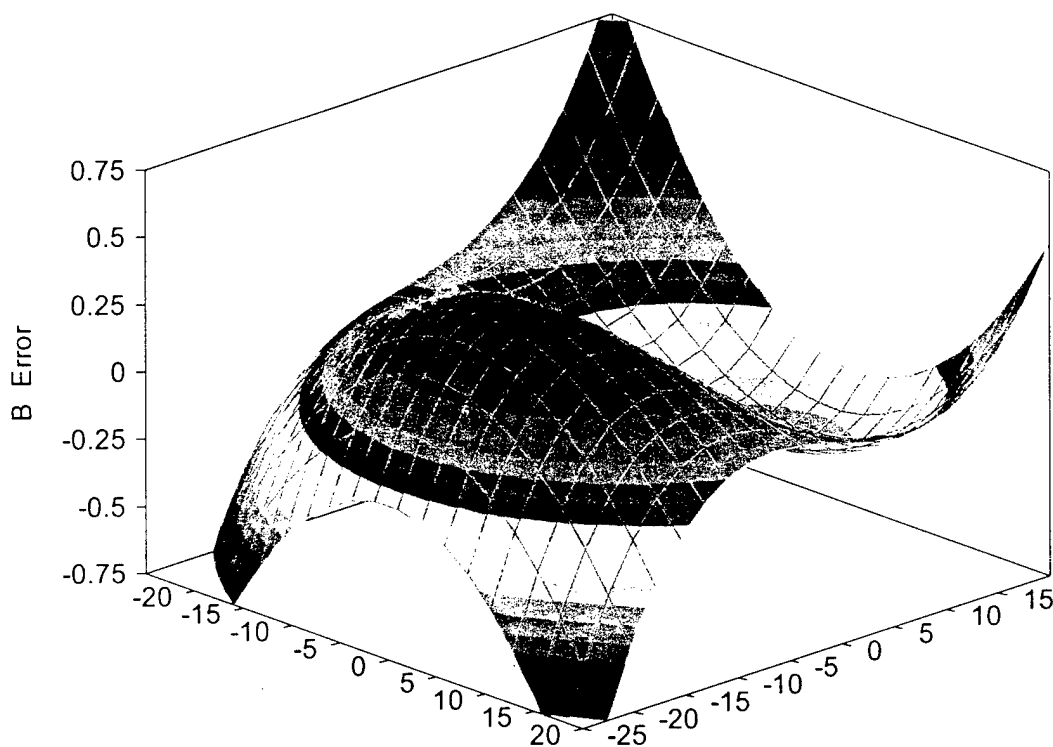
**Fig. 8.25. Comparison of steady and unsteady definitions of $B_\beta$ for a K value of 1.0 vs. pitch and yaw angle. The error is given as a percentage of the range of $B_\beta$.**

At this point it must be reiterated that a K-value of 1.0 is very large (for moderate flow velocities) and the errors observed are quite extreme. The actual error in degrees that results from the error in independent pressure coefficients is dependent on the actual flow angle. However as seen there is very small dependence even for very large values of K. Consider a theoretical spherical 5-hole probe with a tip diameter of 2 mm, placed in a flow with a mean velocity of 30 m/s and a sinusoidal oscillation of +/-20% and frequency of 11 kHz. The flow incidence angle is at zero degree pitch and 15 degrees yaw. A time series of data points is created for this flow and steady independent pressure coefficients are calculated. Fig. 8.26 shows the velocity signal for the example. At this relatively low velocity and large frequency, the maximum value of the rate-of-change coefficient, K is +/-0.5. Fig. 8.27 shows the 5 calculated port pressures for this velocity and flow angle. Note that port pressures 4 and 5 are coinciding due to zero pitch angle and perfect symmetry of the sphere. Port pressures 1 and 2 are nearly identical, due to the flow incidence angle of 15 degrees in yaw which is nearly half the angle between ports 1 and 2 (33 deg / 2). Fig. 8.28 shows the port pressures that would be seen if there were no inertial effects. The independent pressure coefficients $B_\alpha$ and $B_\beta$ are calculated from the pressures in fig. 8.27 (that include the inertial effects) using the polynomial expressions for the flow angles (figs. 8.18 and 8.19). The predicted and exact flow angles are shown in fig. 8.29 and the difference between the two in fig. 8.30.
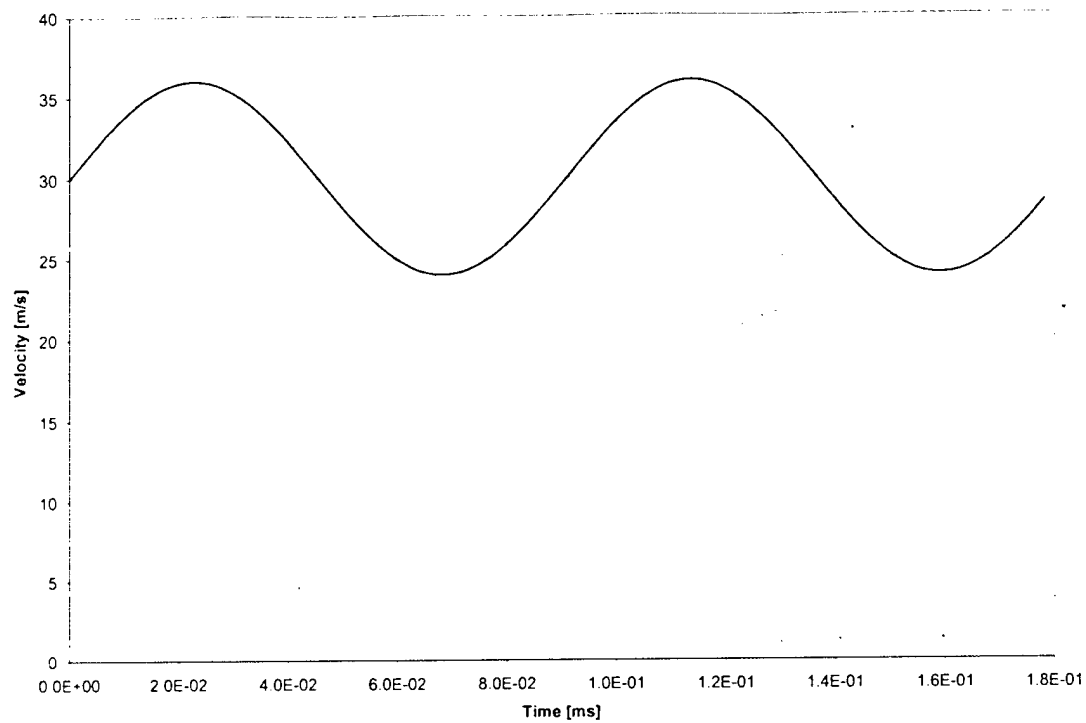
**Fig. 8.26. Flow velocity with mean 30 m/s, amplitude 20% and frequency 11 kHz.**
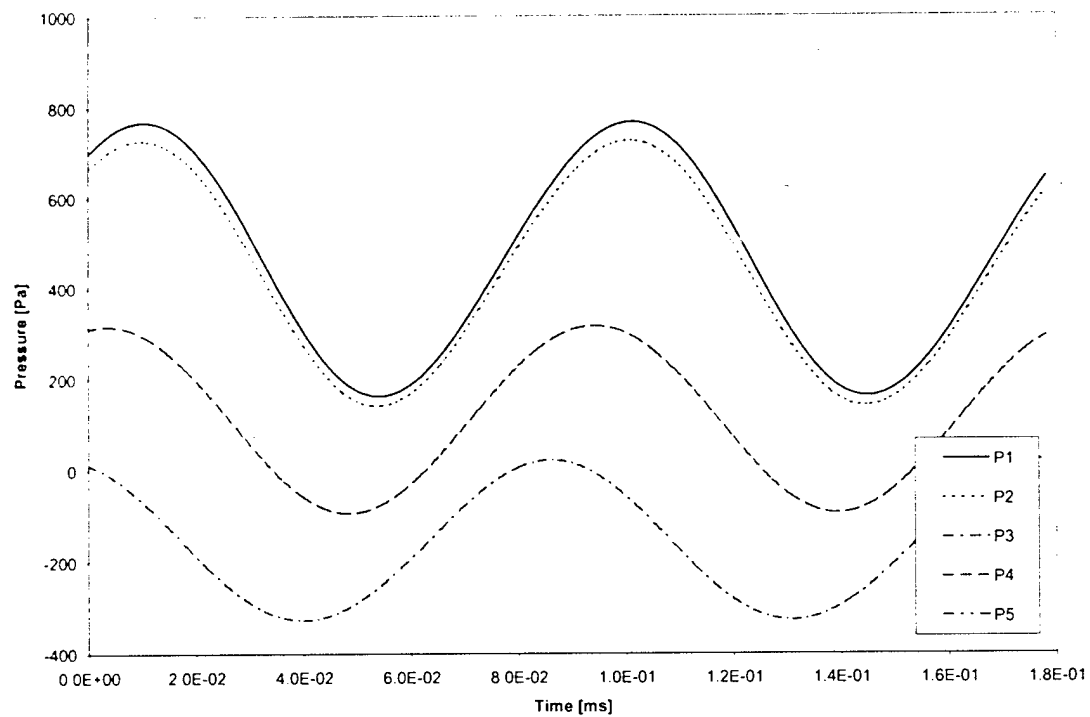


**Fig. 8.27. The five port pressures as calculated from the theoretical model. Pressures from ports 4 and 5 are coinciding due to perfect symmetry of the probe.**
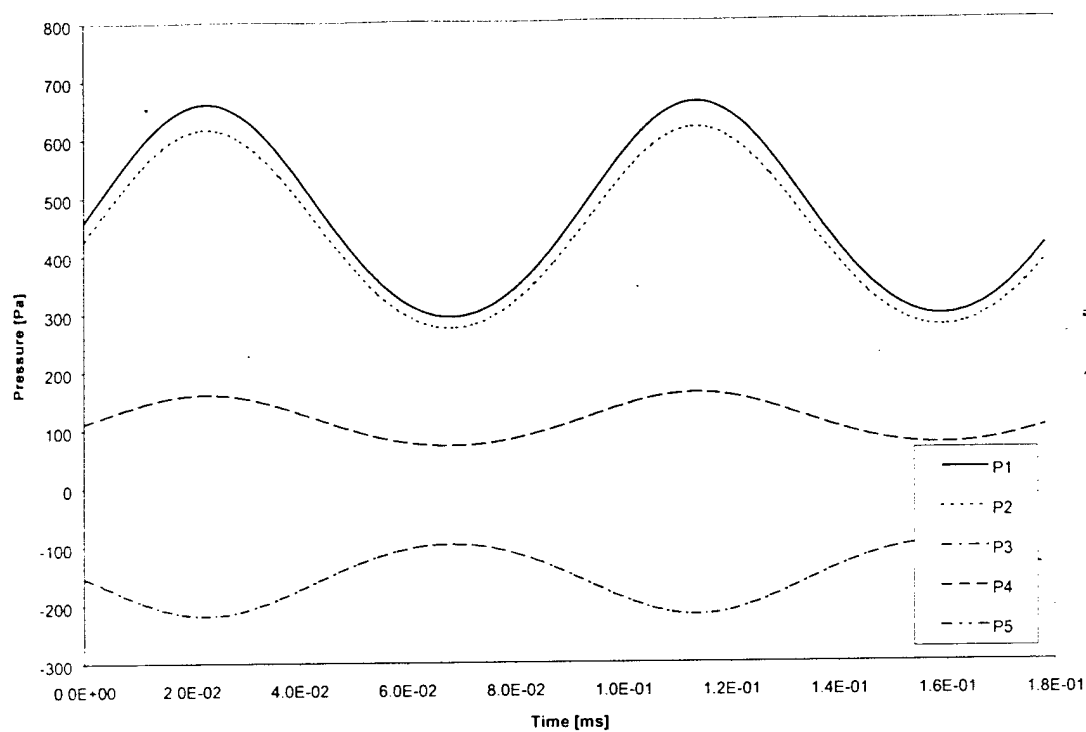
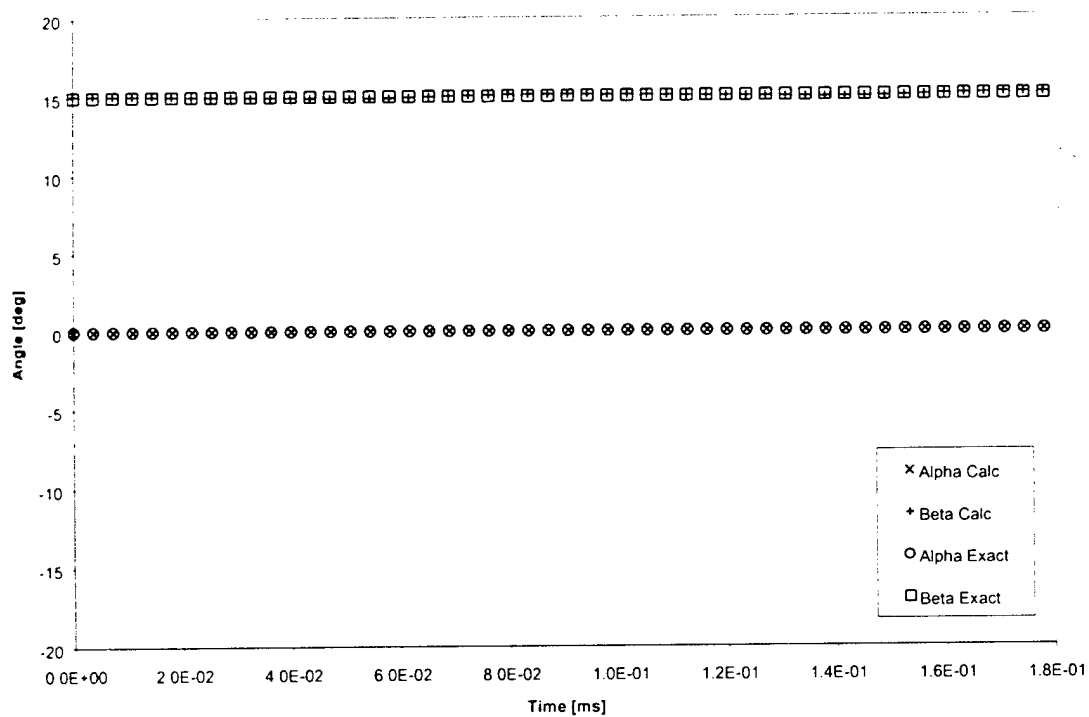**Fig. 8.28. The 5 port pressures that would be seen by the probe if there were no inertial effects.**
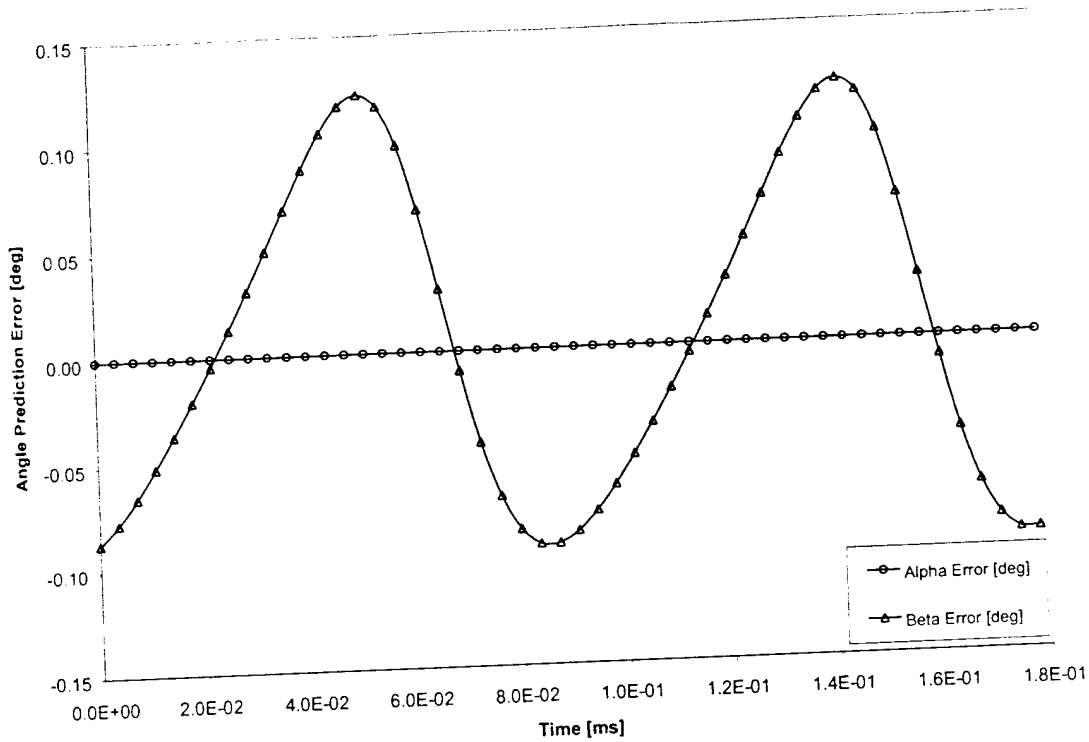


**Fig. 8.29. The predicted pitch and yaw angles in degrees.**

78

Fig. 8.30. Error in predicted pitch and yaw angles in degrees. The mean offset error depends on the flow incidence angle as well as the rate-of-change coefficient, K.

For a sinusoidal velocity signal the rate-of-change coefficient has a zero mean value. However, the predicted angle error in fig. 8.30 shows non-symmetric behavior, with a mean error different from zero. The $B_\beta$ in terms of pressure coefficients is given as:

$$B_\beta(\alpha,\beta,K)=\frac{Cps_2(\alpha,\beta)-Cps_3(\alpha,\beta)+K(Cpu_2(\alpha,\beta)-Cpu_3(\alpha,\beta))}{Cps_1(\alpha,\beta)-\frac{1}{4}\sum_{i=2}^{5}Cps_i(\alpha,\beta)+K\left(Cpu_1(\alpha,\beta)-\frac{1}{4}\sum_{i=2}^{5}Cpu_i(\alpha,\beta)\right)} \qquad (8.21)$$

where Cps and Cpu denote the steady and unsteady pressure coefficients, respectively. In equation 8.21 the rate-of-change coefficient appears in both the numerator and denominator. For zero flow incidence angle, the steady definitions of the pressure coefficients for ports 2 and 3 are equal and also the unsteady definitions are equal. Hence the numerator in equation 8.21 is zero regardless of the magnitude of K. For all other values of flow incidence angle, the influence of the unsteady term depends both on the angle and K. For most flow fields with moderate K values, the mean error is very small and usually within the prediction capabilities of the probe. However, if further accuracy is required a polynomial expression could be created to account for the mean shift as a function of the flow incidence angle and the K parameter. Thus the mean of the predicted quantities can be adjusted after the angles and velocity magnitude have been determined.

The data in the figures above are purely theoretical and given for a sphere, not an imperfect hemisphere of a real probe. Even so, given the agreement between theoretical and experimental values for steady data, the procedure should also be valid for a real probe granted accurate calibration data is available. It is reasonable to believe that the small errors in fig. 8.30 are due to the perfect symmetry of the probe, thus an analysis was performed where each of the pressure port locations were perturbed slightly, within the ranges that could be seen for a real 5-hole probe. The surface is still a perfect hemisphere, but the symmetry and the "canceling effect" from symmetrically opposite pressure ports is no longer present. The new pressure port locations were chosen as:

**Table 8.1. Original and perturbed port locations.**

| Port # | Original | | Perturbed | |
|--------|----------|---------|-----------|---------|
| | Cone [deg] | Roll [deg] | Cone [deg] | Roll [deg] |
| 1 | 0 | 0 | 1 | 0 |
| 2 | 33 | 0 | 37 | 4 |
| 3 | 33 | 180 | 28 | 170 |
| 4 | 33 | 90 | 35 | 93 |
| 5 | 33 | 270 | 32 | 268 |

The theoretical "calibration" of the probe reveals the asymmetry in the port locations (figs. 8.31 and 8.32). The expected difference between the steady and unsteady definitions of the independent pressure coefficients are shown in figs. 8.33 and 8.34.
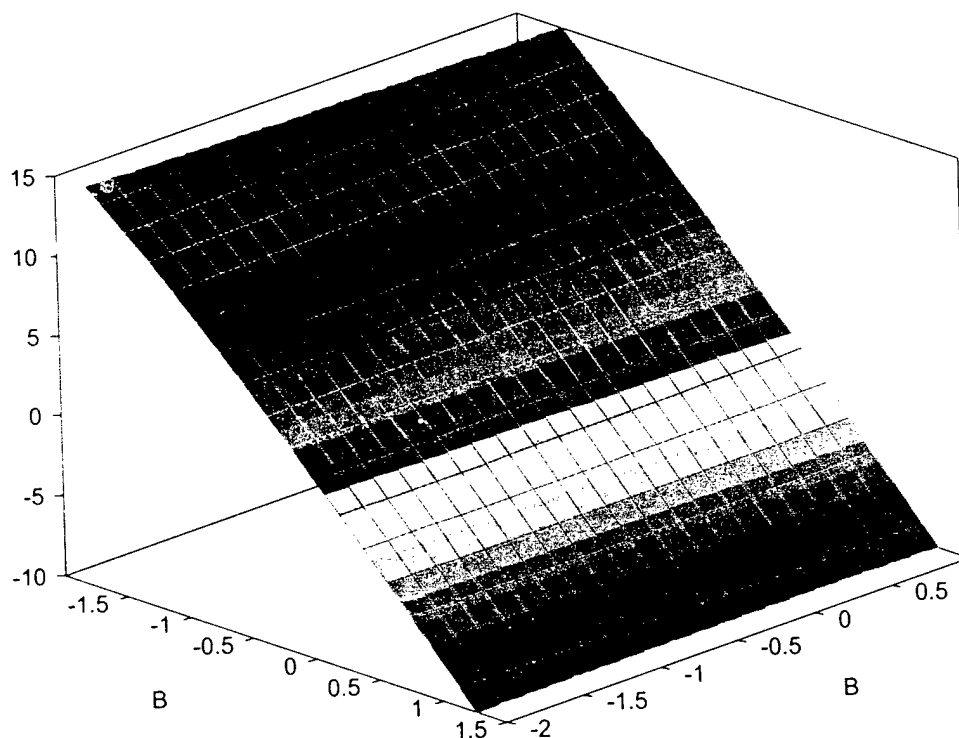


**Fig. 8.31. Pitch calibration surface for the spherical probe with perturbed port locations.**
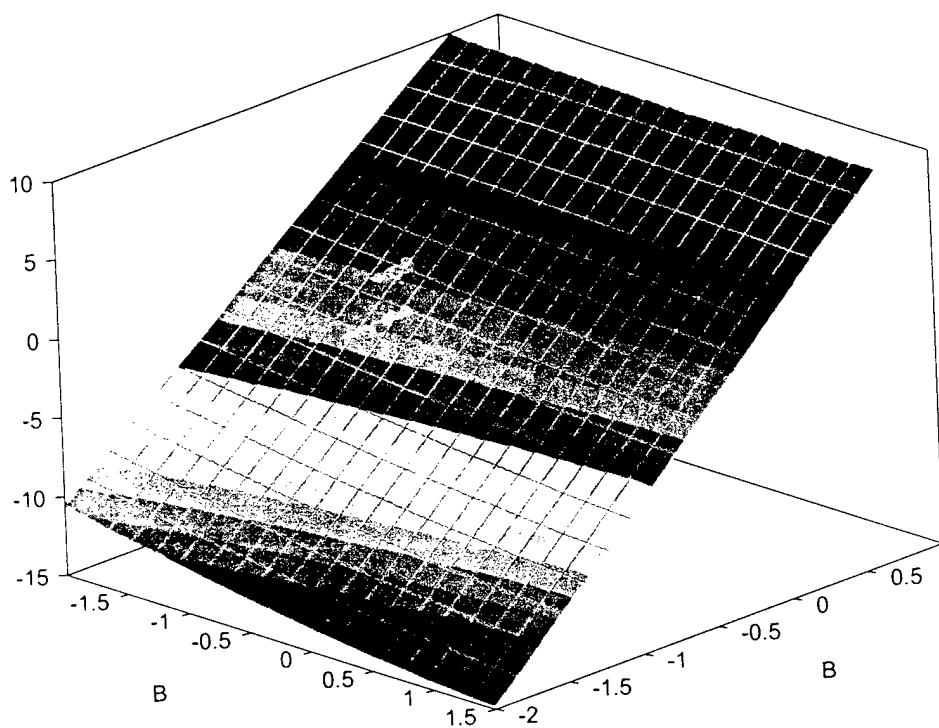
Fig. 8.32. Yaw calibration surface for the spherical probe with perturbed port locations.
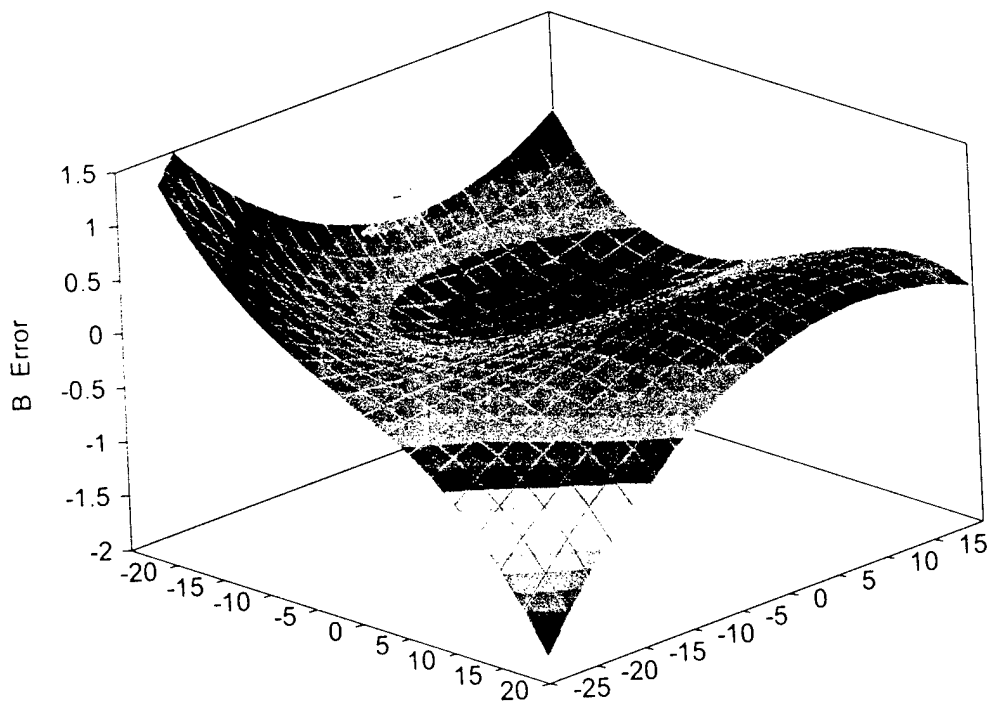


Fig. 8.33. Comparison of steady and unsteady $B_\alpha$ vs. pitch and yaw angle for the perturbed probe. The K-value is 1.0 and the error is given as a percentage of the range of $B_\alpha$.
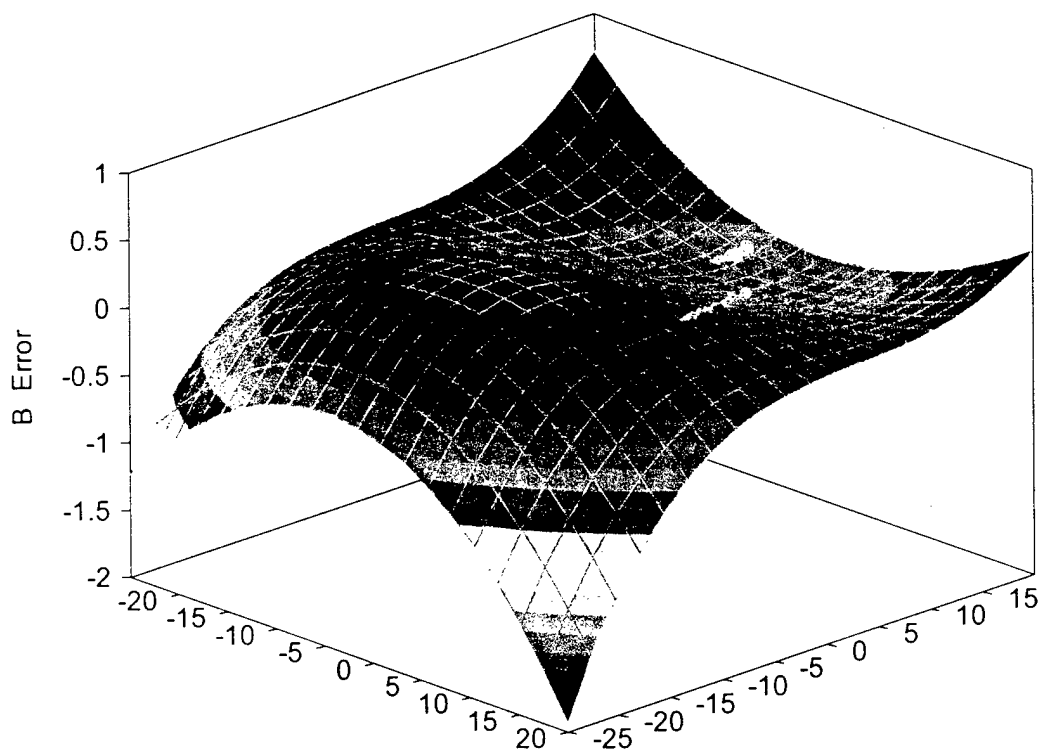
**Fig. 8.34. Comparison of steady and unsteady $B_\beta$ vs. pitch and yaw angle for the perturbed probe. The K-value is 1.0 and the error is given as a percentage of the range of $B_\beta$.**

Creating a time series of data with the same parameters as in the previous example, data reduction (using the new polynomials for pitch and yaw) can subsequently be performed. The new calculated port pressures are seen in fig. 8.35. The independent pressure coefficients $B_\alpha$ and $B_\beta$ are calculated from the pressures in fig. 8.35 using the polynomial expressions for the flow angles. The error in the predicted pitch and yaw angles is seen in fig. 8.36. For the unperturbed probe there was no error in the predicted pitch angle, however for the perturbed probe a small periodic pitch error is observed. An important observation is that the range of the yaw error does not increase from the unperturbed to the perturbed case (the range of yaw error actually has decreased slightly). This shows that the prediction capabilities are not significantly dependent upon port location symmetry (as long as accurate calibration is available).
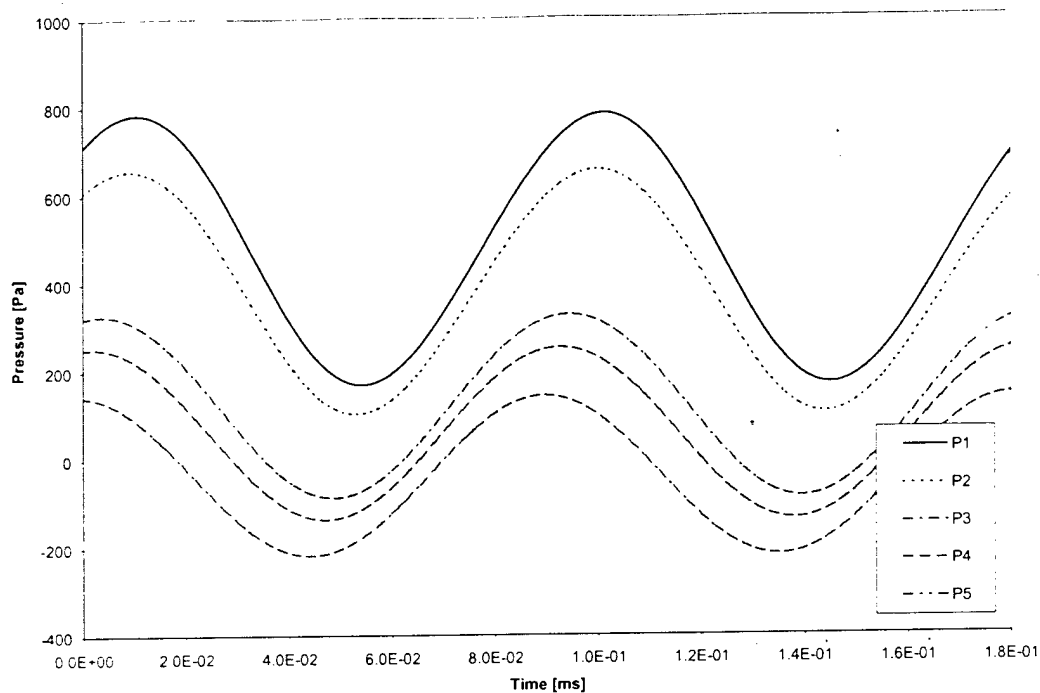
**Fig. 8.36.** The five port pressures as calculated from the theoretical model. Comparing with fig. 8.27 it can be seen that pressures from ports 4 and 5 are no longer coinciding due to the asymmetry in the port locations.
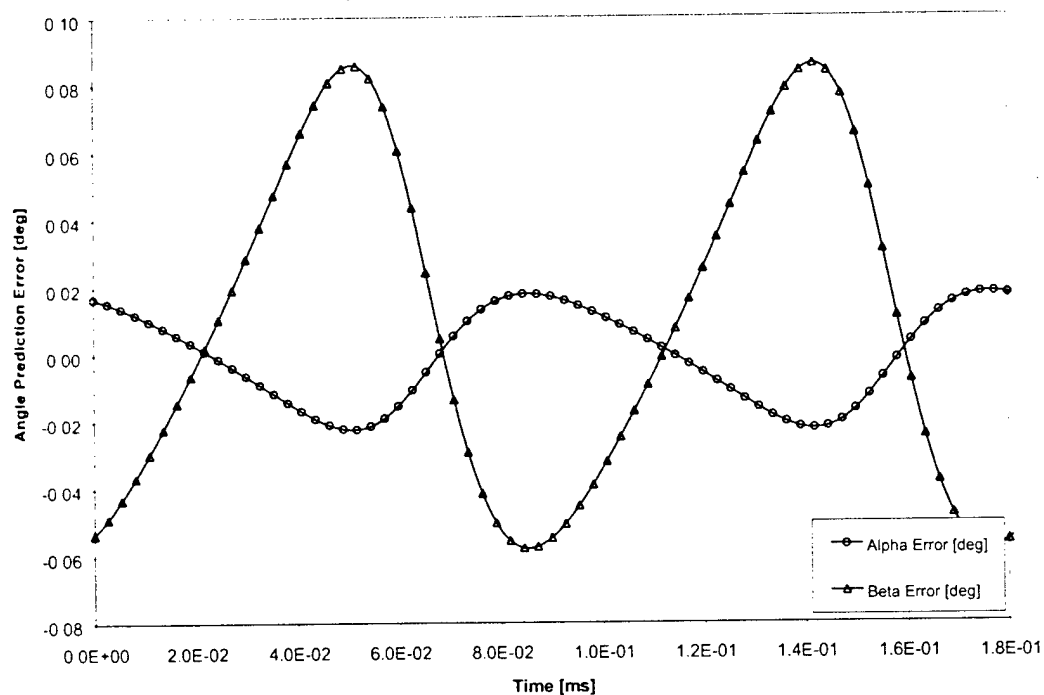


**Fig. 8.37.** Error in predicted pitch and yaw angles in degrees. Due to non-symmetric port locations an error shows up in the pitch angle. Worth noticing is that the maximum observed errors do not increase with the non-symmetric port locations.

83

The issue still lingers that the model is based on a perfect sphere and also the calibration slopes are given very accurately since exact pressures are known. The method does not readily lend itself to perturbing the surface of the sphere, but the individual calculated pressures can be perturbed slightly in a random fashion. If this random perturbation only results in minor errors in the predicted flow angles, there is further reason to believe that the method will be successful on a real probe. Each of the 5-port pressures from the perturbed probe is randomly perturbed by a maximum of 5%. The perturbed port pressures are shown in fig. 8.38, and the same procedure of data reduction is performed with these pressures. The predicted flow angle error are shown in fig. 8.39 and are in the range of 0.5 degrees.
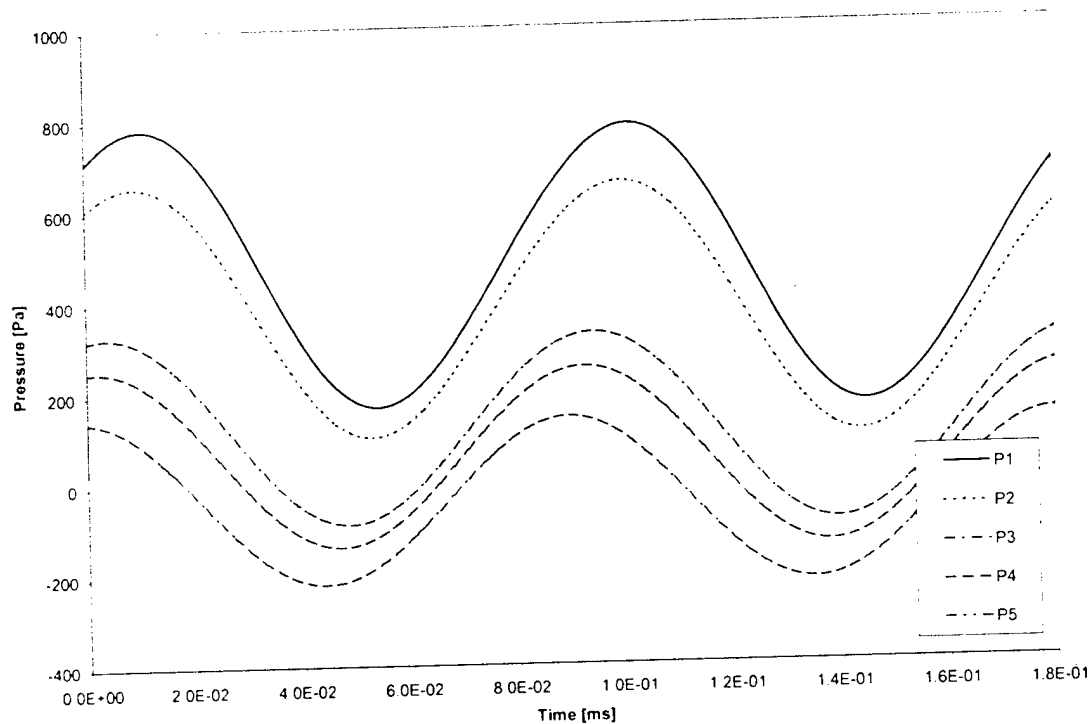


Fig. 8.38. The five port pressures as calculated from the theoretical model in addition a random magnitude up to 5% is added to each of the individual port pressures.

## Calculation of Velocity Magnitude

Determination of the velocity magnitude for a conventional multi-hole probe is typically done by first finding the probe local total and static pressures. The challenge is thus to determine these two pressures from the 5 port pressures. During calibration, all of the port pressures, as well as the total and static pressure, are known. By relating the total pressure to the quasi-dynamic pressure formed by the port pressures a total pressure coefficient can be defined. Similarly the static pressure can also be related to the port pressures using a static pressure coefficient. There are a number of ways such coefficients can be defined; the best definitions are those which show only slight dependence on Mach and Reynolds number. One set of definitions is:

$$A_t = \frac{p_1 - p_t}{p_1 - \frac{1}{4}(p_2 + p_3 + p_4 + p_5)}$$
(8.22)

$$A_s = \frac{p_t - p_s}{p_1 - \frac{1}{4}(p_2 + p_3 + p_4 + p_5)}$$
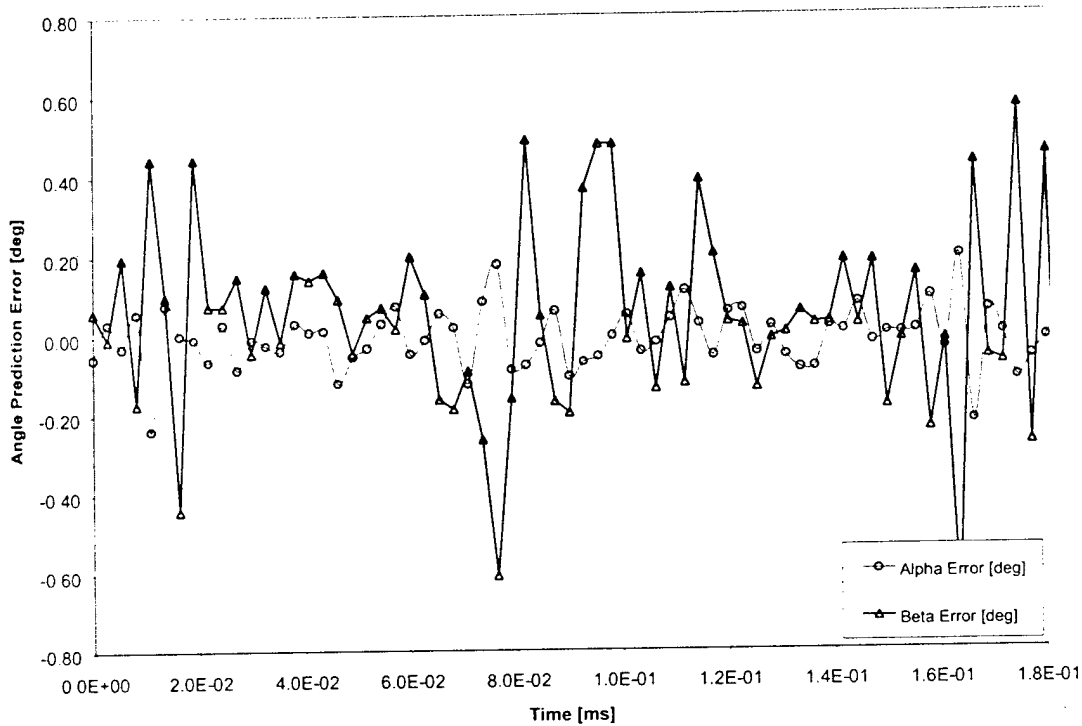(8.23)



**Fig. 8.39. Error in predicted pitch and yaw angles in degrees. The errors in the pressures propagate into a random error in the calculated angles, however nowhere is the data seen to diverge due to the noise in the pressures.**

$A_t$ and $A_s$ denote the total an static pressure coefficients respectively. During steady calibration all of the port pressures and also the total and static pressures for all flow incidence angles are known and surface fits are created for $A_t$ and $A_s$ versus either the pitch and yaw angle (or equivalently the independent pressure coefficients $B_\alpha$ and $B_\beta$). In steady data reduction the pressures from an unknown flowfield are first used to determine pitch and yaw angle (or $B_\alpha$ and $B_\beta$) then surface fitted values for $A_t$ and $A_s$ are found from the calibration curves. Once $A_t$ and $A_s$ are known, eqns. 8.22 and 8.23 can be solved for the total and static pressures. For an unsteady data reduction the total and static pressure coefficients are strongly influenced by the inertial effects seen by the probe and there would be significant difficulty in first finding each of the "corrected" port pressures, that is, the port pressures minus the inertial effects. For this work the static pressure is assumed to be known and constant. The flow will further be assumed to be

incompressible such that constant density and Bernoulli's equation can be used directly to relate the pressures and the velocities. The center port pressure is then given as:

$$p_1(\alpha, \beta, U, t) = \frac{1}{2}\rho\left[U^2 Cp_{steady_1}(\alpha, \beta) + R\frac{dU}{dt}Cp_{unsteady_1}(\alpha, \beta)\right]$$

(8.24)

From the steady calibration a steady pressure coefficient $Cp_{steady}$ can be found versus the pitch and yaw angle as:

$$Cp_{steady1}(\alpha, \beta) = \frac{p_1(\alpha, \beta)}{\frac{1}{2}\rho U^2}$$

(8.25)

For a perfect sphere using the cone and roll angle system, the $Cp_{steady}$ is given in equation 8.9. Similarly, using the cone and roll angle system the unsteady pressure coefficient $Cp_{unsteady}$ can be found from equation 8.9. The experimental determination of the unsteady pressure coefficient is much more complex and will be discussed in a following chapter, but for now it will be assumed that such an expression exists. During data reduction a time history of port pressures $p_1(t)$ is recorded and the pitch and yaw angles are found for each point. Thus for any time instant both angles are known and thus the value of the steady and unsteady pressure coefficients $Cp_{steady}$ and $Cp_{unsteady}$ can be determined. The problem then reduces to solving equation 8.25 which is a non-linear, first-order, ordinary differential equation. Such equations can easily be solved for a time history of data using numerical methods. A modified Euler predictor-corrector scheme is used to solve the following equation for the velocity U:

$$\frac{dU(t)}{dt} = U'(t) = U(t)^2\frac{Cp_{steady_1}(\alpha(t), \beta(t))}{RCp_{unsteady_1}(\alpha(t), \beta(t))} - p_1(t)\frac{2}{\rho RCp_{unsteady_1}(\alpha(t), \beta(t))}$$

(8.26)

The first step in obtaining a solution for the velocity for the time history is to find the best possible prediction of the velocity at the start of the time series. However with no a priori knowledge of the flowfield a good prediction of the starting velocity is nearly impossible. As it will be shown, having a relatively high sampling rate of the data, reasonable starting guesses will help, but is not required to accurately determine the velocity. The starting values will be set as:

$$U(t_0) = \sqrt{\frac{2p_1(t_0)}{\rho Cp_{steady}(\alpha(t_0), \beta(t_0))}}$$

(8.27)

The predictor-corrector scheme is then as follows:

Predictor: $$U(t_{j+1}) = U(t_{j-1}) + 2hU'(t_j)$$

(8.28)

Corrector: $$U(t_{j+1}) = U(t_j) + h\frac{U'(t_{j+1}) + U'(t_j)}{2}$$

(8.29)

where h is the time spacing in between the data points and j is the index of data points in the time series. The errors made in the predictor and corrector steps are on the order of $h^3$ meaning that by doubling the sampling frequency and hence cutting the time between data points in half the error is reduced by approximately 1/8. This means that a high sample rate is a necessary prerequisite for the data reduction using the above method to be accurate.

Considering a probe in a sinusoidally varying flowfield with magnitude of 20%. The maximum K-value for the probe in this flow is 0.25. The first test case has only 10 data point per period and the normalized measured and total pressures are shown in fig. 8.40 revealing significant inertial effects. As mentioned earlier the starting point of the time history is a problem area and thus two periods are discarded from the start of the time series. The velocity prediction reveals significant errors and thus the prediction capabilities of the numerical approach are poor for this sampling rate (fig. 8.41, 8.42). Doubling the sample rate such that there are now 20 points per period the prediction capabilities are much better and the error is expected to drop by a factor of eight. Fig. 8.43 shows the time history of the pressures with 20 points per period, and fig. 8.44 shows the predicted velocity magnitude. Fig. 8.45 shows the error in the predicted velocity magnitude and it is seen that the accuracy of method by doubling the number points per period increased significantly.
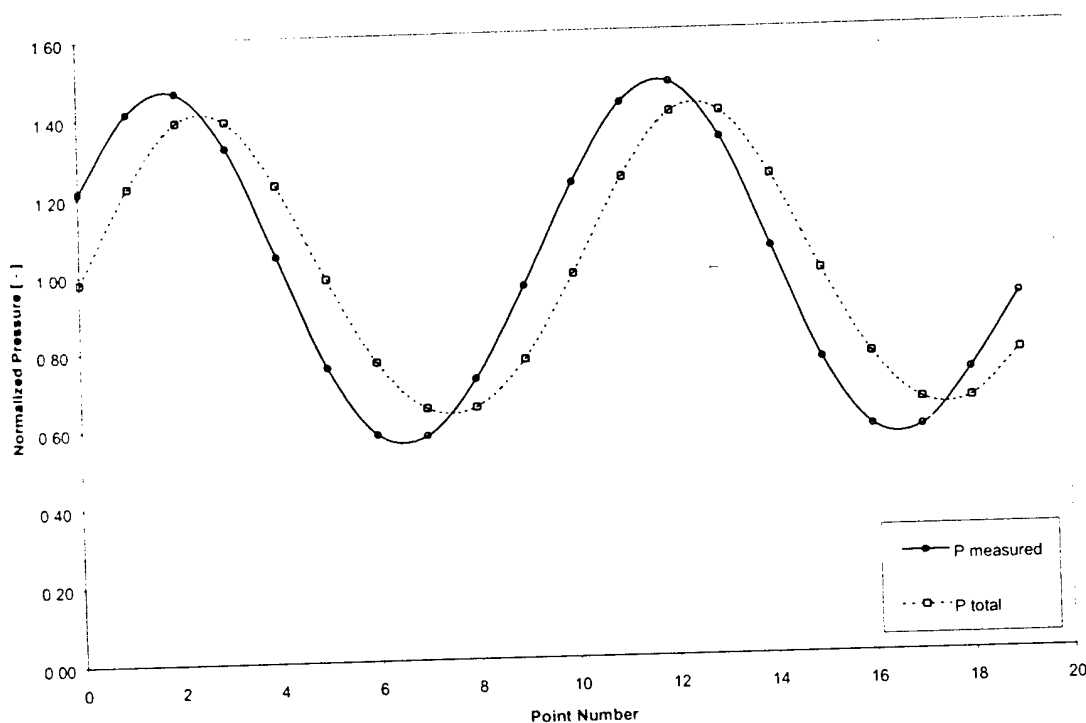


Fig. 8.40. Normalized sphere pressure and total pressure of the flow with 10 points per period.
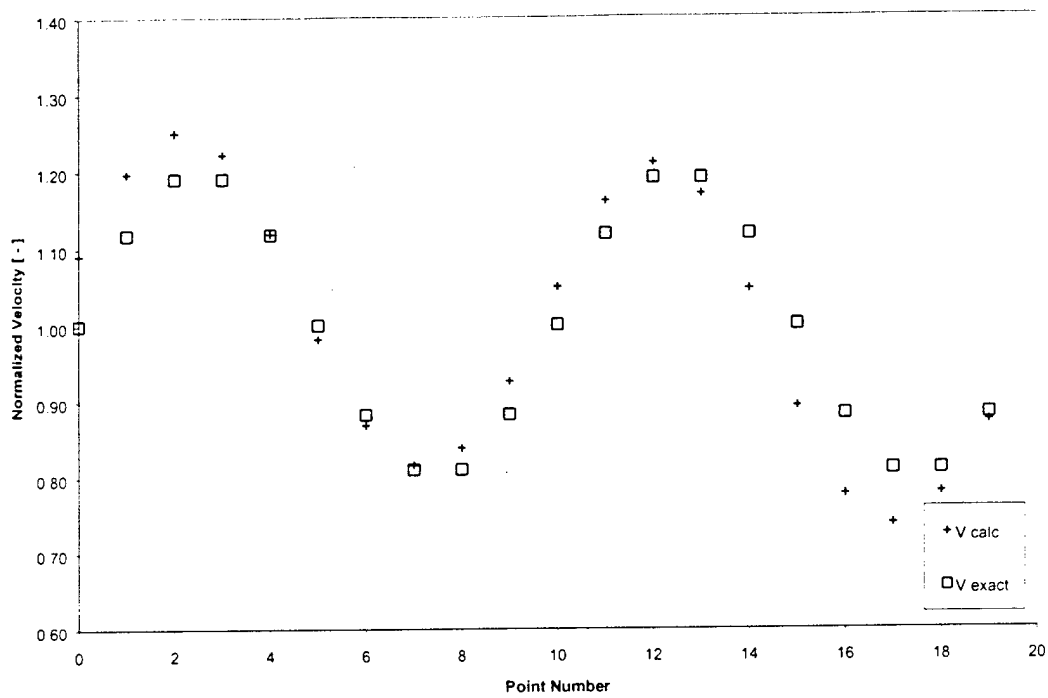
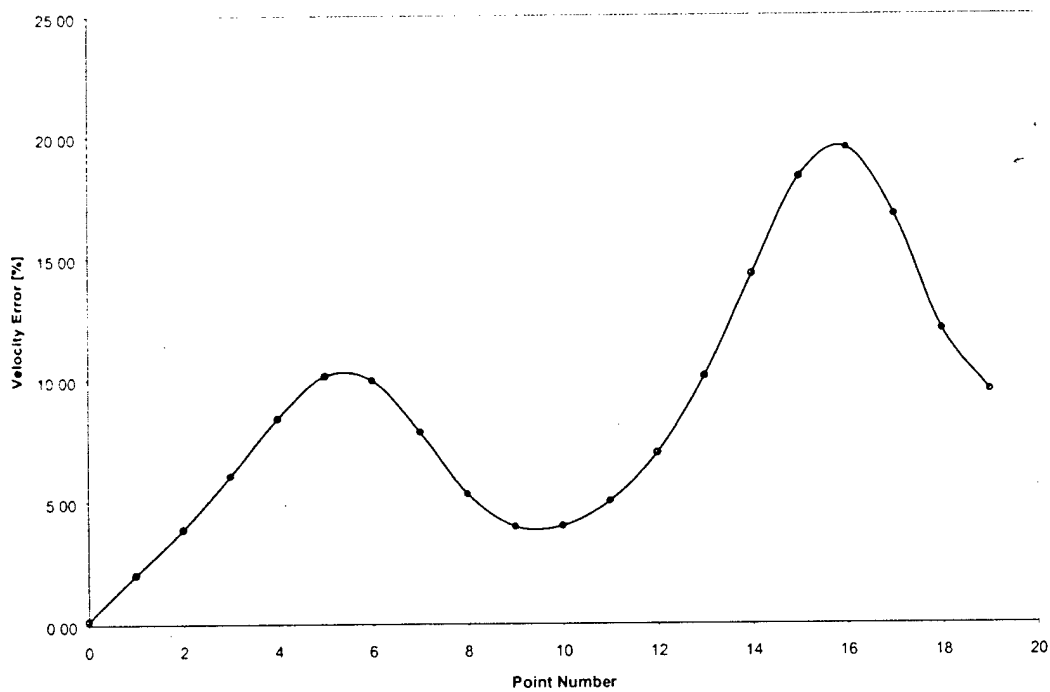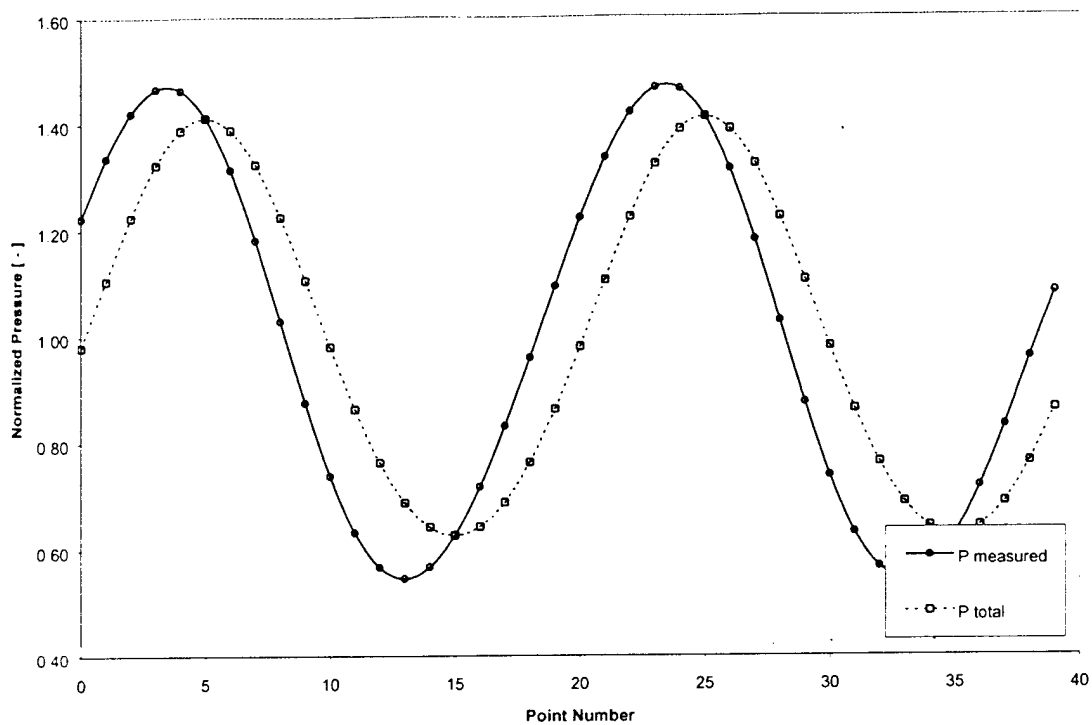**Fig. 8.41. Error in percent for the predictor-corrector with 10 points per period.**



**Fig. 8.42. Velocity error with 10 points per period.**

88

Fig. 8.43. Normalized sphere pressure and total pressure of the flow with 20 points per period.
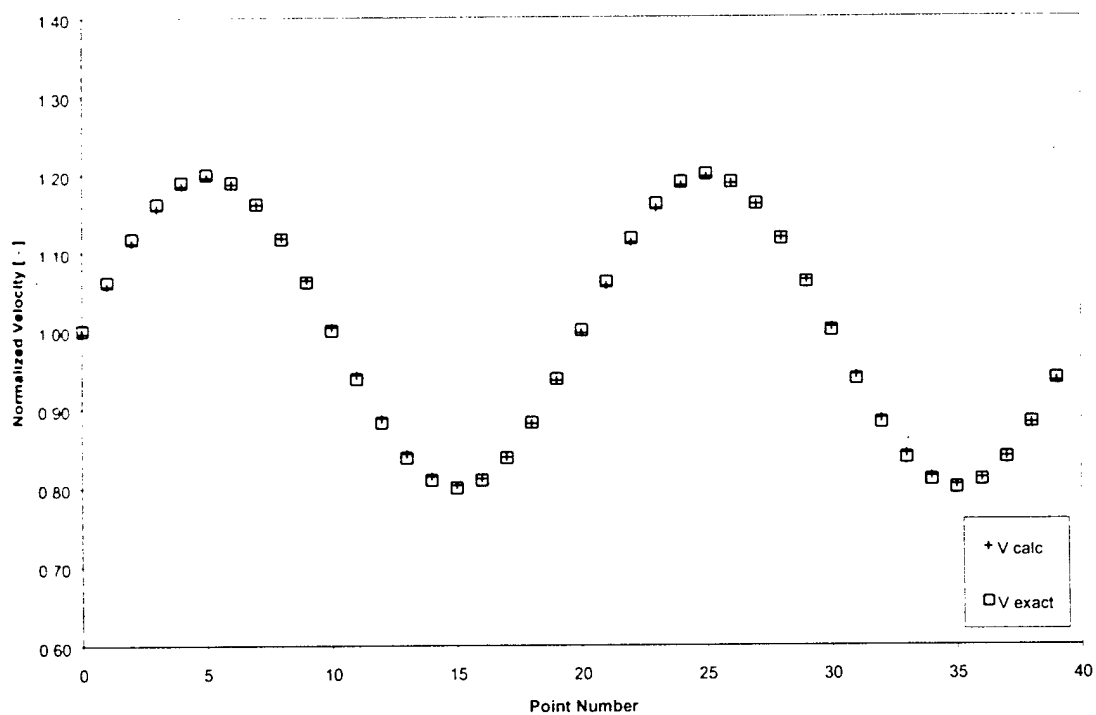


Fig. 8.44. Error in percent for the predictor-corrector scheme with 20 point per period.
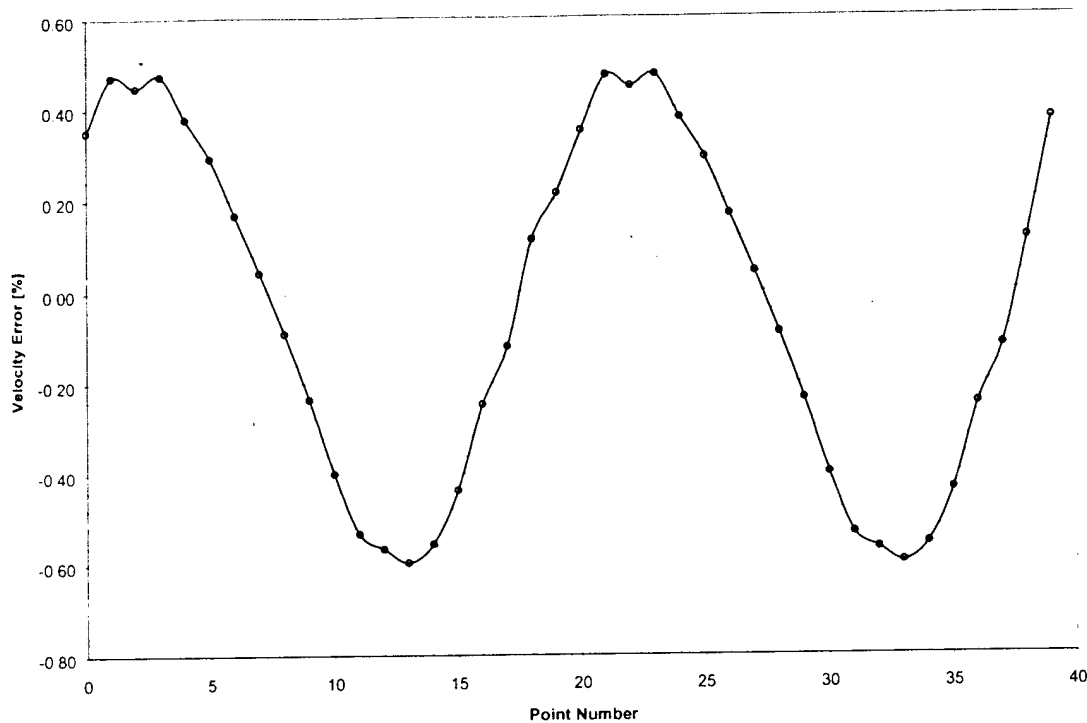
**Fig. 8.45. Velocity error with 20 points per period.**

Further doubling of the sampling rate shows that for 40 point per period there are small errors due to the predictor-corrector scheme (fig. 8.46). It is thus desired to a have a relatively high sampling rate for the predictor corrector method to work well. However, as most experimental data is low-pass filtered the accuracy of the method can, for low point densities, be increased by interpolation, thus virtually increasing the point density of the sampled data.

**Experimental Determination of Steady and Unsteady Cp**

Experimental determination of the steady and unsteady pressure coefficients is sought. During steady calibration, the total and static pressure as well as the port pressures are known; hence the steady Cp is easily calculated as:

$$Cp_{steady_i}(\alpha,\beta) = \frac{p_i(\alpha,\beta)}{\frac{1}{2}\rho U^2} \qquad (8.30)$$

for each of the ports, i, at each calibration point. It is only necessary to determine one coefficient pair for only one of the ports (e.g. port 1) to be able to determine the velocity magnitude from measured pressures. Plotting $Cp_{steady}$ vs. the pitch and yaw angle shows that these surfaces are well behaved and are well suited for sector wide polynomial curve fitting (fig. 8.47).
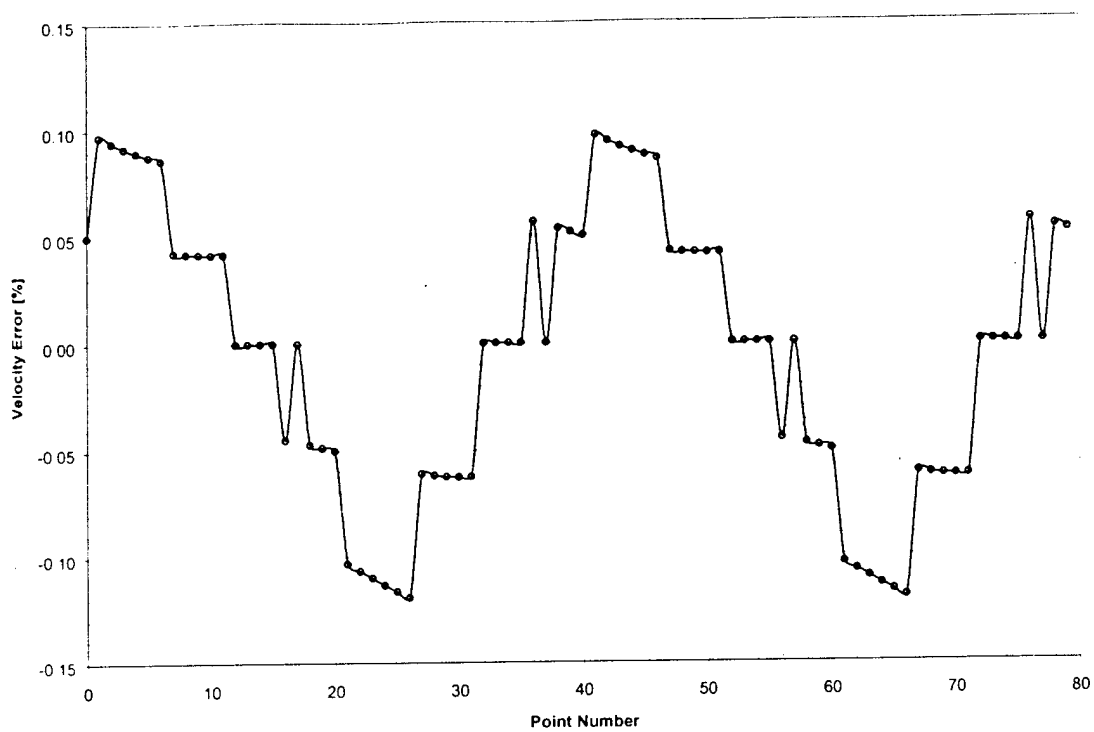
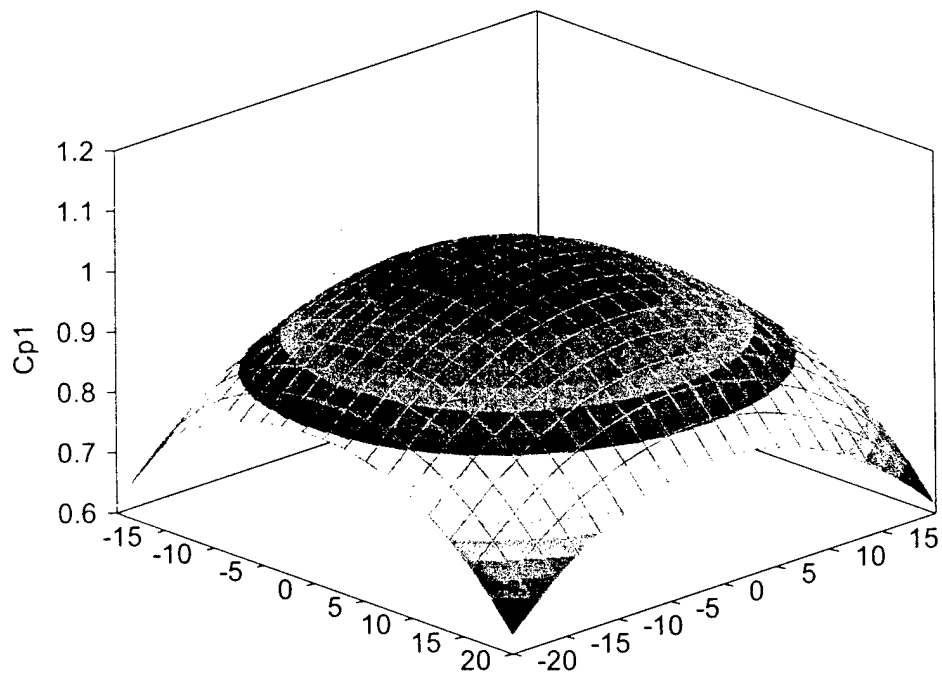**Fig. 8.46. Velocity error with 40 points per period.**



**Fig. 8.47. Steady pressure coefficient for the central port on a 5-hole probe in the low-angle regime (central port sees maximum pressure).**

91

From the curve fit of the data the following is known:

$$Cp_{steady}(\alpha,\beta) = poly(\alpha,\beta)$$

(8.31)

Similarly, for conventional calibration parameters increased accuracy can be achieved using localized surface fitting, LLS. Additionally, the steady Cp might be dependent on Reynolds number (as was found for the independent and dependent pressure coefficients). Reynolds number effects are usually most pronounced for probes where there is an obstruction immediately downstream of the probe tip, such as for L-shaped or C-shaped probes where the probe sting alters the flowfield impinging on the probe face. Similar to the method described in section 7, either a Reynolds number coefficient can be introduced or alternatively the probe can be calibrated at multiple Reynolds numbers and interpolation in between predictions can be performed.

Experimental determination of the unsteady pressure coefficient, $Cp_{unsteady}$, is more challenging than the steady pressure coefficient. The theoretical value is given from potential flow and follows $\cos(\theta)$ for axisymmetric flow over a sphere (fig. 8.48).
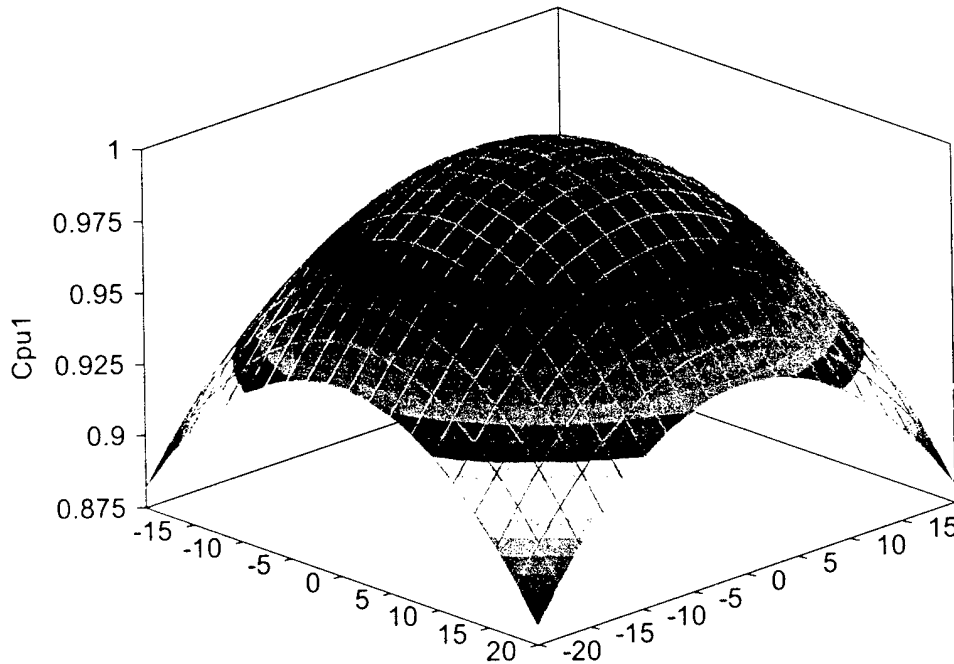


Fig. 8.48. Theoretical $Cp_{unsteady}$ for the central port on a sphere based probe.

The theoretical potential flow based model determines the $Cp_{unsteady}$ coefficient to equal one for zero incidence angle. A partially theoretical and experimental study undertaken by Kovasznay et al. found that this coefficient for a sphere should be 3 at the forward stagnation point. Kovasznay's theoretical results are based on the sum of three potentials; the velocity potential for the steady flow over the sphere, the velocity potential due to the superimposed

velocity disturbance (assumed small) and the velocity potential for the compensating flow (introduced to satisfy the boundary conditions).

For direct experimental determination of $Cp_{unsteady}$, the probe must be inserted into a flowfield with known angularity and velocity. In addition the flowfield must be fluctuating or have a controlled acceleration that yields a significant rate-of-change coefficient, K. The unsteady pressure coefficient for each port can be found from:

$$Cp_{unsteady_i}(\alpha,\beta) = \frac{p_i(\alpha,\beta) - \frac{1}{2}\rho U(t)^2 Cp_{steady_i}(\alpha,\beta)}{\frac{1}{2}\rho R \frac{dU(t)}{dt}}$$

(8.32)

or equivalently

$$Cp_{unsteady_i}(\alpha,\beta) = \frac{\dfrac{p_i}{\frac{1}{2}\rho U(t)^2} - Cp_{steady_i}(\alpha,\beta)}{K(t)}$$

(8.33)

Again, only the pressure coefficient for the central port is needed to resolve the velocity magnitude. The numerator in equation 8.33 will tend to zero for negligible inertial effects (as will the denominator for steady flow). If a periodically varying flowfield is used to calculate $Cp_{unsteady}$ special caution must be exerted to ensure that only data points where the gradient of the velocity is large is used. I.e. the peaks and valleys, where dU/dt is zero must be avoided (fig. 8.49).

Generally any data point along the time history, except where dU/dt is zero can be used to determine $Cp_{unsteady}$, however in the vicinity where dU/dt is small differences between the measured and the true pressure are also small. With given uncertainty and noise in the measurements, one should avoid these parts of the curves and rather use a conditional approach to only use values where both the numerator and denominator have significant values. Technically only one point is required to estimate the $Cp_{unsteady}$, but again due to experimental errors averaging the data for a number of test points is recommended. In fig. 8.49 a sinusoidal velocity signal is presented and the rate-of-change parameter, K, is calculated. Only data points where the magnitude of K is significant (inside the two rectangles) should be considered. The predicted $Cp_{unsteady}$ for each such point can be calculated and averaged. The procedure is repeated for all values of flow angles. In a later section the experimental determination of $Cp_{unsteady}$ is performed on data from water tunnel experiments.
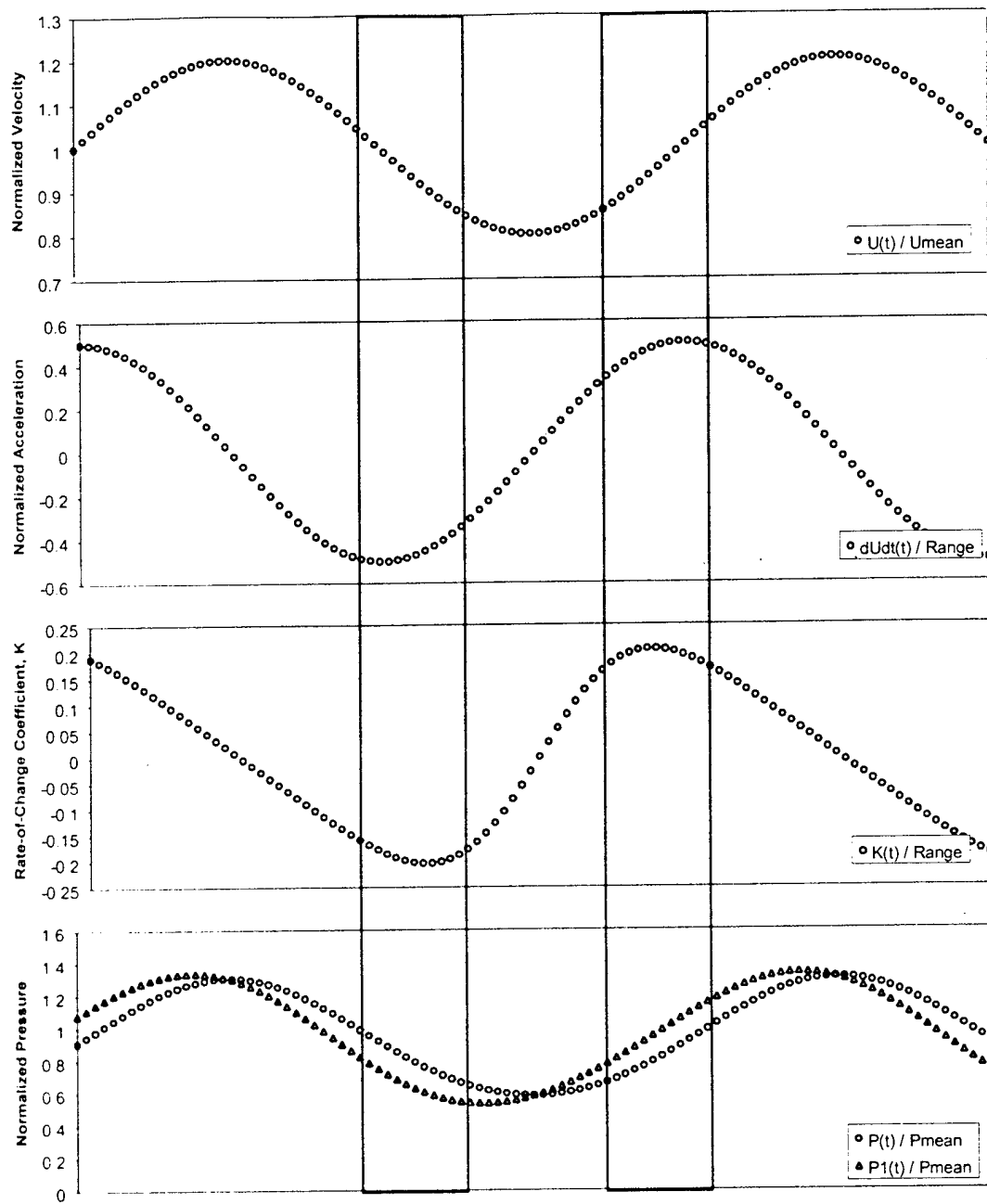
Fig. 8.49. Selection of data for determining the unsteady pressure coefficient.

94

# 9. DEVELOPMENT OF AN UNSTEADY FLOW FACILITY FOR THE CALIBRATION OF FAST-RESPONSE PRESSURE PROBES

## General

A facility has been developed to calibrate fast-response, multi-hole pressure probes in both steady and unsteady flowfields. The response of pressure probes in fluctuating flows is dramatically different than in steady flows. Unsteady effects such as inertial or apparent mass effects result in pressure measurements that cannot be used directly without correction to arrive at the true velocity and pressure of the flow. This effect is quantifiable and in this work we show that potential flow solutions can predict it, however similarly to steady probe calibration the probe should also be calibrated in an unsteady flow to accurately determine the unsteady effects. An accurate and repeatable fluctuating flow is required to experimentally determine the unsteady pressure coefficients, and a facility using a jet of air and a variable speed "flow-pulsator" has been developed. Repeatable fluctuating flows are generated and axial velocity fluctuation is recorded with a hot-wire anemometer. The hot-wire signal is used as the reference or true velocity and compared with the pressures recorded by a 5-hole probe. The central port of the probe at zero incidence angle shows a dramatic increase in the pressure lead and magnitude with increasing frequency, and become non-negligible at relatively low non-dimensional frequencies.

A theoretical and experimental investigation of the pressure distribution around a sphere in an unsteady flowfield was presented by Kovasznay et al. (1982). They found that the pressure on the surface of the sphere was composed of a term proportional to the mean velocity and a term proportional to the rate of change of velocity. Based on this method Matsunaga et al. (1980) developed a theoretical procedure for calibrating a five-hole probe in unsteady conditions. The theoretical part of their algorithm, which consisted of the calculation of the perturbation potential around a perfect hemispherical-tip, was not properly corrected to account for fabrication idiosyncrasies and imperfections of the specific probe. It is now well established that the pressure distribution over the probe tip is sensitive to construction defects. Correction of such effects can only be derived by coupling the theoretical calculations to measurements of the specific probe behavior. The unsteady effects must be either determined by experimental methods or if determined by theoretical or numerical methods, the response must be verified in a controlled unsteady flowfield. Kovasznay et al. developed a jet facility with a dual nozzle and a perforated spinning disk. For their experiments, the mean velocity was 20m/s, the oscillation amplitude was up to 6m/s peak-to-peak and the frequency up to 500 Hz. A large number of averages (1000-2000) was performed to reduce the random fluctuations in the jet and the resulting hot-wire velocity was sine-like.

Humm (1994) designed a cart that used a DC motor to create a sinusoidal motion of the probe holder either longitudinally or in pitch or yaw angle. This cart was towed in a water channel and an oscillation in the velocity was imposed on the mean towing velocity or oscillation of the pitch or yaw angle was generated. A scaled up (30mm) probe was used to match the Reynolds number and non-dimensional frequency range typically encountered in turbomachinery applications. For oscillations in pitch and yaw angle large dynamic effects were identified for wedge-shaped probes, while for cylindrical or half-cylinder shaped probes these effects were much less pronounced. For longitudinal oscillations large dynamic errors were identified for all

probe shapes and increased with both frequency and size of probe. Following Kovasznay, Humm postulated a method of correction of dynamic effects based on the acceleration of the fluid using an inertia coefficient.

As was found by Kovasznay, Matsunaga and others, the unsteady effects increase with probe size, thus miniaturization of the probe tip is desired to reduce the aforementioned dynamic effects. In some instances where frequencies are restricted to a few hundred Hz, pressure tubing can be utilized and transducers can be placed a few inches away from the tip. At lower frequencies the dynamic effects (inertial) from the external probe geometry can be neglected, however pressure transmission effects from the probe tip to the pressure transducer must be corrected (Iberall, 1950; Bergh and Tijdeman, 1965; Rediniotis and Pathak, 1999).

To aid in the development of the facility and subsequently in the development of unsteady probe calibration theory and algorithms, a high-frequency-response, 5-sensor probe was developed. It is designed to house 5 Kulite pressure transducers. The relatively large probe tip (6mm diameter) is large enough to have significant unsteady effects at moderate velocities (30-100m/s) and frequencies (<1000 Hz). The Kulite pressure transducers have a high frequency response (20 kHz) and a pressure range of ±5 psid. A drawing of the assembled probe is shown in figure 8.1. The miniature pressure sensors are located near the tip of the probe to minimize the channel length and thus the time lag induced by the volume from the probe surface to the sensor diaphragm, as well as move the Helmholtz resonance frequency well above the transducer frequency response. The pressure attenuation was calculated following Bergh and Tijdeman and the resonance frequency is estimated to be well above 30kHz.
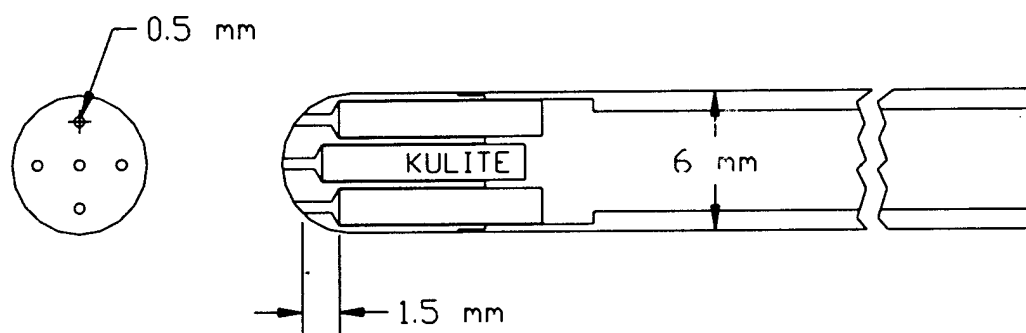


Figure 9.1. Cross-section of the assembled 5-sensor probe.

## Steady and Unsteady Probe Calibration Facility

Multi-hole probes must be calibrated in a steady jet in order to determine the steady pressure coefficients needed to reduce unknown data from a steady flowfield. It is also desired to have a jet that can generate a controlled repeatable fluctuating jet of air for the calibration of fast response probes in an unsteady fashion. A steady calibration jet was developed to provide a steady flow of air with low turbulence and flow angularity. A pulsator was designed to fit at the exit of this jet to, in effect, "pulsate" the steady flow of air from the jet. Figure 9.2 presents the

conceptual design of the calibration jet facility and air supply system, illustrating its main components and structure.

Due to availability reasons, the air supply source is not a design parameter and is fixed to 150 psi, with the capability of delivering a maximum continuous flow rate of 0.15 $m^3$/sec. These air supply specifications, in turn, dictated the choice of the air supply system components and specifications illustrated in figure 9.2. Before the calibration jet facility was dimensionally designed, it was necessary to develop a way to relate the magnitude of the unsteady probe calibration effects to the dimensional and operational parameters of the facility, such as speed, exit nozzle diameter, flow oscillation frequency and amplitude.

**Calibration Jet Facility Design**

The limitation on the available flowrates dictate the maximum size of the exit nozzle to achieve sufficient flow velocity, while the size of the probe sets the minimum size of the exit to avoid excessive flow blockage. The selected exit diameter is 38.1 mm, which give a velocity range of up to Mach 0.3 and a blockage of approximately 2.5% for the 6 mm Kulite probe. Through the use of carefully located screens, the turbulence intensity of this facility has been determined from hot wire measurements to be <0.3%. The settling chamber pressure is measured using a high accuracy pressure transducer and is controlled through a PC with a PID controller and a motorized valve, keeping the jet velocity within 0.2% of the set value. The jet stagnation temperature is continuously monitored and recorded. The flow angularity was determined by using a yaw probe in a "flip-over" method and corrected. A three axis computer controlled traversing system is used for hot-wire and probe positioning during flow mapping experiments.
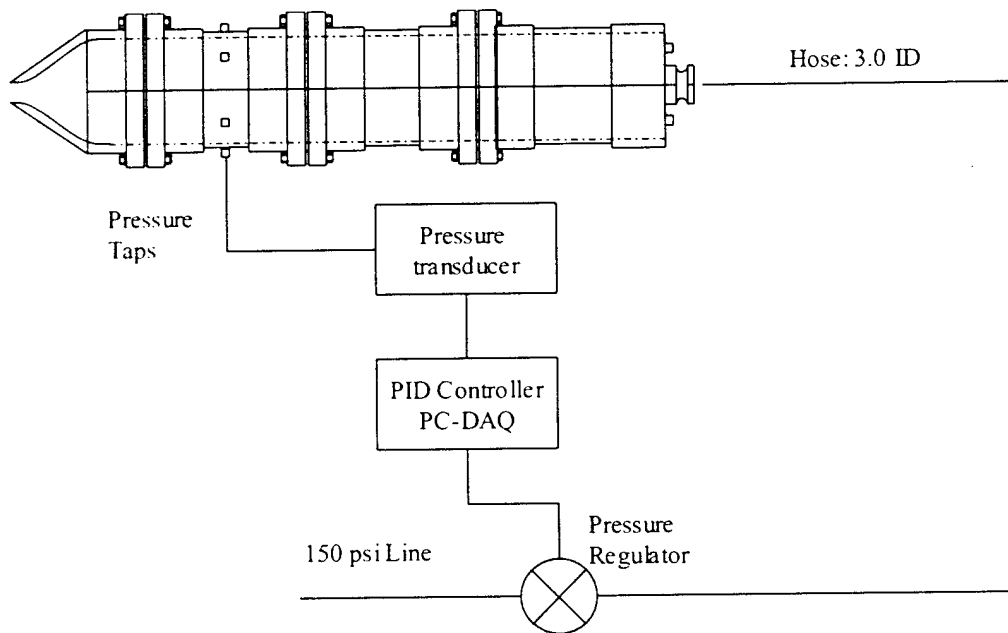


**Figure 9.2. Schematic of the calibration jet facility.**

Probe calibrations typically require the acquisition of data from a wide range of angle inclinations of the probe, and a complete probe calibration may take several hours to complete.

The maximum flow velocity is dictated by the air provided by the compressor system, and as mentioned above this airflow is limited. The required flow rate for an exit nozzle of 1.5" in diameter, is shown in figure 9.3. Keeping in mind that the maximum airflow that can be delivered from the compressor system is about 270 SCFM, the maximum sustainable Mach number is about 0.30. Decreasing the jet exit diameter to 1" by mounting an extension pipe to the nozzle increases the maximum sustainable Mach number to about 0.75 with the current compressor configuration.
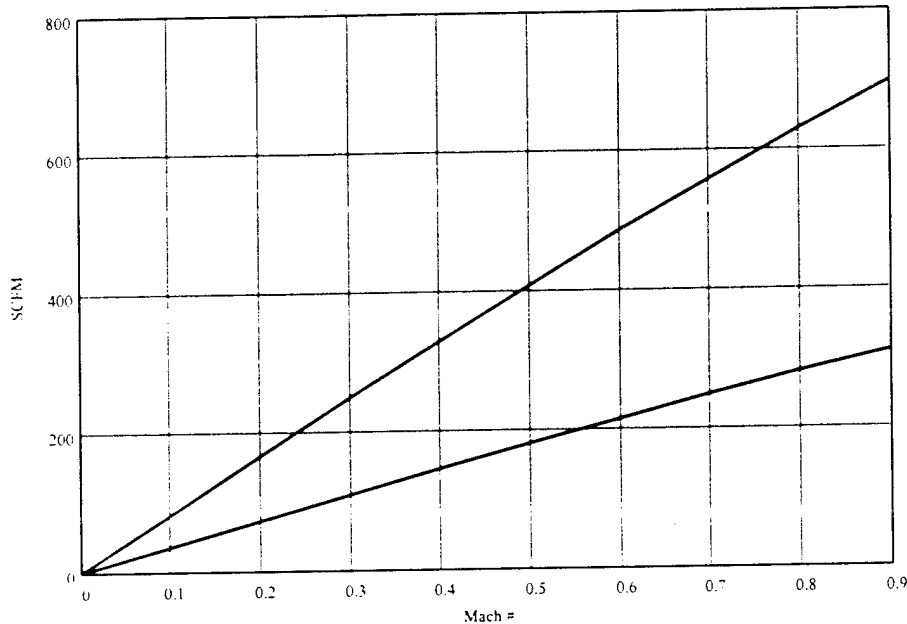


**Figure 9.3. The calibration jet air flow in SCFM vs. Mach number. The upper curve is for an exit nozzle 1.5" in diameter. The lower curve is an exit nozzle 1" in diameter.**

The facility turbulence intensity was measured using hotwire anemometry. The turbulence intensity is defined as:

$$T = \frac{u'}{U}$$

where T is the turbulence intensity, u' the rms value of the velocity fluctuations and U the mean velocity. The data was low-pass filtered with a cut-off frequency of 6.2 kHz. This cut-off frequency was decided upon after looking at the power spectrum of the unfiltered data and seeing that no significant fluctuations existed at frequencies higher than that. Table 1 gives the turbulence intensities for different mean velocities.

**Table 1. Turbulence intensity values.**

| Mean velocity, U [m/s] | Turbulence Intensity, T |
|---|---|
| 47 | 0.00346 |
| 80 | 0.00445 |
| 130 | 0.00376 |

The calibration jet facility is equipped with a fully automated probe positioning system (probe indexer) that can position the probe at a wide range of cone angles (0 to 150 deg.) and roll angles (0 to 360 deg.) with respect to the jet velocity. The indexing system is shown in figure 9.4.
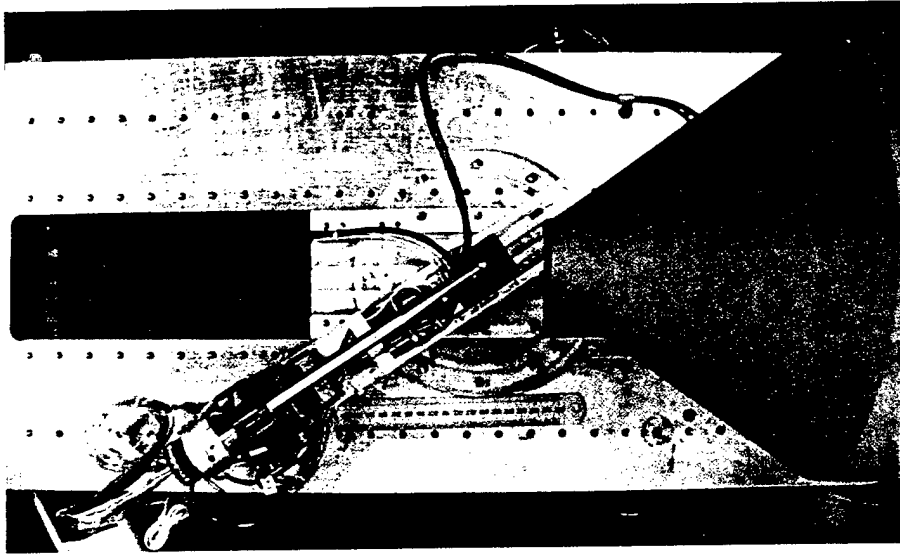


**Figure 9.4. Probe indexing mechanism at the jet exit.**

The flow angularity of the jet can be determined by using a 5-hole probe. The flow angularity was determined by yawing the probe through a set of angle increments (cone angles, as shown in fig. 9.5), the pressures from ports 1, 3 and 5 (refer to fig. 7.1.1 for port numbering) are recorded. Then the probe is rolled 180 degrees and the same procedure is repeated. By plotting a properly defined pressure coefficient vs. the yaw angle for both configurations (fig. 9.6), the flow angularity is the angle that corresponds to the intersection of the two curves. The pressure coefficient is defined as:

$$Cp = \frac{p_5 - p_3}{p_{ave}}$$

where $p_{ave}$ is the average pressure recorded by the three ports. The stepper motor controller enables very precise movement of the probe in small angle increments. The data in figure 9.6 indicates that the flow angularity is 0.065 degrees.

### Steady Calibration and Test of Kulite Probe

The Kulite probe was statically calibrated in the facility, at a mean velocity of 50m/s through a range in cone angle, $\theta$, from 0 through 64.8 degrees in 2.7 degree increments. The range in roll angle $\phi$, was a full 360 degrees in 5.4 degree increments. The resulting calibration database thus contains 1675 data points. A test of the quality of the calibration was performed by removing one data point at a time from the calibration file, treating that point as an unknown test

point and using the LLS algorithm to predict the angles with the remaining calibration data. The difference in the predicted angles and velocity and the recorded angles and velocity is a measure of the quality of the calibration. For the steady calibration of the Kulite-based fast-response probe the following error histograms were obtained (figures 9.7). The histograms show that for steady measurements the fast-response probe is predicting the angles and velocities with high accuracy.
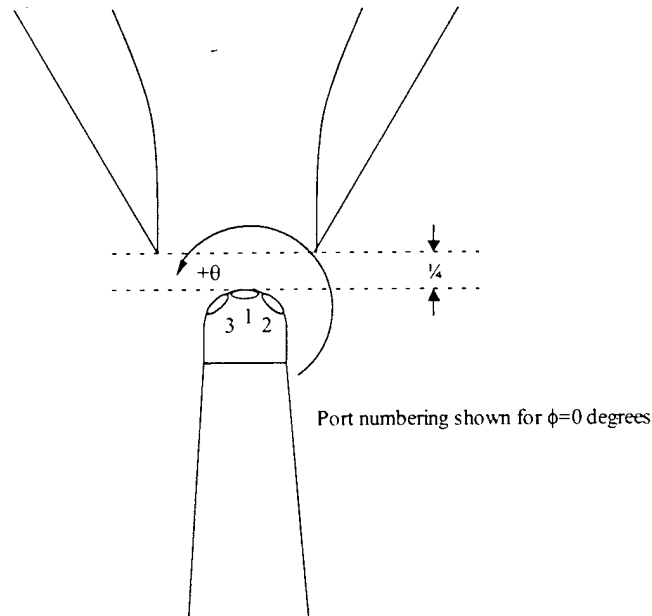


Port numbering shown for φ=0 degrees

**Figure 9.5. Experimental setup to determine flow angularity.**
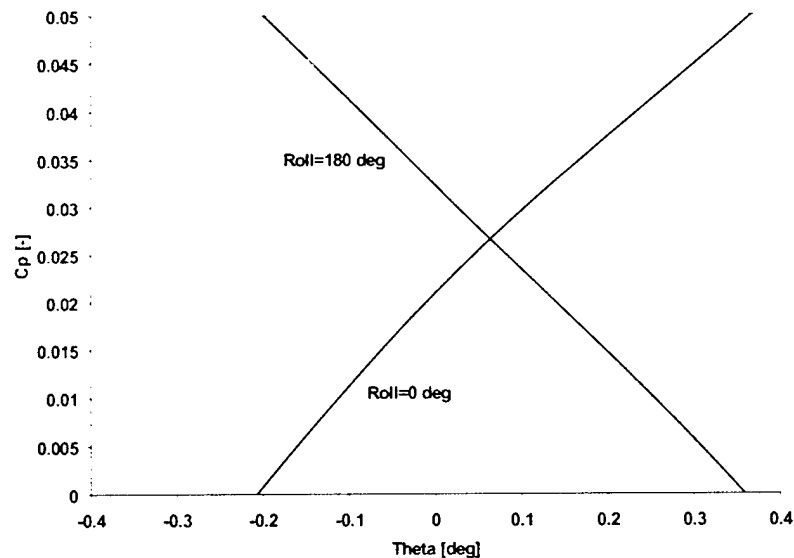


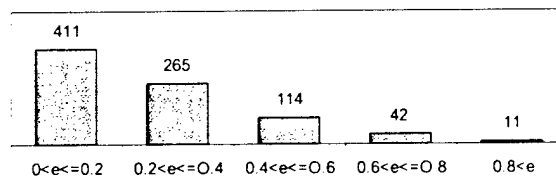**Figure 9.6. Cp vs. theta angle for 0 and 180 degree roll.**
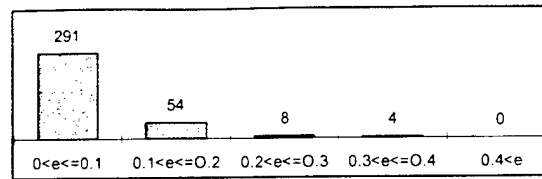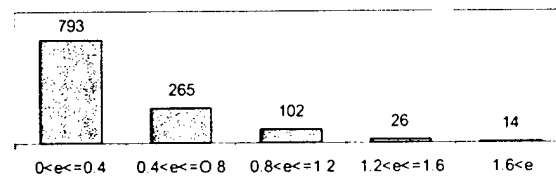
Pitch angle error in degrees.
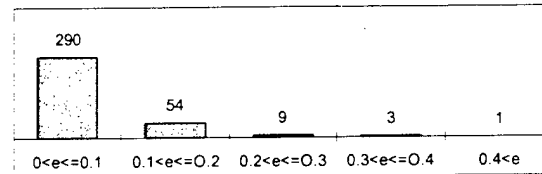

Yaw angle error in degrees.
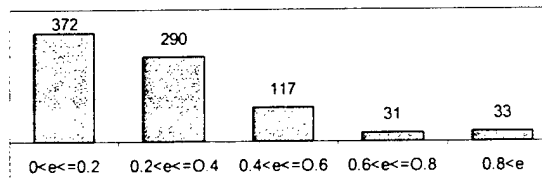

Cone angle error in degrees.


Roll angle error in degrees.


Velocity magnitude error in percent.

**Fig. 9.7. Calibration quality of the Kulite probe in the form of prediction error histograms.**

## Flow Oscillator Design

Unlike the design in Kovasznay et al., featuring a dual nozzle and indirect flow oscillations, a more direct approach was chosen. The idea behind the design is to periodically restrict the cross-sectional area of the flow path and thus also change the velocity proportionally. The high frequencies (up to 1 kHz) restricted the design parameters. It was desired to have a pulsating jet that is as uniform as possible across the entire jet exit. The current design has been proven to perform very well. In figure 9.8 the three drawings show how a rotor and a stator with

three "teeth" that protrude into the flow (normal to paper plane) are combined to generate a periodic restriction of the flow. From left to right, figure 9.8 shows the most open position, followed by clockwise rotation of the rotor and a slight closing of the open area. The last figure shows the flow oscillator in its fully closed position. Due to the design, the area change is not sinusoidal, but rather saw-tooth-like. This shows up in the spectral analysis of the hot-wire trace, where higher order harmonics appear. The rotor is driven by a dc electric motor, and the rotational speed can be varied very accurately from 0 to approximately 600 Hz or from about 0 to 1800 Hz flow pulsation. An optical encoder is used as a phase reference.

The innermost open area of the restriction is 25.4 mm in diameter, while the outer diameter is the same as the jet exit nozzle 38.1 mm. The total change in area is thus 38%. In figure 9.9 the driving gear is mounted to the rotor and the driven gear is mounted to the housing/nozzle with a 65mm id ball bearing. The 5-hole fast response probe is mounted on the xyz traverse system. A picture of the entire facility is also shown.

## Experimental Results and Discussion

A hot-wire system is used to measure the axial velocity fluctuations. The measurement plane is set 25 mm downstream of the throat, where a clean signal is observed. In figures 9.10 and 9.11 non-dimensionalized velocity fluctuations are seen vs. non-dimensional time. The data shown was ensemble-averaged over eight periods, mostly to rid the data of electrical noise. In figure 9.10, at 400 Hz the velocity fluctuations are seen to be quite uniform with large amplitude for the entire range of velocities, apart from a secondary peak emerging at increasing velocities. In figure 9.11, at 1000 Hz, the magnitude of oscillation is low for M=0.1, but increasing with increasing velocity. The same trends are also seen at other frequencies, indicating that magnitude of oscillation is proportional to velocity magnitude and inversely proportional to oscillation frequency.
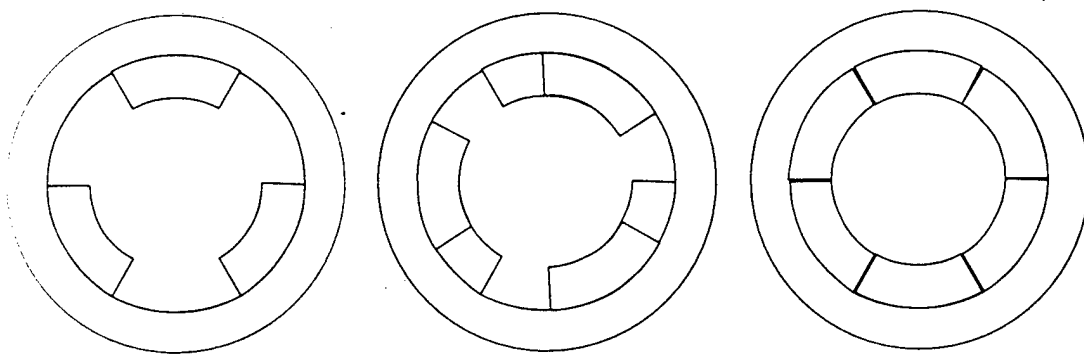


Figure 9.8. The flow oscillator, showing from left to right fully open, closing to fully closed.
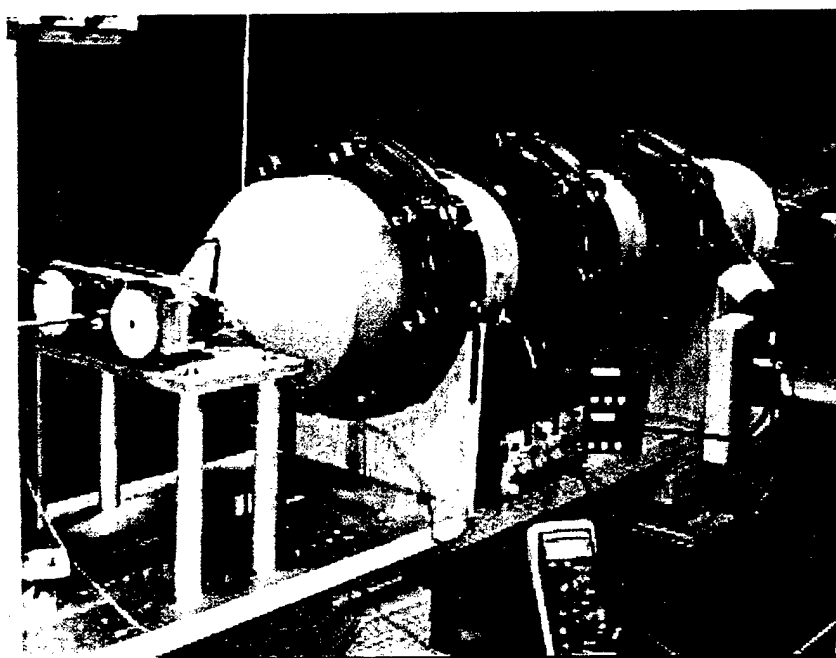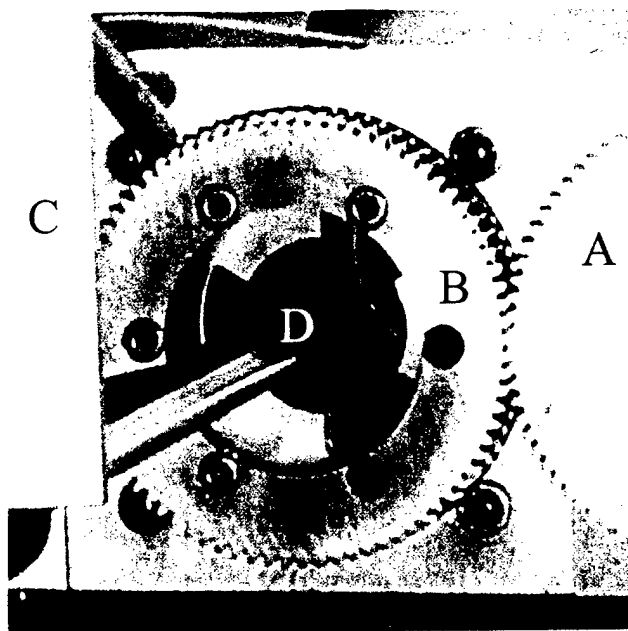
Figure 9.9. (upper) Flow pulsator in it most open position. A: Driving gear, B: Driven gear, C: xyz traverse, D: 5-hole probe. (lower) Picture of the entire facility.
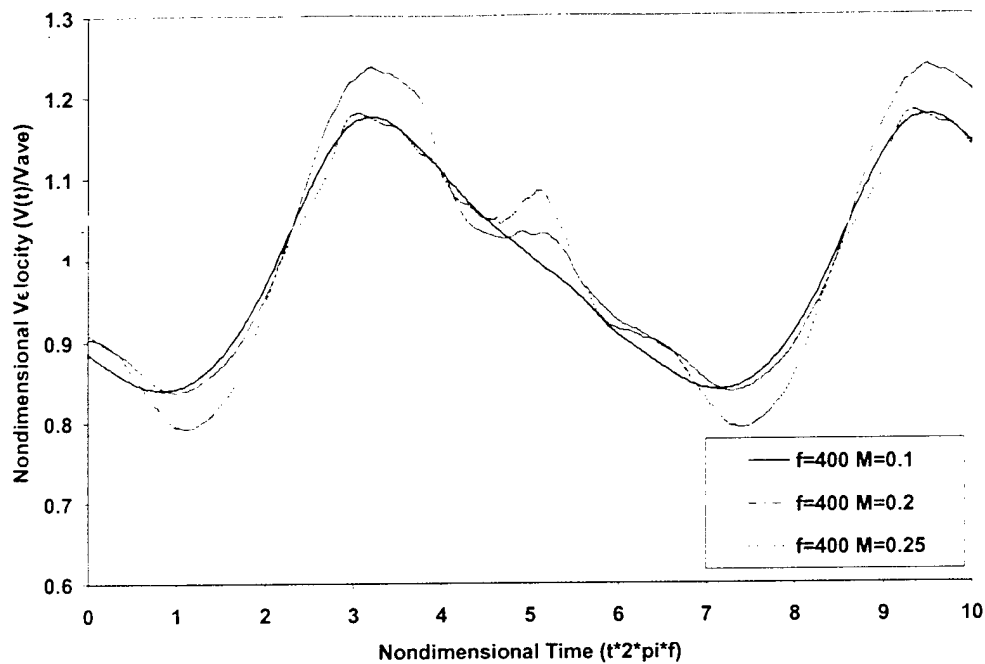
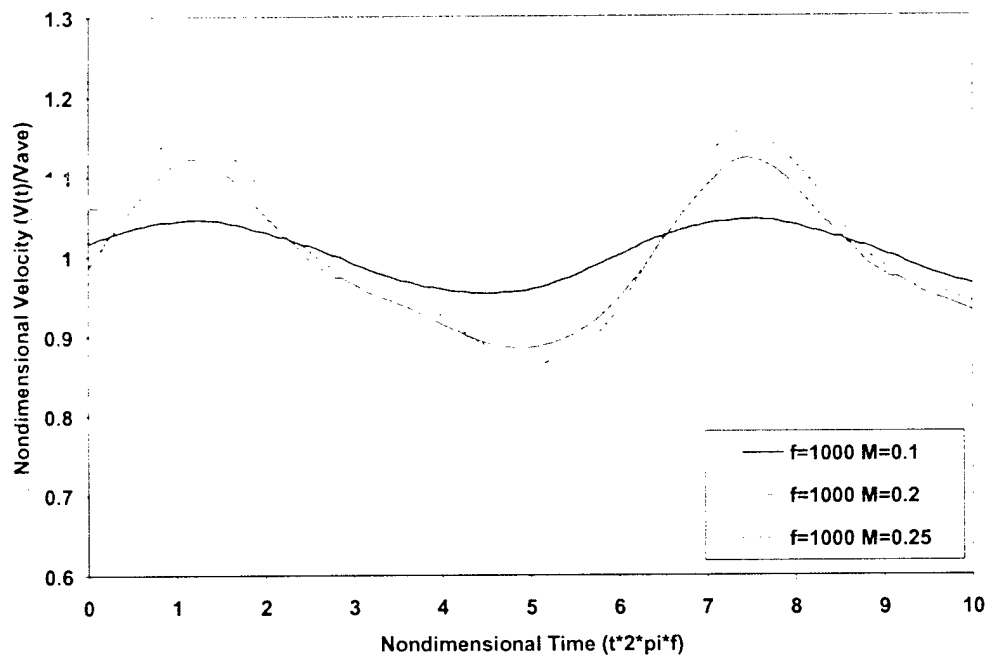**Figure 9.10. Non-dimensional velocity fluctuations for f=400Hz, Mach 0.1-0.25.**



**Figure 9.11. Non-dimensional velocity fluctuations for f=1000Hz, Mach 0.1-0.25.**

For lower frequencies and higher velocities the magnitude of the velocity fluctuation approaches the theoretical maximum value of 38% dictated by the change in area at the throat. A

decrease in the oscillation magnitude is seen at higher frequencies and lower velocities, while the signal still remains sine-like. For all such measurements the optical phase reference is recorded and enables this reference velocity signal to be superimposed onto data from e.g. the 5-hole probe. Data is acquired using a simultaneous sampling and hold system with sampling frequencies up to 100kHz for all channels. The data is ensemble-averaged. The ensemble averaging is used with the pressure data to get rid of mostly electrical noise, which is non-negligible in the low velocity range where the dynamic pressure fluctuations are small. Whereas the hot-wire measures the velocity, the 5-hole probe records the pressures which is composed of the stagnation pressure and the acoustic pressure signal. The probe is mounted downstream of the nozzle exit such that the mean static pressure equals the ambient pressure. The pressures measured by the probe ports is thus described by the unsteady Bernoulli equation:

$$H(t) = 1/2 \rho v(t)^2 + p(t) + \rho \frac{\partial \phi}{\partial t} \tag{9.1}$$

where $H(t)$ is the instantaneous port pressure measured by the probe, $v(t)$ and $p(t)$ the instantaneous velocity and static pressure respectively and $\phi$ is the velocity potential which describes the inertial contribution to be determined. Thus for measurements to be useful, it is necessary to accurately determine the velocity $v(t)$, which is performed using the hot-wire anemometer, and the static pressure $p(t)$, which is the sum of the mean ambient pressure and the acoustic pressure, which is measured with a microphone or a surface flush mount pressure transducer at the exit of the jet. From Kovasznay et al. the pressure measured by the probe can be described by:

$$H(t) = p(t) + c_p \frac{\rho v(t)^2}{2} + c_{inertial} \frac{dv(t)}{dt} \tag{9.2}$$

where $c_p$ is the steady pressure coefficient for the probe, as determined by steady probe calibration. $c_{inertial}$ is the "unsteady" or inertial pressure coefficient. Both of these pressure coefficients are unique to each pressure port and are functions of the relative incidence angle of the oncoming unsteady flowfield. Kovasznay et al. determined these coefficients for a sphere in an unsteady flowfield to be functions of the angular position on the surface from the incidence point. The maximum value of the inertial coefficient was found at the forward stagnation point and agreed well with potential flow theory, but their experimental results deviated from the potential flow predictions at higher angles. This stresses the need for an experimental determination of these coefficients. In an experimental investigation the steady pressure term is determined from probe calibration in a steady flow by pitching and rolling the probe through a range of incidence angles and recording the port pressures at each position. Similarly the inertial pressure coefficient can be determined by probe calibration in the pulsating flowfield. Knowing the exact velocity, $v(t)$, the measured port pressure, $H(t)$, and the pressure coefficient $c_p$ at the particular incidence, the inertial coefficient can be determined. Thus the probe is calibrated both in steady and unsteady fashion and can be used to measure temporal three-dimensional velocity flowfields. As it was found by Kovasznay et al. these coefficients are believed to be only weakly dependent on Reynolds number and nearly independent of the fluctuating frequency. Thus a constant frequency calibration covers the calibration for the probe over a wide range of velocity and frequencies.
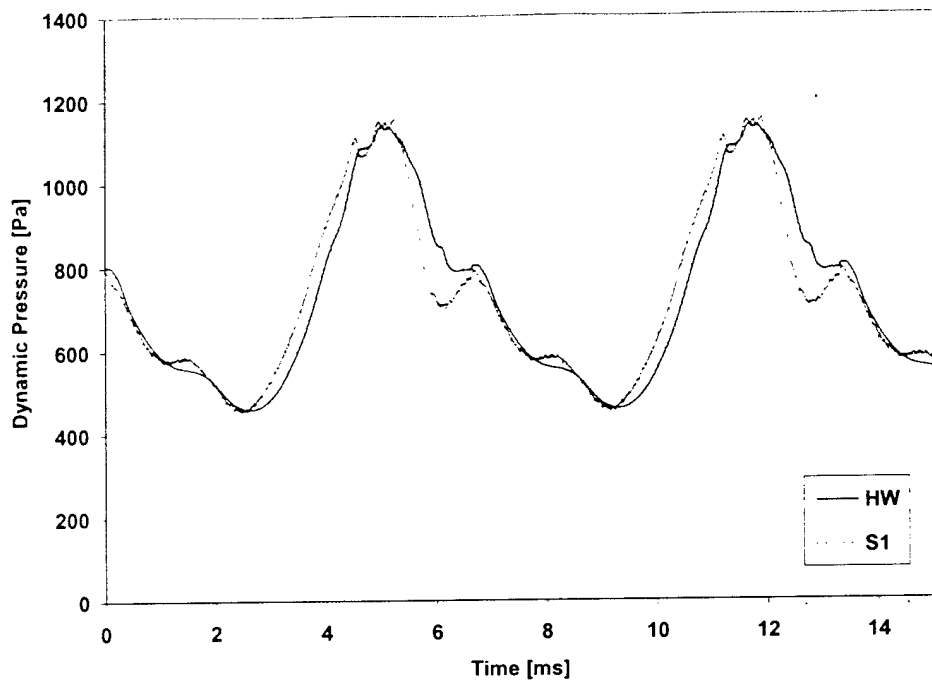
Figure 9.12. Hot-wire velocity converted to dynamic pressure and central port of 5-hole probe, at zero incidence angle, for f=150Hz.



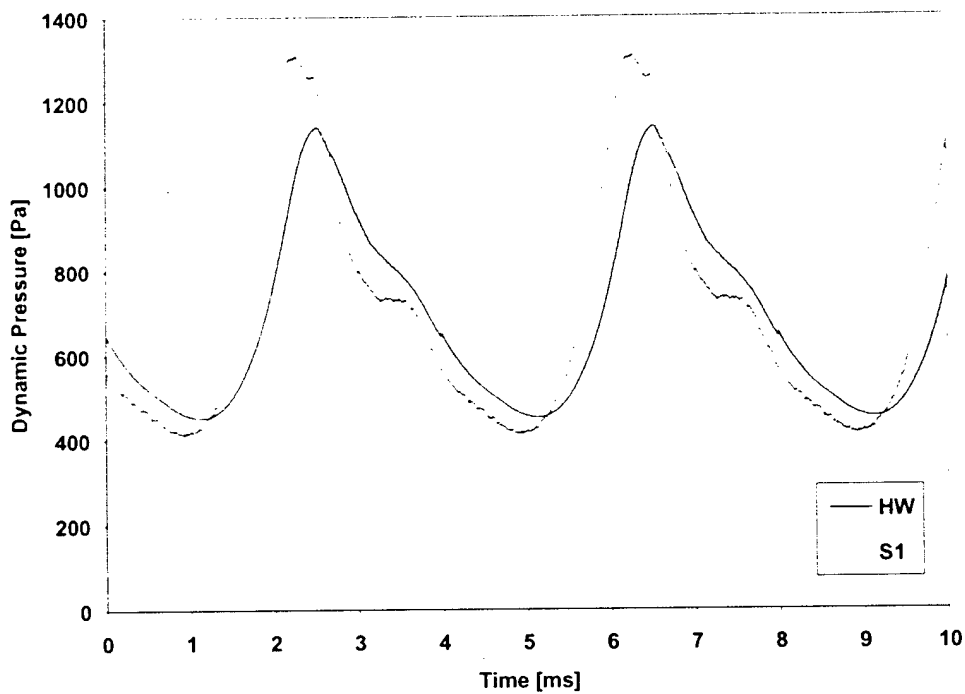Figure 9.13. Hot-wire velocity converted to dynamic pressure and central port of 5-hole probe, at zero incidence angle, for f=250Hz.
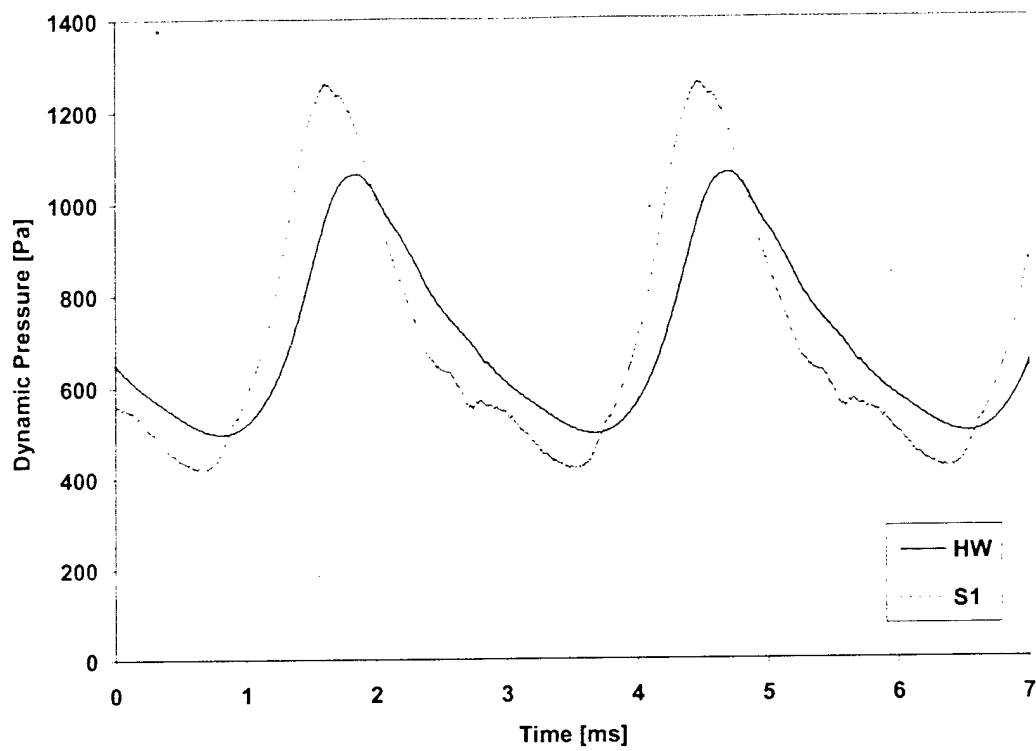
**Figure 9.14. Hot-wire velocity converted to pressure and central port of 5-hole probe, at zero incidence angle, for f=350Hz.**

In figures 9.12 to 9.14 the time trace (eight-period ensemble averaged) of the hot-wire velocity (converted to dynamic pressure) and the pressure at the central port of the 5-hole probe for Mach=0.1 and frequencies 150, 250 and 350 Hz, are shown. The data is recorded at zero incidence angle, such that the central port sees the forward stagnation point (where the inertial effects are the most pronounced). As can be seen from the figures, the phase lead and the magnitude of the central port pressure increases with increasing frequency (hence also increasing $dv/dt$). The same trends are also seen at higher Mach number and frequencies, thus verifying the need to correct the pressures even at relatively low non-dimensional frequencies, k.

107

# 10. WATER TUNNEL EXPERIMENTS

## *General*

In section 8 the determination of the steady and unsteady pressure coefficients was covered and it was found that the factor that determines the unsteady effects is the non-dimensional rate-of-change parameter, K. It was also found that the unsteady or inertial effects increase with increasing magnitude of K. In all experimental work there are always experimental errors, sensitivity problems and background (electrical) noise that become predominant for all instruments when very small physical quantities are measured. For these reasons it is desired to have a magnitude of K as large as possible to ensure significant and distinguishable inertial effects. From the definition of K as given in eqn. 8.7, this can be obtained in three different ways: large probe size, high frequency or low velocity. For air tests very low velocity will result in poorly read pressure signals due to the sensitivity of the pressure transducer (most miniature or micro pressure transducers have ranges on the order of psi). High frequency and moderate velocities are thus the answer for air tests.

As it will be discussed in a later section, obtaining a repeatable, periodic, well-behaved, unsteady air stream is difficult and hence alternative methods for verification of the methods was sought. In water the much higher density provides significant dynamic pressures at low velocities. Also, using a large probe the frequency of the oscillation can be kept very low while still matching the Reynolds number range and K values that would be seen for a real miniature·micro multi-hole probe in air. A spherical probe with a diameter of 50.8mm was designed and tested in a water tunnel to determine the unsteady effects and validate the inertial correction routine proposed in section 8. A spherical probe was chosen to verify the theoretical results as best as possible. Further, as shown in section 8, it is expected that such a spherical probe will behave similarly to a hemispherical multi-hole probe for moderate angle inclinations.

## *Experimental Setup*

A system consisting of a·crankshaft and a pushrod was devised to oscillate the probe in a near-sinusoidal manner. By oscillating the probe in a steady stream of water the flow velocity relative to the profile is the mean velocity of the water tunnel plus the velocity of the probe itself due to its oscillatory motion. Fig. 10.1 shows the conceptual design of the system. The crankshaft is mounted on a dc-motor and a flywheel, connecting the pushrod to the linear motion system. The probe assembly is sliding on a linear bearing that allows for linear translation only. Fig. 10.2 shows a picture of the system.
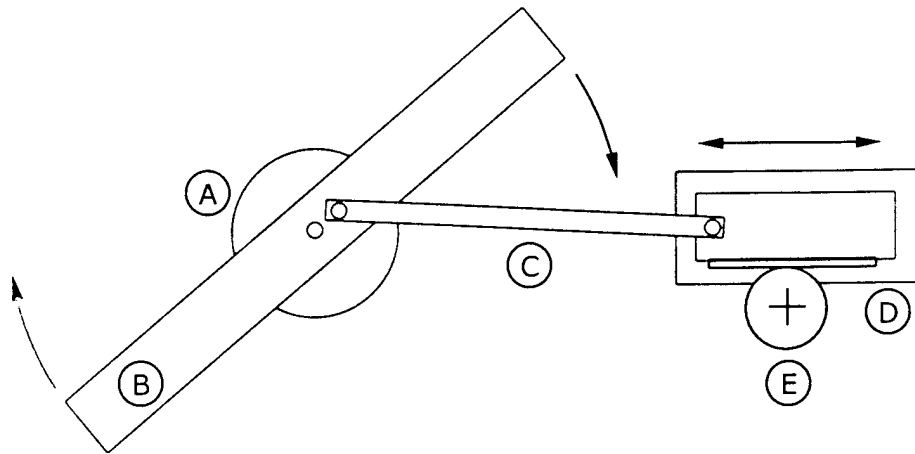
Fig. 10.1. Schematic of the crankshaft linear motion system. A: dc-motor; B: flywheel; C: pushrod; D: linear bearing; E: potentiometer.



Fig. 10.2. Linear motion system.

The position of the probe mount is measured using a potentiometer with a gear connected to a gear rack on the linear bearing. The potentiometer is connected to a 10V voltage supply and the output is a voltage linearly proportional to the position of the sliding assembly. The probe velocity is calculated as the time derivative of the position given by the potentiometer. The linear motion of the sliding assembly is not exactly sinusoidal versus time for a constant rotation speed due to the finite length of the crankshaft (25.4mm) and the pushrod (304.8mm).
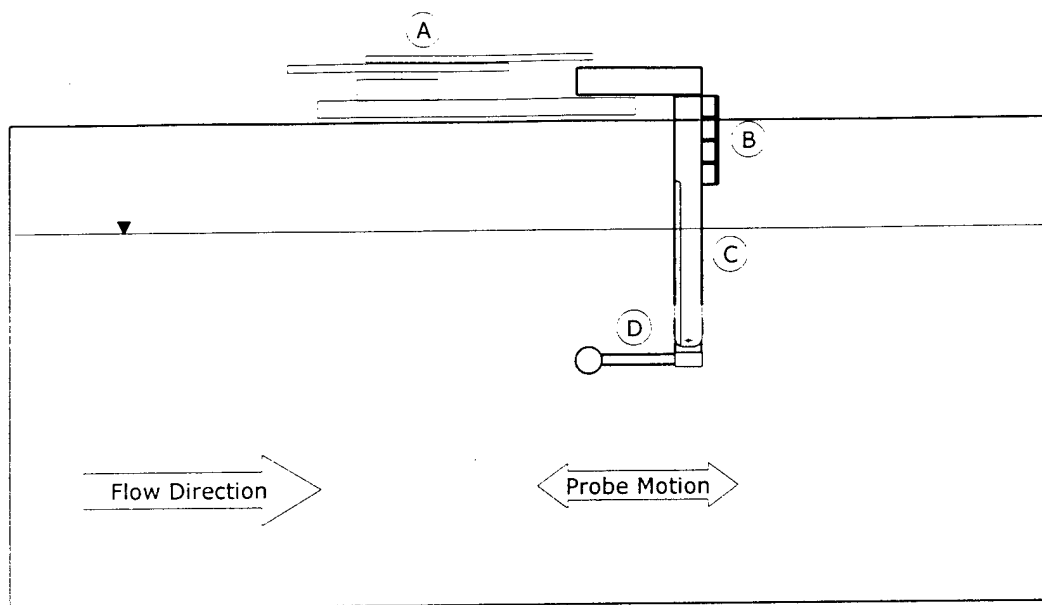
**Fig. 10.3. Schematic of the water tunnel setup. A: linear motion system; B: vibration dampers; C: vertical probe mount; D: probe shaft.**

Fig. 10.3 shows the schematic of the probe assembly mounted in the water tunnel. The vertical probe mount is connected to the linear motion system with eight rubber vibration dampers. It was found that without these dampers high frequency (about 250 Hz) structural vibration was transmitted from the linear ball bearing to the probe shaft and a significant 250Hz signal was observed in the measured probe pressure. The vibration dampers cause some loss of rigidity in the vertical mount, however the displacement of the end of the bar was measured for a range of loads (simulating the loads from the acceleration). Negligible deflection was observed for the range of forces corresponding to the range of frequencies of testing. The probe shaft is mounted to the vertical mount and can be manually set to any angle from 0 to 90 degrees downward using a digital inclinometer with a 0.1 degree resolution (Fig. 10.4).

A 50.8 mm diameter spherical probe (fig. 10.5) with a pressure port located at the forward center point was machined from aluminum. The probe head has a threaded mounting port for the pressure transducer and also threaded mounting for the probe shaft. A modified Endevco 8510B-1 transducer was used in the spherical probe assembly. This transducer in its original design is a fast-response 1 psig transducer with very high sensitivity (200 mV/psi). The transducer uses a four-arm piezoresistive bridge mounted on a sculptured silicon diaphragm and features an internal temperature compensation module. The original sensor was modified by Endevco to allow for use in water. The protective screen in front of the diaphragm was removed and replaced with a non-conducting gel (Endevco, proprietary), thus ensuring that the diaphragm is not directly exposed to water. Fig. 10.6 shows pictures of the spherical probe and the transducer.
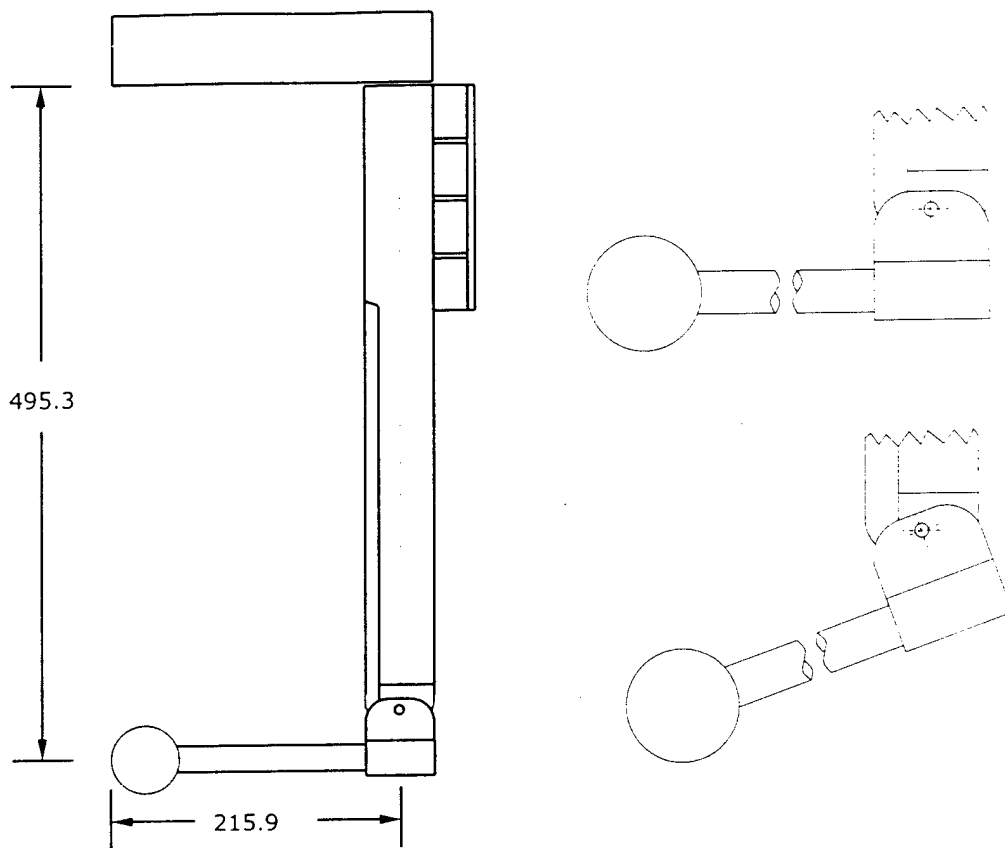
**Fig. 10.4. The complete probe assembly showing four of the eight vibration dampers that connects the vertical bar to the linear motion system. Probe also shown at zero and 20 degrees pitch angle (dimensions in mm).**
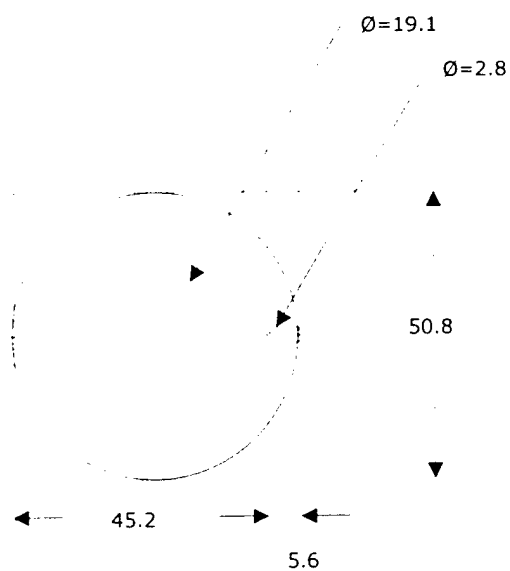


Ø=19.1

Ø=2.8

50.8

45.2

5.6

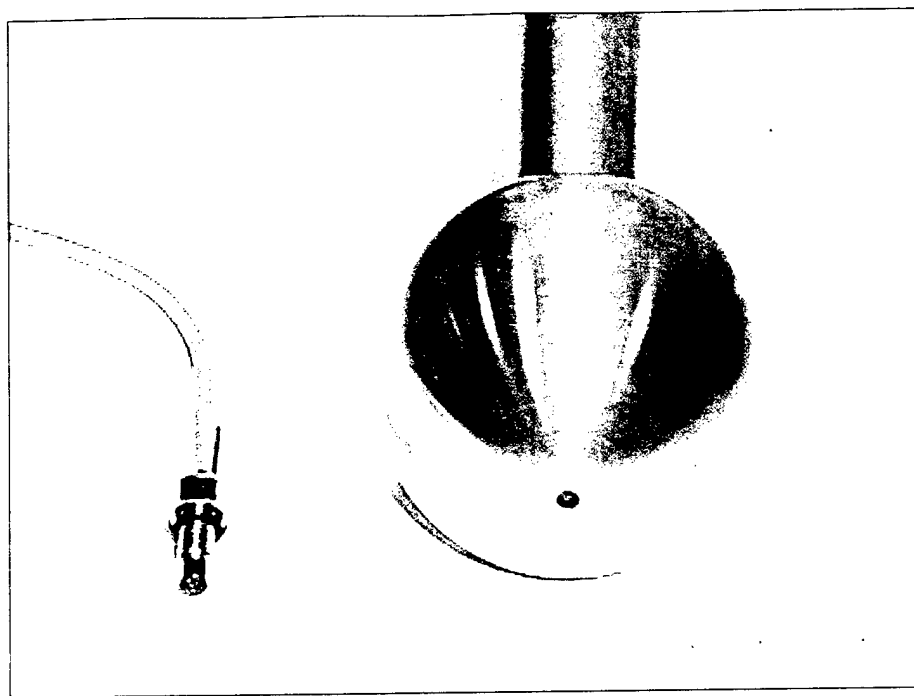**Fig. 10.5. Schematic of the spherical probe (dimensions in mm).**

**Fig. 10.6. The modified Endevco pressure transducer and the spherical probe head.**

The modified Endevco transducer is not in production quality and thus it was expected that frequent calibration for zero drift and non-linearity compensation would be necessary. It was, however, observed that the transducer behaved remarkably well and kept a nearly constant calibration slope for both air and water. Significant drift in the zero-offset was observed for about 45 minutes in water, however after this "warm-up-time" no additional zero-offset compensation was necessary. Air calibration of the transducer was performed by placing the probe in a pressure chamber and using a Barocel pressure transducer as the reference. Figure 10.7 shown the probe and the pressure chamber. The sensor output was amplified using an Entran IMV-15 amplifier with gain of 100+/-10%. From the design values the slope should be around 20V psi or 2.9mV/Pa = 345Pa/V+/-10%.

The air calibration of the transducer is shown in figure 10.8 and exhibits very good linearity and small zero drift; however since the transducer is used in water it was also desired to calibrate the sensor in water. A computer controlled traverse was used to submerge the probe into the water tunnel. For the first point the probe is placed such that it touches the water surface, then it is submerged in 1" increments. For each position the voltage was recorded and correlated to the pressure (given directly in inches of water). Thus, the air calibration was also validated in water.
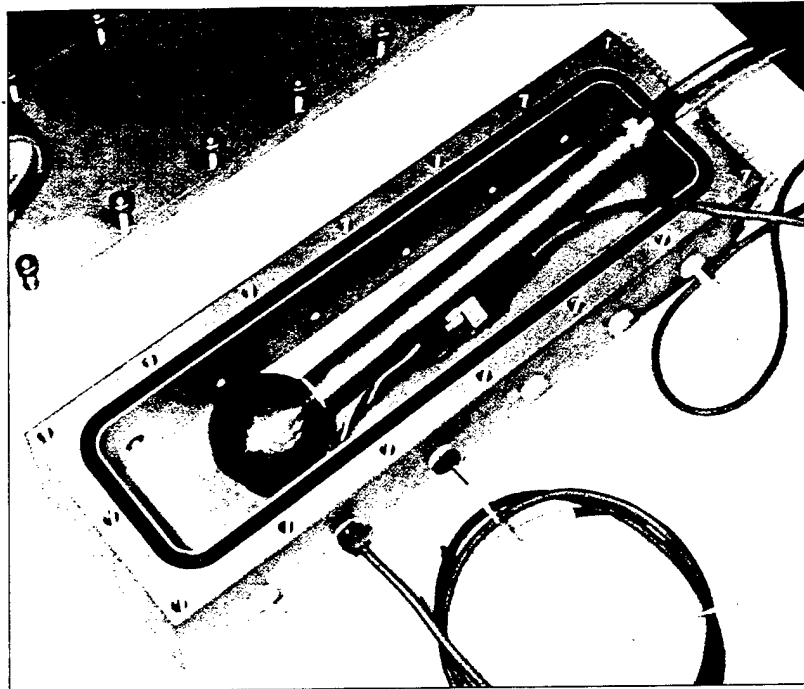
**Fig. 10.7. Calibration of the probe in pressure chamber.**



First set, quadratic fit:
$y = -0.40161x^2 + 388.40303x + 52.24877$
$R^2 = 1.00000$

First set, linear fit
$y = 384.89693x + 56.76890$
$R^2 = 0.99999$

Second set, quadratic fit:
$y = -0.5463x^2 + 390.94x + 50.114$
$R^2 = 0.9999$

Second set, linear fit.
$y = 386.37x + 54.936$
$R^2 = 0.9999$

○ Set 1
△ Set 2
—— Poly. (Set 1)
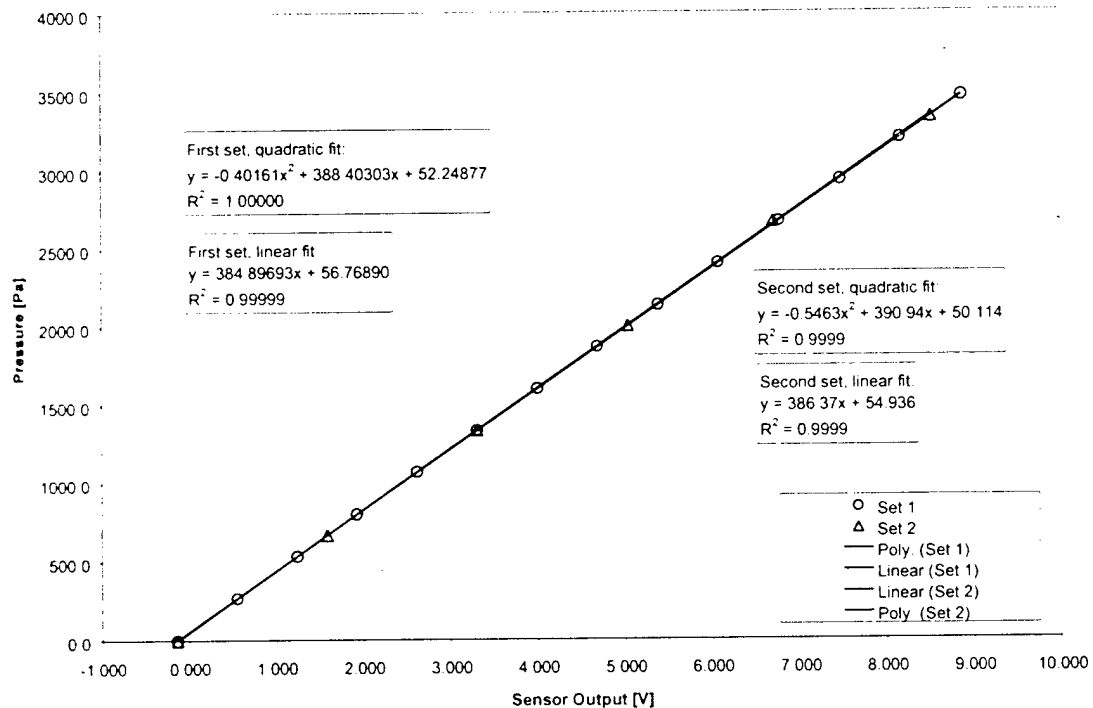—— Linear (Set 1)
—— Linear (Set 2)
—— Poly. (Set 2)

**Fig. 10.8. Calibration of the modified Endevco transducer in air, howing very good linearity and negligible zero drift for two data sets taken 1 hour apart with 20 minutes warm up time before first set.**

113

The acceleration of the probe and transducer due to the oscillatory motion causes a false periodic signal to be imposed on the measured pressure. The standard version of the transducer has an acceleration response equivalent to 0.0002 psi/g ≈ 1.4 Pa/g, however since the modified version has the gel directly on the diaphragm a set of tests were performed to quantify the magnitude of the acceleration effects. The probe was mounted on the linear motion system and data was recorded for oscillation frequencies from 1 to 6 Hz.
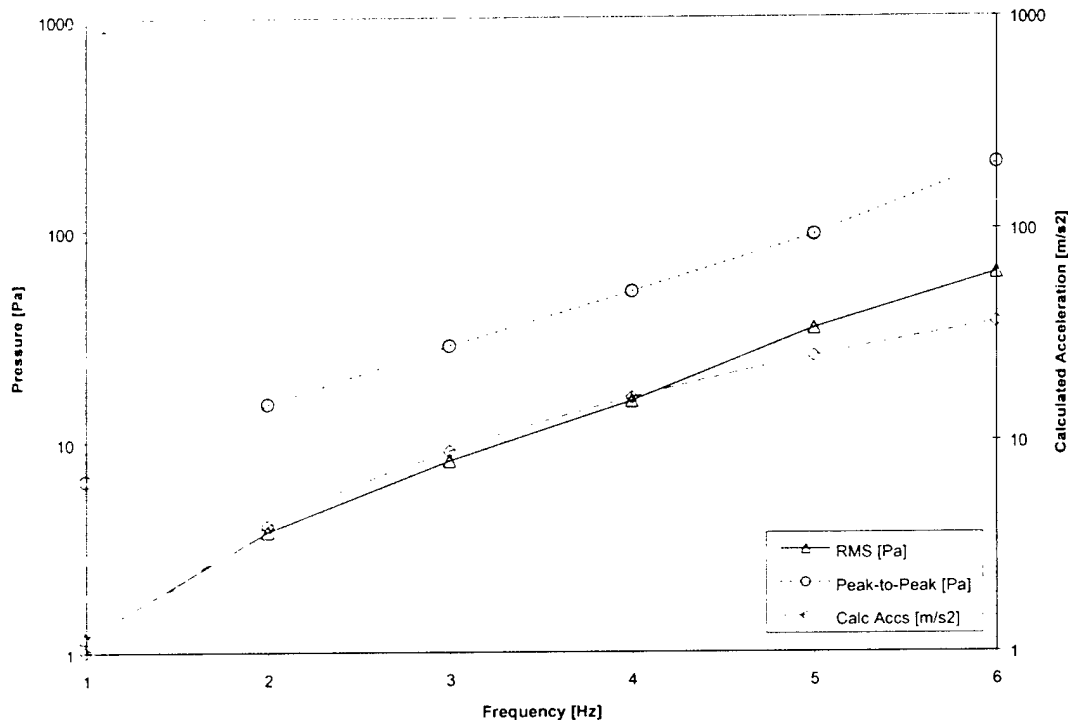


**Fig. 10.9. Effects of axial acceleration on the pressure transducer.**

Fig. 10.9 shows the effects of acceleration on the pressure transducer. The acceleration in $m/s^2$ is calculated from the second derivative of the position sensor. For a frequency of 3 Hz the maximum magnitude of acceleration is approximately 1 g and the peak-to-peak magnitude of the acceleration (over one full period) is about 30 Pa, i.e. a response of about 15 Pa/g or one order of magnitude larger than the standard version of the sensor. For all data sets the curves in fig. 10.9 were used to correct for the acceleration effects in the pressure signals.

The Texas A&M University Active Flow Control Laboratory's 2' by 3' water tunnel facility was used for the experiments. This water tunnel is a free surface, closed circuit facility that holds approximately 5000 gallons of water and has a 24" wide, 36" deep and 72" long test section. The tunnel is powered by a 25 Hp pump, with flow rates as high as 7500 gallons per minute yielding test section velocities as high as 0.9 m/s. The tunnel has a 6:1 contraction ratio and less than 1% rms turbulence level, +/-2% in velocity uniformity and less than 1 degree flow angularity in both pitch and yaw angles.

Since this is a free surface facility and the pump controller sets the flow rate in gallons per second the actual water level in the tunnel determines the velocity. The tunnel was calibrated to relate the pump controller setting, the amount of water in the tunnel (water level in test section at zero velocity) and the actual test section velocity. It was however found that such an expression further depends on the model blockage in the test section. Thus the tunnel velocity had to be determined with the probe assembly present in the tunnel. Determination of the water velocity was done by injecting dye in the water (approximately 0.3m below the surface) and measuring the time for the dye to travel in between two marks placed 1.5 m apart. A modified stopwatch with two switches for start and stop was used, one person starts the stopwatch when the dye passes the first line, and the second person stops the timer when the dye passes the second line. Naturally such measurements potentially have errors due to the reaction time of the persons starting and stopping the timer. There is also some diffusion of the dye, such that judging when the dye passes the start and stop lines is subject to some interpretation. For the tests, 40 repeated samples were taken, to provide a statistical distribution of the measurement.
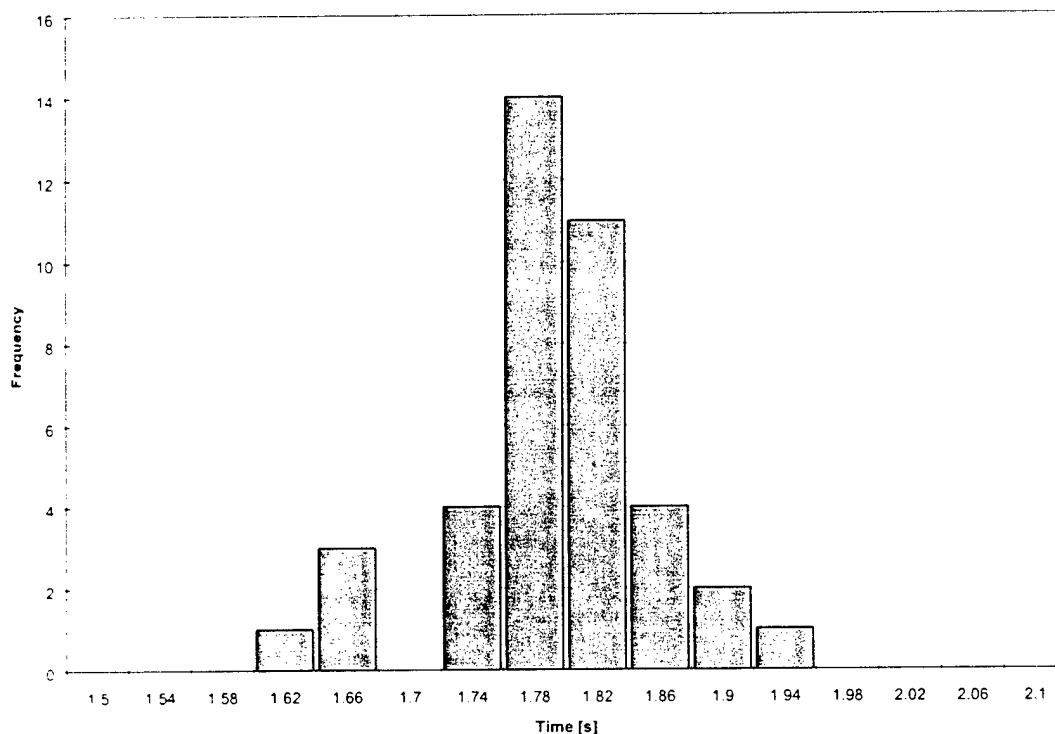


**Fig. 10.10. Measured times for the water tunnel dye tests.**

As shown in figure 10.10, the mean measured time for one velocity setting was 1.78 sec with a standard deviation of 0.064 sec. Using a 99% confidence interval and a sample size of 40 (no samples were rejected as outliers) the velocity was determined to be 0.845 m/s +/- 1.5%. The true velocity is possibly slightly different from the estimated mean, but it is believed from the experiments to be within the error range given. While different means of velocity determination could also be used, such as our PIV system, the marginally better accuracy did not warrant the additional complications, especially if one considers the comparative nature of the study.

As mentioned earlier the water tunnel test section has a free surface, which means that the water level drops significantly from zero velocity to operating velocity conditions. When the sensor is placed in the tunnel the offset is set such that even though the transducer sees a significant positive pressure due to the water column, the pressure given by the calibration slope is zero. For each millimeter of water level the associated pressure is about 10 Pa hence the change in water level (approximately 50mm) from zero velocity to running velocity must be accurately known and the probe pressure must be corrected accordingly.

During tunnel operation waves with an approximate magnitude of 5 mm peak-to-peak and wavelength on the order of meters were observed. Naturally, this periodic increase and decrease in water column above the probe will show up in the measured pressure and hence these waves must also be accounted for. A static pressure sensor was thus designed to measure the water column without measuring the dynamic effects of the water velocity. This probe uses a Honeywell 40PC amplified transducer with a range of 1.8 psig. (Figure 10.11). The probe in fig. 10.11 is placed in the water tunnel with the pressure port at approximately the same depth as the spherical probe. The exact depth is not crucial, since differential quantities are sought (figures 10.12 and 10.13).
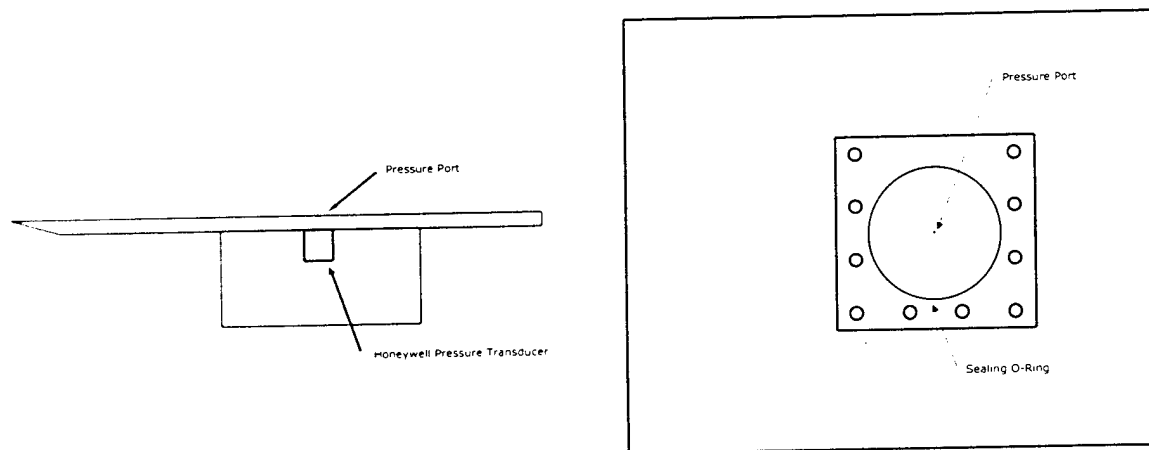


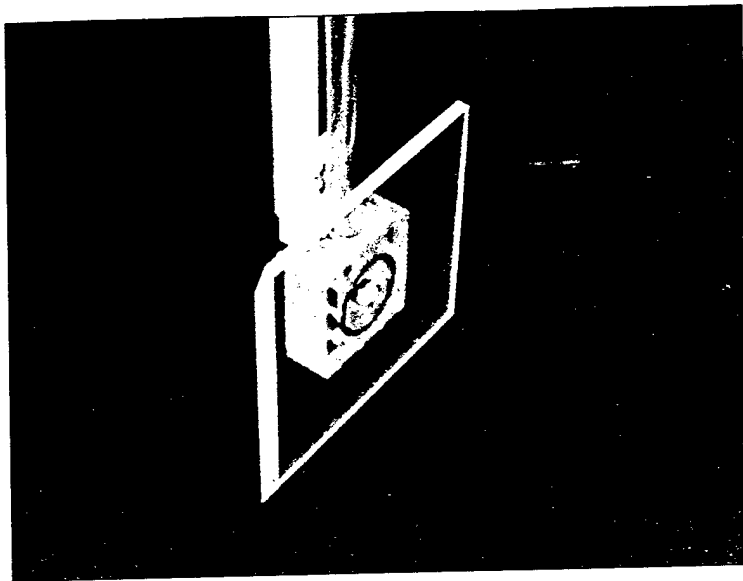**Fig. 10.11. The static pressure probe.**
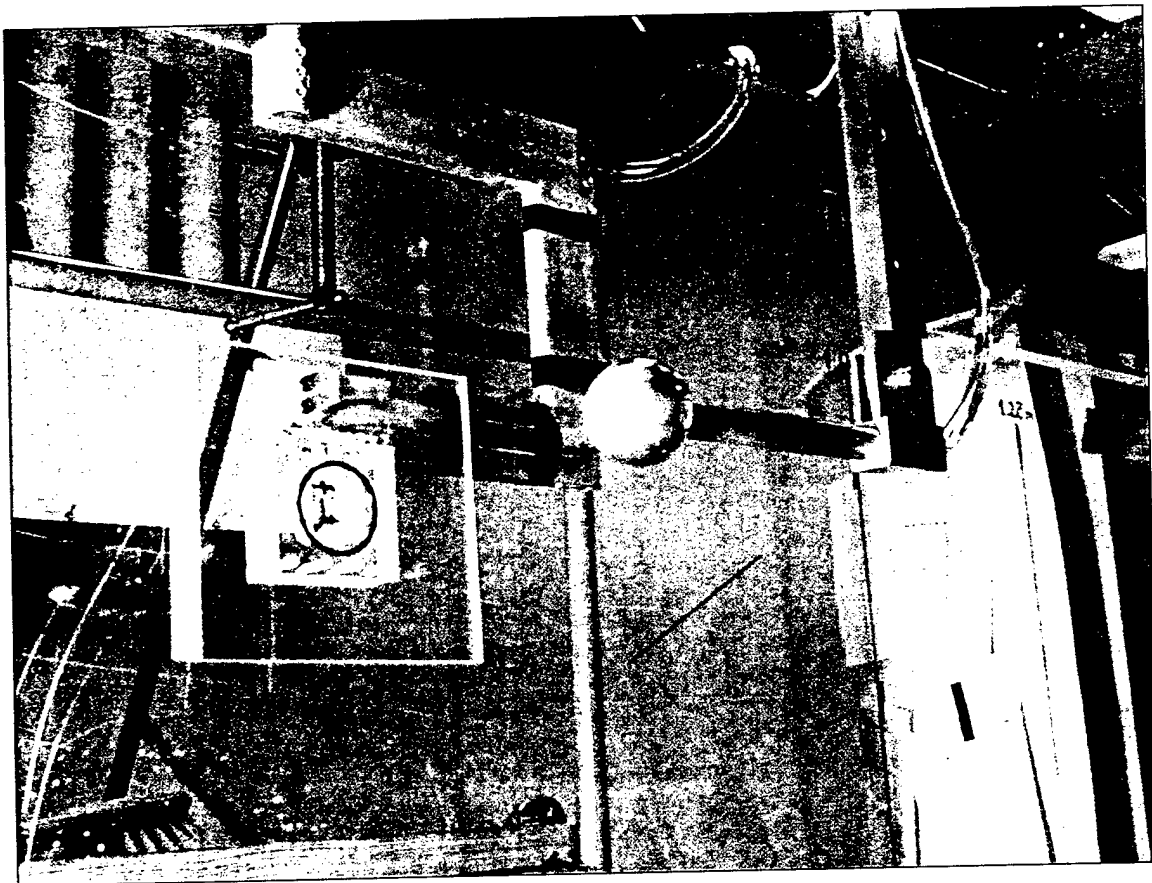
Fig. 10.12. Assembled static pressure probe.



Fig. 10.13. Static probe and spherical probe mounted in water tunnel facility.

The motion of the linear motion system is not exactly sinusoidal for a constant rotation speed of the crankshaft. Viscous and fluid inertia effects will further contribute and cause the rotation to be non-constant hence further diverging from the sinusoidal motion. Since the position sensor is sampled continuously no assumptions are made on the motion, but it is rather measured directly. If one assumes that the rotation speed of the crankshaft is constant the experimental envelope is as shown in table 10.1.

| Freq. [Hz] | Mean Vel. [m/s] | Max. Rel. Vel. [m/s] | Min. Rel. Vel. [m/s] | Max. Accs. [m/s$^2$] | Max. K [-] |
|---|---|---|---|---|---|
| 1 | 0.85 | 1.01 | 0.69 | 1.08 | 0.04 |
| 2 | 0.85 | 1.17 | 0.53 | 4.35 | 0.20 |
| 3 | 0.85 | 1.33 | 0.37 | 9.78 | 0.67 |
| 4 | 0.85 | 1.49 | 0.21 | 17.38 | 2.49 |

**Table 10.1. The test envelope for the spherical probe in the water tunnel.**

Important parameters in table 10.1 are the mean velocity, providing insight into the Reynolds number and the mean dynamic pressure to be measured. The minimum velocity must never go below zero to avoid flow reversal. The acceleration is never above values where the deflection of the probe mount is non-negligible due to the vibration dampers. The K parameter is an indicator of the expected inertial effects to be seen by the probe. Notice the very large maximum magnitude of this parameter for f=3 and f=4 Hz. This is due to the inverse proportionality to the square of the velocity and the probe relative velocity is very low during the downstream motion of the probe. The mean Reynolds number for the probe at the test velocity is $43 \times 10^3$ which is in the range seen by miniature multi-hole probes in air flows. The Reynolds number is also sub-critical, meaning that we can expect to see laminar separation at around 80 degrees.

## Acquisition of data, filtering and data corrections

The three basic quantities the time series of which we want to measure are: probe dynamic pressure, probe relative flow velocity and probe relative flow acceleration. The pressure signals from both the static probe and the spherical probe are both offset to give zero pressure for zero flow velocity, even though there is a significant pressure due to the water column. As the flow is accelerated the water level drops, the static pressure sensor will thus see a negative pressure proportional to the difference in water column drop. Similarly, the sphere probe sees this drop in pressure, but in addition it also measures the (for zero pitch angle) dynamic pressure of the flow. To find the true differential pressure for the sphere probe the static probe pressure must be subtracted from the measured sphere pressure. For the entire time series, both the static and sphere probe pressures are sampled such that this correction is done on a point-by-point basis.

The position sensor is calibrated for the range of motions where the maximum and minimum values are given directly by the radius of the crankshaft. As with all digitized data, the

present data time series are not perfectly smooth for two reasons: the resolution of the DAQ system (10V / 12 bit = 2.44 mV) and background electrical noise (on the order of 10 mV p-p). From such discretely digitized data the derivatives cannot be calculated without first smoothing or low-pass filtering the data. Rather than using analog filters where phase and magnitude information is easily lost, digital filtering of the sampled data was chosen. The topic of digital filtering is extensive and there is a number of filter parameters that have to be decided upon when designing a filter. For example, some of those parameters are: required kernel length, roll-off rate and stop-band attenuation. Implementing digital filters in a quasi-real-time system requires a comprehensive study on the speed of the filtering since some filters are computationally intensive and can be very slow. For this work, no optimization or quantification of speed and performance is studied, rather a stable conventional filtering technique was chosen. The method uses a Fast Fourier Transform (FFT) convolution technique based on the principle that multiplication in the frequency domain corresponds to convolution in the time domain. The basic function is to transform the entire time series into the frequency domain using FFT, then multiply the frequency spectrum with the frequency response of the filter and then transform the spectrum back into the time domain using in inverse FFT. Large sample sizes ($2^{14}$ = 16384) are used for all of the acquired data with 200 points per period (the sampling frequency is adjusted to 200 × oscillation frequency). Thus for each data set more than 80 periods of oscillations are recorded. Filtered and corrected quantities are shown in fig. 10.14 for a frequency of 4 Hz and zero pitch angle.
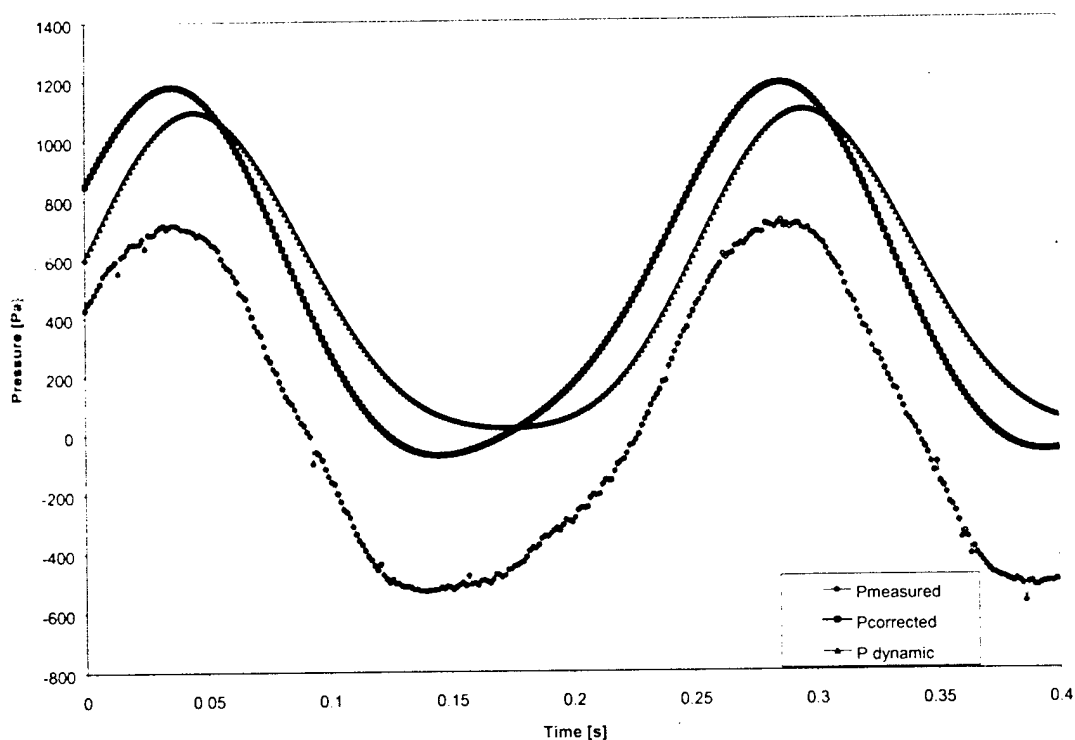


Fig. 10.14. Data for a frequency of 4 Hz, tunnel velocity of 0.85 m/s and zero degrees pitch angle.

## Prediction of Steady and Unsteady Pressure Coefficients

We will call "true dynamic pressure" the stagnation pressure corresponding to the instantaneous probe relative flow. This is the pressure the probe would measure, at zero pitch angle, if there were no inertial effects. However, the actually measured pressure at the forward stagnation point has larger magnitude and leads the true dynamic pressure in phase due to the inertial effects. It should also be noted, as seen in figure 10.14 for zero degrees pitch, that the measured sphere pressure does not cross the true dynamic pressure at the peaks (point where dU/dt is zero). In the valleys this is the case, however at the peaks the sphere pressure appears to cross the true dynamic pressure at a later point. This trend has been observed in a wide range of data and may be due to viscous effects.

The steady pressure coefficient is calculated from the pressures seen by the probe in steady flow (probe is not oscillated) for pitch angle from 0 to 90 degrees (fig. 10.15).
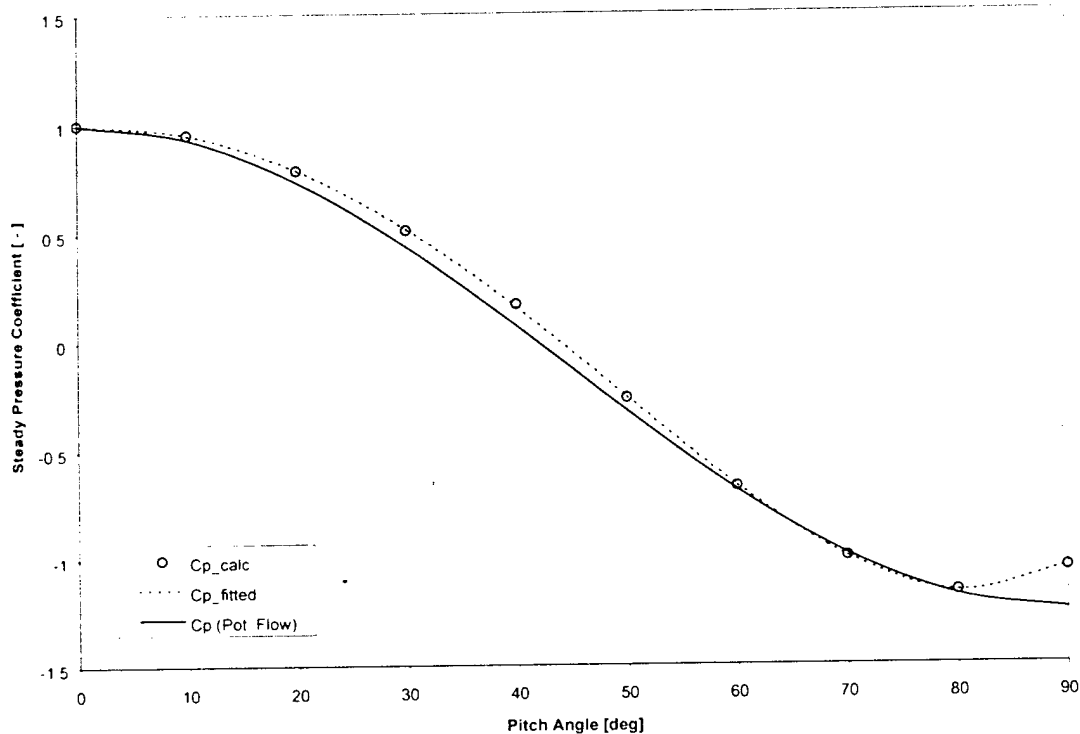


Fig. 10.15. The steady pressure coefficient calculated from the experimental sphere data. The data is curve fitted and plotted up to 90 degrees. The Reynolds number is sub-critical and laminar separation is observed.
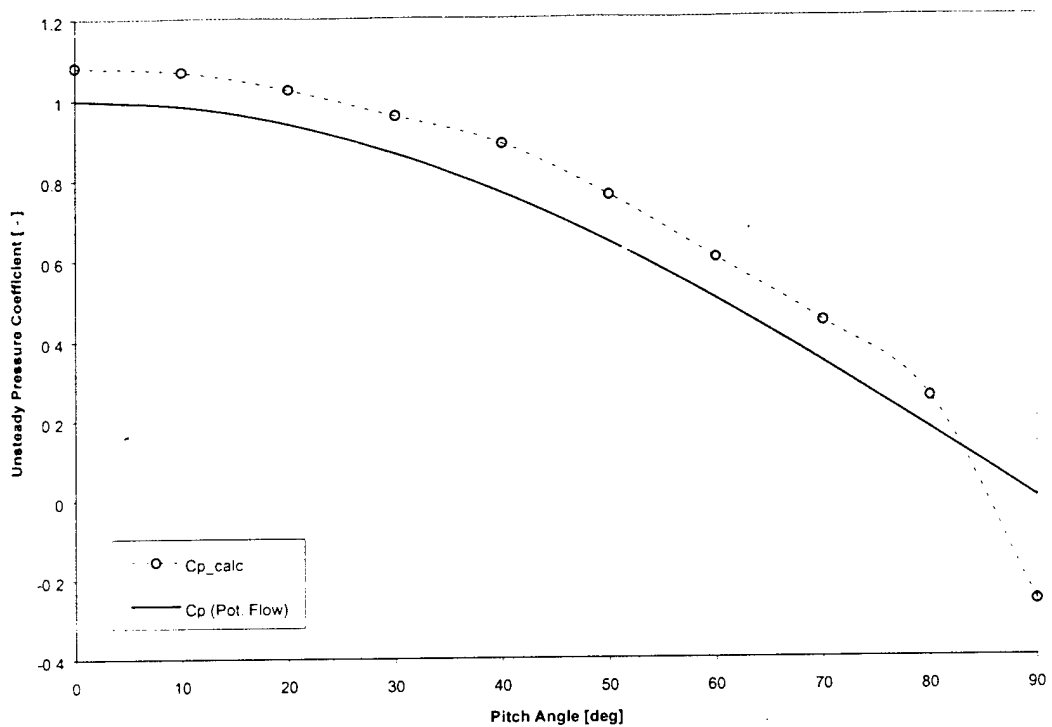
120

**Fig. 10.16. Calculated unsteady pressure coefficient from experimental data at f=4Hz.**
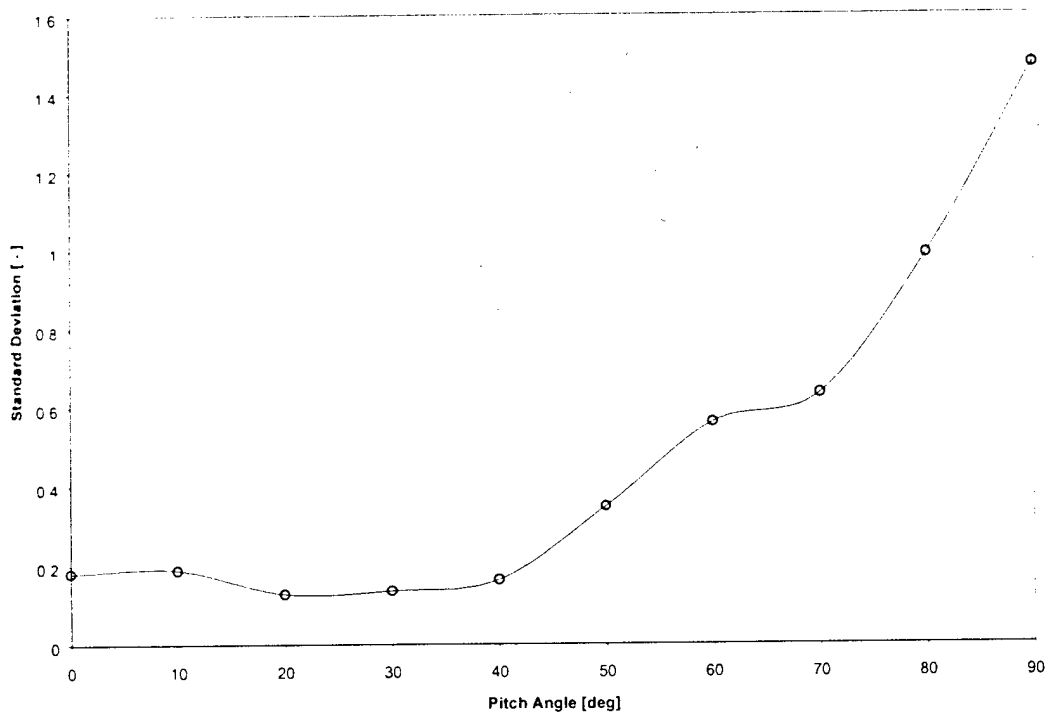


**Fig. 10.17. Standard deviation of the predicted mean unsteady Cp.**

The determination of the steady pressure coefficient is seen to follow theory well and the standard deviation of the measurements is low. Determination of the unsteady pressure coefficient is significantly more challenging than finding the steady pressure coefficient. As discussed in section 8, it is necessary to chose data from a time series where the inertial effects are significant (high K-value). For each point in the time series the value K is calculated and only data points that are above a certain absolute value of K (e.g. above the rms value) are used to find an average unsteady pressure coefficient for that angle. The results are shown in figure 16. The agreement between the experimentally calculated pressure coefficient and that predicted by unsteady potential flow is remarkable, if one considers the fact that the theoretical curve does not take into account viscous effects, steady or unsteady and that, as already described earlier, the experimental setup and procedures for the unsteady measurements are very extensive and elaborate with several potential sources for experimental error. In fig. 10.17, the standard deviation in the predicted mean value for the unsteady coefficient is seen to be very large, however the large number of points used to predict the mean Cp gives a 99% confidence interval for the mean value.
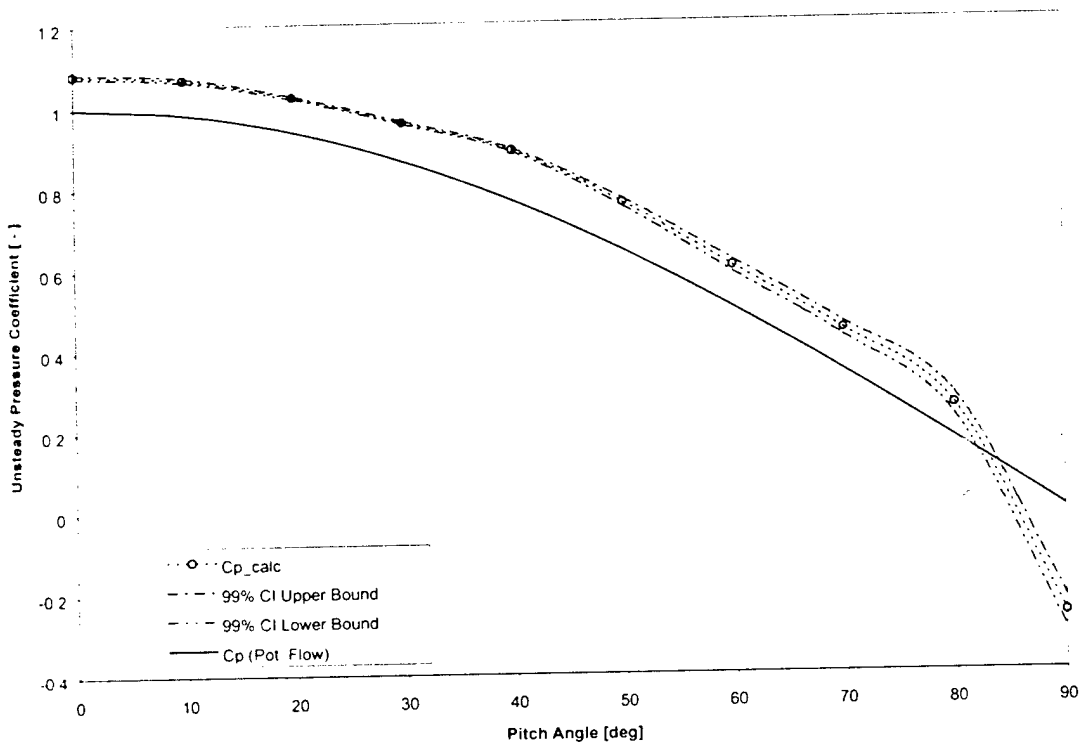


Fig. 10.18. The 99% confidence interval for the predicted mean unsteady pressure coefficient.

In fig. 10.18 it is seen that even though the standard deviation and hence the spread in the data is large the mean is predicted within a narrow range due to the large number of data points used to estimate the mean. Increasing the accuracy of the tunnel velocity by using a continuous measurement such as a hot-film probe might improve the accuracy of the predicted pressure coefficient, however the largest error source is believed to be the probe velocity derived from the

position sensor. For the above analysis the filtered position signal is differentiated to give the velocity of the linear motion system directly. Potential error sources in the velocity estimation are: non-linearity of the potentiometer, sampling error and the differentiation of discrete data.

The main purpose of the water tunnel tests was to evaluate the feasibility of experimentally determining the steady and unsteady pressure coefficients. However, it was also desired to test, using the water tunnel data, the velocity prediction routine given in section 8. The spherical probe has only one pressure sensor and predicting, from this one pressure reading, simultaneously the instantaneous velocity and flow angle (or probe pitch angle) is impossible. For this reason the pitch angle was assumed constant and known, and determination of the velocity magnitude follow the procedure outlined in section 8. The experimentally determined steady and unsteady pressure coefficients calculated above were used to predict the velocity magnitude for several time series of corrected sphere pressures. From the filtered data also the "exact" relative velocity is known and is used as a reference.

### Test Case 1: Frequency 4 Hz and Pitch Angle 0 Degrees

The first test case is for frequency 4 Hz. The inertial effects for this test are very large with a maximum K value of about 2.5. This data set was also used to determine the unsteady pressure coefficient for zero pitch angle. The filtered probe pressure and the true flow dynamic pressure are shown in fig. 10.19. The data in fig. 10.20 show that the velocity magnitude is predicted with reasonable accuracy from the measured pressure.
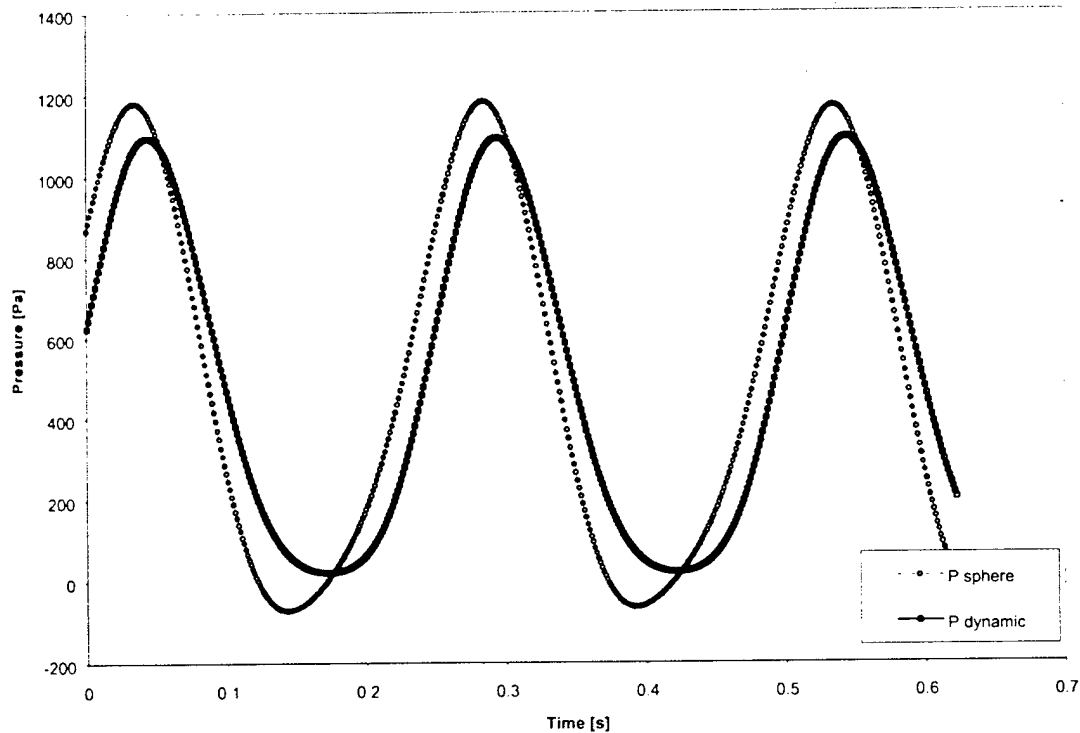


Fig. 10.19. Filtered sphere pressure and the true probe relative dynamic pressure of the flow for f=4 Hz, pitch = 0 degrees.
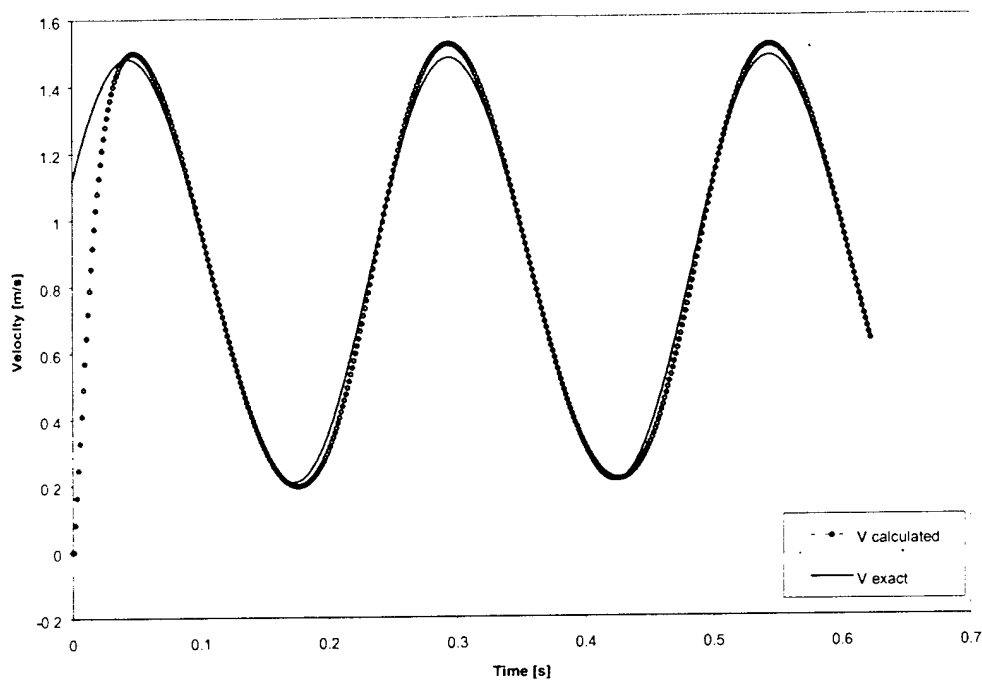
Fig. 10.20. Velocity prediction using the modified Euler predictor-corrector method for f=4 Hz and pitch angle = 0 degrees.
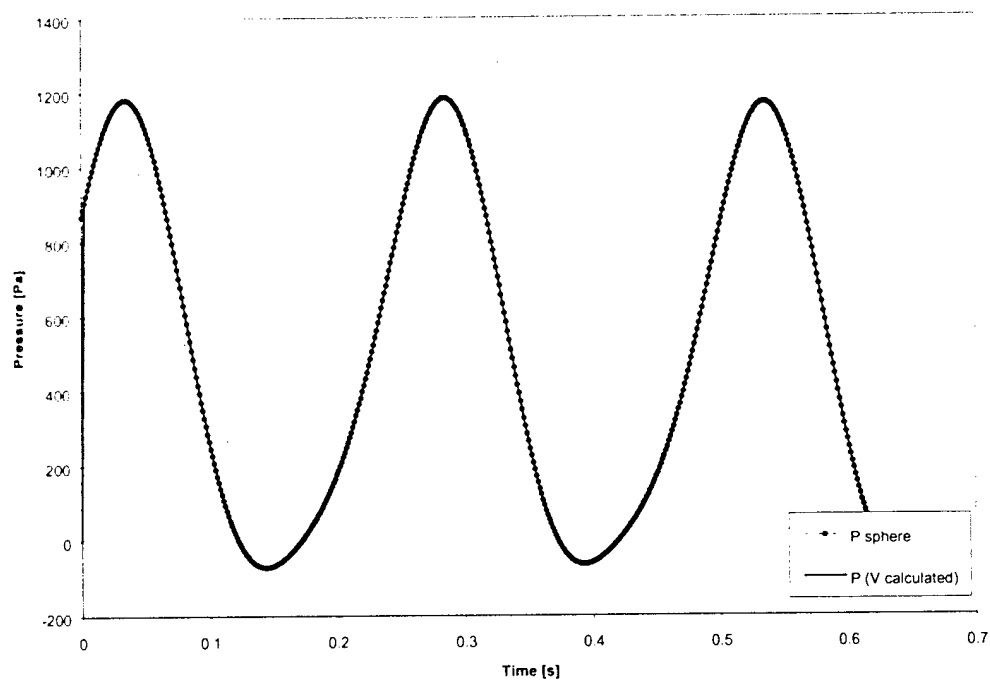


Fig. 10.21. Sphere pressure and calculated sphere pressure from the predictor-corrector method for f=4 Hz and pitch angle = 0 degrees.
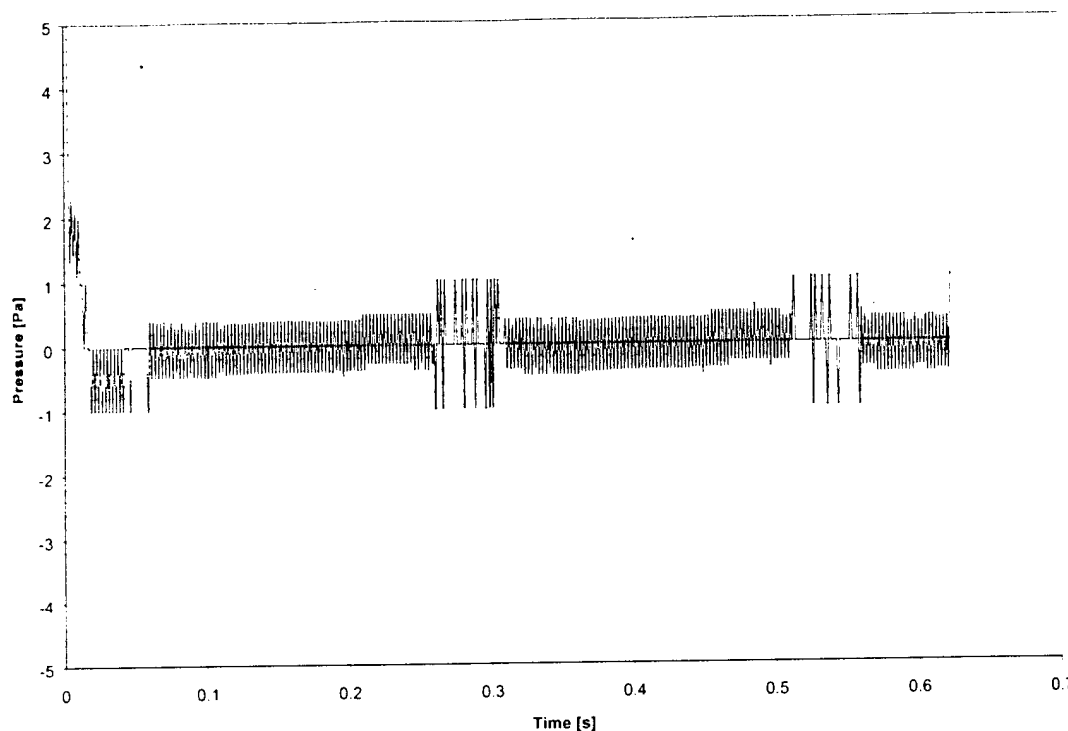
124

**Fig. 10.22. Difference between measured sphere pressure and calculated sphere pressure from the predictor-corrector method for f=4 Hz and pitch angle = 0 degrees.**

In section 8 it was shown that the accuracy of the predictor-corrector method depends heavily on the sampling rate or time between data points. It was shown that the error is proportional to the step size to the third power (Error $\propto h^3$) thus for each doubling of the sampling frequency (half the time between data) the error is expected to be reduced by a factor of eight. It was also shown that with 20 points per period for a sine wave the expected error is around 5%. The data in these tests was sampled with 200 points per period and thus very small errors are expected from the predictor-corrector routine. In fig. 10.21 the sphere pressure is shown, and also the calculated sphere pressure from the velocity magnitude and rate-of-change calculated by the predictor-corrector method. Negligible difference between the two pressures are observed and plotted in fig. 10.22.

**Test Case 2: Frequency 4 Hz and Pitch Angle 20 Degrees**

For a non-zero pitch angle the measured pressure has a completely different waveform and phase than the true dynamic pressure of the flow. For the tests using the sphere probe the pitch angle is known such that the steady and unsteady pressure coefficient values are given directly by the curve-fitted data from figs. 10.15 and 10.16 (Cp curves). Fig. 10.23 shows the filtered sphere pressure and the true dynamic pressure of the flow for a pitch angle of 20 degrees.
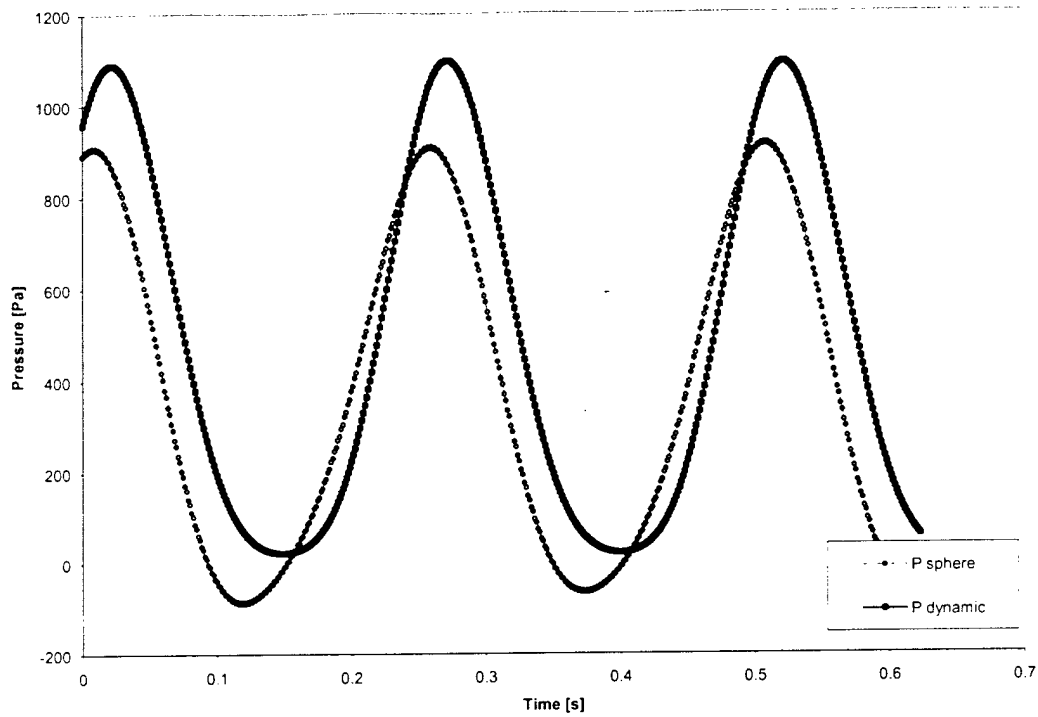
**Fig. 10.23. Filtered sphere pressure and the true probe relative dynamic pressure of the flow for f=4 Hz, pitch = 20 degrees.**
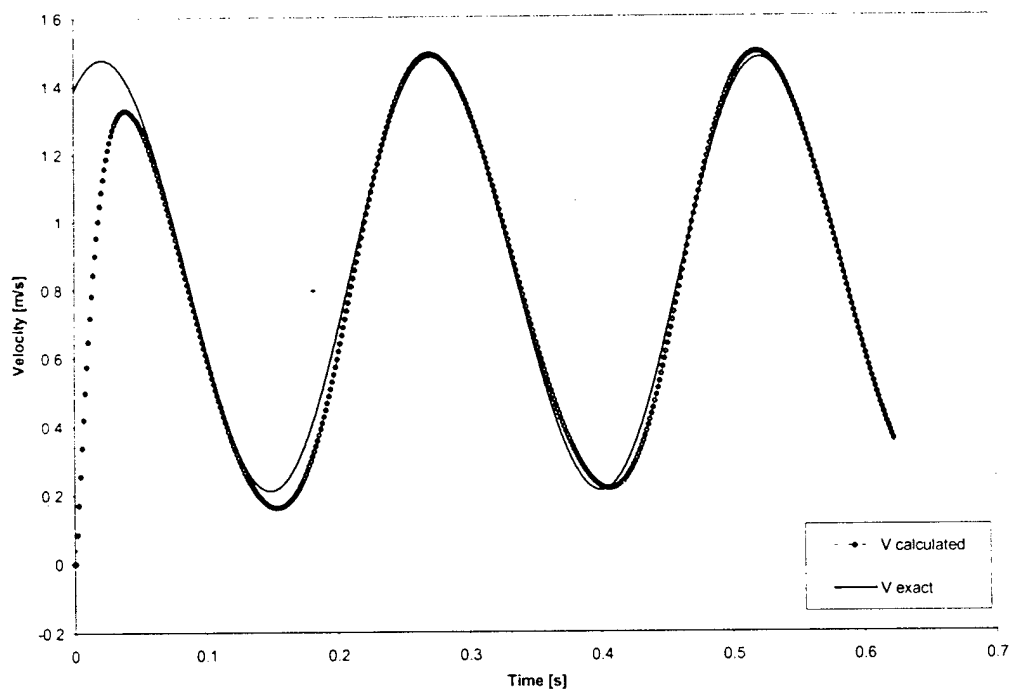


**Fig. 10.24. Velocity prediction using the predictor-corrector method for f=4 Hz, pitch = 20 · degrees.**

In fig. 10.23 large amplitude difference between the sphere pressure and the true dynamic pressure of the flow is seen. Using the predictor-corrector routine the velocity is still predicted well (fig. 10.24).

### Test Case 3: Frequency 2 Hz and Pitch Angle 0 Degrees

For frequency 2 Hz the inertial effects are much smaller than for 4 Hz, but still significant. The experimental determination of the unsteady pressure coefficient used data recorded at 4 Hz. Using this unsteady pressure coefficient to determine the velocity magnitude at a different frequency, will show the technique's independence from frequency. In fig. 10.25 large unsteady effects are still seen for this lower frequency (as compared to 4 Hz). Fig. 10.26 shows that even for frequencies different from the calibration frequency the method works well in predicting the velocity magnitude.

### Test Case 4: Frequency 2 Hz and Pitch Angle 70 Degrees

The steady and unsteady pressure coefficients are continuous and well-behaved up to about 80 degrees where laminar separation causes divergence from the potential flow solution. The steady pressure coefficient is negative for angles above approximately 42 degrees, meaning that a steady pressure at 42 degrees or higher will be negative.
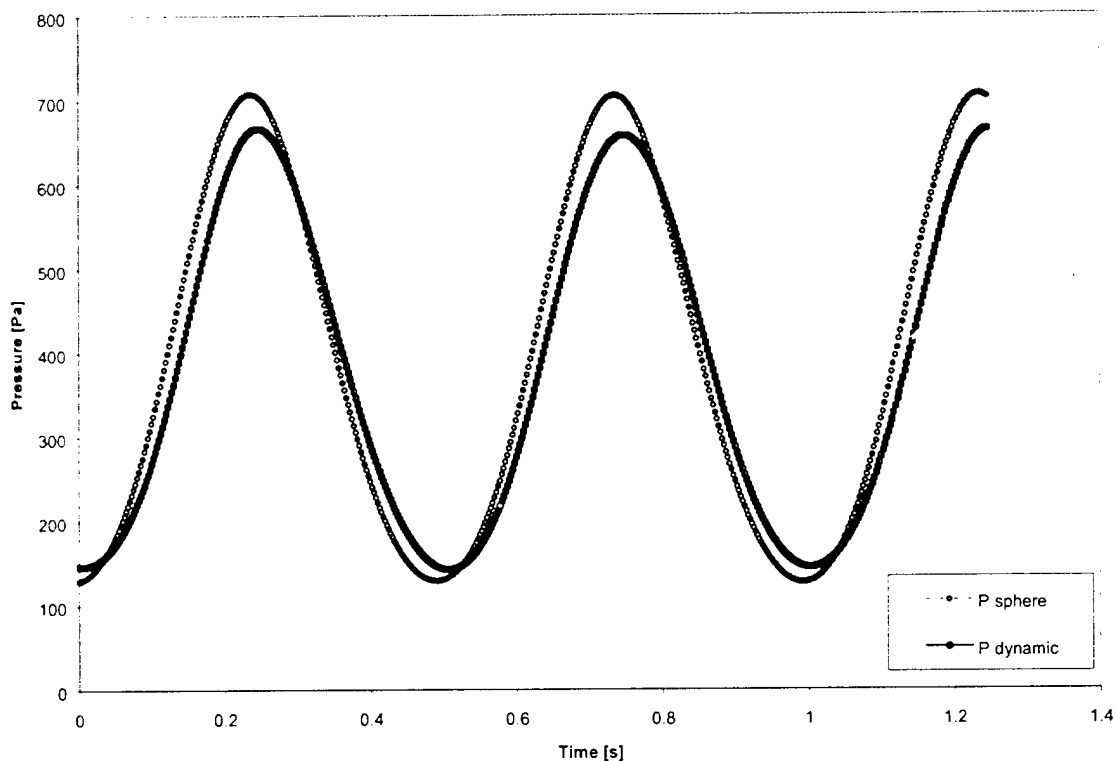


Fig. 10.25. Filtered sphere pressure and the true probe relative dynamic pressure of the flow for f=2 Hz, pitch = 0 degrees.
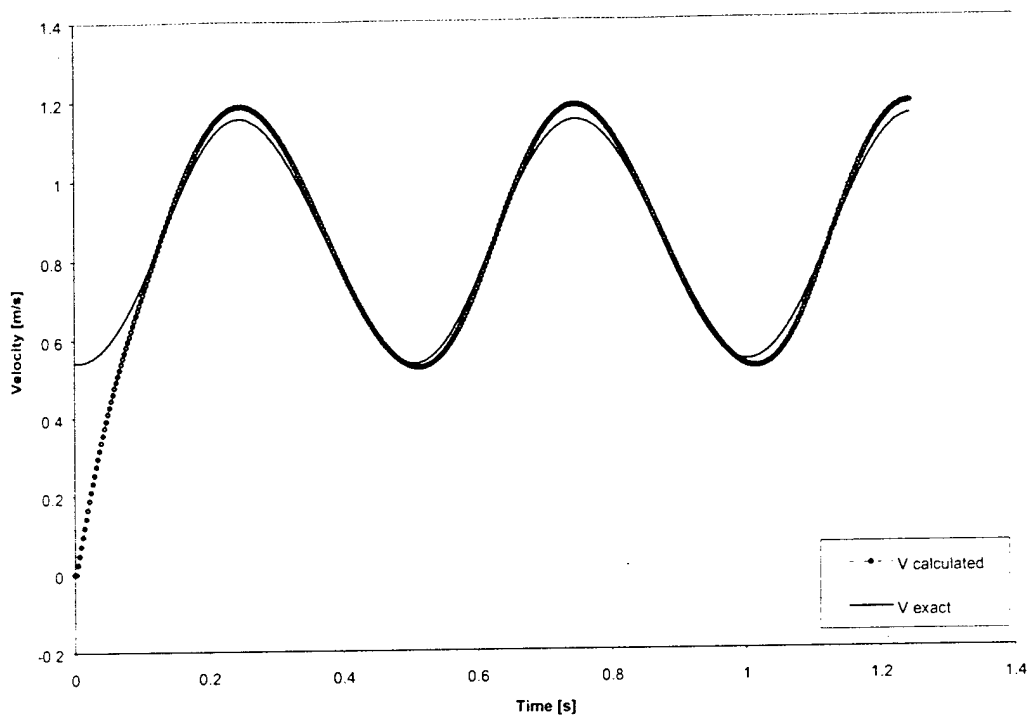
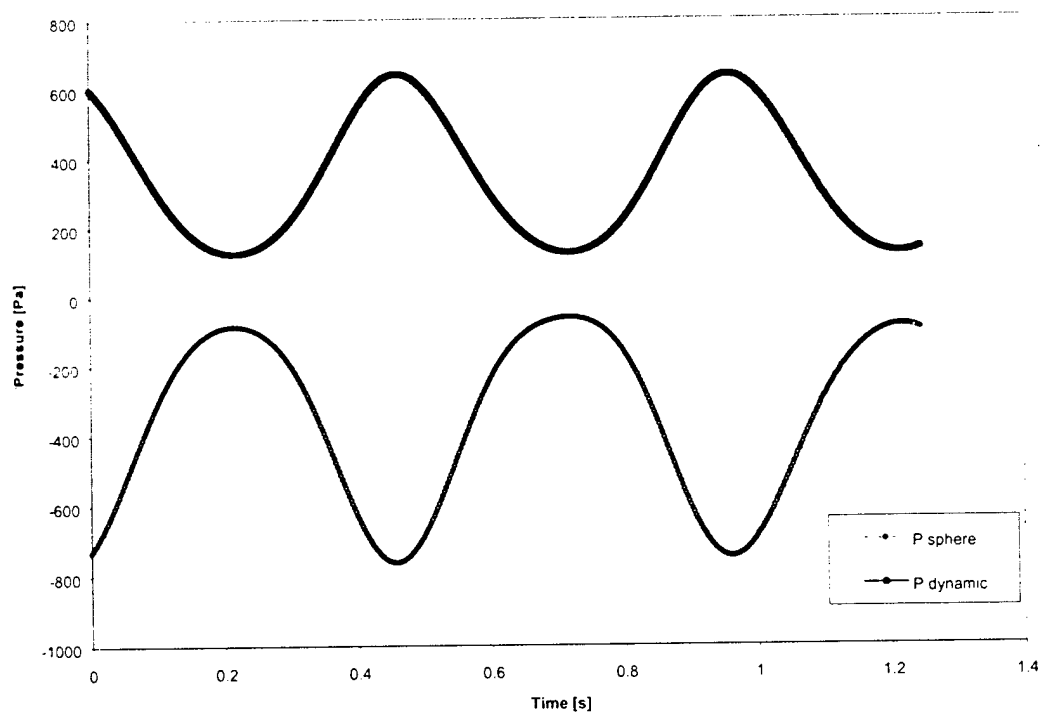**Fig. 10.26. Velocity prediction using the predictor-corrector method for f=2 Hz, pitch = 0 deg.**



**Fig. 10.27. Filtered sphere pressure and the true probe relative dynamic pressure of the flow for f=2 Hz, pitch = 70 degrees.**
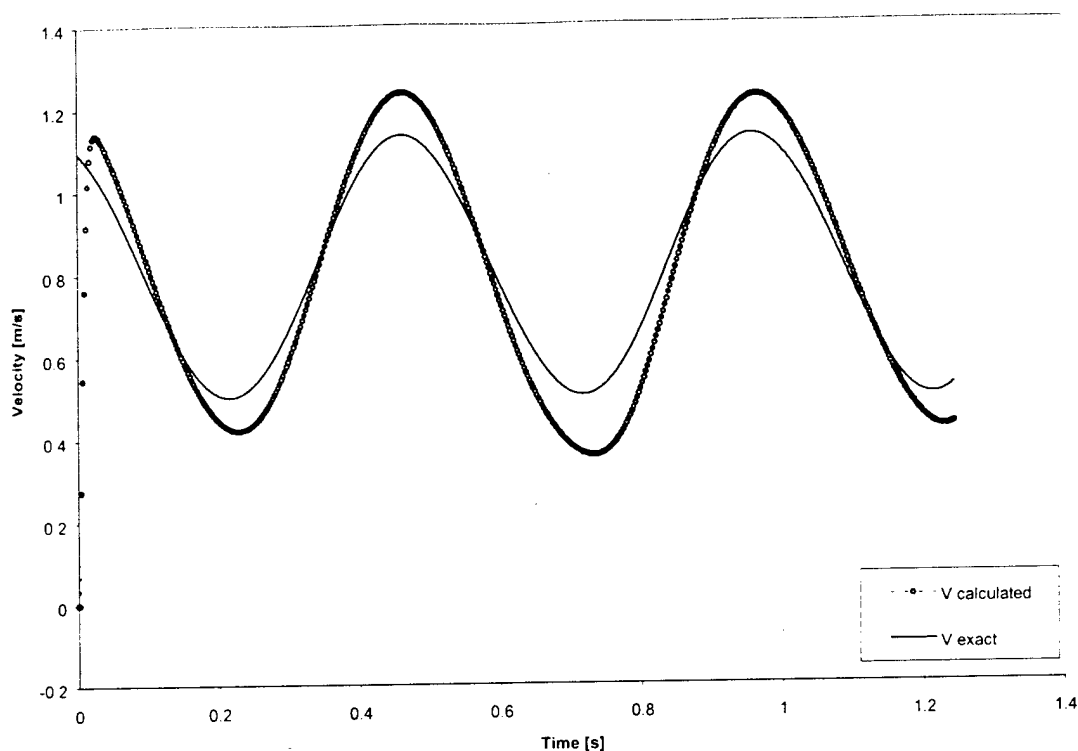
128

**Fig. 10.28. Velocity prediction using the predictor-corrector method for f=2 Hz, pitch = 70 degrees.**

Fig. 10.27 shows that the measured pressure and the true dynamic pressure of the flow are opposite in sign with their absolute values very similar. For this high angle the velocity magnitude is still predicted accurately in phase (fig. 10.28), but significant over prediction in magnitude is observed. For each of the four cases considered the velocity is consistently over-predicted to a lesser or greater degree. This over-prediction may be due to a number of reasons. The indirect method of measuring the probe relative velocity can introduce errors, which means that in the four examples given above the error might not be in the predicted velocity, but rather in the "exact" or reference velocity. Additional refinement could also be done in the starting points for the predictor corrector method. Due to the non-linearity of the governing equation some instability problems can occur in the starting region unless proper precautions are taken. For the above tests zero values were used as starting values and relatively slow convergence to the true velocity is seen. For periodic flows this may not impose a problem since a long time series can be used and the first few points can be discarded, however for non-periodic flows further refinement of the starting conditions should be attempted.

# 11. ANALYTIC PREDICTION OF SURFACE PRESSURES OVER A HEMISPHERE-CYLINDER AT INCIDENCE AND EXPERIMENTAL VALIDATION

The utility of the hemisphere cylinder configuration lends itself to widespread application, with the specific application of interest to us being its use in pressure probes. An explicit method to estimate the surface pressures over this configuration would be of use for both conceptual design and for understanding the relation of the design variables. Consequently, an explicit equation is developed that requires only the hemisphere cylinder incidence and the location of the point of interest to yield the final surface flow. Surface pressures are calculated using perturbation potentials calculated from least square curve fits to numerically estimated potentials. Comparisons of the expression with experimental data show good agreement.

## Nomenclature

$C_P$ = pressure coefficient
$f^c$ = source ring strength
$K^c$ = kernel function
$k$ = geometric parameter
$l$ = body length
$P_n$ = source ring influence parameter
$r$ = orthogonal coordinate
$R$ = hemisphere radius
$U$ = freestream
$V_\theta$ = tangential velocity
$W$ = transverse velocity
$w_1$ = lateral velocity
$w_2$ = axial velocity
$x, y, z$ = cartesian coordinates, origin at hemisphere nose
$x', y, z$ = cartesian coordinates, origin at hemisphere-cylinder juncture
$\rho, \zeta$ = orthogonal coordinates
$\alpha$ = geometric parameter
$\lambda$ = geometric parameter
$\phi'$ = perturbation potential
$\phi$ = potential
$\theta_H$ = hemisphere cylinder incidence angle
$\theta_V$ = angle to the point of interest measured from the attachment line
$\theta$ = spherical coordinate angle, measured from nose of hemisphere

## General

The wide range of applications of the hemisphere-cylinder (H-C) configuration has led to numerous investigations to elucidate its aerodynamic characteristics. Hemisphere-cylinders form the baseline shape of many underwater vehicles, subsonic missiles as well as measurement probes. Both experimental (Hoang, H. T., 1991; Meade and Schiff, 1987; Meier and Kreplin, 1980)

and numerical (Ying et al., 1987) studies have clarified effects of incidence and Re number on surface pressure loads and on and off-surface flow topology. Generally, at low incidence for $-15 < \theta < 15$ deg, the effect of the cylinder on the surface pressures over the hemisphere is marginal, such that the flow resembles that over a sphere. Note that $\theta = 0$ deg indicates the H-C nose, and $\theta = 90$ deg the hemisphere-cylinder junction. For larger $\theta$'s, the source like effect of the cylinder results in reduced tangential velocities compared to the sphere. At zero incidence in the laminar sub-critical range, the minimum recorded pressures for the H-C generally occur[1] at $\theta \approx 67$ (Re $= 27,000$) - 76 (Re $> 290,000$) deg compared to $\theta \approx 72$ deg for a sphere (Schlichting, 1979) (Re $= 163,000$). At these Re numbers, the minimum recorded pressure coefficient for the H-C is typically $\approx -0.64$ while that for a sphere is $\approx -0.56$. Increasing the Re past critical shows an aft movement of the point of minimum pressure with a concomitant increase in the minimum pressure attained.

Viscous effects have a pronounced effect on the flow behavior over a H-C. At low incidence, pressure recovery at the intersection of the hemisphere with the cylinder generally causes localized flow separation in the form of a ring shaped bubble (Hoang, H. T., 1991). Turbulent transition generally closes the separation. As the incidence of the H-C increases, the separation region looses axi-symmetry and moves from the windward side towards the leeward side of the H-C. A localized separation bubble may still exist on the leeward surface, at $x/R \approx 1$, however it may terminate in two unstable foci which mark the lift off location for two "horn vortices". Further down the cylindrical body, cross flow separation also results in the formation of vortices (which may connect with the aforementioned horn vortices). This vortex formation is dependent on the state of the cross flow boundary layer and hence Re. Consequently, the flow over a H-C at incidence may be considered to be constituted of both potential (windward) and viscous flow regions (leeward) with the boundaries determined by the operating conditions, e.g. incidence, Re, turbulence, etc. The above statement combined with the fact that in the use of pressure probes it is mainly the pressures of the windward side that are important, viscous effects are of secondary importance. Pointed nose axisymmetric bodies are prone to asymmetric wake development for large angles of attack. The asymmetry of the vortex wake can be caused by any slight surface perturbation. H-C's are generally not as prone to vortex asymmetry as sharp axisymmetric bodies, however, a moderately small surface perturbation in the nose vicinity of a H-C can cause asymmetrical vortex development. For H-C incidence angles ($\theta_H$) greater than 15 deg and less then 42 deg, the wake of the cylinder can also contain unsteadiness. The unsteadiness is due to periodic heaving of the vortices as they convect downstream (Hoang, H. T., 1991). For incidences greater then 42 deg, H-C's exhibit vortex shedding.

The wide ranging application of H-C configurations makes it valuable for the designer to have a simple analytic tool that would allow estimates of the surface pressures over a H-C at incidence. Traub (Traub, 1999; Traub, 1997a; Traub 1997b; Traub, 2001) has shown that analytic prediction methods can offer simplicity and utility to the designer, and allow a "feel" for the respective design variables. Consequently, an analytic method has been developed. The method uses the surface singularity methods of Landweber (Landweber, 1951) and Lotz (Lotz, 1932) to estimate the perturbation potentials for axial and transverse flow, respectively. These potentials are then approximated using a least squares curve fit. Potential theory is then used to develop a final single expression which allows for pressure estimation. An experimental study was also undertaken to provide data for comparison. Numerous theoretical and experimental data

comparisons are presented. Agreement is seen to be very good, which is encouraging considering the simplicity of the final analytic expression.

## Theoretical Development

As Laplace's equation is linear, the perturbation potential due to axial flow and that due to transverse flow can be decomposed and solved independently. For simplicity, different methods were used for the axial and transverse flow solutions. A brief overview of these methods is presented. Specific details may be found in the cited references.
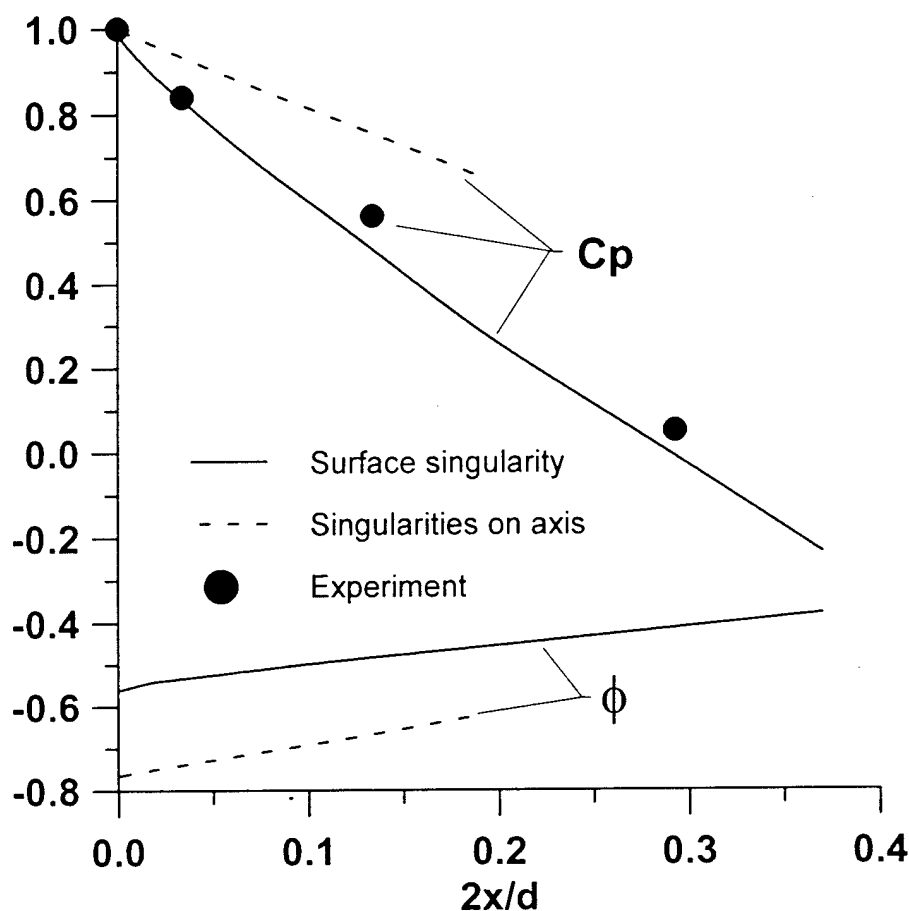


**Fig.11.1. Effect of singularity location on the perturbation potential and predicted pressure coefficient over a H-C.**

## Axial Flow

Initially, the accuracy of surface and axis distributed singularity methods was investigated. Figure 11.1 shows comparisons (the axis method used doublets, the surface method will be detailed below). It may be seen that for this type of body, an axial distribution of singularities does not yield an accurate representation of the flow, essentially due to a discontinuous second derivative of the surface at the H-C juncture. It was thus decided that the surface singularity method would be used to model the flow despite a significant increase in complexity. The axial flow over the H-C was solved for using the method of Landweber, as presented by Albone (Albone, 1972). Landweber has shown

that by applying Green's theorem to the solution of the boundary value problem for $\phi$, an integral expression for the surface velocity may be obtained. Thus, the method consists of solving the integral equation for the surface velocity:

$$\int_{0}^{P} \frac{U(x)v(x)^2 \, ds}{2r(x,t)^3} = 1 \quad \text{where} \quad r(x,t) = \sqrt{(x-t)^2 + y^2} \tag{11.1}$$

U(x) is the total fluid velocity on the body surface non-dimensionalised by the free stream velocity and t is the location of a unit strength source at an arbitrary location on the bodies axis of symmetry. This equation is solved by iteration to minimise an error function within a user prescribed tolerance (see Albone, 1972, for details). This method is more rapid than other surface singularity methods, but yields velocity on the body surface only. Within the user prescribed tolerance, the method is exact. The perturbation potential was found by integrating the perturbation velocity, using cubic splines to describe the velocities. Fig. 11.2 shows comparisons between the present method (i.e. Landweber's method) and the results of Vandrey (Vandrey, 1953), who used a surface source ring method. A least square curve fit of the present method's data is also included.
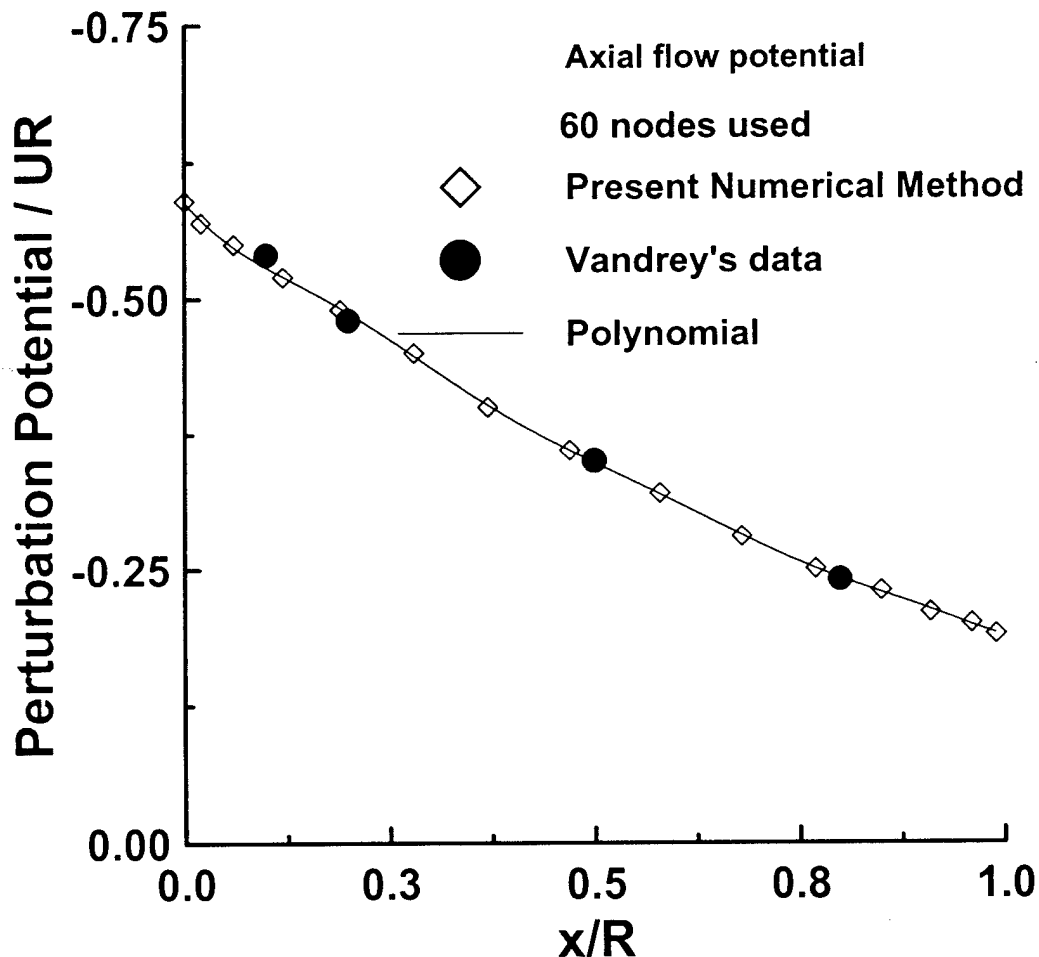


Fig. 11.2. Predicted axial perturbation potential over a H-C.

## Transverse Flow

The transverse flow was solved for using the more general, but computationally more expensive method of Lotz. This method uses an axial distribution of surface source/sink rings in combination with the no penetration boundary condition to determine the source strengths. The method is complicated by the behaviour of the kernel or core functions which are singular when the effect of the element on itself is evaluated, requiring careful implementation of suitable limits. The method consists of calculating the geometric Kernel:

$$K^e = \frac{1}{\sqrt{(\alpha^2 + \underline{k}^2)}} \left( G_1(k^2)[(r - \rho) - r'(x - \zeta)] - \rho G_2(k^2)] \right) \tag{11.2}$$

where $G_1$ and $G_2$ are functions of complete elliptic integrals of both the first and second kind:

$$G1 = \frac{(2 - k^2)E(k^2)}{2(1 - k^2)} - K(k^2) \tag{11.3}$$

$$G2 = 2\frac{(2 - k^2)}{k^2}\left(E(k^2) - K(k^2)\right) + \left(E(k^2) - K(k^2)\right) \tag{11.4}$$

with

$$K(k^2) = \int_0^{\pi/2} \frac{dz}{\sqrt{1 - k^2 \sin^2 z}} \quad \text{elliptic integral of the first kind}$$

$$E(k^2) = \int_0^{\pi/2} \sqrt{1 - k^2 \sin^2 z}\, dz \quad \text{elliptic integral of the second kind}$$

$\alpha, \rho, k, \underline{k}, x, \zeta$ and r are geometric parameters given by:

$$\alpha^2 = (x - \zeta)^2 + r^2 + \rho^2 \qquad \underline{k}^2 = 2r\rho \tag{11.5a}$$

$$\lambda^2 = \frac{\alpha^2 - \underline{k}^2}{\alpha^2 + \underline{k}} \quad \text{and} \quad k^2 = 1 - \lambda^2 \tag{11.5b}$$

The method then consists of solving for each P(x,r) by varying the running point RP($\zeta$,$\rho$), taking care to evaluate P=RP so as to avoid a singular solution (due to the elliptic integral G1), (see Fig. 11.3) where

$$P_n(x,r) = \int_0^1 \frac{P_{n-1}(\zeta,\rho)K^e}{\rho}\, d\zeta \quad \text{and} \quad P_1(x,r) = \int_0^1 K^e d\zeta \tag{11.6}$$
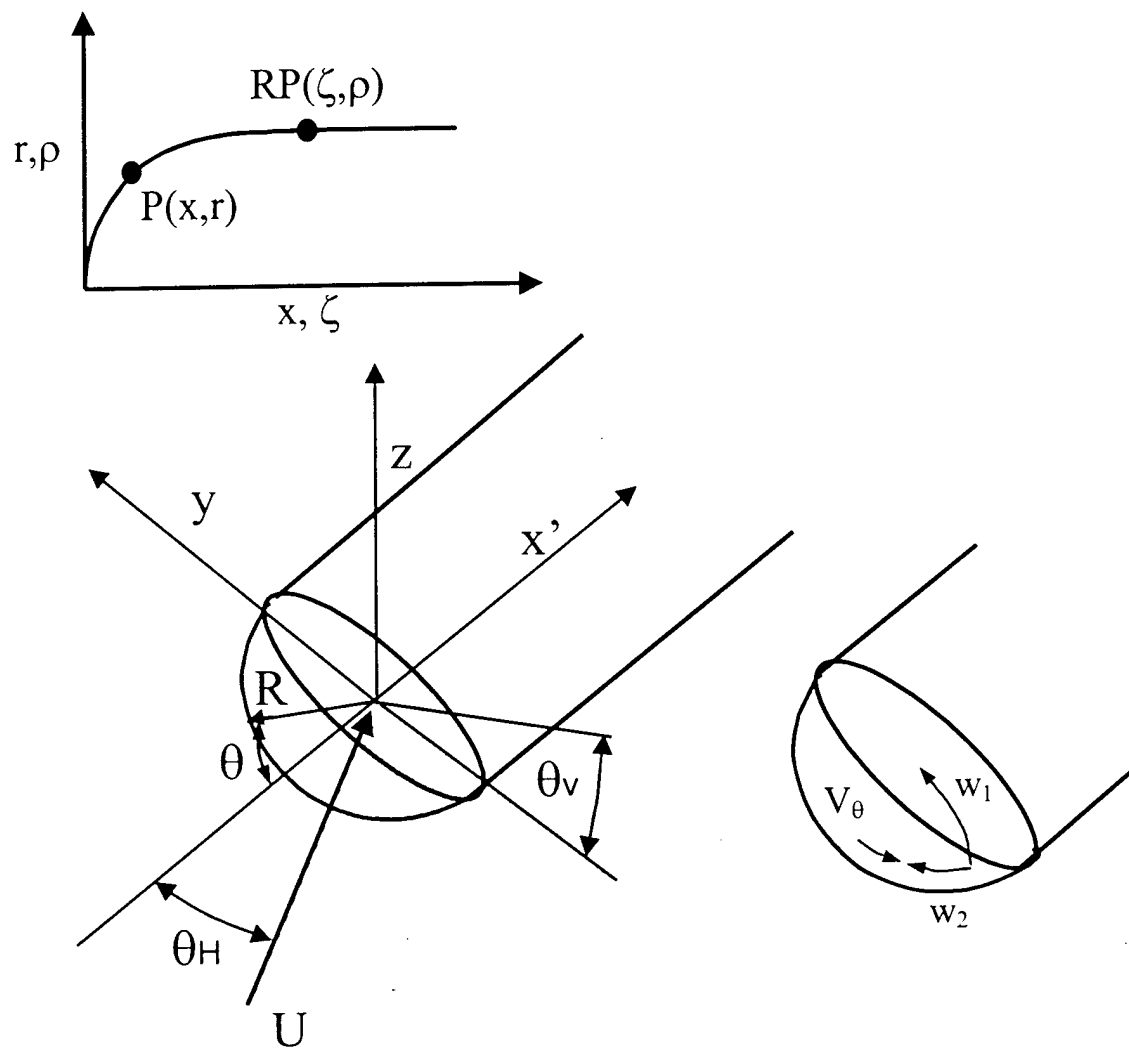
134

**Fig. 11.3. Theoretical development geometric variables and calculated velocity components.**

The solutions of the preceding equations are then combined in a rising power series of $\pi$ for the source ring strengths at any fixed point location:

$$f^e(x,r) = f^e_0(x,r) - \frac{f^e_0(x,r)}{r}\left(\frac{P_1(x,r)}{\pi} - \frac{P_2(x,r)}{\pi^2} + \frac{P_3(x,r)}{\pi^3} - ....\right) \tag{11.7}$$

Finally, the perturbation potential at any point in the flowfield is found using:

$$\phi' = -4W\cos\theta_V \cdot \int_0^l \frac{f^e(\zeta,\rho)\sqrt{1+\rho'^2}}{\sqrt{\alpha^2+k^2}} G_3(k^2)\rho d\zeta \qquad (11.8)$$

where W is the transverse velocity, $G_3$ is a function of complete elliptic integrals of the first and second kind, i.e.

$$G3 = \frac{1}{k^2}\left[(2-k^2)K(k^2)-2E(k^2)\right] \qquad (11.9)$$

$\theta_V$ is the angle to the point of interest measured from the attachment line. Although tedious, the method does yield essentially exact solutions. Fig. 11.4 shows comparisons of the transverse potential between the present method and the results of Vandrey, who used a surface source ring method. A polynomial curve fit is also presented.

## Prediction of Pressures

Using the axial and transverse perturbation potentials determined using the surface singularity methods above allows the determination of the attached flow surface pressures at any location on the H-C as will be detailed. As mentioned previously, the contributions of the axial and transverse flow can be determined separately due to the linear nature of Laplaces' equation.

### *Velocity Due to Axial Flow: 0 < x/R < 1*

Figure 11.3 shows the variables used in the present development. For utility, the formulation uses the position variable $\theta$ for location over the hemisphere body (rather than x/R). A least squares curve fit of the perturbation potential in Fig. 11.2 yields, using x/R=1-cos($\theta$) with x'=x-R (after some manipulation):

$$\phi' = URcos(\theta_H)\left[\begin{array}{l} \sin(\theta)(0.1375-0.0744\cos(\theta)-0.1869\cos^2(\theta)-0.0457\cos^3(\theta) \\ +0.1276\cos^4(\theta)+0.06404\cos^5(\theta)-0.0608\cos^6(\theta)-0.0658\cos^7(\theta) \\ -0.0220\cos^8(\theta)-0.0026\cos^9(\theta))+0.1650\theta \end{array}\right] \qquad (11.10)$$

The tangential velocity is then

$$V_H = \frac{1}{R}\frac{\partial\phi_{tot}}{\partial\theta} \qquad (11.11)$$

where $\phi_{tot}$ is the freestream potential (= $-URcos(\theta)cos(\theta_H)$) plus the perturbation potential. Evaluation yields, where $Ucos(\theta_H)sin(\theta)$ is the freestream contribution

$$V_\theta = U\cos(\theta_H)\begin{bmatrix} \sin(\theta) + 0.5115\cos(\theta) - 0.0115\cos^2(\theta) - 1.0714\cos^3(\theta) - 0.5032\cos^4(\theta) \\ +1.003\cos^5(\theta) + 0.8445\cos^6(\theta) - 0.2496\cos^7(\theta) - 0.5029\cos^8(\theta) \\ -0.1982\cos^9(\theta) - 0.026\cos^{10}(\theta) + 0.2394 \end{bmatrix} \quad (11.12)$$

### *Velocity Due to Transverse Flow: 0 < x/R < 1*

The calculation of the induced velocities due to the transverse component of the decomposed freestream is straightforward but contains a subtlety. The transverse flow induces two velocity components on the hemisphere surface: one lateral ($w_1$) and one axial ($w_2$) such that it opposes the velocity due to axial decomposition of the freestream. It is this component, $w_2$, that is responsible for the rearward movement of the attachment line stagnation point with incidence.

Using the numerical data in Fig. 11.4 gives a transverse perturbation potential of

$$\phi' = UR\sin(\theta_H)\cos(\theta_V)\begin{bmatrix} 0.7146 - 0.2789\cos(\theta) - 0.1396\cos^2(\theta) - 0.0802\cos^3(\theta) - 0.1802\cos^4(\theta) \\ +0.1363\cos^5(\theta) + 0.4177\cos^6(\theta) + 0.0194\cos^7(\theta) - 0.3272\cos^8(\theta) \\ -0.2033\cos^9(\theta) - 0.0369\cos^{10}(\theta) \end{bmatrix} \quad (11.13)$$

The lateral velocity component is found using

$$w_1 = \frac{1}{R}\frac{\partial\phi_{tot}}{\partial\theta_V} \quad (11.14)$$

where $\phi_{tot}$ is the freestream potential (= $UR\cos(\theta_V)\sin(\theta_H)\sin(\theta)$) plus the perturbation potential. Evaluation yields

$$w_1 = -U\sin(\theta_H)\sin(\theta_V)\begin{bmatrix} 0.7146 - 0.2789\cos(\theta) - 0.1396\cos^2(\theta) - 0.0802\cos^3(\theta) - 0.1802\cos^4(\theta) \\ +0.1363\cos^5(\theta) + 0.4177\cos^6(\theta) + 0.0194\cos^7(\theta) - 0.3272\cos^8(\theta) \\ -0.2033\cos^9(\theta) - 0.0369\cos^{10}(\theta) + \sin(\theta) \end{bmatrix} \quad (11.15)$$

The axial component $w_2$ is determined using

$$w_2 = \frac{1}{R}\frac{\partial\phi_{tot}}{\partial\theta} \quad (11.16)$$

Evaluation of $w_2$ gives

$$w_2 = U\sin(\theta_H)\cos(\theta_r)\begin{bmatrix} 0.2407\cos^2(\theta)\sin(\theta) + 0.7208\cos^3(\theta)\sin(\theta) - 0.6815\cos^4(\theta)\sin(\theta) \\ -2.5059\cos^5(\theta)\sin(\theta) - 0.1355\cos^6(\theta)\sin(\theta) + 0.2793\cos(\theta)\sin(\theta) \\ +0.2789\sin(\theta) + \cos(\theta) + 2.6179\cos^7(\theta)\sin(\theta) + 1.8297\cos^8(\theta)\sin(\theta) \\ +0.3698\cos^9(\theta)\sin(\theta) \end{bmatrix} \quad (11.17)$$

The surface pressure coefficient is then found using

$$C_p = 1 - \left( \frac{(V_\theta - w_2)^2 + w_1^2}{U^2} \right) \quad (11.18)$$

*Surface Velocities: $1 < x/R < 2$*

A similar procedure is used for the after-body, noting that for this region, $w_2 = \partial\phi_{tot}/\partial x$ and $V_\theta = \partial\phi_{tot}/\partial x$. The resulting expressions for the three velocity components are:

$$V_\theta = U\cos(\theta_H)\begin{bmatrix} 0.0359 + \frac{x}{R}2.4668 - (\frac{x}{R})^2 11.1589 + (\frac{x}{R})^3 32.7894 - (\frac{x}{R})^4 57.1212 \\ (\frac{x}{R})^5 58.7740 - (\frac{x}{R})^6 37.0220 + (\frac{x}{R})^7 14.4878 - (\frac{x}{R})^8 3.4418 - (\frac{x}{R})^9 0.4549 \\ -0.0257(\frac{x}{R})^{10} + 1 \end{bmatrix} \quad (11.19)$$

$$w_1 = -U\sin(\theta_H)\sin(\theta_r)\begin{bmatrix} 0.0141 + \frac{x}{R}3..0142 - (\frac{x}{R})^2 11.5727 + (\frac{x}{R})^3 30.2474 - (\frac{x}{R})^4 48.8443 \\ (\frac{x}{R})^5 50.2109 - (\frac{x}{R})^6 33.4521 + (\frac{x}{R})^7 14.3547 - (\frac{x}{R})^8 3.8209 + (\frac{x}{R})^9 0.5731 \\ -(\frac{x}{R})^{10} 0.0369 + 1 \end{bmatrix} \quad (11.20)$$

$$w_2 = U\cos(\theta_r)\sin(\theta_H)\begin{bmatrix} 3.0142 - \frac{x}{R}23.1454 + (\frac{x}{R})^2 90.7422 - (\frac{x}{R})^3 195.3772 + (\frac{x}{R})^4 251.0545 \\ -(\frac{x}{R})^5 200.7126 + (\frac{x}{R})^6 100.4829 - (\frac{x}{R})^7 30.5675 + (\frac{x}{R})^8 5.1577 \\ -(\frac{x}{R})^9 0.3698 \end{bmatrix} \quad (11.21)$$

As before, pressures on the cylinder are estimated by substituting Eqs. (11.19) - (11.21) into Eq. (11.18).
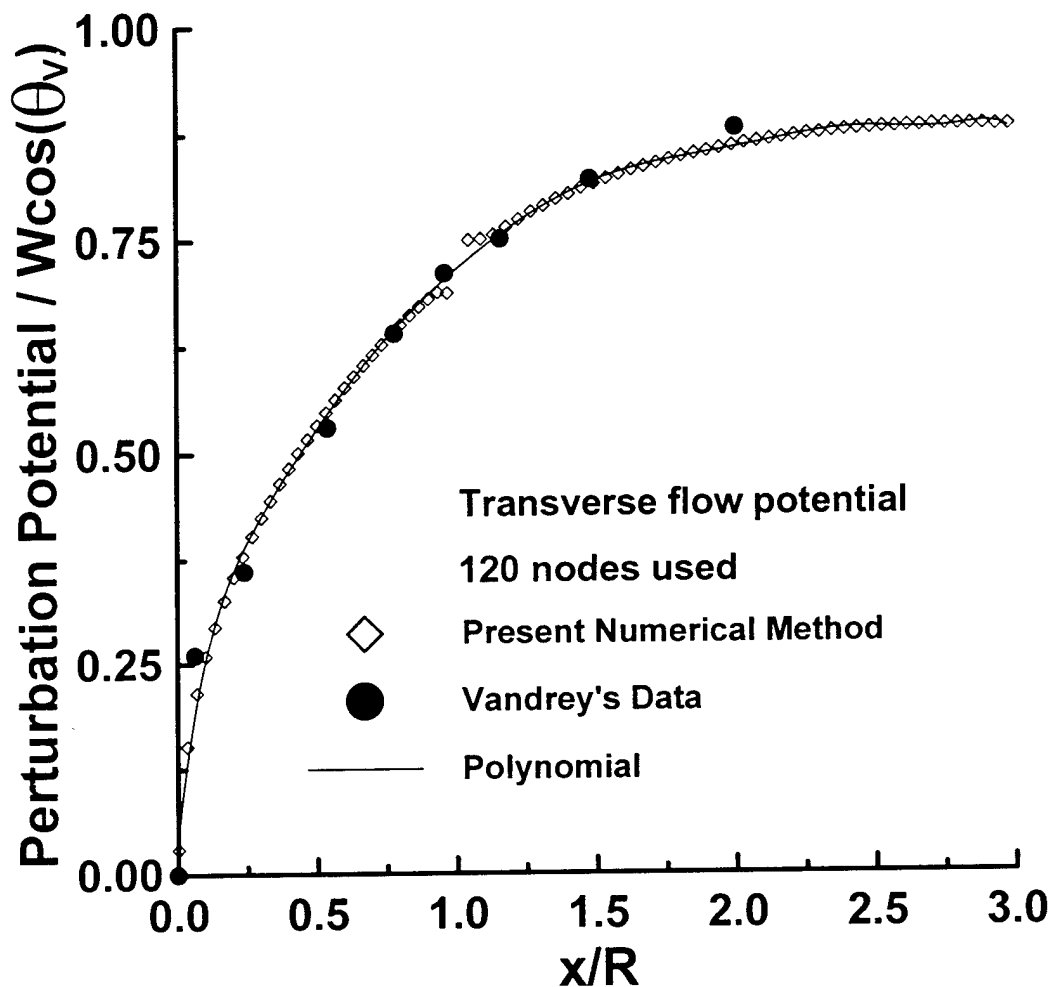
138

**Fig. 11.4. Predicted transverse perturbation potential over a H-C.**

## Experimental Equipment And Procedure

The wind tunnel model was manufactured from Aluminum. Relevant dimensions are shown in Fig. 11.5. The H-C's diameter was 1.5" (38.1mm) to accommodate the pressure tappings. The hemisphere had 25 tappings in three rows of 8 (spaced 20 deg apart) in addition to a center tap. The pressure ports were spaced at $\Delta\theta = 10$ deg intervals along the periphery of the nose. The internal diameter of the tappings was 0.01" (0.25mm). The tappings were as small as possible to minimize their effect on the flow. In order to determine the length of the H-C such that the influence of its blunt base would be minimized, numerical experiments were undertaken to determine the effect of a blunt aft portion. The simulation was conducted using the surface vortex ring method to simulate the axial flow, and a surface source ring method to simulate the transverse flow, as described above. The numerical data suggested that the effects of the cylinder base (on the hemisphere) were minimal for base locations greater than 6 cylinder diameters from the front of the model. The model was attached to a pitching mechanism to allow accurate incidence variation of the model from 0 to 45 deg. The model could be set to $\theta_H$ within 0.05 deg of the required value.
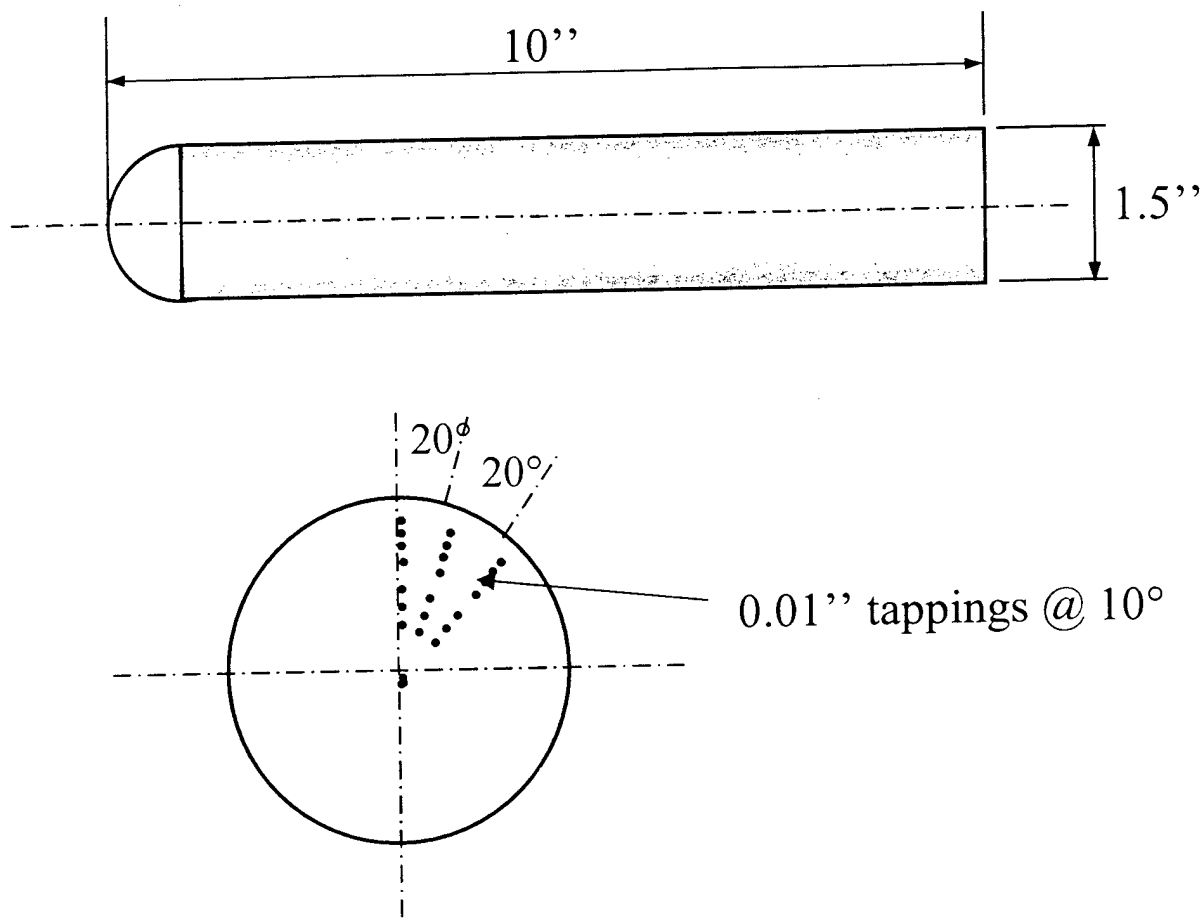
**Fig. 11.5. Wind tunnel model details.**

The tests were undertaken in the Texas A&M University 3' x 4' continuous wind tunnel at velocities of 10.4 and 20.5m/s, corresponding to Re = 26,000 and 53,000 based on the diameter of the H-C. At these velocities the turbulence intensity is typically < 0.3%. The wind tunnel jet velocity uniformity is typically within 0.1%. The tunnel has active cooling and is normally maintained at 20 °C for the duration of a run.

Pressures were recorded using an ESP 32-port electronic pressure scanner with a range of ±2500 Pa. The signals from the ESP were digitized using a 12-bit A/D board giving a resolution of ±0.24% of full scale. The A/D's sampling frequency was 2kHz. The ESP was monitored using a factory calibrated Air Neotronics digital micro-manometer with a resolution of 0.1 Pa. Before each test, the ESP was recalibrated to reduce errors. Repeated data runs yielded an estimated uncertainty of the data of 0.3% of full scale for a 95% (2σ) confidence interval. During the testing, after the model was pitched to a new incidence, approximately 10-15s was allowed to elapse to allow the pressures to reach their steady-state values. The model was pitched through 0, 15, 30 and 45 deg. At each $\theta_H$, the ESP was sampled 200 times and averaged. No corrections to account for wall effects, i.e. solid and wake blockage, were applied to the data, as a large

majority of the test cases would encompass significant extents of separated flow making accurate application of corrections uncertain. Furthermore, for the worst case scenario, $\theta_H = 45$ deg, the combined blockage of the model and mount is less than 1.4% suggesting that wall effects would be negligible.

## Comparisons With Theory

Predictions of the surface pressure coefficient measured over a hemisphere cylinder at zero incidence using Landwebers method and Eq. (11.18) are shown in Fig. 11.6. Agreement with the present experimental data is seen to be good. Also included in the figure is the potential solution for the flow over a sphere (= $1-9/4\sin^2(\theta)$) as well as an empirical modification to this formula to account for the effect of the cylinder on the hemisphere (= $1-2.07\sin^2(\theta)$). As noted prior, for $\theta = \pm 15$ deg, the presence of the cylinder has a negligible effect on the hemisphere surface pressure. For greater x/R, the cylinder acts as a downstream source, retarding the surface velocities thus causing comparatively higher surface pressures. The empirical relation is seen to accurately estimate the surface pressures over the forward $\theta = 55$ deg of the hemisphere.
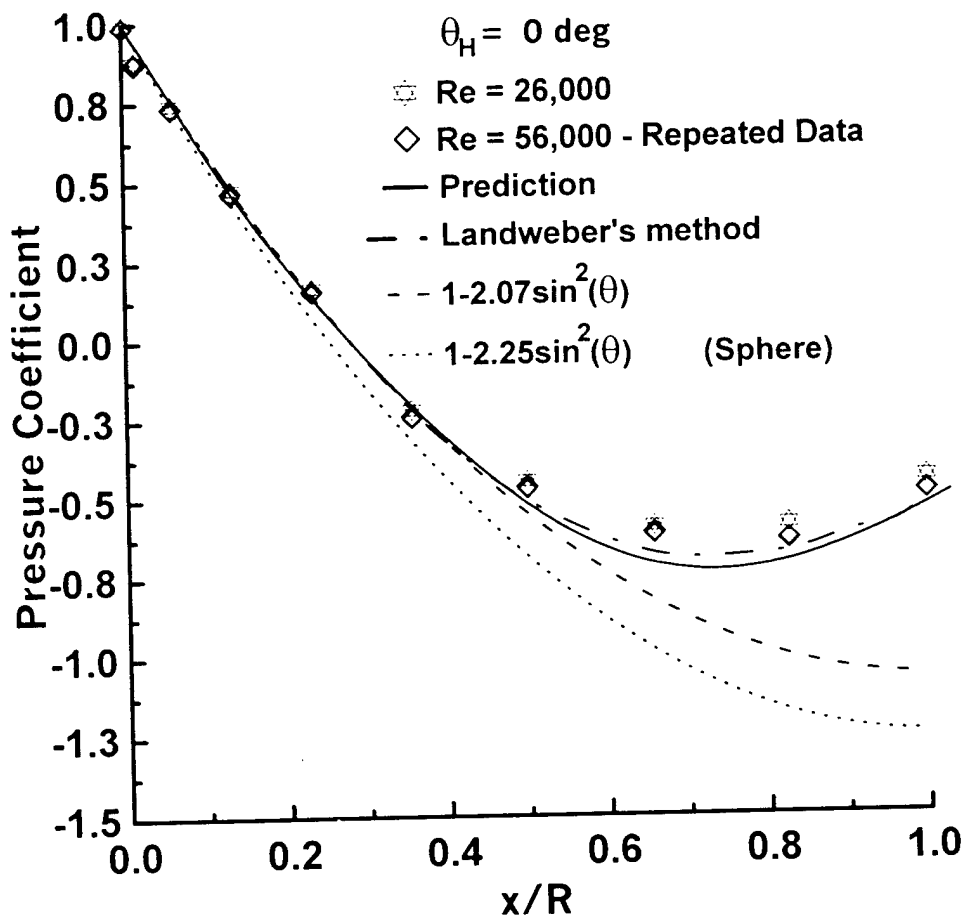


Fig. 11.6. Predicted surface pressure coefficient over a H-C, $\theta_H = 0$ deg. Present experimental data.

141

Hoang performed a comprehensive study on the behavior of a H-C at incidence. His data included surface pressure, surface flow topology, as well as Hot Wire and LDV measurements. Consequently, Hoang's data (Re= 42,000), in addition to the present experimental effort, will be used for prediction validation. To correctly evaluate the potential of the present expression, it is necessary to know its natural limitations following from the unique inherent viscous characteristics of a H-C. Consequently, these characteristics/flow behaviors will be discussed briefly although touched upon in the introduction. At the Re range of the experimental data included in this study, the surface flow displays a marked and systematic variation with $\theta_H$ as elucidated by Hoang. At zero incidence, surface skin friction patterns indicate the existence of an axisymmetrical closed separation bubble (as mentioned prior) propagating from the H-C juncture. Incidence causes an asymmetry of this bubble with a leeward displacement of the separation borders. Increasing $\theta_H$ to 10 deg sees the formation of two horn vortices (representing unstable foci) from the upper lateral edges of the bubble at $\theta_V \approx \pm 130$ deg. Two symmetric cross flow separation lines are also apparent on the cylinder at this incidence and indicate the possible existence of leeward vortices. These separation lines are clearly distinct from the horn vortices and originate approximately 2R aft of the horn vortices. Increasing incidence shows a leeward displacement of the separation region located at the hemisphere-cylinder juncture. Skin friction patterns from Hoang[1] are reproduced in Fig. 11.7b-11.7c representing the H-C at $\theta_H = 20$ deg, as this is the incidence of most of the data comparisons presented in this study. A summary of the surface flow features is also presented, Fig. 7a. The cross flow separation line is clearly seen running along the side edge of the cylinder. This separation point is seen to move progressively windward with increasing x/R. A trace of the surfaces pressures experienced along a skin friction line originating from x/R = 1, $\theta_V = 0$ deg and x/R = 5, $\theta_V = 0$ showed that the movement of this separation line to smaller $\theta_V$ (i.e. windward) with increasing x/R is not due to a more favorable pressure distribution downstream (the large x/R pressure distributions are more favorable). The trajectory of this separation line is thus probably due to the increasing boundary layer thickness downstream increasing the tendency for separation. Two darker lines running over the top of the H-C are identified as vortex induced separation lines, suggesting the presence of two vortices per side, a primary and secondary separation vortex. The primary vortex causes the secondary flow separation. Vortex induced pressure gradients convect fluid laterally outwards under the primary vortex core, such that the fluid encounters an adverse pressure gradient which causes the boundary layer to separate. The ensuing free shear layer rolls-up and forms a vortex of opposite rotation (to the primary). The skin friction lines emanating from the attachment line are seen to progressively reduce in inclination relative to the body, see Fig. 11.7c, and at x/R > 4.8 they are inclined at 40 deg to the freestream. This condition corresponds to Munk's (Munk, 1923) "$2\alpha$" type of flow (where local lift development assuming no flow separation is proportional to $2\alpha$; here, $\theta_H = \alpha$) and suggests that over this region of the H-C, the flow is essentially inviscid. Fig. 11.7d shows a sketch, proposed by Maskell (Maskell, 1955), showing a 3D representation of the off surface flow features detailed above.

Hoang's skin friction data indicate that the vortex induced flow separation lines (associated with the leeward vortices) gradually approach the horn vortices and at $\theta_H \approx 25$ deg these flow features connect. The cross flow separation lines also gradually move towards larger $\theta_V$ values (the back of the cylinder) with incidence as the axial surface flow component reduces relative to the transverse (effectively increasing the cross flow Re number). Beyond about 33 deg incidence, the presence of the horn vortices cannot be established.

Leeward vortex side wash pattern — **(a)** — Attached axial flow region

Vortex induced flow separation line — **(b)** — Horn vortex

Cross flow separation line — **(c)**
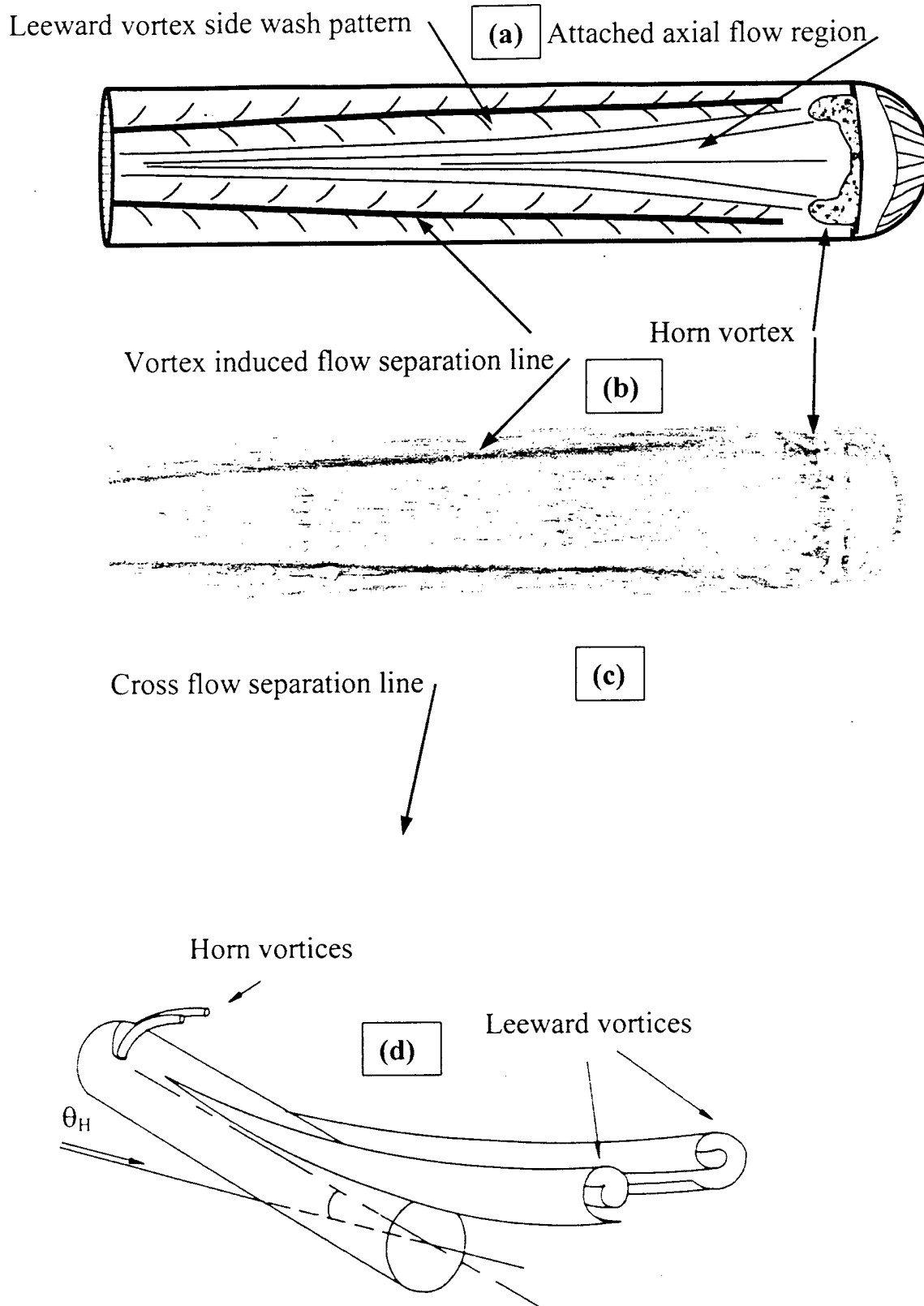
Horn vortices — **(d)** — Leeward vortices

$\theta_H$

Fig. 11.7. Flow patterns over a H-C, $\theta_H = 20$ deg: (a) Skin friction pattern summary, (b) Surface skin friction patterns, top view, (c) Surface skin friction patterns, side view, (d) Three dimensional off-surface flow reprasentation.

Theoretical and experimental comparisons for a H-C at 20 deg incidence (= $\theta_H$) are presented in Figs. 11.8-11.17. Values for $\theta_V$ from 0 to 180 in 20 deg increments are presented to clearly demonstrate the accuracy of the predictions (i.e. Eq. (11.18)) as the flow develops. Figure 8 shows predictions of the surface pressure coefficient along the attachment line. Good agreement over the forward envelope of the cylinder is seen. The minimum recorded pressures are somewhat under-predicted. The pressure recovery region is relatively well captured. Downstream pressures on the cylinder (x/R > 1.5) are well approximated. Notice that although the location of the minimum pressure region is predicted slightly too far aft, the form of the theoretical distribution, with a sharp pressure recovery following the suction peak, is representative.
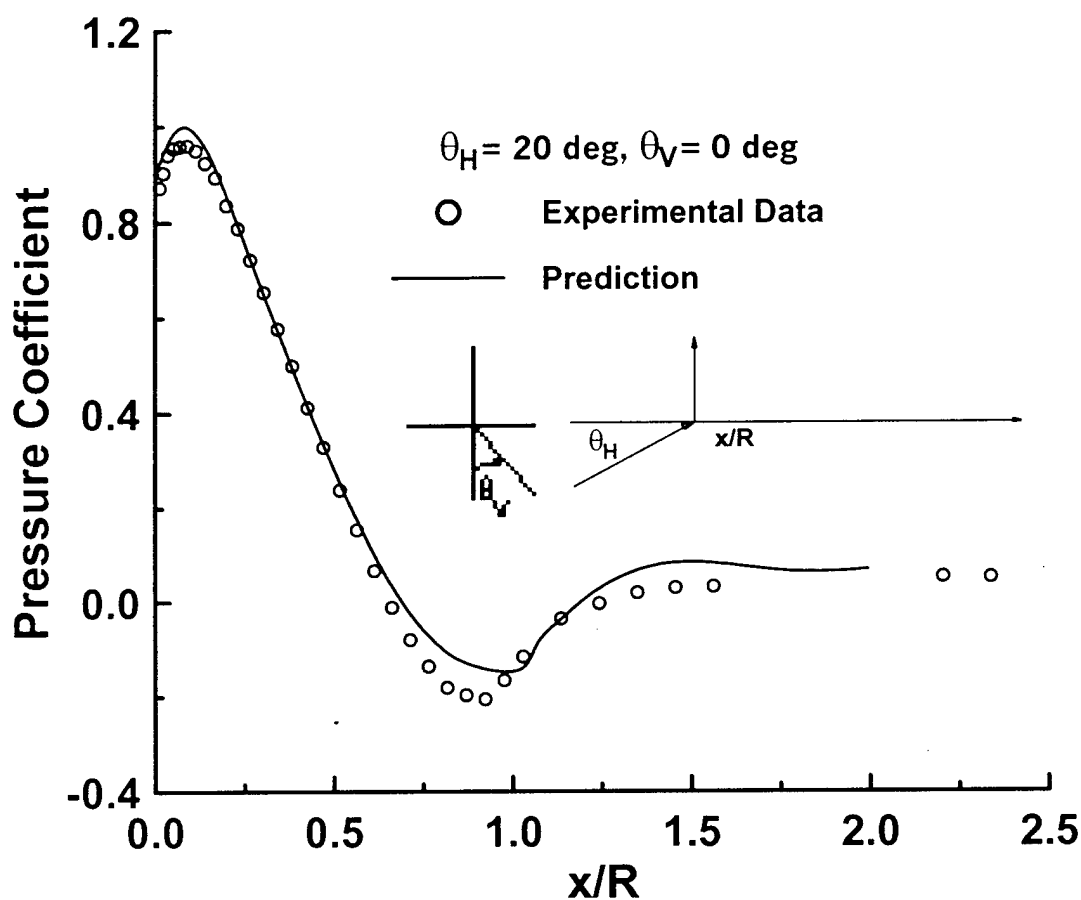


Fig. 11.8. Comparison of predicted (Eq. (11.18)) and experimental pressure coefficients over a H-C, $\theta_H$ = 20 deg, $\theta_V$ = 0 deg. Experimental data from Hoang.

Similar trends are seen in Figure 9 ($\theta_V$ = 20 deg). Increasing $\theta_V$ to 40 deg, Fig. 11.10, shows an over-prediction and under-prediction respectively of the maximum and minimum measured pressures, although the general form of the pressure distribution is well captured as are the after-body pressures. $\theta_V$ = 60 deg shows similar characteristics, see Fig. 11.11. Increasing $\theta_V$

144

beyond 60 deg, Fig. 11.12, shows good correlation of predicted pressures with experiment, except for small x/R where pressures are over-predicted. Pressures on the cylinder after-body are well captured. Also note that the x/R location of the minimum pressure is more accurately captured than for lower $\theta_V$, where the predicted minimum pressures are further aft than that of the experiment data. Increasing $\theta_V$ shows increasing dominance of the cross flow $w_1$ velocity term ($\propto \sin(\theta_V)$) and a reduction in the $w_2$ ($\propto \cos(\theta_V)$) term which opposes $V_\theta$.
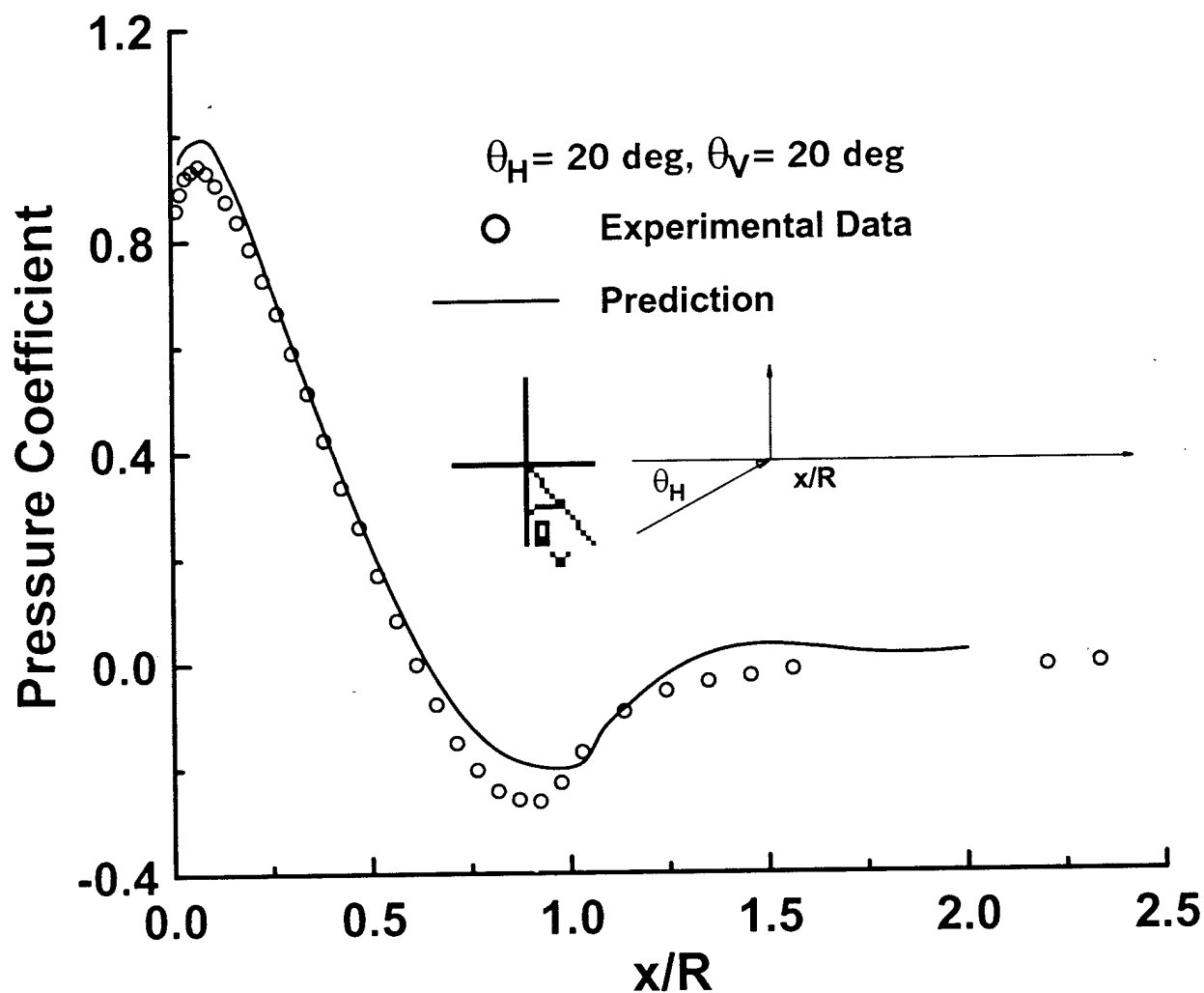


Fig. 11.9. Comparison of predicted (Eq. (11.18)) and experimental pressure coefficients over a H-C, $\theta_H$ = 20 deg, $\theta_V$ = 20 deg. Experimental data from Hoang.
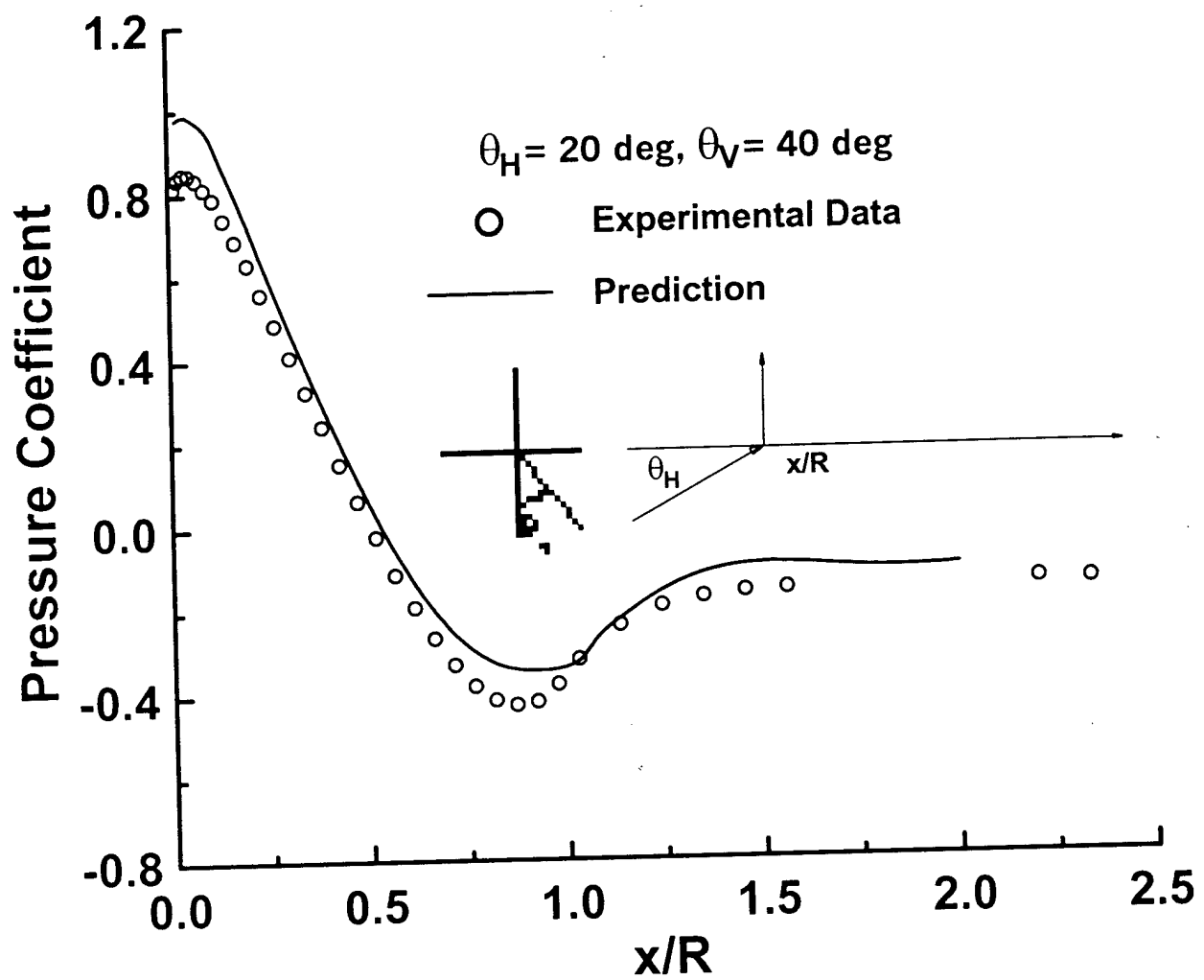
Fig. 11.10. Comparison of predicted (Eq. (11.18)) and experimental pressure coefficients over a H-C, $\theta_H = 20$ deg, $\theta_V = 40$ deg. Experimental data from Hoang.
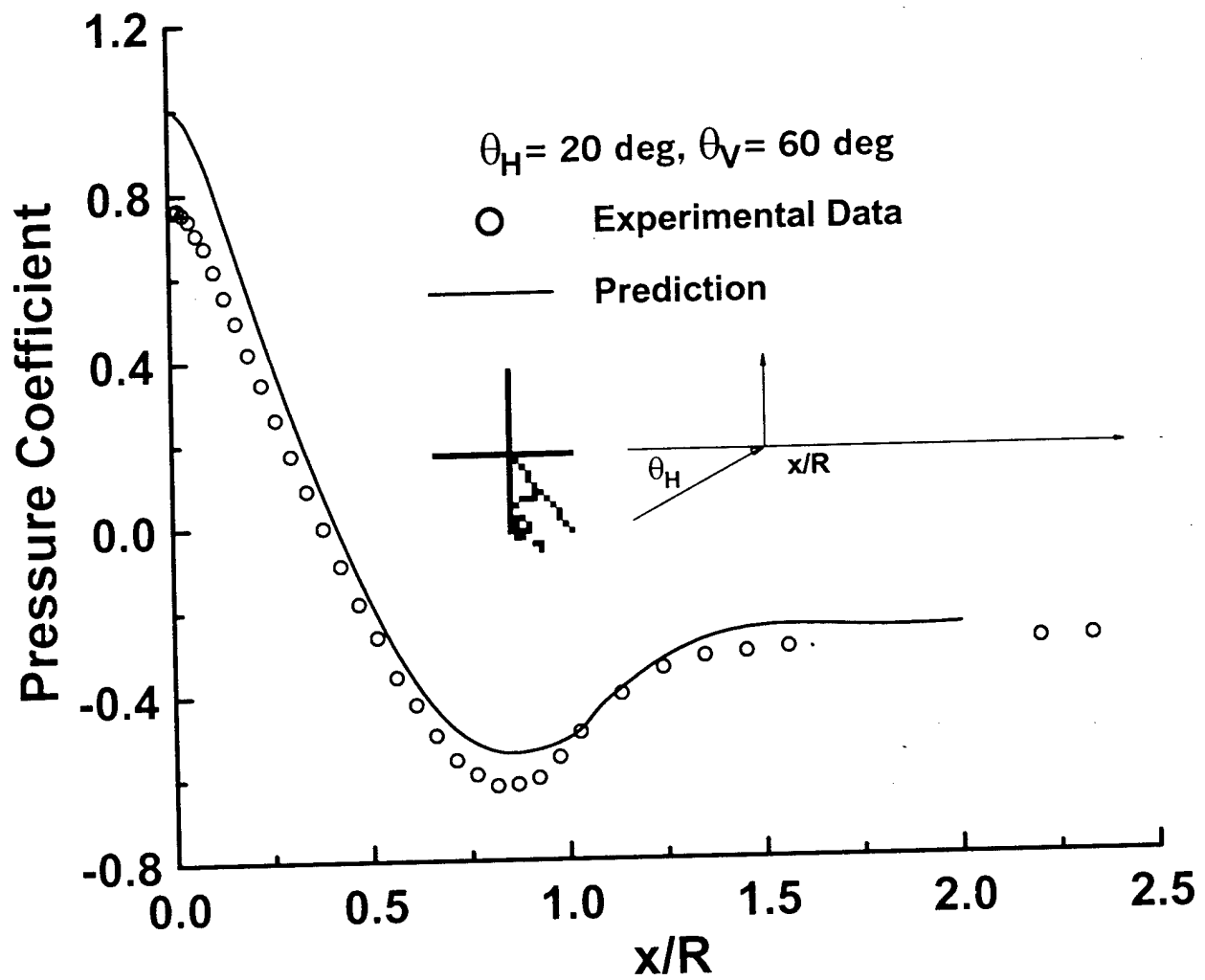
Fig. 11.11. Comparison of predicted (Eq. (11.18)) and experimental pressure coefficients over a H-C, $\theta_H$ = 20 deg, $\theta_V$ = 60 deg. Experimental data from Hoang.
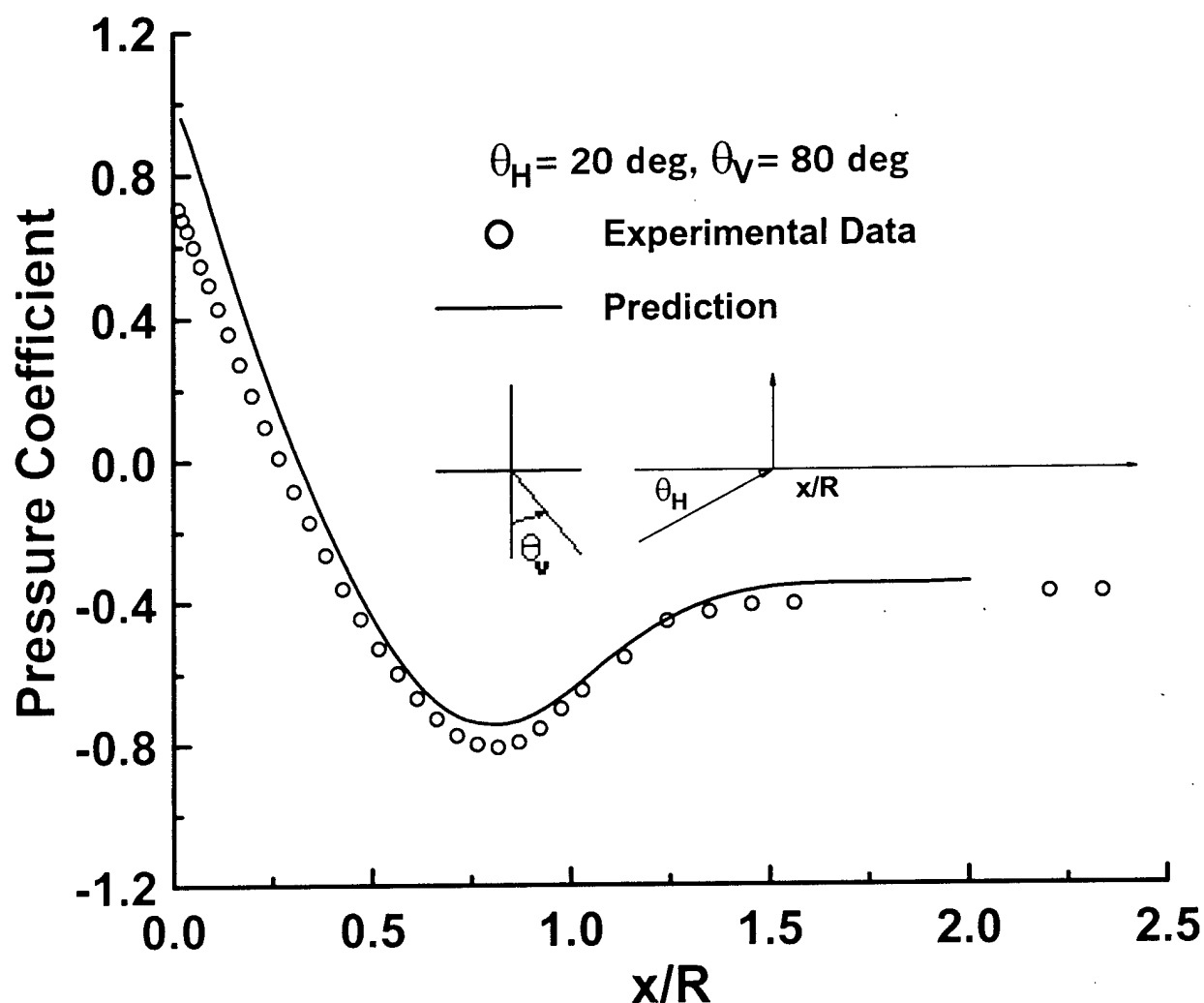
Fig. 11.12. Comparison of predicted (Eq. (11.18)) and experimental pressure coefficients over a H-C, $\theta_H$ = 20 deg, $\theta_V$ = 80 deg. Experimental data from Hoang.

For $\theta_V$ > 90 deg, the experimental data shows evidence of separation effects (x/R ≈ 1.25, see Fig. 11.13), with Hoang's data indicating the presence of a closed separation bubble laterally terminating in two "horn" vortices, see Fig. 11.7. These flow effects are viscous in origin, and could not be captured by the present inviscid method. The form of the pressure distribution, i.e. flat, between 1.25< x/R < 1.6 is clearly that of a closed separation bubble (despite the horn vortices). However, for $\theta_V$ ≤ 140 deg, pressures over the forward region of the hemisphere as well as the minimum pressure region are well estimated (Figs. 11.13-11.15) as are the final after-body pressures. Examination of Figs. 11.8-11.15 indicates that Eq. (11.18) describes the changing form of the pressure recovery region well, from a sharp initial recovery following the point of minimum pressure for small $\theta_V$, see Figs. 8-10, to a milder recovery (Figs. 11.11-11.15) for larger $\theta_V$.
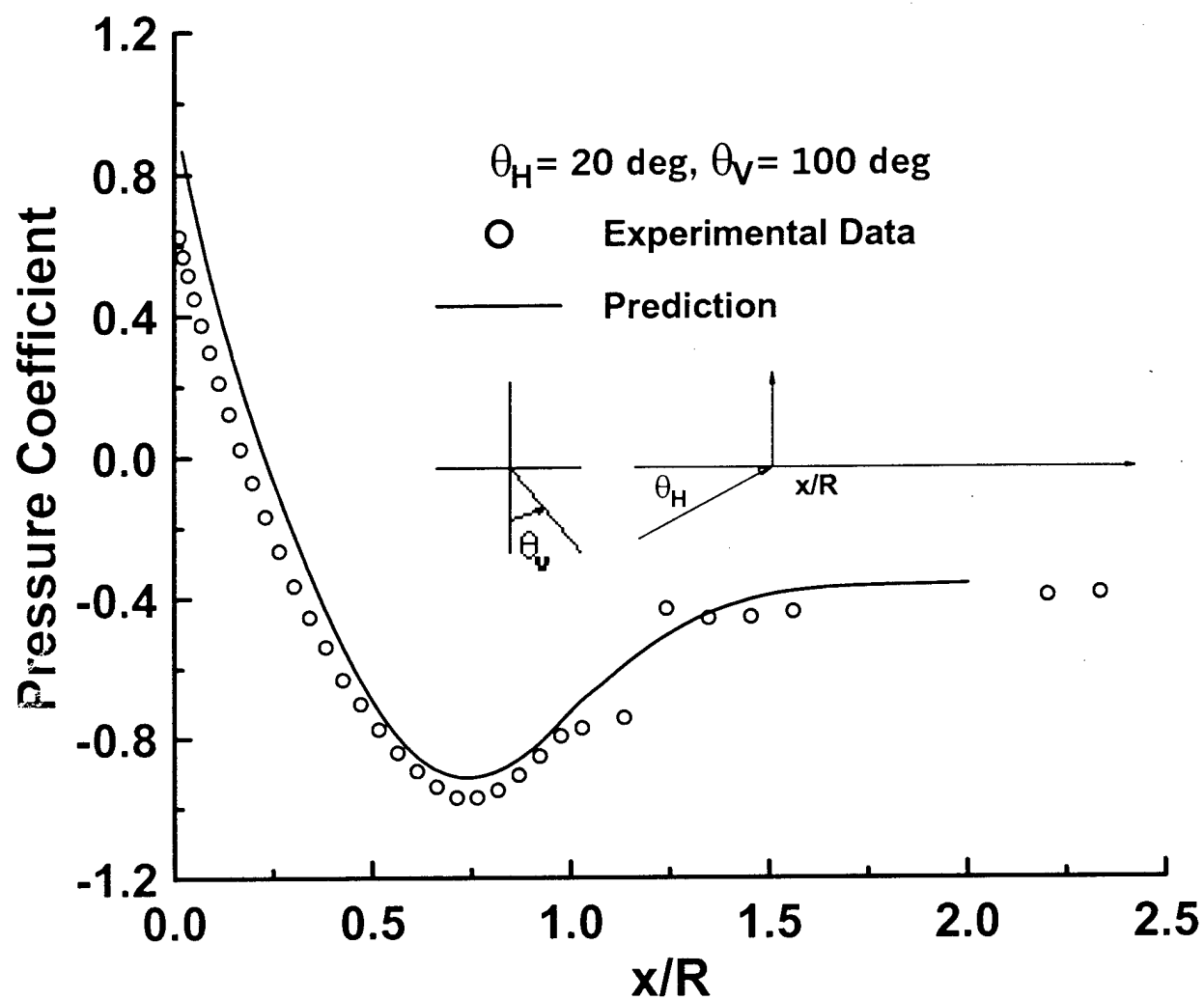
Fig. 11.13. Comparison of predicted (Eq. (11.18)) and experimental pressure coefficients over a H-C, $\theta_H = 20$ deg, $\theta_V = 100$ deg. Experimental data from Hoang.

Fig. 11.14. Comparison of predicted (Eq. (11.18)) and experimental pressure coefficients over a H-C, $\theta_H$ = 20 deg, $\theta_V$ = 120 deg. Experimental data from Hoang.
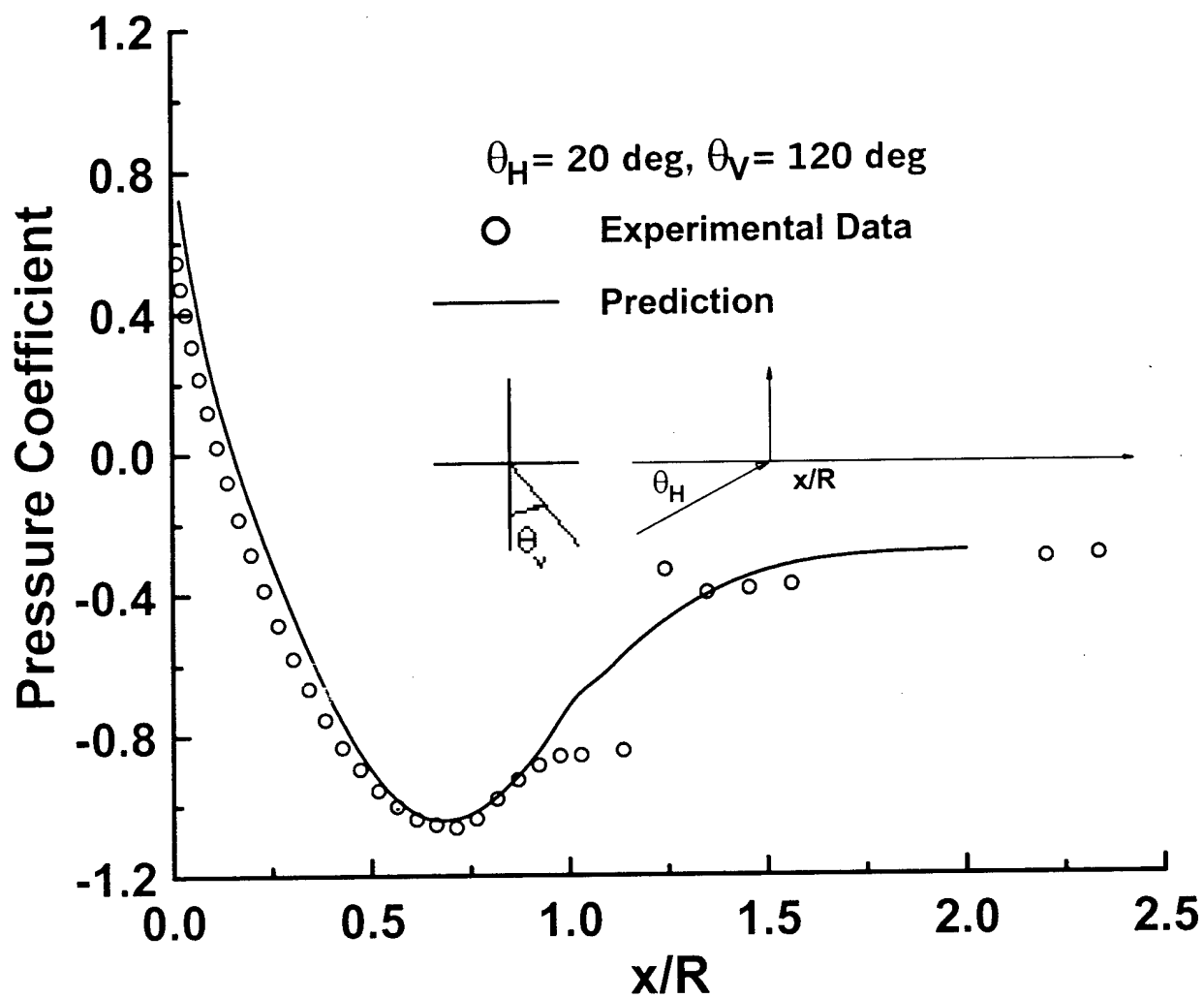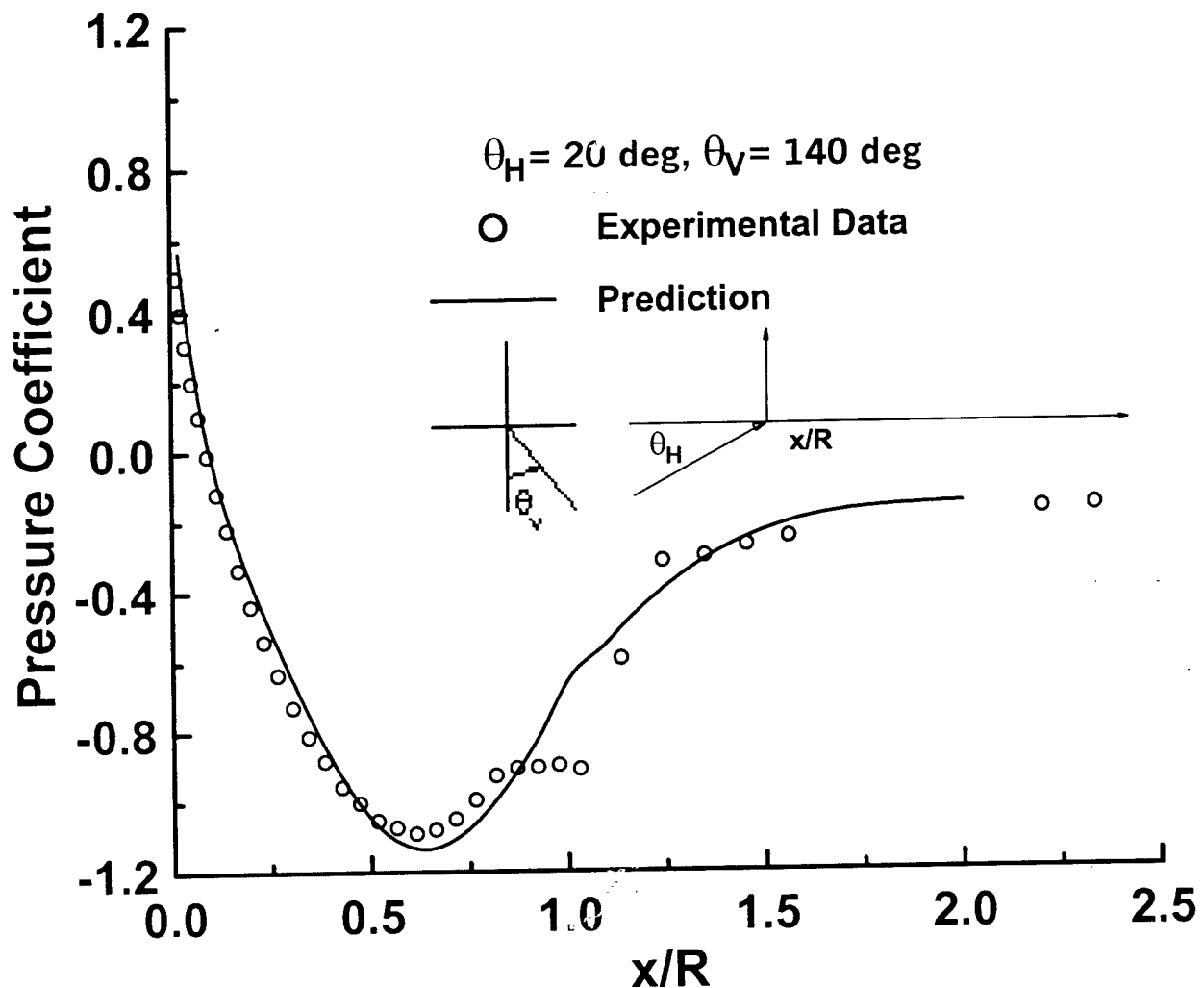
Fig. 11.15. Comparison of predicted (Eq. (11.18)) and experimental pressure coefficients over a H-C, $\theta_H$ = 20 deg, $\theta_V$ = 140 deg. Experimental data from Hoang.

For $\theta_V$ = 160 and 180 deg (Figs. 11.16 and 11.17) pressures over the forward portion of the hemisphere are still well captured ($\theta$ < 55 deg). Interestingly, pressures over the cylinder are well estimated despite the presence of separated flow. This is probably due to the mutual downwash from the leeward vortices creating a region of attached flow between them, which is approximately potential, as is also seen in delta wings at moderate angles of attack.
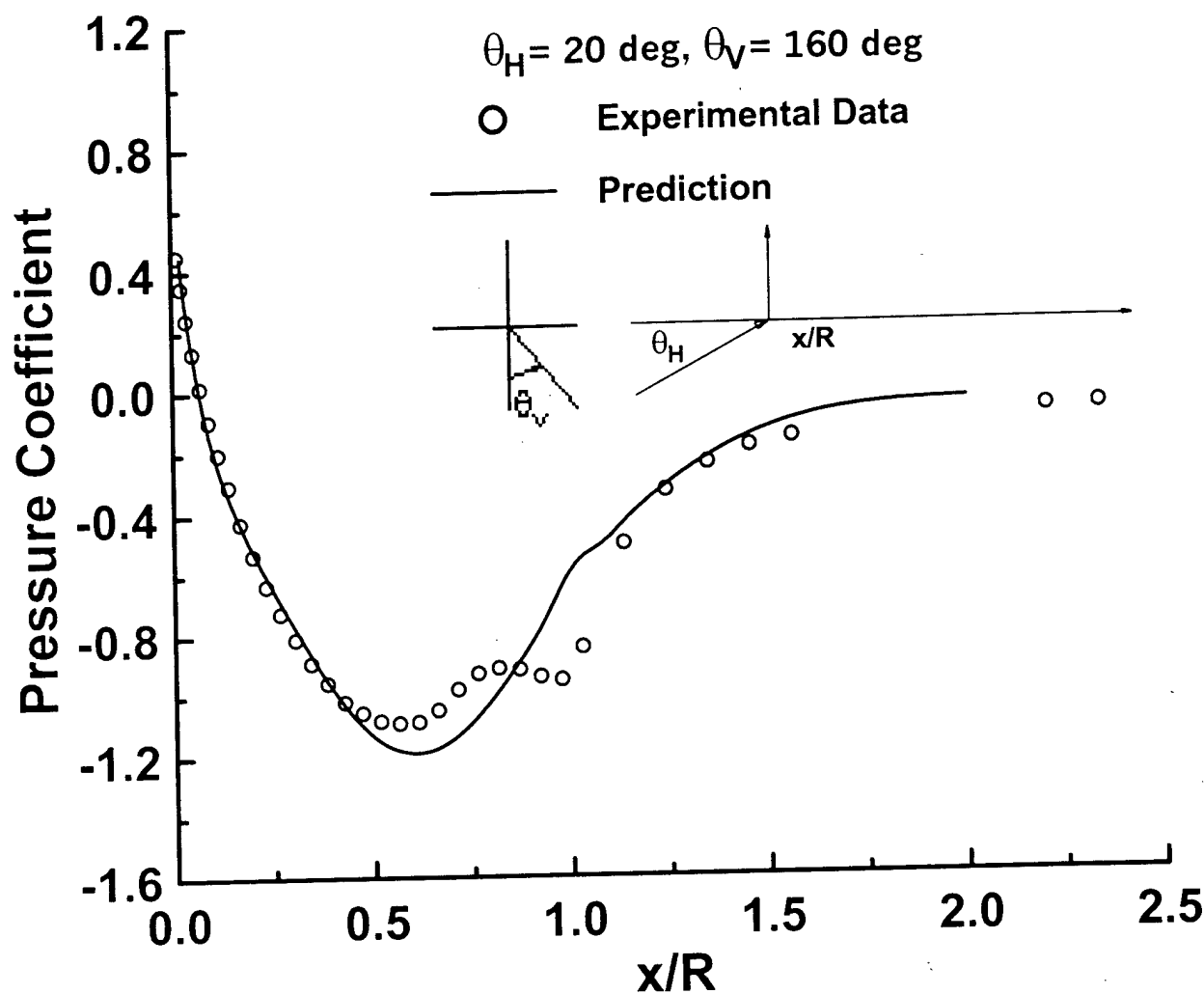
Fig. 11.16. Comparison of predicted (Eq. (11.18)) and experimental pressure coefficients over a H-C, $\theta_H$ = 20 deg, $\theta_V$ = 160 deg. Experimental data from Hoang.

It is instructive to explicitly investigate the ability of the theory to predict pressure as a function of $\theta_V$ at a particular axial location. This data is presented in Fig. 11.18 along with data from Hoang. The predictions faithfully capture the magnitude and dependence of the pressure coefficient on $\theta_V$ although accuracy improves for larger x/R. Comparisons of the method with the current experimental data at higher incidence, $\theta_H$ = 30 and 45 deg are presented in Figs. 11.19 and 11.20. Even at these extreme incidences, close accord is demonstrated for moderate $\theta_V$ (< 40 deg).

The experimental data used for comparison in this study was acquired at relatively low Re number, which may cast doubt as to the validity of the comparisons at higher Re. However, the theoretical development is inviscid and thus would be representative for higher Re flows.
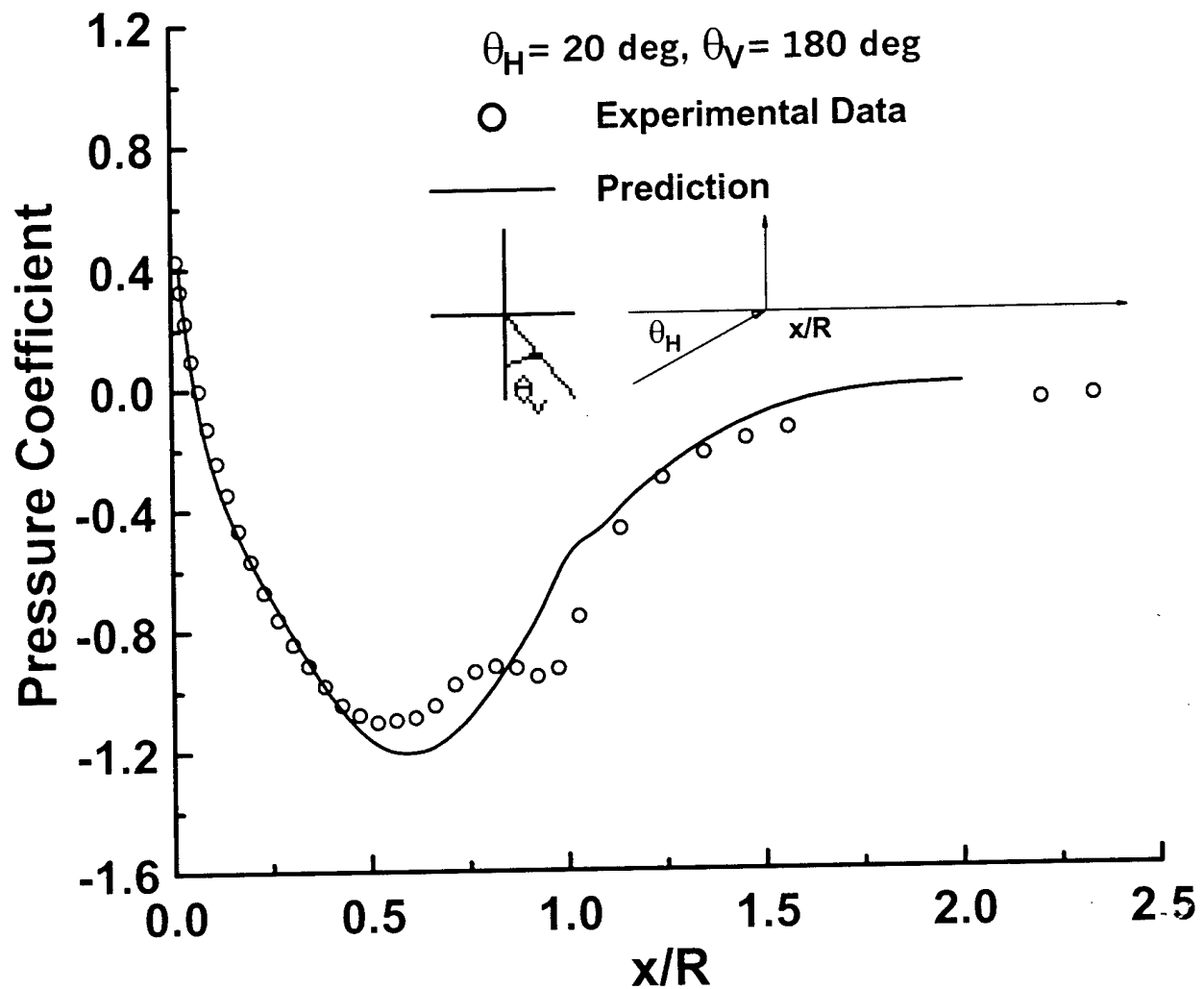
Fig. 11.17. Comparison of predicted (Eq. (11.18)) and experimental pressure coefficients over a H-C, $\theta_H$ = 20 deg, $\theta_V$ = 180 deg. Experimental data from Hoang.

In summary, a potential flow based equation was developed to estimate the surface pressures over a hemisphere cylinder. The expression used least square regression curve fits of numerically generated axial and transverse perturbation potentials. These potentials were calculated using surface singularity methods. Numerous comparisons of surface pressure estimates using the resulting expression with experimental data are presented. The equation showed the ability to closely predict incidence effects on pressure around the hemisphere cylinder's surface.

Fig. 11.18. Effect of $\theta_V$ on predicted (Eq. (11.18)) and experimental surface pressure coefficients, $\theta_H = 20$ deg. Experimental data from Hoang.

Fig. 11.19 Effect of $\theta_V$ on predicted (Eq. (11.18)) and experimental surface pressure coefficients, $\theta_H$= 30 deg. Present experimental data.
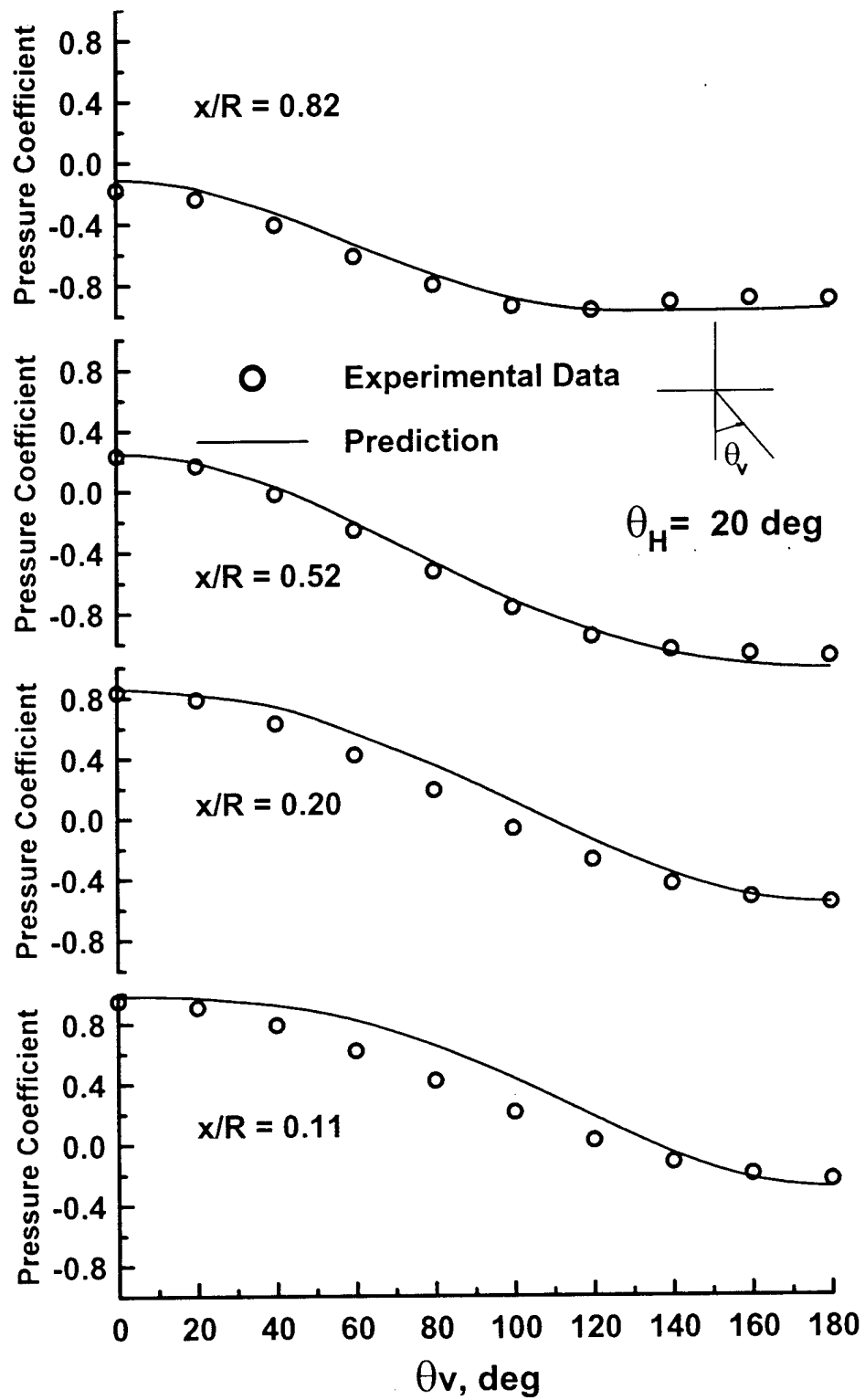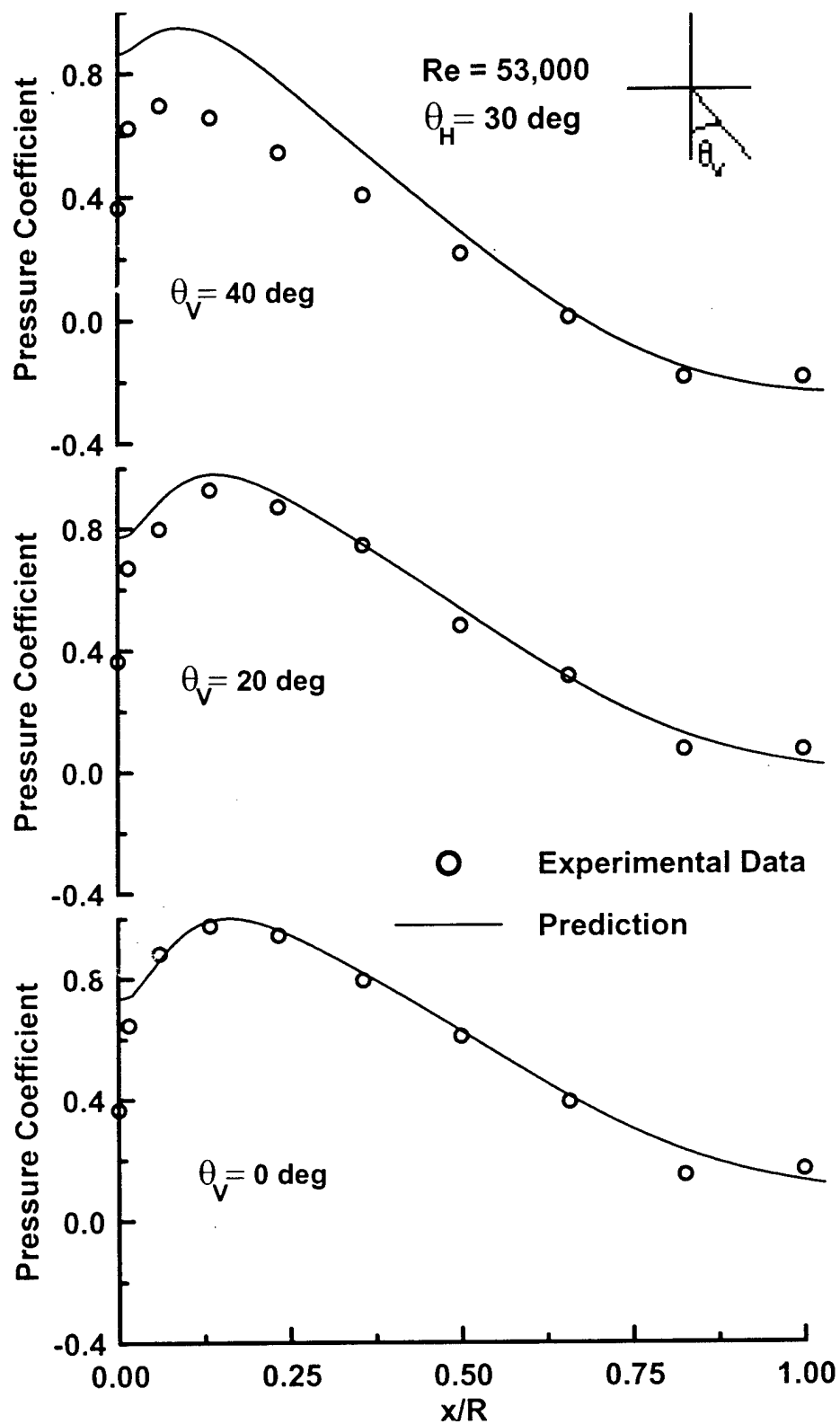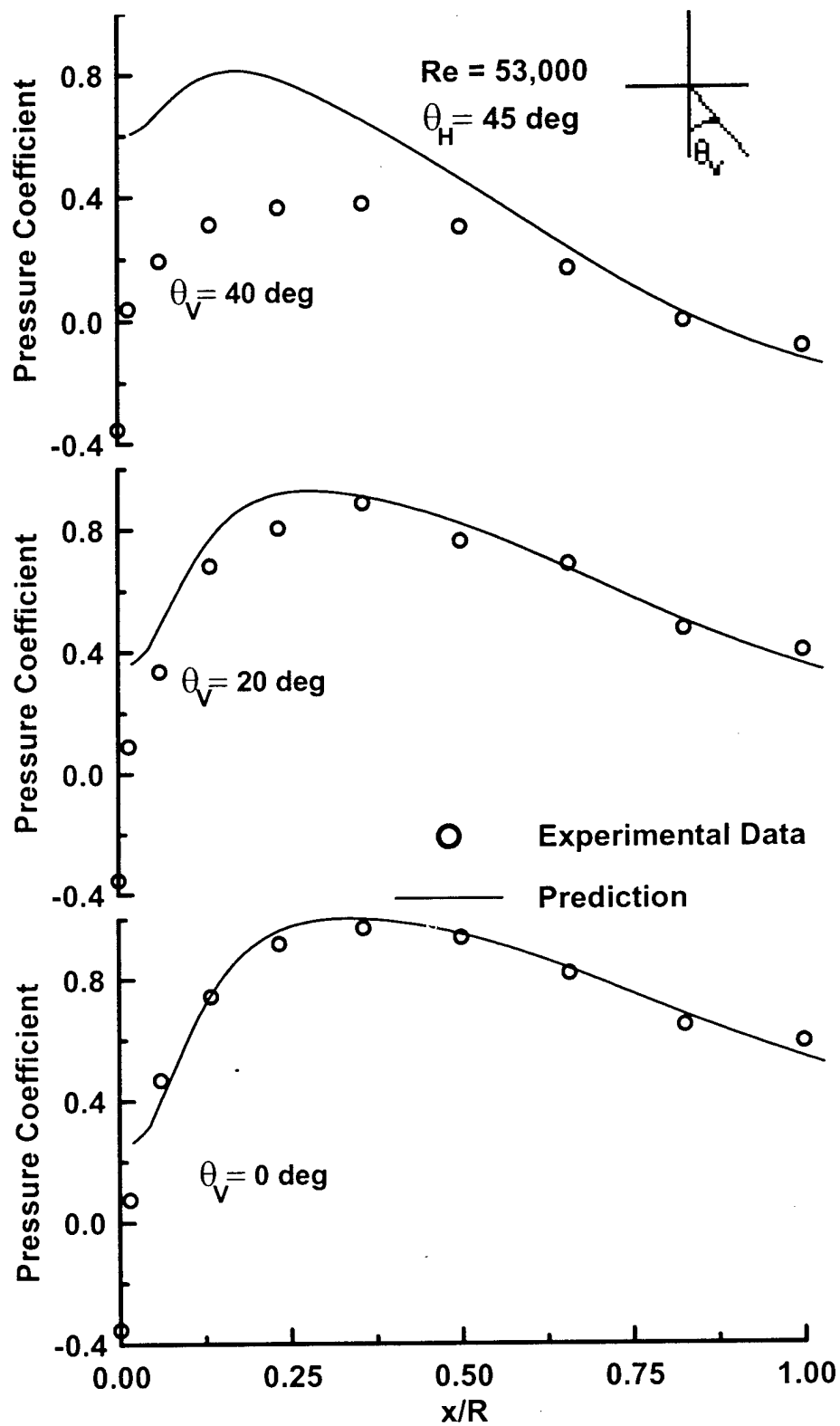
Fig. 11.20. Effect of $\theta_V$ on predicted (Eq. (11.18)) and experimental surface pressure coefficients, $\theta_H$= 45 deg. Present experimental data.

# 12. METHODOLOGY TO DETERMINE EXPERIMENTALLY THE POTENTIAL OF A HEMISPHERE CYLINDER RESULTING FROM ERRORS IN MANUFACTURING

## Nomenclature

$C_P$  = pressure coefficient
$p_i$  = static pressure at port i
$R$  = hemisphere radius
$t$  = time
$U$  = freestream
$V_\theta$  = tangential velocity
$V_i$  = total velocity at port i
$W$  = transverse velocity
$w_1$  = lateral velocity
$w_2$  = axial velocity
$x,y,z$  = cartesian coordinates, origin at hemisphere nose
$x',y,z$  = cartesian coordinates, origin at hemisphere-cylinder juncture
$\phi'$  = perturbation potential
$\phi$  = potential
$\theta_H$  = hemisphere cylinder incidence angle
$\theta_V$  = angle to the point of interest measured from the attachment line
$\theta$  = spherical coordinate angle, measured from nose of hemisphere

## Experimental Determination of $\phi$

The potential cannot be measured directly, but it can be determined from the surface pressures, and in turn the surface velocities (as $\bar{V} = \bar{\nabla}\phi$), for specific orientations of the probe. The axial potential is a function of U, R, $\theta_H$ and $\theta$ while the transverse potential is a function of U, R, $\theta_H$, $\theta_V$ and $\theta$. The total potential is composed of two components, an axial and a transverse component. As Laplace's equation is linear, these components can be added to yield the total potential. Suitable orientation of the probe in a steady freestream should allow determination of the 2 potential components.

## Velocity and Potential due to Axial Flow: $0 < x/R < 1$

Figure 12.1 shows the variables used in the present development. For utility, the formulation uses the position variable $\theta$ for location over the hemisphere body (rather than x/R). A least squares curve fit of the perturbation potential in Fig. 12.2 (left) yields, using x/R=1-cos($\theta$) with x'=x-R (after some manipulation):

$$\phi' = UR\cos(\theta_H)\left[\begin{array}{l}\sin(\theta)(0.1375 - 0.0744\cos(\theta) - 0.1869\cos^2(\theta) - 0.0457\cos^3(\theta) \\ + 0.1276\cos^4(\theta) + 0.06404\cos^5(\theta) - 0.0608\cos^6(\theta) - 0.0658\cos^7(\theta) \\ - 0.0220\cos^8(\theta) - 0.0026\cos^9(\theta)) + 0.1650\theta - 0.59\end{array}\right] \quad (12.1)$$

$$\tilde{\phi}_{tot-axial} = k_{axial}UR\cos(\theta_H)\left[\begin{array}{l}\sin(\theta)(0.1375 - 0.0744\cos(\theta) - 0.1869\cos^2(\theta) - 0.0457\cos^3(\theta) \\ + 0.1276\cos^4(\theta) + 0.06404\cos^5(\theta) - 0.0608\cos^6(\theta) - 0.0658\cos^7(\theta) \\ - 0.0220\cos^8(\theta) - 0.0026\cos^9(\theta)) + 0.1650\theta - \cos(\theta) - 0.59\end{array}\right] \quad (12.2)$$



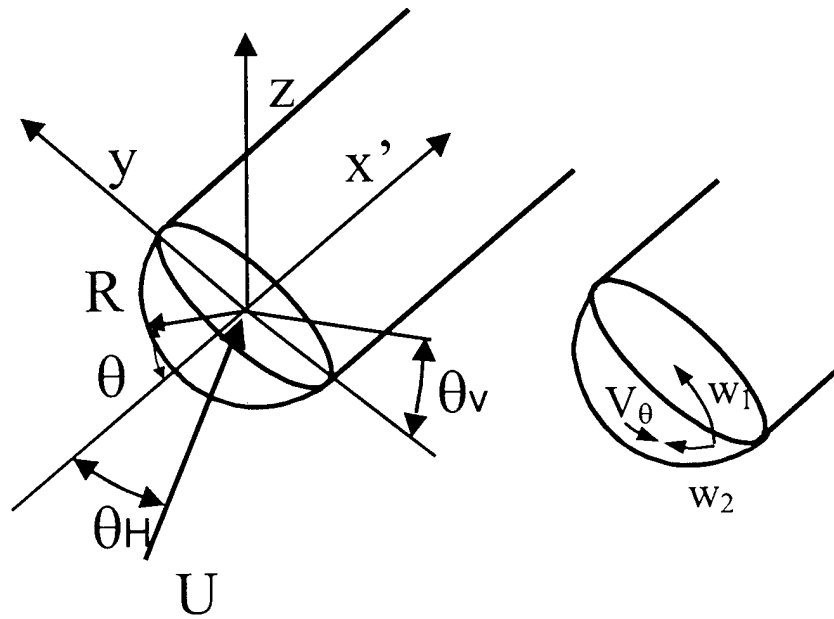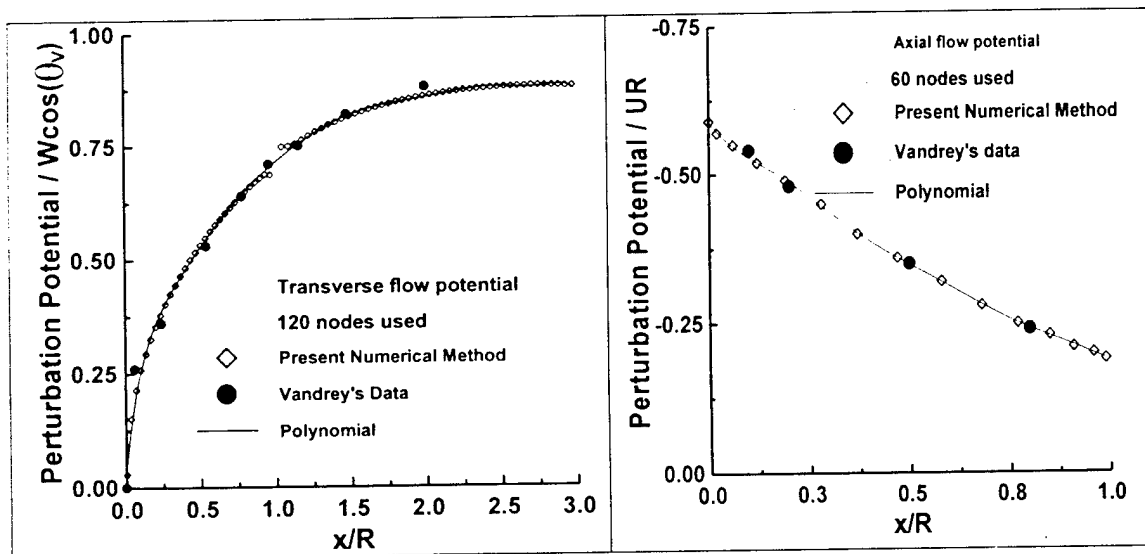**Fig. 12.1. Variable definitions.**



**Fig. 12.2. Axial (left) and transverse (right) potentials.**

158

Equation (12.2) includes the free stream contribution (= -URcos($\theta$)cos($\theta_H$)). It is assumed in Eq. (12.2) that errors in the potential are due to geometry, and hence scale linearly with dimension. As such, a correction constant for this component $k_{axial}$ is included. The tangential velocity is then

$$V_\theta = \frac{1}{R}\frac{\partial \widetilde{\phi}_{tot-axial}}{\partial \theta} \tag{12.3}$$

Evaluation yields, where Ucos($\theta_H$)sin($\theta$) is the freestream contribution

$$V_\theta = k_{axial}U\cos(\theta_H)\begin{bmatrix} \sin(\theta)+0.5115\cos(\theta)-0.0115\cos^2(\theta)-1.0714\cos^3(\theta)-0.5032\cos^4(\theta) \\ +1.003\cos^5(\theta)+0.8445\cos^6(\theta)-0.2496\cos^7(\theta)-0.5029\cos^8(\theta) \\ -0.1982\cos^9(\theta)-0.026\cos^{10}(\theta)+0.2394 \end{bmatrix} \tag{12.4}$$

*Velocity Due to Transverse Flow: 0 < x/R < 1*

The calculation of the induced velocities due to the transverse component of the decomposed freestream is straightforward but contains a subtlety. The transverse flow induces two velocity components on the hemisphere surface: one lateral ($w_1$) and one axial ($w_2$) such that it opposes the velocity due to axial decomposition of the freestream. It is this component, $w_2$, that is responsible for the rearward movement of the attachment line stagnation point with incidence. Using the numerical data in Fig. 12.3 gives a transverse perturbation potential of

$$\phi'=URsin(\theta_H)\cos(\theta_v)\begin{bmatrix} 0.7146-0.2789\cos(\theta)-0.1396\cos^2(\theta)-0.0802\cos^3(\theta)-0.1802\cos^4(\theta) \\ +0.1363\cos^5(\theta)+0.4177\cos^6(\theta)+0.0194\cos^7(\theta)-0.3272\cos^8(\theta) \\ -0.2033\cos^9(\theta)-0.0369\cos^{10}(\theta) \end{bmatrix} \tag{12.5}$$

The total potential (including the freestream potential (= URcos($\theta_V$)sin($\theta_H$)sin($\theta$)), and assuming a correction constant $k_{transv}$ is given by:

$$\widetilde{\phi}_{tot-transv}=k_{transv}URsin(\theta_H)\cos(\theta_v)\begin{bmatrix} 0.7146-0.2789\cos(\theta)-0.1396\cos^2(\theta)-0.0802\cos^3(\theta)-0.1802\cos^4(\theta) \\ +0.1363\cos^5(\theta)+0.4177\cos^6(\theta)+0.0194\cos^7(\theta)-0.3272\cos^8(\theta) \\ -0.2033\cos^9(\theta)-0.0369\cos^{10}(\theta)+\sin(\theta) \end{bmatrix} \tag{12.6}$$

The lateral velocity component is found using

$$w_1 = \frac{1}{R}\frac{\partial \widetilde{\phi}_{tot-transv}}{\partial \theta_v} \tag{12.7}$$

$$w_1 = -k_{transv}U\sin(\theta_H)\sin(\theta_v)\begin{bmatrix} 0.7146-0.2789\cos(\theta)-0.1396\cos^2(\theta)-0.0802\cos^3(\theta)-0.1802\cos^4(\theta) \\ +0.1363\cos^5(\theta)+0.4177\cos^6(\theta)+0.0194\cos^7(\theta)-0.3272\cos^8(\theta) \\ -0.2033\cos^9(\theta)-0.0369\cos^{10}(\theta)+\sin(\theta) \end{bmatrix} \tag{12.8}$$

The axial component $w_2$ is determined using

$$w_2 = \frac{1}{R}\frac{\partial \tilde{\phi}_{tot-transv.}}{\partial \theta} \qquad (12.9)$$

Evaluation of $w_2$ gives

$$w_2 = k_{transv} \, U \sin(\theta_H)\cos(\theta_v) \begin{bmatrix} 0.2407\cos^2(\theta)\sin(\theta) + 0.7208\cos^3(\theta)\sin(\theta) - 0.6815\cos^4(\theta)\sin(\theta) \\ -2.5059\cos^5(\theta)\sin(\theta) - 0.1355\cos^6(\theta)\sin(\theta) + 0.2793\cos(\theta)\sin(\theta) \\ +0.2789\sin(\theta) + \cos(\theta) + 2.6179\cos^7(\theta)\sin(\theta) + 1.8297\cos^8(\theta)\sin(\theta) \\ +0.3698\cos^9(\theta)\sin(\theta) \end{bmatrix} \qquad (12.10)$$

*Determination of constants $k_{transv.}$ and $k_{axial}$*

1. **$k_{axial}$**
   a. Set the probe with $\theta_H = 0°$. Then $\phi_{transv.} = 0$.
   b. $V_\theta = \sqrt{U^2 + \frac{2\Delta p_i}{\rho}}$ where $\Delta p_i = p_\infty - p_i$ $\qquad (12.11)$
   c. Measure $V_\theta$. Calculate $k_{axial-i}$ for ports 2-5 ($\theta \approx 42°$ typically). Average the values to get single $k_{axial}$.

2. **$k_{transv.}$**
   a. Set the probe with $\theta_H = 90°$ and align a lateral port with the flow so $\theta_v = 0°$. Then $\phi_{axial} = 0$. Thus $V_\theta = 0$. Also $w_1 = 0$ for the port facing the oncoming flow. Rotate the probe through $90°$ after measurement to find $k_{transv-i}$ for the next lateral port, i: $2 \rightarrow 5$.
   b. $w_2 = \sqrt{U^2 + \frac{2\Delta p_i}{\rho}}$ where $\Delta p_i = p_\infty - p_i$ $\qquad (12.12)$
   c. Measure $w_2$. Calculate $k_{transv-i}$ for ports 2-5 ($\theta \approx 42°$ typically). Each port will have its own $k_{transv-i}$ value. These values will then be curve fitted to provide a global map for all $\theta_H$ and $\theta_v$ (this may not be necessary, as coefficients are determined using differences for specific port locations, e.g. P2-P4 and P3-P5 etc).

**Basic Concept - Dynamic Determination**

Assume a fluctuating freestream. Application of the unsteady Bernoulli equation yields:

$$H(t) = \frac{1}{2}\rho U(t)^2 + p_\infty(t) + \rho\frac{d\phi_\infty(t)}{dt}^{\,0} = \frac{1}{2}\rho V_i(t)^2 + p_i(t) + \rho\frac{d\phi_i(t)}{dt} \qquad (12.13)$$

where i refers to port i. Freestream properties are determined using a Hot Wire. The small wire diameter eliminates inertial effects. A similar definition of the potential to the static case is then used.

**Determination of constants $k_{transv.}$ and $k_{axial}$**

## 1. $k_{axial}$

a. Set the probe with $\theta_H = 0°$. Then $\phi_{transv.} = 0$. As the front port is a stagnation port, $V_1 = 0$. However $\phi_1(t) \neq 0$. Bernoulli's equation follows as:

$$\frac{1}{2}\rho U(t)^2 = p_i(t) + \rho \frac{d\phi_i(t)}{dt} \text{ and} \tag{12.14}$$

$$\tilde{\phi}_{tot\,axial}(t) = \phi_i(t) = k_{axial}U(t)R\cos(\theta_H)\begin{bmatrix} \sin(\theta)(0.1375 - 0.0744\cos(\theta) - 0.1869\cos^2(\theta) - 0.0457\cos^3(\theta) \\ + 0.1276\cos^4(\theta) + 0.06404\cos^5(\theta) - 0.0608\cos^6(\theta) - 0.0658\cos^7(\theta) \\ - 0.0220\cos^8(\theta) - 0.0026\cos^9(\theta)) + 0.1650\theta - \cos(\theta) - 0.59 \end{bmatrix} \tag{12.15}$$

with $\theta = 0°$. Thus the equation simplifies to:

$$\tilde{\phi}_{tot-axial}(t) = \phi_i(t) = -1.59 k_{axial}U(t)R \tag{12.16}$$

Substitition of Eq. (12.16) into Eq. (12.14) allows determination of $k_{axial}$. Note this method is using the front port only.

## 2. $k_{transv.-i}$

a. Set the probe with $\theta_H = 90°$ and align a lateral port with the flow so $\theta_v = 0°$. Then $\phi_{axial} = 0$. Thus $V_\theta = 0$. Also $w_1 = 0$ for the port facing the oncoming flow. Rotate the probe through 90° after measurement to find $k_{transv-i}$ for the next lateral port, i: $2 \rightarrow 5$. Bernoulli's equation gives:

$$\frac{1}{2}\rho U(t)^2 = \frac{1}{2}\rho w_{2-i}(t)^2 + p_i(t) + \rho \frac{d\phi_i(t)}{dt} \tag{12.17}$$

b. Calculate $w_{2-i}(t)$ and $\phi_i(t)$

$$w_2(t) = k_{...}U(t)\sin(\theta_H)\cos(\theta_v)\begin{bmatrix} 0.2407\cos^2(\theta)\sin(\theta) + 0.7208\cos^3(\theta)\sin(\theta) - 0.6815\cos^4(\theta)\sin(\theta) \\ - 2.5059\cos^5(\theta)\sin(\theta) - 0.1355\cos^6(\theta)\sin(\theta) + 0.2793\cos(\theta)\sin(\theta) \\ + 0.2789\sin(\theta) + \cos(\theta) + 2.6179\cos^7(\theta)\sin(\theta) + 1.8297\cos^8(\theta)\sin(\theta) \\ + 0.3698\cos^9(\theta)\sin(\theta) \end{bmatrix} \tag{12.18}$$

where $\theta_H = 90°$ and $\theta_v = 0°$. $\theta$ is the location of the lateral port tapping and is known. Also, the potential is given by:

$$\tilde{\phi}_{...}(t) = \phi_i(t) = k_{transv}U(t)R\sin(\theta_H)\cos(\theta_v)\begin{bmatrix} 0.7146 - 0.2789\cos(\theta) - 0.1396\cos^2(\theta) - 0.0802\cos^3(\theta) - 0.1802\cos^4(\theta) \\ + 0.1363\cos^5(\theta) + 0.4177\cos^6(\theta) + 0.0194\cos^7(\theta) - 0.3272\cos^8(\theta) \\ - 0.2033\cos^9(\theta) - 0.0369\cos^{10}(\theta) + \sin(\theta) \end{bmatrix} \tag{12.19}$$

$U(t)$ is measured by the H/W and $p_i(t)$ is measured by the pressure transducer. Evaluate $k_{transv.-i}$ for ports 2-5. Then add the axial and transverse potentials together.

# 13. PRESSURE LINE ATTENUATION

## Discussion of Available Techniques

A pressure-measuring instrument, such as a 5 or 7-hole probe, has a dynamic pressure response that is dependent upon the geometric tubing that connects the measurement point (at the tip of the probe) to the transducer diaphragm, the gas or fluid properties and the temporal rate-of-change of the measured pressure. For a given tubing-transducer system the dynamic response, or transfer function, can be determined either from theoretical models or experimental data. Theoretical models use the exact geometric dimensions of the tubing and transducer system, the fluid properties and the time history of the pressure signal. In the measurement of periodic pressures, the tubing system can, for an underdamped system, resonate, resulting in higher measured pressures than the true pressure at the measuring point. The first studies were performed on resonating tubes seen in musical instruments such as organs and flutes (Helmholtz, 1885; Rayleigh, 1894).
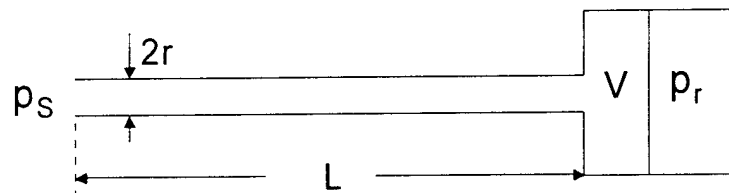


**Fig. 13.1. Schematic of the system, with inlet pressure $p_s(t)$, tube, transducer volume (V) and pressure transducer ($p_r$).**

Figure 13.1 shows a schematic of the basic system, a pressure measuring transducer connected to a tubing system of length L and diameter 2r. The true pressure $p_s(t)$ is the instantaneous true pressure at the measuring point, while the measured pressure $p_r(t)$ will be distorted in amplitude and phase. The acoustic time lag for such a tubing system, using pure acoustical theory is given by (Helmholtz, 1885):

$$\tau = \frac{L}{a} \tag{13.0}$$

where a is the speed of sound. For the tubing system alone the resonance frequency is given by:

$$f_n = \frac{a}{4L}, \frac{3a}{4L}, \frac{5a}{4L} \cdots \tag{13.1}$$

The combination of the tubing and volume will act as a Helmholtz resonator with resonance frequency (for a long cylindrical tube, connected to a spherical volume):

$$f_n = \frac{a}{2\pi}\left[\frac{\pi r^2}{VL}\right]^{1/2}$$

(13.3)

with other similar relations existing for other tube and volume shapes.

Since the 1920's there has been extensive research on aircraft pneumatic systems, where long pressure lines connect the measurement point, e.g. a Pitot probe to a manometer (Hemke, 1927; Wildhack, 1937; Huston, 1946; Whitmore et al., 1987, 1988, 1990, 1990, 1991. 1991; Franke and Pletcher, 1985). The response of such systems has also been studied at very low pressures (high Knudsen number) associated with high altitude flight (Davis, 1958; Whitmore et al., 1991). Another area of research has been on pressure measuring systems for high-speed blow-down wind tunnels with very short operating times. For these wind tunnel systems usually some length of small diameter steel or rubber tubing is used to connect the model to an external pressure transducer (see e.g. Sinclair and Robins, 1952; Bergh and Tijdeman, 1965; Franke, 1986; Franke and Chepren, 1987).

In recent publications pressure attenuation models have been applied to fast-response pressure probes that use tubing from the probe tip to the transducer (Rediniotis and Pathak, 1999; Gizzi and Gyaramthy, 1998; Paniagua and Denos, 2000). The theoretical models are typically divided into models that use a step or a ramp in the measured pressure (Wildhack, 1937; Hougen et al., 1963; Rediniotis and Pathak, 1999) and models that assume sinusoidally varying pressures (Hemke, 1927; Nichols, 1962; Karam and Franke, 1967; Tijdeman, 1969; Strunk, 1971; Holmes and Lewis, 1987; Benade and Ibisi, 1987). The first models used laminar Poiseuille flow for ramped input pressures to describe the transfer function of the system (Wildhack, 1937). This model was followed by electrical transmission line analogies for sinusoidally varying pressure inputs (Taback, 1949). Mechanical spring-mass-damper systems have also been used to describe the tubing response to pressure inputs (Huston, 1946).

Further, some researchers have studied purely overdamped systems (Sincalir and Robins, 1952), while others have discussed both underdamped and overdamped systems (Hougen et al., 1963), specifying criteria that need to be satisfied for the system to fall under one of these categories. In the early NACA work for manometer readings in aircraft, Hemke (1927) used small diameter tubing with large lengths (20-226 feet). The experimental measurements used two pressure sensors where one was acting as the reference. Hemke found empirical correction curves for time lag and attenuation as a function of tubing length and pressure signal. Wildhack (1937) developed a theory based on laminar Poiseuille flow:

$$p_s - p_r = \lambda \frac{dp_r(t)}{dt}$$

(13.4)

where $p_s$ is the actual pressure at the inlet, $p_r$ is the measured pressure and the lag constant, $\lambda$, is defined as:

$$\lambda = \frac{128\mu\,LV}{\pi d^4 p}$$

(13.5)

where $\mu$ is the viscosity of the fluid, L and d are the length and diameter of the tube respectively, V is the combined volume of the transducer cavity and the tube and p is the mean pressure. For a given tubing and transducer system the lag constant of the system can either be determined from the above equation or using experimental methods (Huston, 1946; Rediniotis and Pathak, 1999). For complex tubing systems the theoretical determination of $\lambda$ can be difficult and potentially inaccurate. Experimentally, the lag constant can be determined using a reference transducer measuring the pressure $p_s$ at the inlet of the tubing system with a step input while continuously monitoring the measured pressure $p_r$. The lag constant for the tubing assembly can then be determined from:

$$\lambda = \frac{p_s - p_r}{\dfrac{dp_r(t)}{dt}}$$

(13.6)

The criterion that need to be satisfied to assume a first order model (always overdamped) is:

$$\omega << \frac{32\mu}{d^2\rho}$$

(13.7)

Fig. 13.2 shows the response of a tubing system using a first order model. The tubing system used is a 153mm long 1.96mm ID steel tube in air at standard conditions. The dimensions for transducer volume are based on an Endevco 8507C-2 transducer, with $V_{trans}$=0.8mm$^3$. The calculated $\omega$ for this tube-transducer system is 125rad/s i.e. the assumption for first order model for this tubing system is only valid for frequencies much lower than 20Hz.

Huston used the analogy of a one-degree of freedom damped spring-mass system, identifying parameters that need to be satisfied to assume an underdamped, critically damped or overdamped system. Such a mechanical system is governed by the equation (13.8):

$$m\ddot{p}_r(t) + R\dot{p}_r(t) + \frac{p_r(t)}{C} = \frac{p_s(t)}{C}$$

(13.8)

where m is the mass of the medium in the tube, and R represents the viscous damping while 1/C is the elastic constant. For small volumes and small diameter tubes the volume and hence the mass is negligible thus the mass term can be ignored and the system is governed by viscous effects. For overdamped systems Huston arrived at the same basic relation as Wildhack who the Poiseuille laminar flow model. Taback used electrical transmission line analogy to describe the pressure attenuation and lag in pressure tubes. Table 13.1 gives equivalence between electrical and acoustic terms. These theories assume sinusoidally varying pressures applied to a tubing system and an instrument volume.
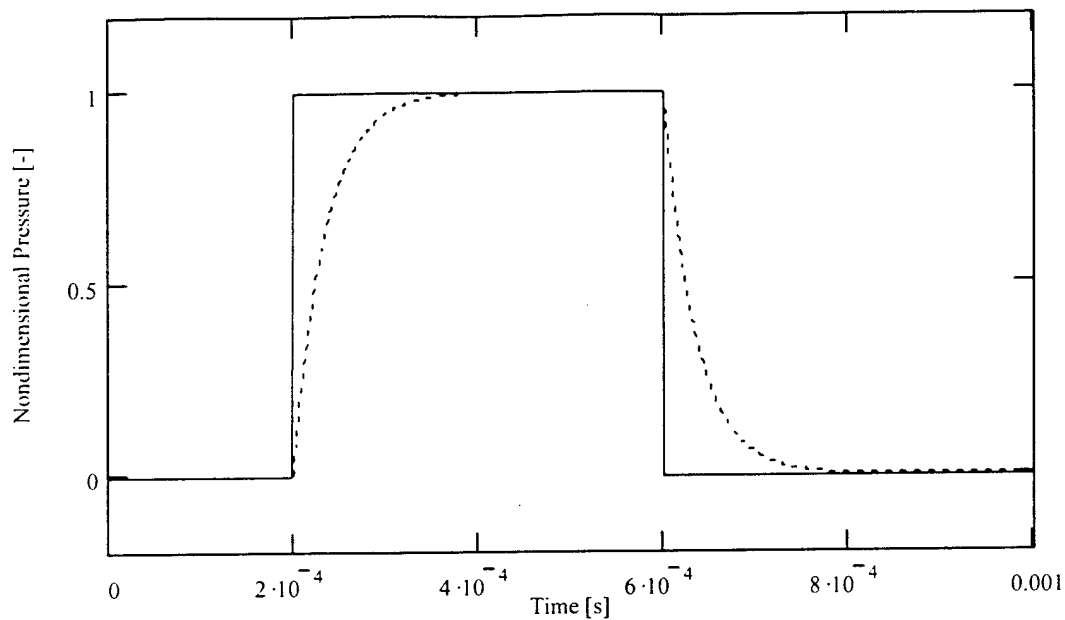
**Fig. 13.2.** The first order system response to step inputs. The solid line is the input step $p_s$ while the dotted line is the first order response, $p_r$. The data shown is for a 153mm long tube with 1.96mm inner diameter, with a lag-constant, $\lambda$=3.473E-5s.

**Table 13.1. Electrical-pneumatic equivalent terms.**

| Electrical | Equivalent Acoustical |
|------------|----------------------|
| Inductance | Inertance (mass) |
| Capacitance | Volumetric Capacity |
| Resistance | Flow Resistance |
| Current | Volume Flow |
| Voltage | Pressure |

Using this analogy Taback arrived at:

$$\frac{p_s}{p_r} = \frac{\sqrt{\sinh^2(\alpha L) + \cos^2(\beta L)}}{\tan^{-1}(\tan(\beta L)\tanh(\alpha L))} + \frac{Z_0}{Z_r} \frac{\sqrt{\sinh^2(\alpha L) + \sin^2(\beta L)}}{\tan^{-1}(\tan(\beta L)/\tanh(\alpha L))} \qquad (13.9)$$

where $\alpha$ is the attenuation per unit length and $\beta$ is the phase lag per unit length. $Z_0$ and $Z_r$ are the characteristic impedances for the tube and the transducer volume, respectively. For a very small transducer volume, negligible air flows at the transducer end of the tube and $Z_r$ approaches infinity, hence for negligible transducer volume the above equation simplifies to:

165

$$\frac{p_s}{p_r} = \cosh(\alpha L + i\beta L) \tag{13.10}$$

Iberall (1950) derived similar expressions for sinusoidally varying inlet pressures based on fluid dynamics rather than electrical transmission line theory. Similarly to Wildhack he started with laminar Poiseuille flow, but later expanded it to include large fluid accelerations, end effects and heat transfer. Bergh and Tijdeman (1965) expanded upon Ibearll's theory to include multiple tubes with varying cross sectional areas connecting multiple volumes. This model was derived from the N-S equations assuming: small sinusoidal disturbance, circular tube with radius much smaller than its length and laminar flow throughout the system. For a single tube volume system, Bergh and Tijdeman found the following relation:

$$k = \left[ 1 + \frac{\gamma - 1}{\gamma} \frac{J_2\left(i^{3/2}s\sqrt{\text{Pr}}\right)}{J_0\left(i^{3/2}s\sqrt{\text{Pr}}\right)} \right]^{-1} \tag{13.11}$$

where k is the polytropic factor, $\gamma$ is the ratio of specific heats, $J_0$ and $J_2$ are Bessel functions of the first kind of order zero and two respectively. Pr is the Prandtl number and s is the shear wave number defined as:

$$s = r\sqrt{\omega \frac{\rho}{\mu}} \tag{13.12}$$

where r is the inner radius of the tube, $\omega$ the oscillation frequency, $\mu$ the viscosity and $\rho$ is the mean density of the gas. The propagation constant, $\Gamma$, is defined as:

$$\Gamma = (\alpha + i\beta) = \frac{\omega}{a}\left[ \frac{J_0(i^{3/2}s)}{J_2(i^{3/2}s)} \frac{\gamma}{k} \right]^{1/2} \tag{13.13}$$

where again $\alpha$ and $\beta$ are the attenuation and phase angle per unit length, respectively. The pressure attenuation can also be written as:

$$\frac{p_s}{p_r} = \cosh(\Gamma L) + \frac{V}{V_t}\frac{1}{\gamma}\Gamma L \sinh(\Gamma L) \tag{13.14}$$

where V is the tube volume and $V_t$ is the transducer volume. If one assumes negligible transducer volume the above equation reduces to a solution identical to that of Taback who used electrical transmission line theory. Figures 3 and 4 show the gain and phase angle curve, respectively, using Bergh and Tijdeman's model.
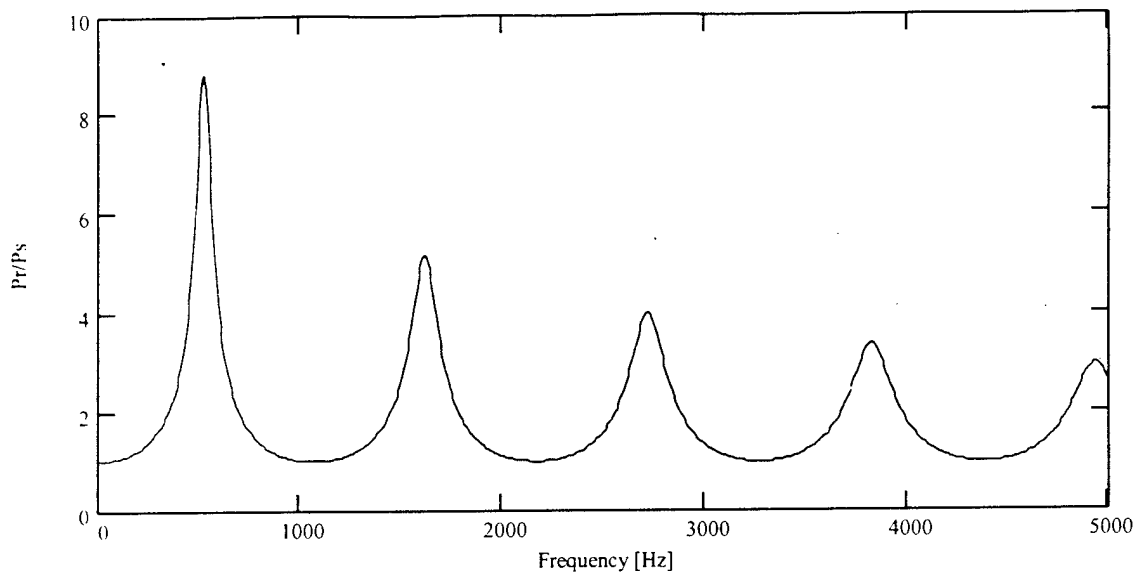
**Fig. 13.3. Pressure gain vs. frequency for 153mm long, 1.96mm ID steel tube for air at standard conditions using Bergh and Tijdeman's model.**
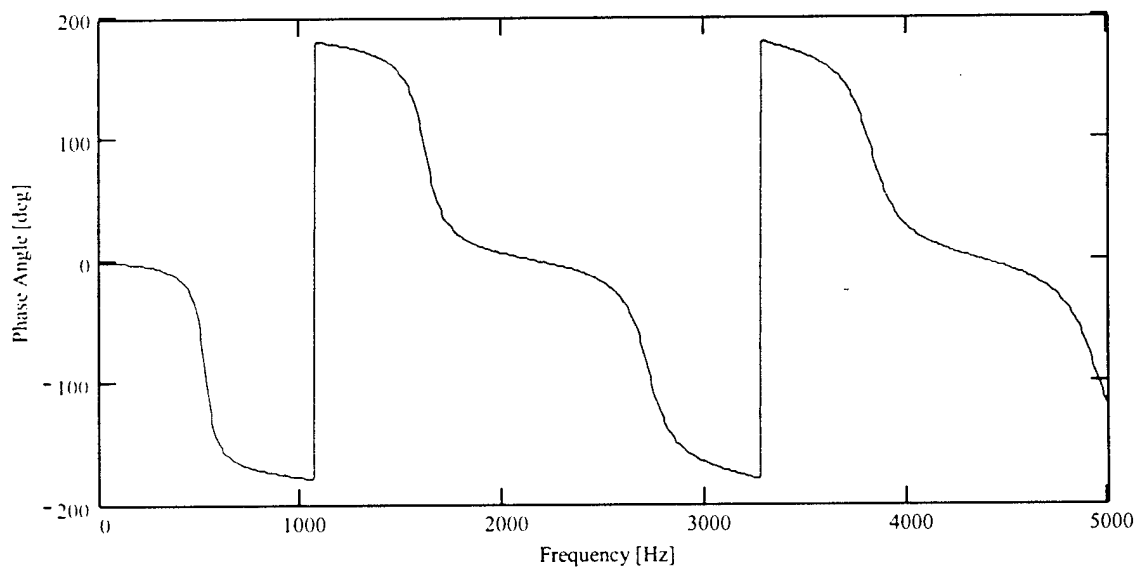


**Fig. 13.4. Phase angle vs. frequency for 153mm long, 1.96mm ID steel tube for air at standard conditions using Bergh and Tijdeman's model.**

As seen in figures 13.3 and 13.4, unless this tube is used for very low frequencies, massive gain and phase angle shift will occur. The first resonance frequency as predicted with this method is 525Hz with a gain of 8.8. Also, Whitmore and Leondes (1990, 1991) and Holman (1994) arrived, based on the N-S equations, at similar solutions as those by Bergh and Tijdeman, but used an inverse Laplace transformed solution that holds an infinite number of harmonic terms. They further truncated this solution to only include the first harmonic. Thus for a tube

connected to a finite size transducer volume, they ignored higher order resonance frequencies. From Holman (1994):

$$\frac{p_S}{p_r} = \sqrt{\left[1 - \left(\frac{\omega}{\omega_n}\right)^2\right]^2 + 4h^2\left(\frac{\omega}{\omega_n}\right)^2}$$ (13.15)

where $\omega$ is the frequency, with the natural frequency for the system, $\omega_n$ and the damping coefficient, h, given by:

$$\omega_n = \sqrt{\frac{3\pi r^2 a^2}{4LV}}$$ (13.16)

$$h = \frac{2\mu}{\rho a r^3}\sqrt{\frac{3LV}{\pi}}$$ (13.17)

The phase angle, according to Holman, is given by:

$$\phi = \tan^{-1}\left[\frac{-2h(\omega/\omega_n)}{1 - (\omega/\omega_n)^2}\right]$$ (13.18)

Holman's method does not predict well the properties of the 153mm tube in combination with the Endevco transducer used in the above example since the transducer volume is negligible when compared with the tubing volume. However for a second example, a 53mm long, 0.25 mm ID tube good predictions can be made.

Chepren and Franke (1988) developed a numerical technique for determining the pressure distribution in a straight tube, using a finite difference model. A number of features were compared such as laminar and turbulent flow, linear and nonlinear effects, for several waveforms, sinusoidal, steps and ramps. Good agreement with a few experimental cases was shown.


**Critical Design Parameters for Pressure Tubing System for Fast-Response Pressure Probes**

A Pitot or multi-hole probe is an intrusive flow measurement technique and derives its flow measurement from disrupting the flowfield in an adiabatic stagnation or deceleration. The presence of the probe will alter the measured flow hence minimization of the probe size is desirable. One of the limiting factors for the design of fast-response probes is the availability of small, sensitive transducers. The smallest commercially available transducers are on the order of 1mm diameter, thus mounting 5 or 7 of these transducers in a probe creates a probe that will have a diameter of at least 4-5mm.

In several cases, where a probe frequency response of a few hundred Hz is sufficient, a tubing system can be used from a very small probe tip (on the order of 1mm) to the transducers mounted downstream in a larger body. Such a tubing system must be carefully designed and analyzed to be able to fully reconstruct the measured pressure at the probe tip. In any process that involves miniaturization, fabrication accuracy and tolerances become important. The relative importance of some of these parameters will emerge in a comprehensive uncertainty analysis, however the purpose here will be to show how these parameters change the theoretical gain and phase angle curves. Fig. 13.5 shows the basic tubing system that could be used in a fast-response probe. The scale is shown for an Endevco 8507C-2 transducer with outer diameter of 2.3mm. The inner diameter of the tube is 0.25mm, and could be used in a 5-hole probe with a tip diameter of 1mm to 1.5mm and a downstream body diameter (about 50mm downstream) of 8-10mm.
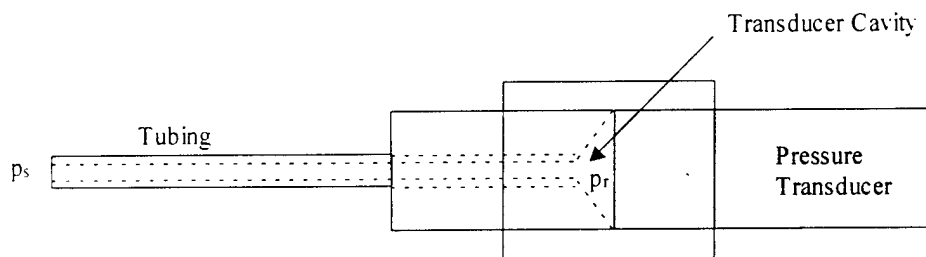


**Fig. 13.5. Typical mounting of a miniature pressure transducer to a small pressure tube. The scale shown is for a 0.25mm ID tube and a 2.3mm OD pressure transducer (length of tubing is not shown to scale).**

The connection between the small diameter tubing to the larger pressure transducer results in a small cavity in front of the transducer, usually in the form of a cone, from the drill bit that was used to make the hole. The total transducer cavity will be the cavity inside the transducer itself ($0.8mm^2$ for the Endevco transducer) in addition to the cavity immediately in front of the transducer. The following will be an example of the dimensions and tolerances in fig. 13.5. The numbers are used as example, but the dimensions and tolerances are collected from the manufacturers' catalogs. The Endevco transducer outer diameter and tolerance is given as: 2.34mm +/- 0.08mm. Inner diameter and tolerance for the stainless steel tubing is given as 0.254mm +0.0254mm / -0.0127mm, or +10% / -5%. The drill bit used for the cavity is 2.58mm, with a tip angle of 110 degrees, assumed constant, but will certainly be dependent on the sharpness of the drill and the quality of the hole drilled. The actual mounting of the transducer to the part will also be subject to some uncertainty and for the sake of argument this number is assumed to be +0.2mm / -0.0mm. The tubing length is taken as 53mm +/- 0.1mm. Most uncertainty analyses use the most probable error and would use an expected error based on standard deviations for the above measurements. Here, however the extremes will be calculated for the numbers presented above using the theory of Bergh and Tijdeman. As seen in fig. 13.6a and 13.6b the tubing diameter has a very large effect on the response of the system.
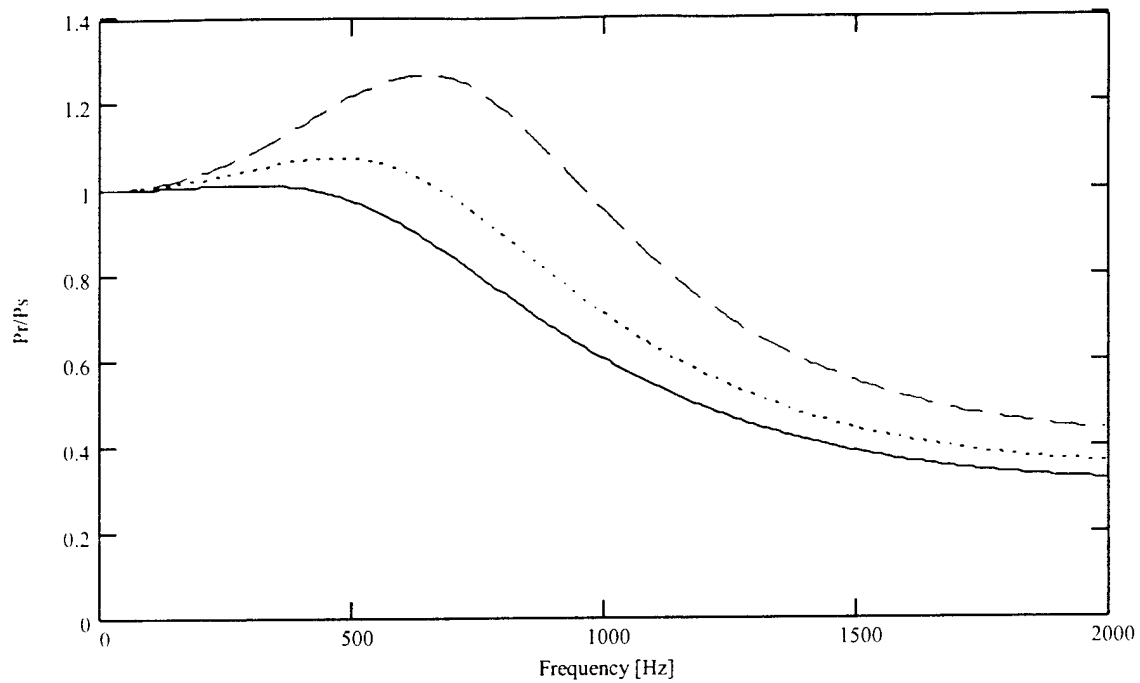
Fig. 13.6a. Effect of tubing diameter on gain. The dotted line corresponds to the design value, the solid line to the minimum tube diameter while the dashed line corresponds to the maximum tubing diameter.
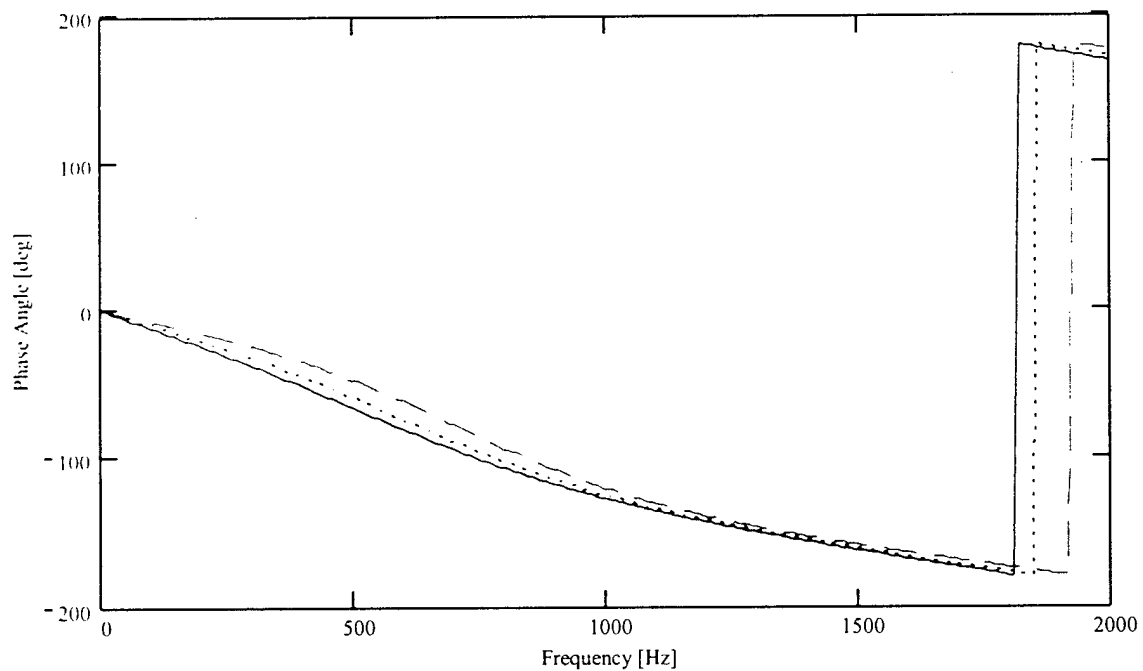


Fig. 13.6b. Effect of tubing diameter on phase angle. The dotted line corresponds to the design value, the solid line to the minimum tube diameter while the dashed line corresponds to the maximum tubing diameter.
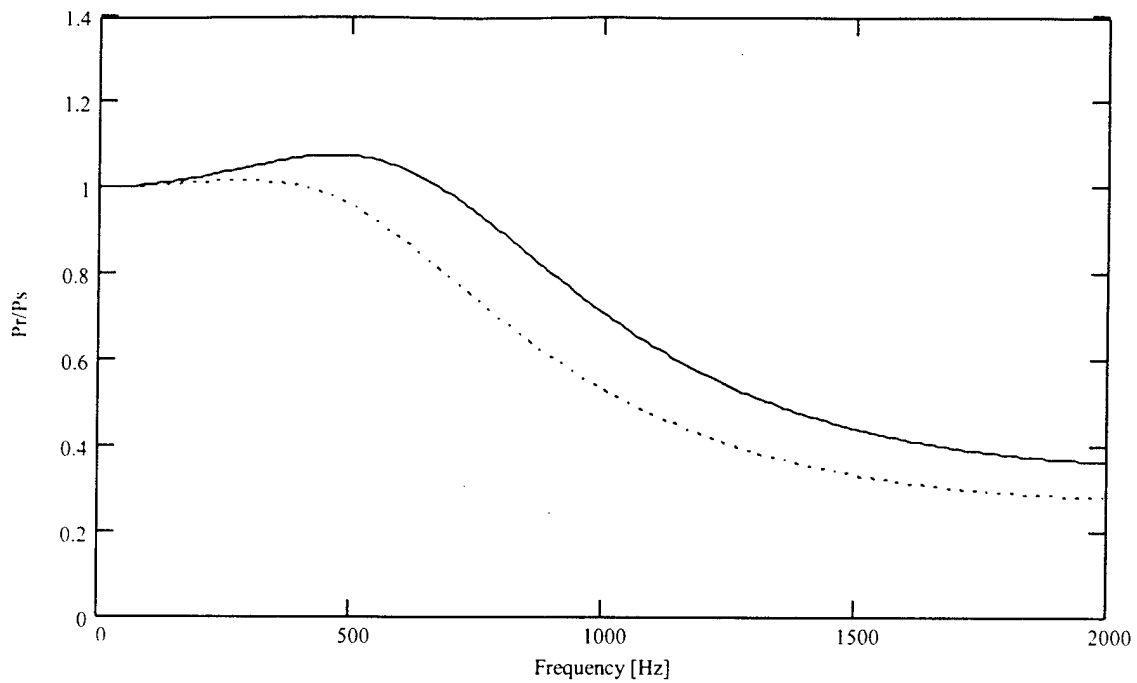
**Fig. 13.7a. Effect of transducer volume on gain. The solid line corresponds to the minimum calculated volume based on the design values and the dotted line to the maximum volume.**
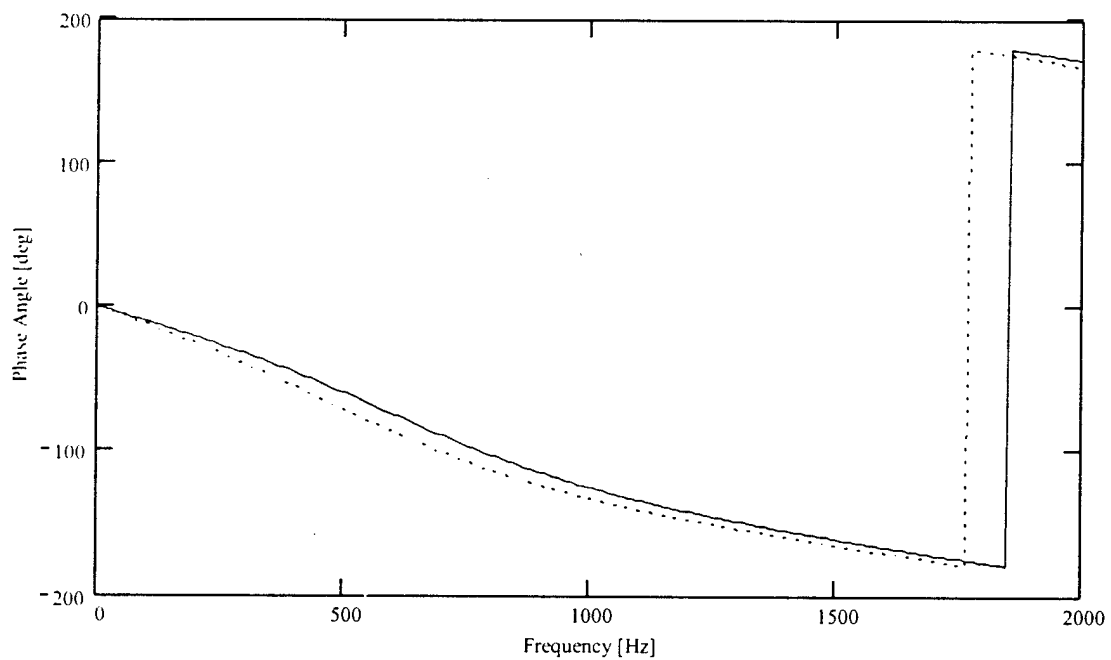


**Fig. 13.7b. Effect of transducer volume on phase angle. The solid line corresponds to the minimum calculated volume based on the design values and the dotted line to the maximum volume.**

Increasing the tube diameter will increase the resonance frequency and also the maximum gain significantly. Varying the tubing length within the prescribed uncertainties does not change the gain and phase curves noticeably, but the general effect for larger changes (tube length increase) is a lowering of the resonance frequency and maximum gain. Increasing the transducer volume will also lower the resonance frequency and the maximum gain (figs. 13.7a and 13.7b). The combined effect of both tubing diameter and transducer volume is shown in figs. 13.8a and 13.8b.

The dramatic effect of the tolerances is shown in figs. 13.8a and 13.8b. For the design values the system acts slightly underdamped, however for a smaller tube diameter and larger transducer volume, the gain curve shows that the system is overdamped for all frequencies. A number of other factors could also complicate the theoretical determination of the gain and phase angle curves, such as discontinuities in the tubing cross sectional area due to bends. For larger tubing systems, the relative importance of tolerances is less pronounced. For the 1.96mm ID steel tube the tolerances are the same as for the 0.25mm ID tube, and the effect of these tolerances is not visible in the gain and phase angle plots.

The results from these figures shows that there is an increasing effect of the uncertainty in the transducer volume for decreasing tubes sizes, and that for capillary sized tubes accurate theoretical determination of the gain and phase angles might be impossible. This impact of the uncertainties call for a method of determining the gain and phase angle curves experimentally on the complete tubing-transducer system.
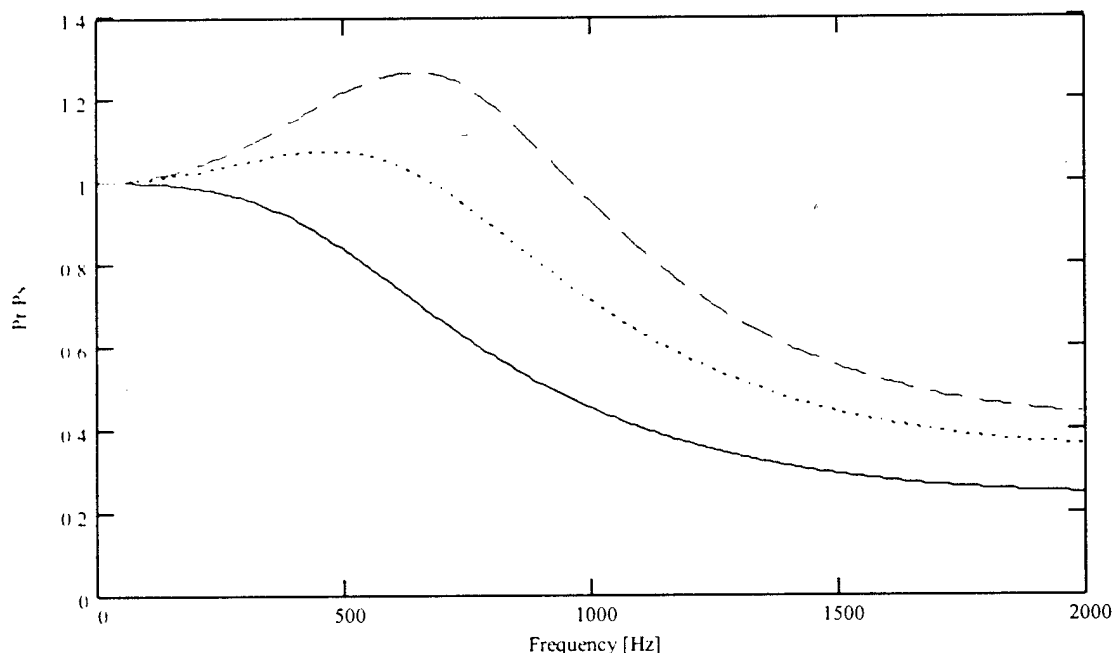


Fig. 13.8a. Combined effect of tubing diameter and transducer volume on gain. The dotted line corresponds to the design values, the solid line to the minimum tube diameter and maximum transducer volume, while the dashed line corresponds to the maximum tubing diameter and minimum transducer volume.
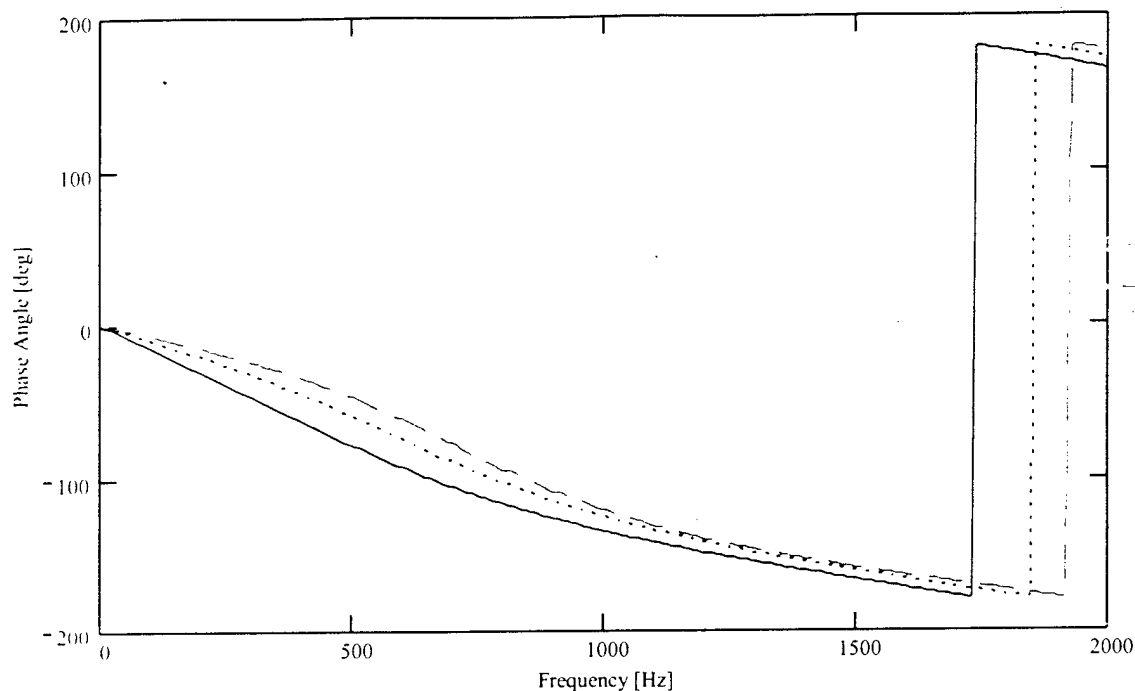
**Fig. 13.8b. Combined effect of tubing diameter and transducer volume on phase angle. The dotted line corresponds to the design values, the solid line to the minimum tube diameter and maximum transducer volume, while the dashed line corresponds to the maximum tubing diameter and minimum transducer volume.**

In the design of a fast response probe that uses some tubing system, one must also consider transducer sensitivity/resolution issues, since the pressure sensed by the transducer is significantly attenuated at high frequencies. Even though accurate gain and phase angle curves for very high frequencies are obtained the system might still be useless in this region due to the attenuation of the pressure sensed by the transducer. For example, for the tubing system in figs. 8a and 8b the attenuation at 2kHz leaves, at the trasducer, only about 38% of the input pressure magnitude. Thus, to resolve small scale pressures the transducer resolution must be considered and becomes increasingly important. At even higher frequencies, such as 10kHz the attenuation is even more pronounced, leaving very little pressure to be measured. Thus, the specific probe design, which is overdamped for almost all frequencies, might be difficult to use for e.g. turbomachinery flows where frequencies of 5-15kHz are typical (fig. 13.9).

For fast response pressure measurements, an underdamped tubing system, with a larger diameter tube, could be used, since there is hardly any pressure attenuation at the transducer. For example, the 153mm long, 1.96mm ID tube with the Endevco transducer can be used up to very high frequencies with little attenuation in pressures (fig. 13.10). Of course for this specific system, care should be taken such that the amplification of the pressures at resonance frequencies does not overload the transducer.
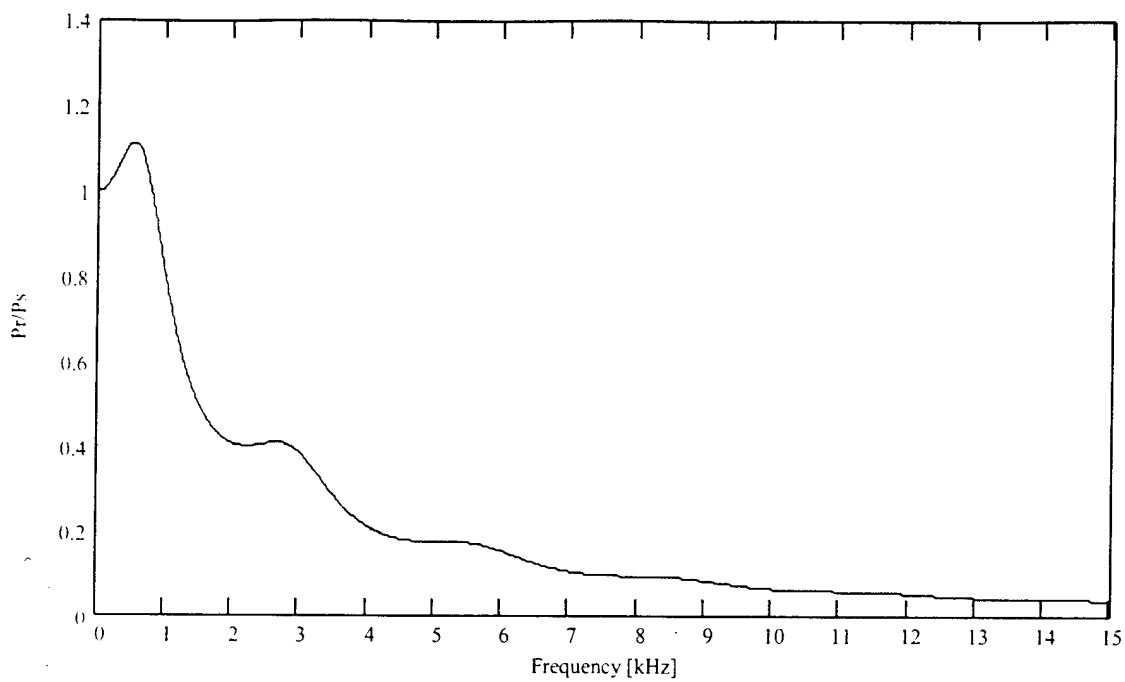
**Fig. 13.9. Attenuation of pressure for 53mm long, 0.25mm ID tube and Endevco transducer system.**
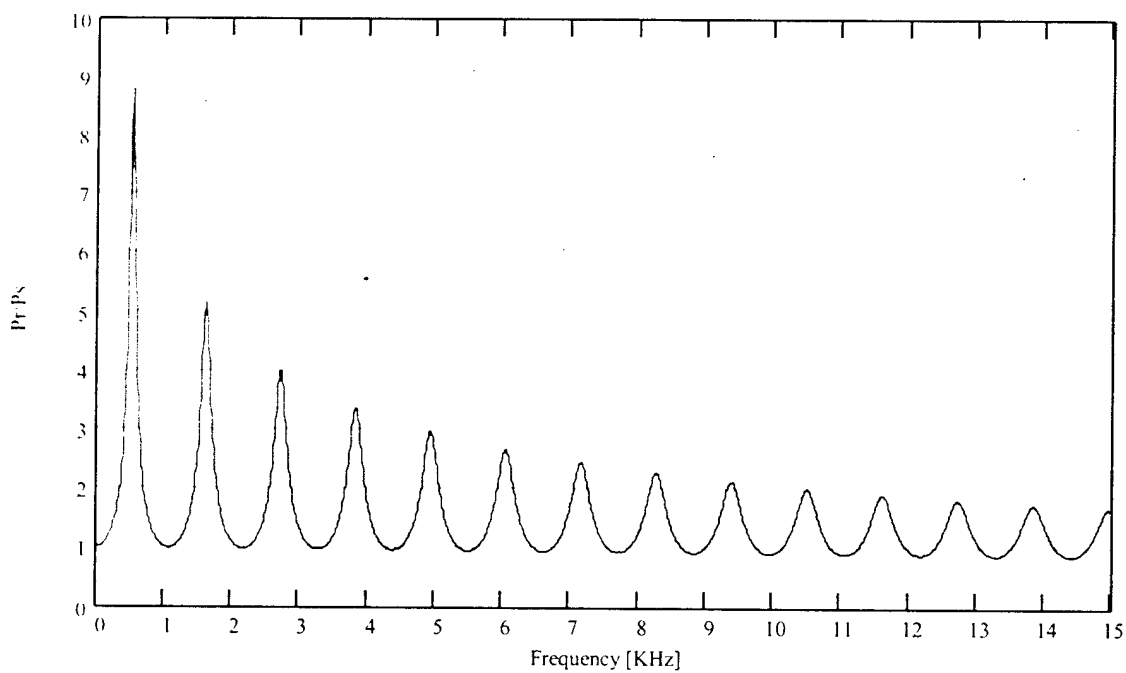


**Fig. 13.10. The gain of pressure for a 153mm long, 1.96mm ID tube.**

The above discussion aims to illustrate the point that the tubing-transducer should be carefully designed, depending on the frequency range it intends to measure. The system shown in fig. 13.10 has a relatively large size and can not be used in some flowfields where small length scales are to be resolved. However a combination of two or more tubes with different lengths and diameters (for example small tube diameter at the tip, expanding to a larger diameter at a small distance from the tip) can be designed to meet the frequency, transducer resolution and spatial resolution needs.

## Experimental Determination of Gain and Phase Angle Curves

As noted above, the importance of accurately knowing the exact volumes and tubing dimensions makes a theoretical model nearly impossible to attain for small diameter tubes. Furthermore, the assumptions for e.g. Bergh and Tijdeman's model include circular cross-section and laminar flow, which might not be satisfied for many tubing applications. A facility was designed to be able to accurately determine the frequency response of tubing systems that are used in miniature fast-response pressure probes. Two pressure transducers are used, one at the inlet of the tubing system ($p_s$) and one at the transducer end of the tubing ($p_r$), while an oscillatory pressure is generated by a loudspeaker. A mid-range loudspeaker with a frequency range of 300-5000Hz was chosen as the driver for the system. This loudspeaker is mounted one of the walls of a closed cavity. On the opposite wall, two holes were drilled, equidistant from the center of the loudspeaker. The reference pressure transducer is mounted in one hole while the test tubing is connected to the other hole (fig. 13.11).
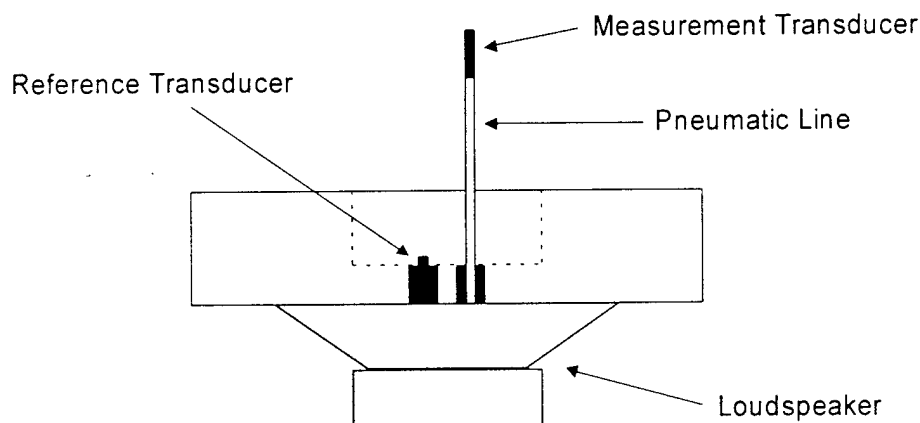


**Fig. 13.11. Loudspeaker system for the determination of gains and phase angles for pressure tubes.**

A wide range of frequencies is scanned by the system (typically 10-5000Hz in 10Hz increments), and for each frequency the ratio of $p_r/p_s$ as well as the phase angle is determined from the nearly simultaneously sampled pressures. The data-acquisition system (National Instruments PCI-MIO-16E-1) is used to generate the output signal (+/-10V) to the speaker power amplifier and acquire the pressure transducer signals. The two channels are sampled sequentially

with a delay of $10^{-6}$ seconds for the frequency span (up to 5kHz). This delay will only cause a miscalculation of phase angle of less than 3.6 degrees for a 5kHz signal, or 0.72 degrees per 1000Hz. Since the delay time is known and constant the time stamps are adjusted accordingly.

The data is sampled at a rate proportional to the test frequency, typically 200-1000 times the actuation frequency. A voltage signal is generated by the data-acquisition system as a series of values that form a sine wave (or any other waveform) and is connected to the loudspeaker through a power amplifier. A PID loop continuously monitors the input pressure $p_s$ and adjusts the amplitude of the signal wave to maintain a constant rms pressure signal. The rms pressure level that the loudspeaker can give at very low frequencies (<500Hz) is in the range of 800Pa, however at higher frequencies (>2kHz), the maximum rms pressure that can be generated in the system is approximately 30Pa. For a constant rms pressure response the amplitude of the driving signal is adjusted over a wide range (from less than 0.05Vrms to more than 14Vrms). The output signal is connected to a Kepco BOP36-12M voltage proportional power amplifier. This amplifier has a fixed gain of 3.6, i.e. a 1V input signal will produce a 3.6V output signal, DC to 20kHz (figs. 12, 13).
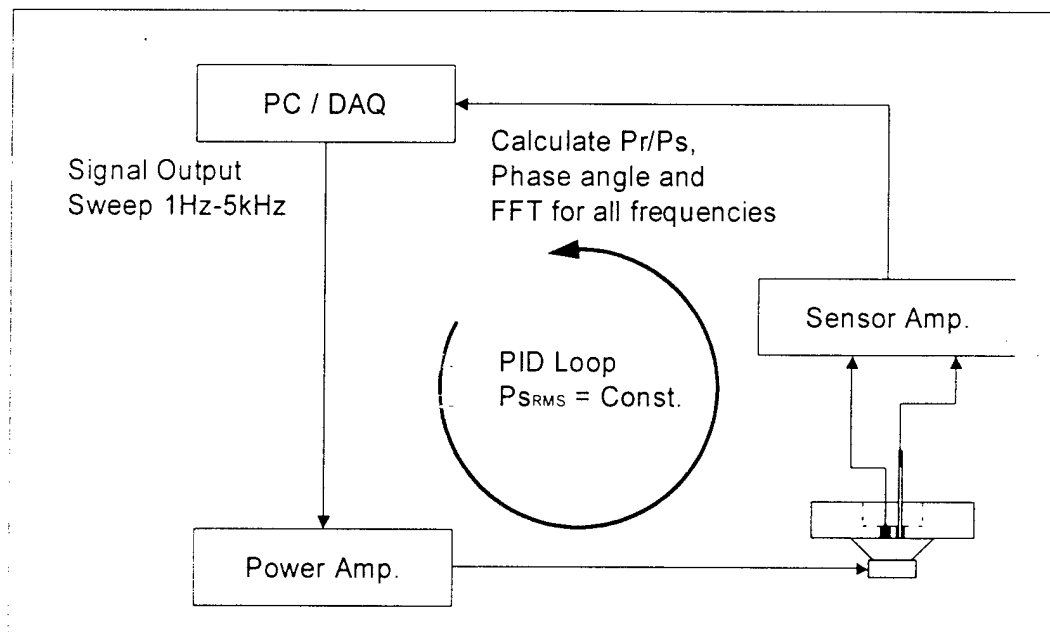


**Fig. 13.12. Schematic of loudspeaker tubing test system. The signal amplitude is adjusted at each frequency to maintain constant pressure rms.**
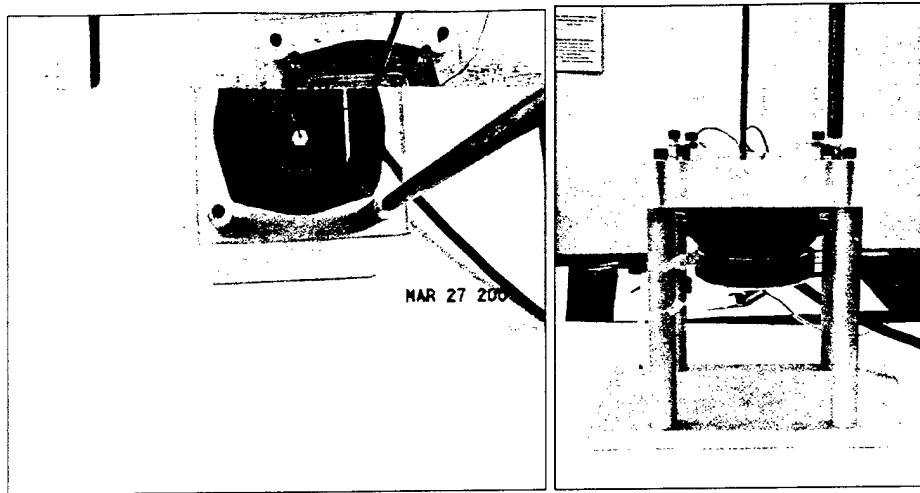
**Fig. 13.13. Pictures of the loudspeaker assembly, arrows showing the reference transducer measuring the input pressure $p_s$ and the location of the port for connecting the tube to be tested.**

The reference or input transducer and the connection for the tube to be tested are connected using standard NPT threaded plugs. Fig. 13.14 shows some of the tubes tested as well as the mounting plugs. The Endevco 8507C-2 transducer is also shown.
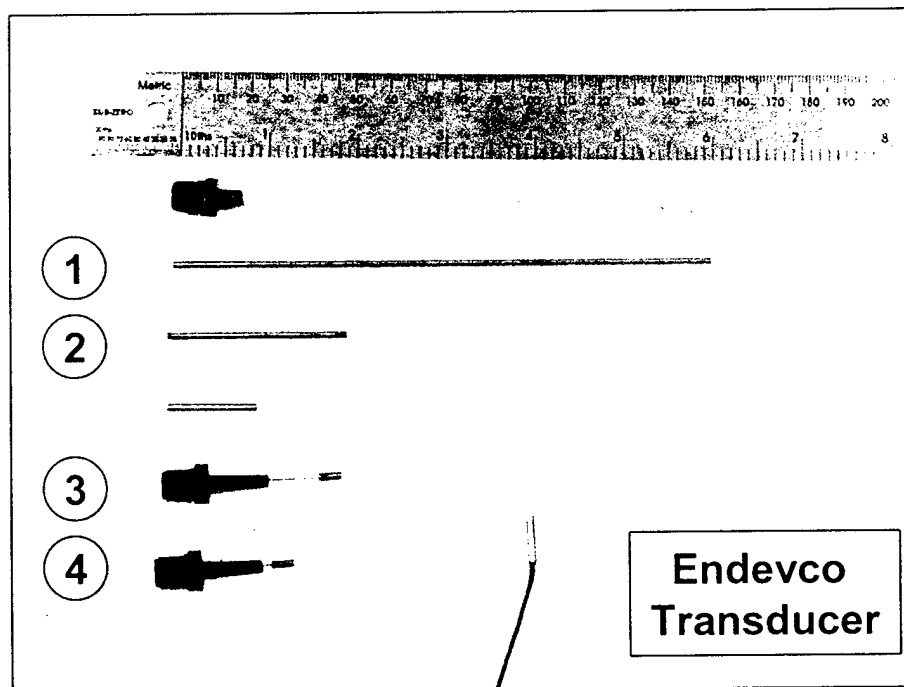


**Fig. 13.14. Different tubes tested. Picture also shows the Endevco 8507C-2 pressure transducer used in the experiments. 1) L=153mm, ID=1.96mm, 2) L=51mm, ID=1.96mm, 3) L=53mm, ID=0.25mm, 4) L=25mm, ID=0.25mm.**

The Endevco pressure transducer has the capability of resolving static and dynamic pressures up to about 15kHz and has a diaphragm resonance frequency of 70kHz. The pressure range is +/- 2psi, with sensitivity of approximately 150mV/psi. The signals from the transducers are amplified using Entran amplifiers with a gain of 100. The combined sensitivity is calculated approximately as 2mV/Pa. The sensors are frequently calibrated to a Barocel pressure reference and the zero offset is recorded before each test. The two ports are mounted equidistant from the center of the loudspeaker thus equal response was expected for both transducers when flush mounted in the ports. The expected gain should show a flat response of 1.0 and the phase angle should always be 0 degrees. The measured results, however show that there is an increasing difference between the two measured pressures from very low frequency up to about 1400Hz where a significant jump is seen and the two ports see different pressures (fig. 13.15).
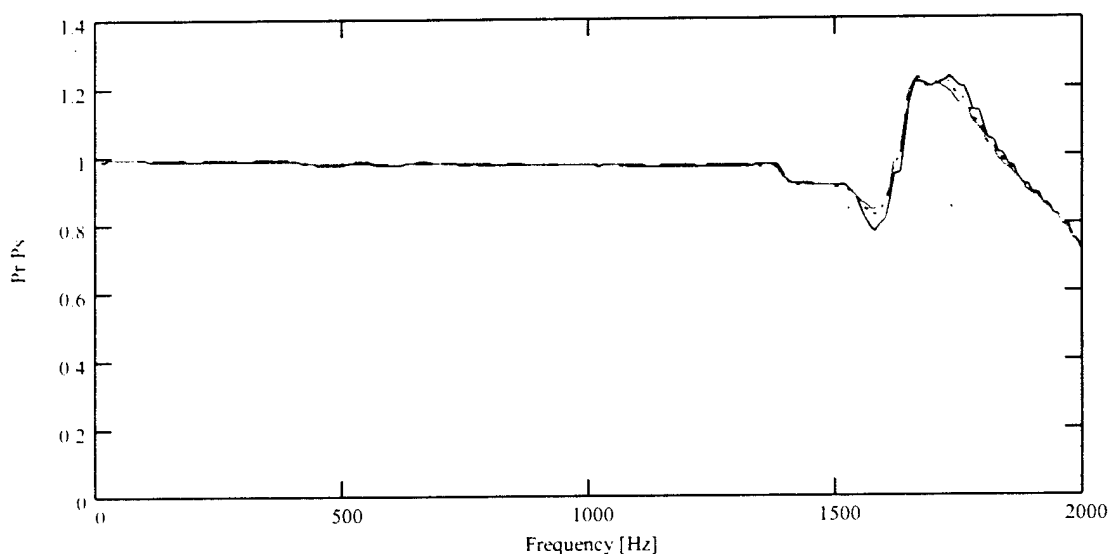


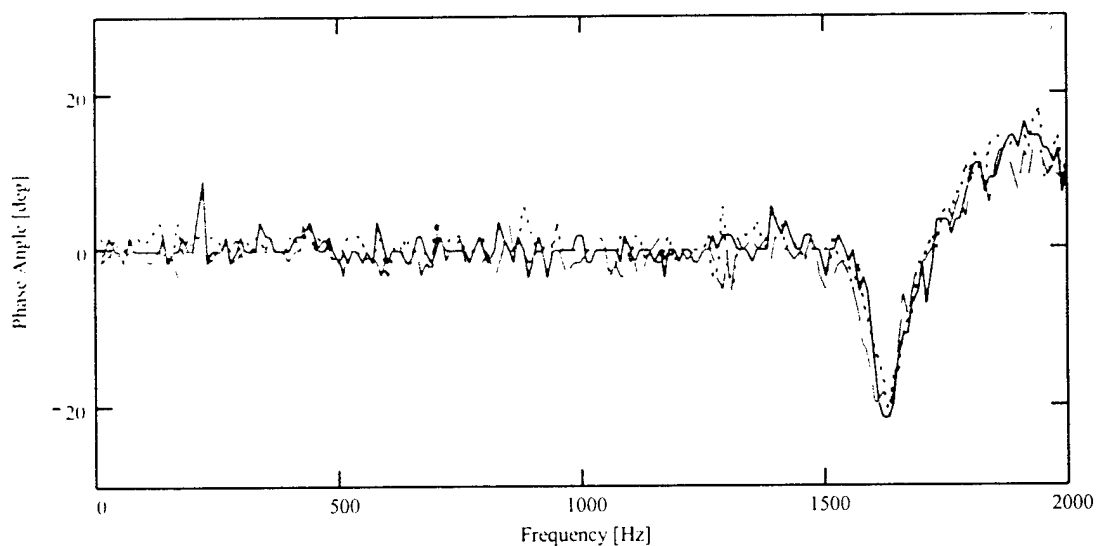**Fig. 13.15a. Experimental gain for transducer mounted side-by-side for three tests.**



**Fig. 13.15b. Experimental phase angle for transducer mounted side-by-side for three tests.**

178

The design of the facility and the quality of the loudspeaker may be responsible for this discrepancy in the measured pressures. In figs. 13.15a and 13.15b three tests were performed for the same $p_{s\_rms}$ = 50Pa. The three tests show that the discrepancy in the measured pressures is repeatable for all tests. It is further assumed that this is the case for all tests such that the curves in figs. 13.15a and 13.15b can be used as a correction to all subsequent tests. In any subsequent test, the actual recorded gain is therefore divided by the gain found for the transducers mounted side by side and the recorded phase angle is subtracted from the phase angle curve corresponding to the transducers mounted side by side.

Figs. 13.16a and 13.16b show the recorded gain and phase angle curves for the 53mm long, 0.25mm ID tube tested in the facility. The data was recorded with $p_{s\_rms}$=50Pa in the range of frequencies from f=10 to 2kHz. The step size was 10 Hz. The solid lines in figs. 13.16a and 13.16b are the recorded gain and phase angle, respectively. The dotted lines are the corrected curves using the data in figs. 13.15a and 13.15b. The dashed lines show the theoretical gain and phase angles from Bergh and Tijdeman's theory, using the design parameters of the system. The difference in the theoretical model and the corrected experimental results further illustrates the need for an experimental procedure. Better quality signals could not be obtained in this loudspeaker facility, but we are currently carefully redesigning the facility with much better quality loudspeaker components and anechoic features. The new design uses different loudspeakers for different frequency ranges, such as a woofer for low frequencies, a mid-range for medium frequencies and a tweeter or compression driver for high frequencies.
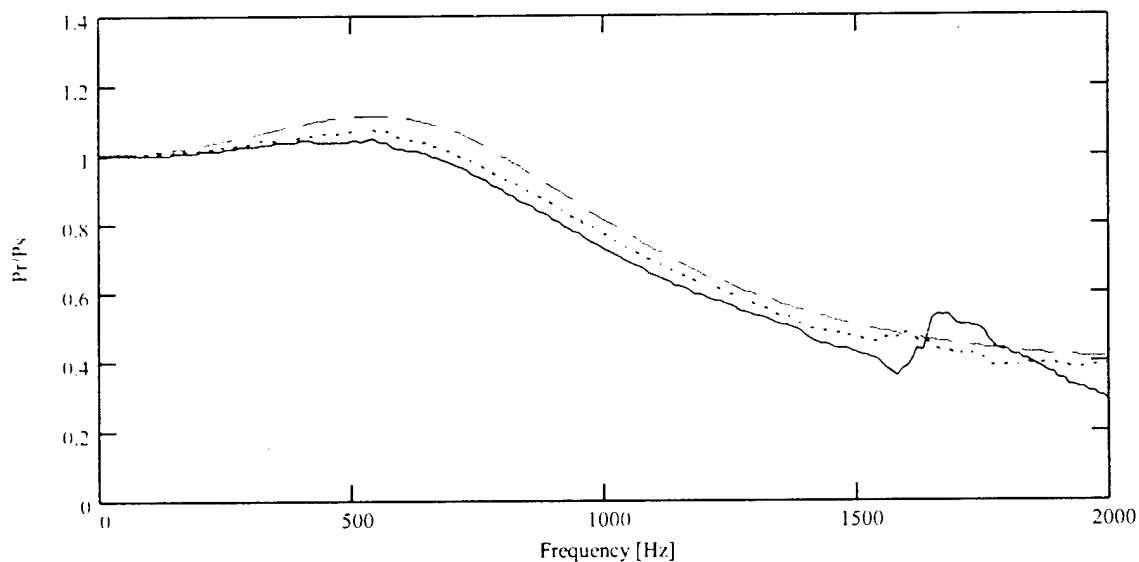


**Fig. 13.16a. Corrected gain curves for a L=53mm, ID=0.25mm tube. Solid line is raw gain curve, dotted line is corrected gain curve, while dashed line is the theoretical gain as predicted by Bergh and Tijdeman model.**

**Fig. 13.16b. Corrected phase angle curves for a L=53mm, ID=0.25mm tube. Solid line is raw gain curve, dotted line is corrected gain curve while dashed line is the theoretical gain as predicted by Bergh and Tijdeman model.**
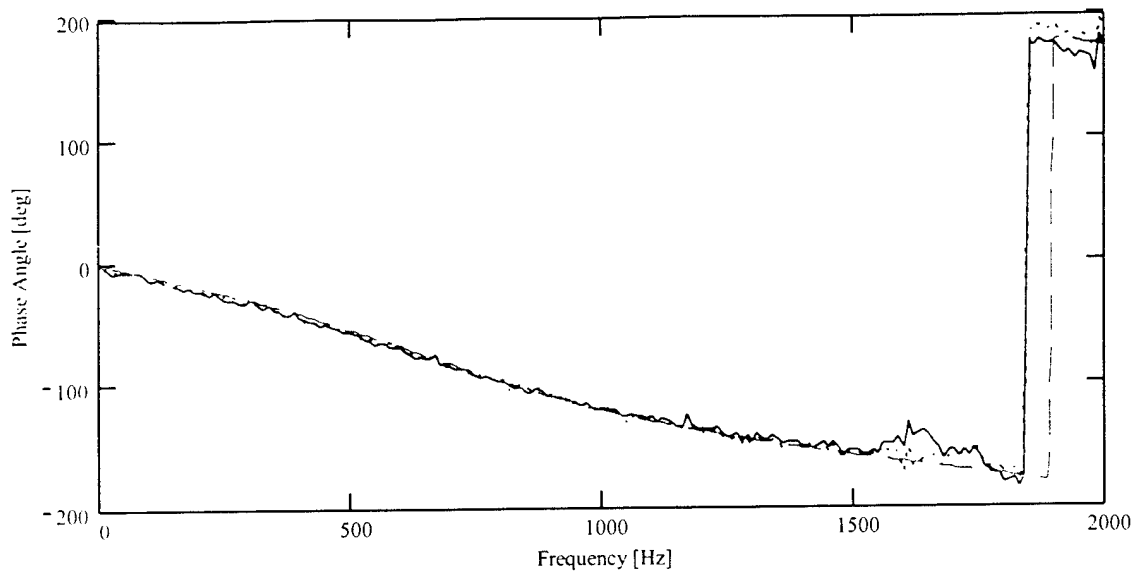
## Pressure Reconstruction Routine

The purpose of a correction routine for a pressure sensing system is to accurately reconstruct the instantaneous pressure at the measurement point from the pressure measured by the transducer. As discussed above there might be, depending on the tubing-transducer system, significant pressure attenuation and pneumatic lag in such systems and a procedure is needed to reconstruct the pressure using the tubing-transducer transfer function. Whether the transfer function is found by theoretical models (not recommended for very small diameter tubes) or by experimental means, the accuracy of this function will determine the quality of the reconstructed signal.

Data reconstruction has typically been divided into post-processing and real-time techniques. Post-processing is typically the method used in laboratory work and is most common for fast-response probe measurements. Real-time methods are such as those required, for example, in the control system in a fighter jet, and require a continuous flow of real-time data. In the past rigorous correction routines have been avoided to ensure that near-real-time, or "quasi-real-time" is achieved. This is due to the fact that they are computationally intensive. However, using modern computers this might no longer be the limiting factor. Thus, "quasi-real-time" non-parametric spectral methods, though computationally expensive, can be used at very high frequencies. One method to increase the speed of FFT transformations is the "one-in-one-out" method. The method results in significant lag only for the first sampled array ($2^N$ points), while any subsequent data point is added to the end of this array while erasing the first entry of the array. This way $2^N$ points are always kept in the array. For each sampled point, the FFT can be calculated and the spectrum is used as part of a correction routine.

Theoretical or experimental parametric models have the advantage that only a few parameters are needed to describe the transfer function, but often they fail to describe the system response accurately for high frequencies or beyond the first harmonic frequency (Whitmore and Leondes, 1990). The gain and phase angle parameters can be determined experimentally using a reference transducer at the inlet of the system, in addition to a transducer at the end of the system. Making sure that the system is over-determined (more states than coefficients) the coefficient values in the transfer function can be estimated using a least-squares fit. The procedure outlined in Paniagua and Denos (2000) promises to reconstruct the pressure signal with a high degree of accuracy in particular for parameter determination using step or ramp tests, rather than sinusoidal inputs. This method, or the simpler method outlined by Rediniotis and Pathak [30] can be used for non-periodic flowfields where the pressure value at the end of a test sample is at a different level than that at the beginning of the sample. For these methods special care must be taken when calculating the time derivative of the pressure for digitally sampled data, since this type of data is inherently jagged.

For periodic flows, where the pressure signal fluctuates around a mean value, a spectral reconstruction technique is proposed. Whitmore and Moes (1991) developed a spectral deconvolution method for a high AOA flush-airdata sensing system (HI-FADS) where pressure ports are located on the nosecone of a F-18. The pressure reconstruction scheme is described in fig. 13.17. The method of Whitmore and Moes was not used exclusively on periodic flows, but was altered to also reconstruct non-periodic flows, with the restriction that it now was a parametric model, not purely a non-parametric model. For the present discussion the first step of the model will be analyzed and applied to periodic flows.
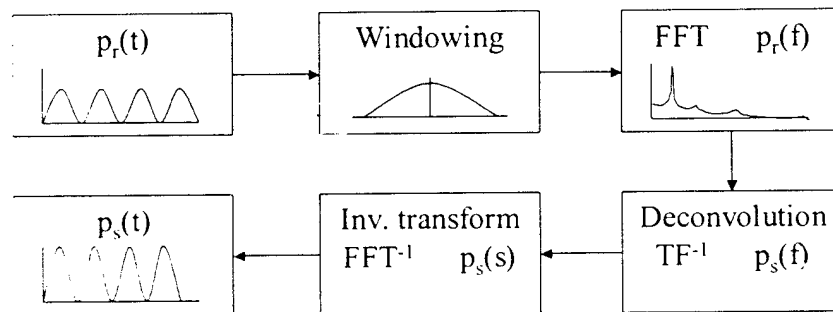


Fig. 13.17. Spectral deconvolution scheme proposed by Whitmore and Moes.

FFT transforms assume that the signal is perfectly periodic within the sample set. The purpose of a windowing function is to reduce what is known as leakage for signals that are not perfectly periodic within a specified time trace. The windowing function will force the beginning and the end of a sample set to zero, hence imposing a quasi-periodicity to the time data. There are a number of recognized and widely used windowing functions. Some have better characteristics than others when it comes to maintaining gain accuracy (e.g. flattop) and phase accuracy (e.g. Hanning window). Some tests might be self-windowing, meaning that the value is zero at both ends of the sample set. For a perfectly periodic signal with careful timing and

181

sampling a number of periods can be recorded in the sample set where the value of sample 1 equals the value of sample N+1. For such a signal no windowing function would be necessary.
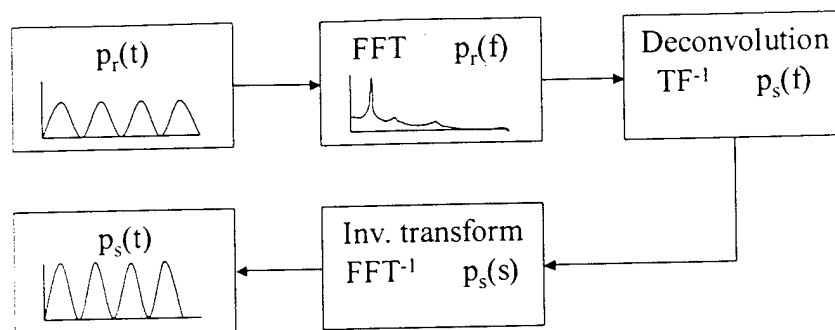


**Fig. 13.18. Five-step pressure reconstruction routine.**

Fig. 13.18 shows a five-step pressure reconstruction routine, similar to Whitmore and Moes' routine without the windowing function of the measured data. The restriction on such a method is that the data must be periodic, i.e. the pressure fluctuates around a constant mean value, and several full periods must be contained in the sample set. If experimental gain and phase angle curves are used in the analysis, the modulus of the FFT spectrum is divided by the gain, and the argument of the FFT spectrum is subtracted from the phase angle for the entire spectrum. Spectral filtering can easily be performed to smooth out high frequency noise, by, for example, forcing all spectral values above a certain frequency (much higher than the frequency in question) to zero. The reconstructed signal from the inverse FFT will, depending on the quality of the transfer function and the periodicity of the flow, quite accurately reproduce the true pressure.

### Test Cases

Figure 13.19 presents gain and phase angle curves for 6", 0.077ID tube. As previously discussed the discrepancies above 1500 Hz are due to the poor quality of the speaker system. This tube system was used to test our reconstruction algorithm. For that, several different pressure signals were applied, at various frequencies and amplitudes. For each such test, the applied, recorded and reconstructed signals are presented at the figures below.
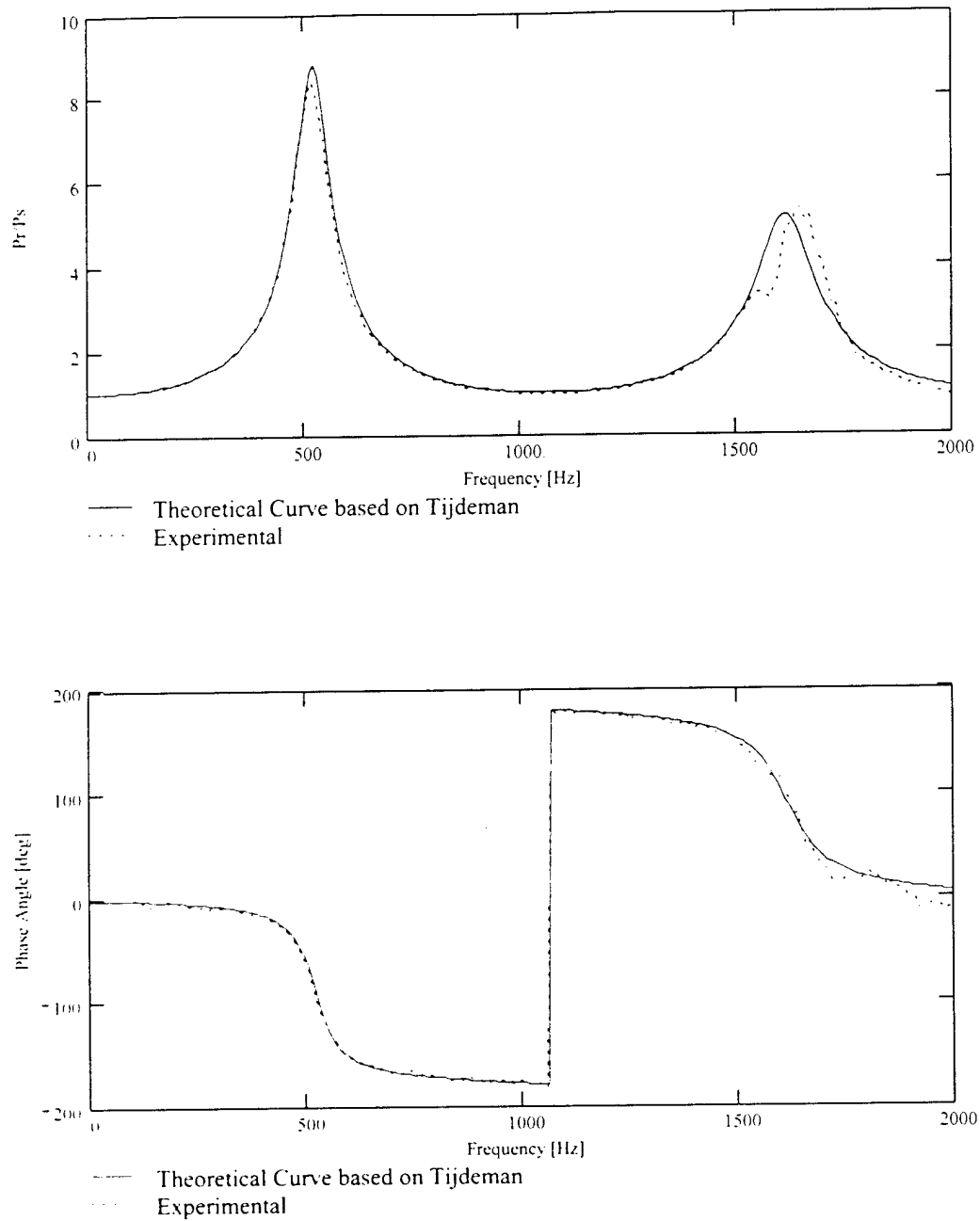
**Fig. 13.19. Gain and phase angle curves for a 6" long, 0.077ID tube.**

Fig. 13.20. Example 1. Pressure signal consists of: 500Hz at 100% amplitude + 1000Hz at 50% amplitude. Prms=200Pa. Ps (red line) is the true signal and Pr (blue line) is the recorded signal. Massive gain can be observed.



Fig. 13.21. FFT modulus and argument of the timetrace of fig. 13.20.

**Fig. 13.22. Reconstructed signal for Example 1. The green dashed line is the recorded signal, the blue dotted line is the true signal, while the red solid line is the reconstructed signal.**

185
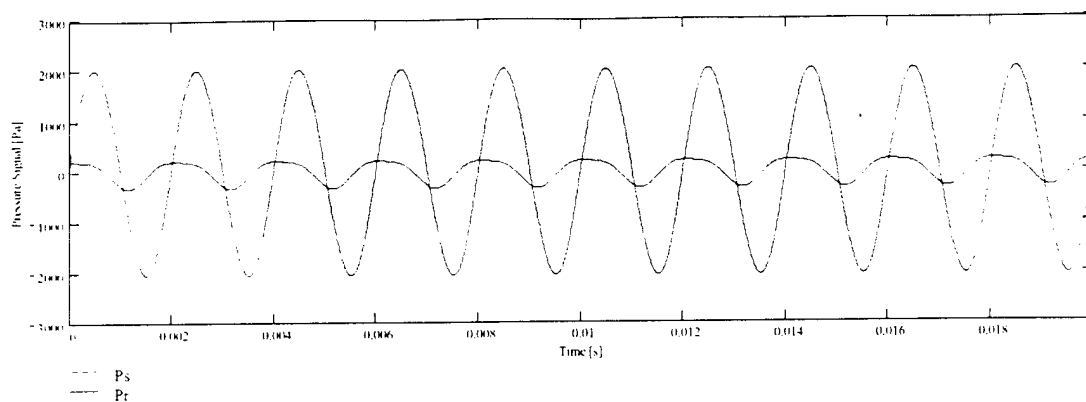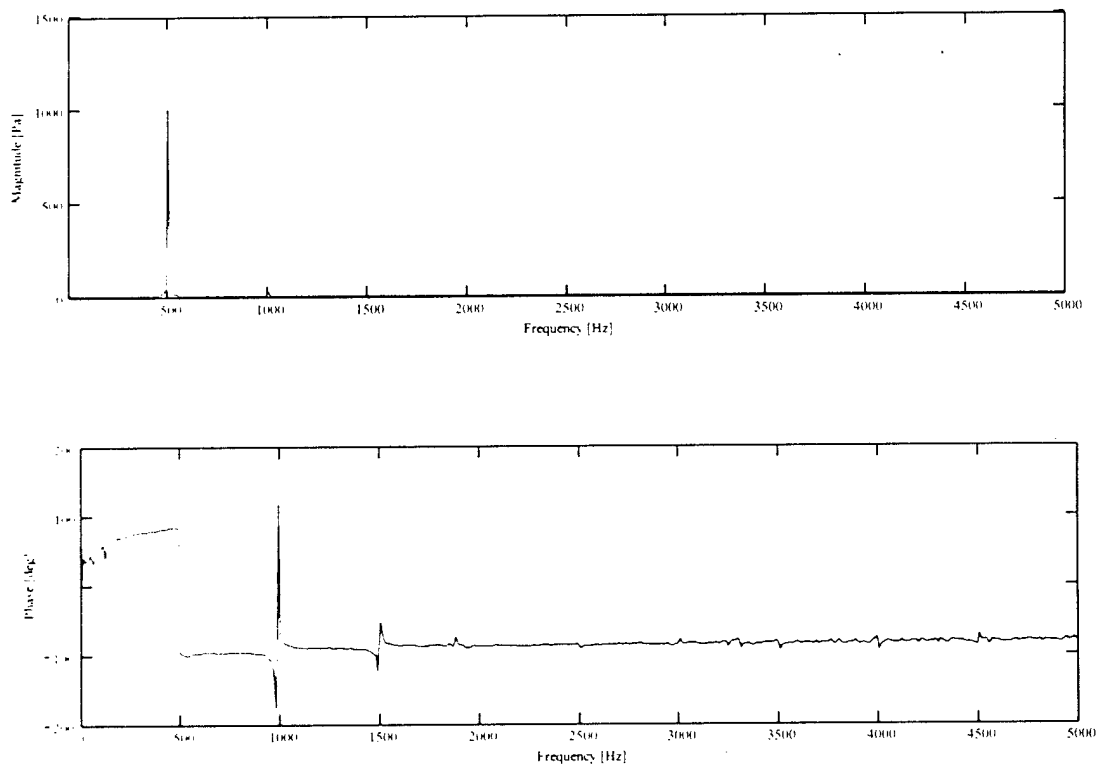
Fig. 13.23. Example 2. Pressure signal consists of: 100Hz at 100% amplitude + 1000Hz at 100% amplitude. Prms=200Pa. Ps (red line) is the true signal and Pr (blue line) is the recorded signal. Very little attenuation, but massive phase shifts can be observed.



Fig. 13.24. Reconstructed signal for Example 2. The green dashed line is the recorded signal, the blue dotted line is the true signal, while the red solid line is the reconstructed signal.
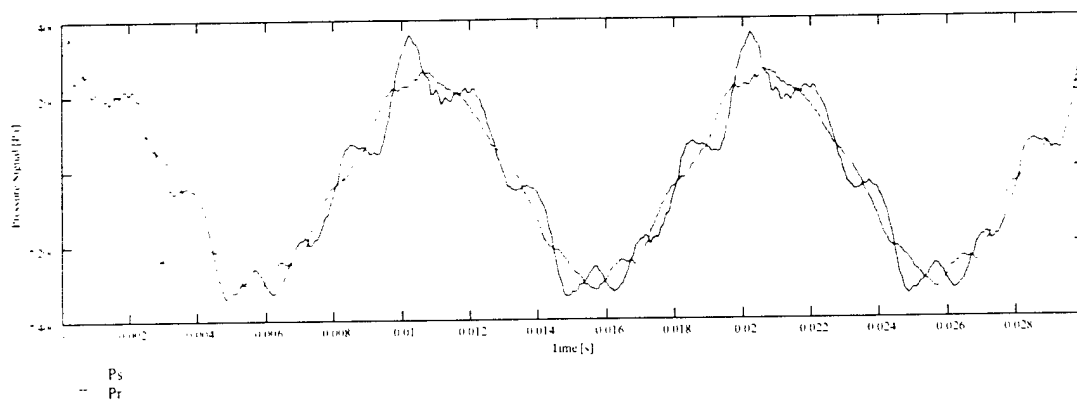
**Fig. 13.25.** Example 3. Pressure signal consists of: 100Hz at 100% amplitude + random at 25% amplitude. Prms=200Pa. Ps (red line) is the true signal and Pr (blue line) is the recorded signal.
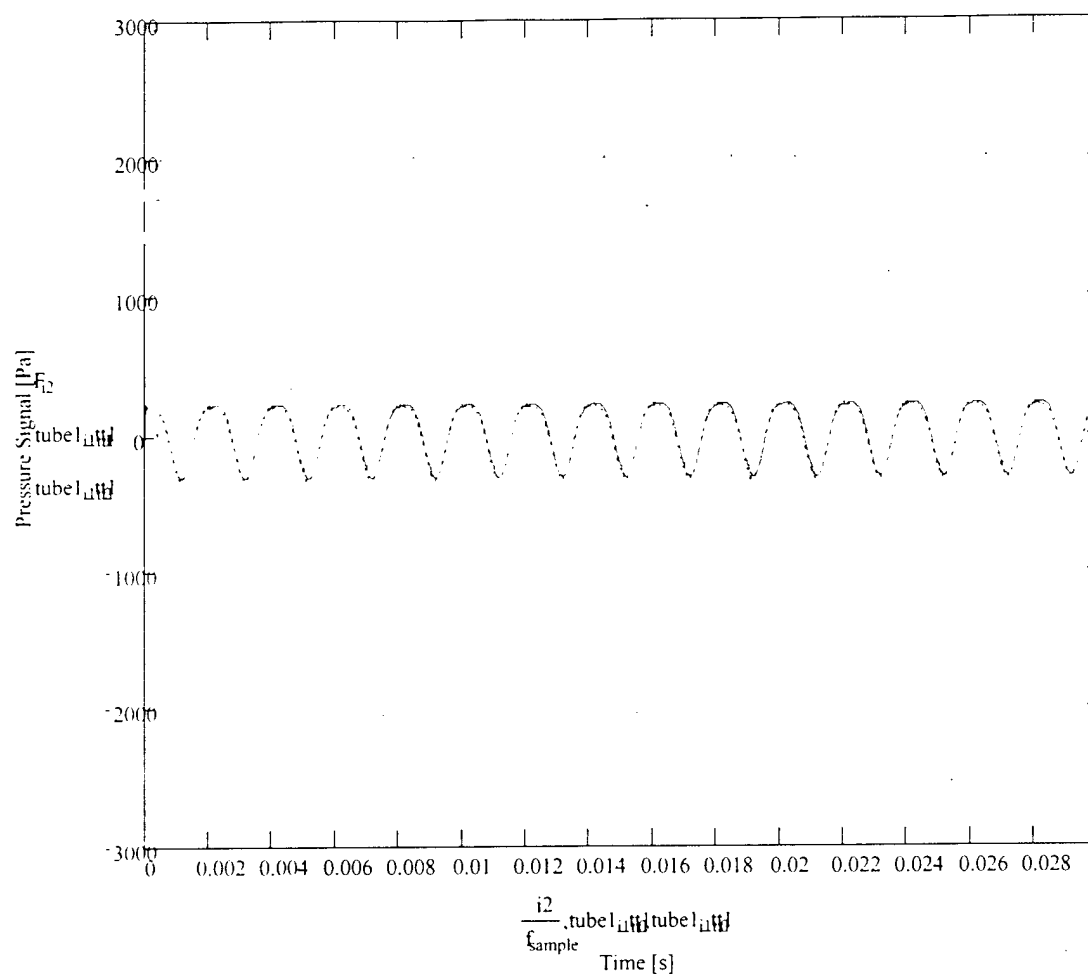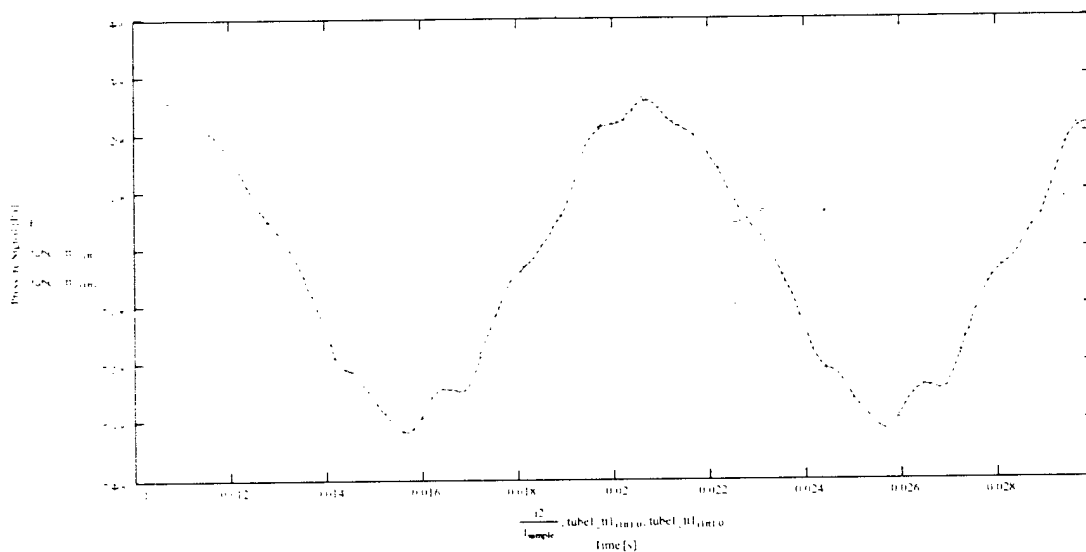


**Fig. 13.26.** Reconstructed signal for Example 3. The green dashed line is the recorded signal, the blue dotted line is the true signal, while the red solid line is the reconstructed signal.
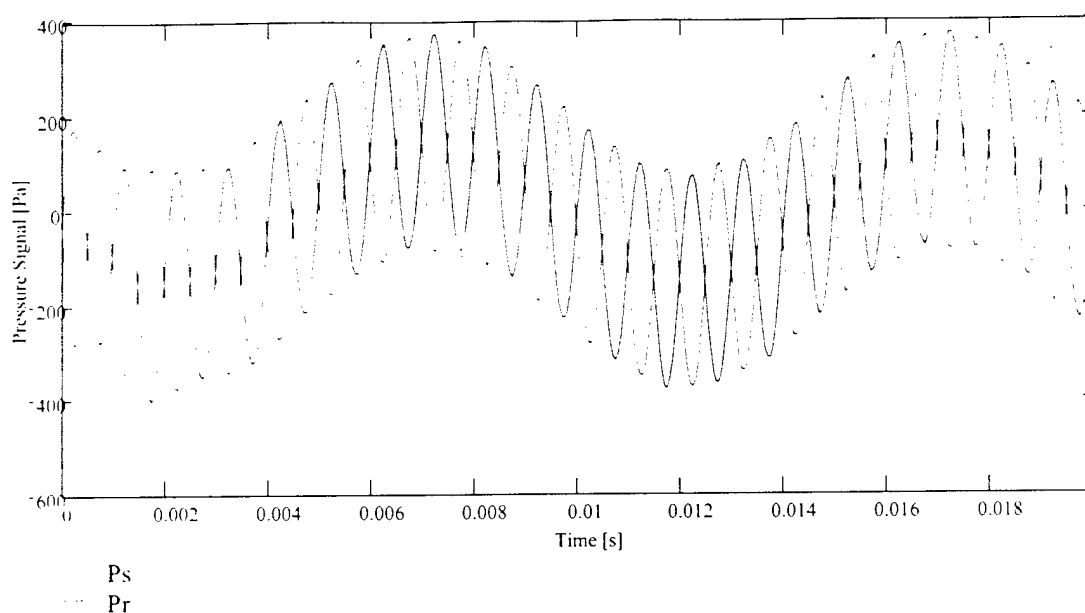
Fig. 13.27. Example 4. Pressure signal consists of: random at 100% amplitude. Prms=200Pa. Ps (red line) is the true signal and Pr (blue line) is the recorded signal.
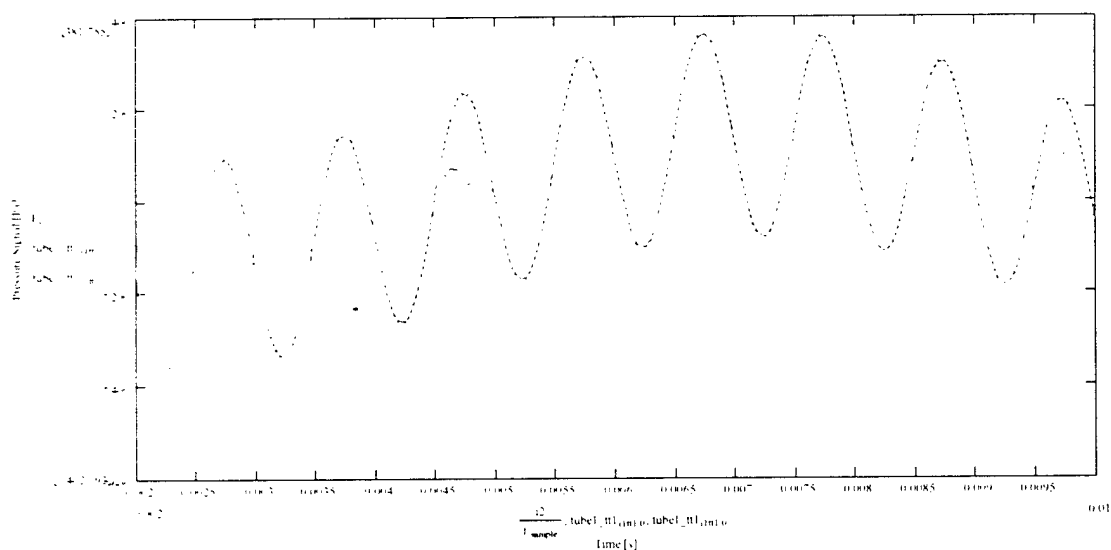


Fig. 13.28. Reconstructed signal for Example 4. The green dashed line is the recorded signal, the blue dotted line is the true signal, while the red solid line is the reconstructed signal.
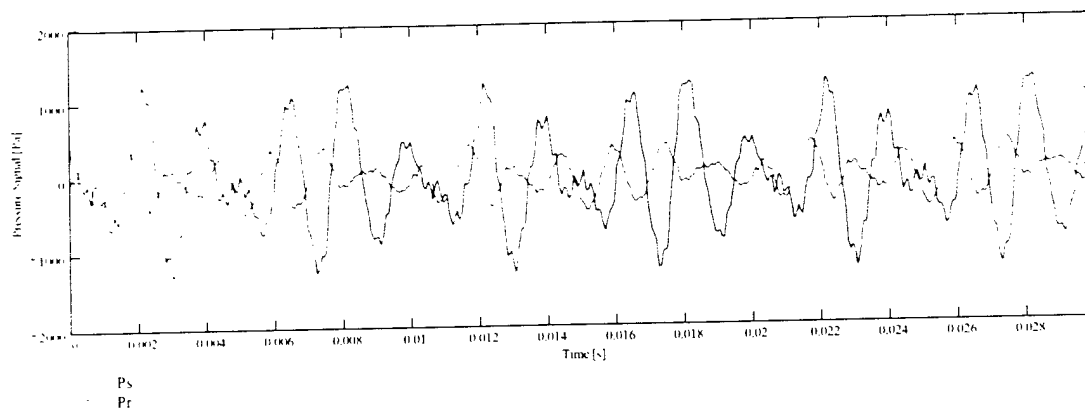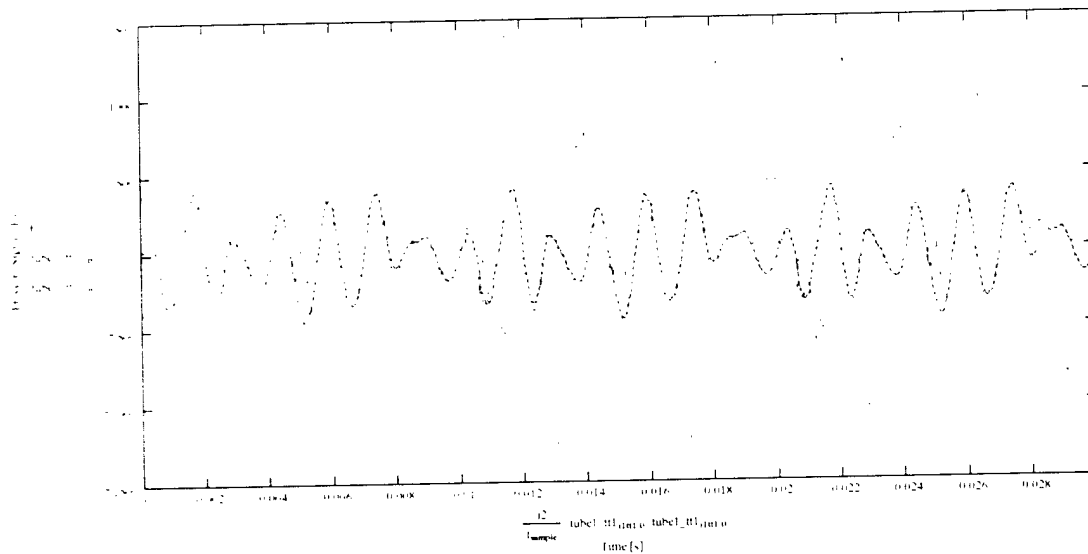
# 14. ACKNOWLEDGEMENTS

# 15. REFERENCES

Albone, C. M., "Fortran Programmes for Axisymmetric Potential Flow Around Closed and Semi-Infinite Bodies," A.R.C., C.P. 1216, London, 1972.

Ainsworth, R. W., Allen, J. L. and Batt, J. J., 1995, "The Development of Fast Response Aerodynamic Probes for Flow Measurement in Turbomachinery," Journal of Turbomachinery, Vol. 117, pp. 625-634.

Benade, A. H. and Ibisi, M. I., 1987, "Survey of Impedance Methods and a New Piezo-Disk-Driven Impedance Head for Air Columns," J. Acoust. Soc. Am., 81, pp 1152-1167.

Bergh, H., Tijdeman, H., " Theoretical and Experimental Results for the Dynamic Response of Pressure Measuring Systems," NLR-TR F.238, Dutch National Aerospace Laboratory, 1965.

Bryer, D.W. and Pankhurst, R. C., 1971, "Pressure-Probe Methods for Determining Wind Speed and Flow Direction," Her Majesty's Stationary Office / National Physics Laboratory, The Campfield Press, St. Albans.

Castorph, D., and Raabe, J., "Measurement of Unsteady Pressure Unsteady Relative velocity Field of a Kaplan Runner by Means of an Electronic Multi-miniature Probe as a Basic Contribution to Research on Unsteady Runner Load," *Proceedings of the 7$^{th}$ IAHR Symposium*, Vienna, 1974.

Centolanzi, F. J., 1957, "Characteristics of a 40° Cone for Measuring Mach Number, Total Pressure and Flow Angles at Supersonic Speeds," NACA TN 3967.

Chepren, W. P. and Franke, M. E., 1988, "A Numerical Method for Transients in Fluid Lines with Unsteady Friction."

Clark, E. L., Henfling, J. F. and Aeschliman, D. P., 1992, "Calibration of Hemispherical-Head Flow Angularity Probes," AIAA-92-4005, 17$^{th}$ Aerospace Ground Testing Conference, Nashville, Tennessee.

Cooper, M. and Webster, R. A., 1951, "The Use of an Uncalibrated Cone for Determination of Flow Angles and Mach Numbers at Supersonic Speeds," NACA TN 2190.

Davis, P. A. and Zasimowich, R. F., 1985, "High Frequency Dynamic Pressure Calibration Technique," ISA Paper #85-0109

Davis, W. T., 1958, "Lag in Pressure Systems at Extremely Low Pressures," NACA TN 4334.

Demuth, H. and Beale, M., "Matlab Neural Network Toolbox," The Mathworks, Inc., Massachusetts, December 1997.

Dominy, R. G. and Hodson, H. P., 1993, "An Investigation of Factors Influencing the Calibration of Five-Hole Probes for Three Dimensional Flow Measurement," J. Turbomachinery, Vol. **115**, pp.513-519.

Everett, K. N., Gerner, A. A. and Durston, D. A., "Seven-Hole Cone Probes for High Angle Flow Measurements: Theory and Calibration," AIAA Journal, Vol. 21, No. 7, July 1983, pp. 992-998.

Everett, K. N., Gerner, A. A. and Durston, D. A., 1982, "Theory and Calibration of Non-Nulling Seven-Hole Cone Probes for Use in Complex Flow Measurement," AIAA-82-0232, 20th Aerospace Sciences Meeting, Orlando, Florida.

Fan, X., Herbert T. and Haritonidis, J. H., "Transition Control with Neural Networks," AIAA Paper No. 95-0674, Reno, Nevada, January 1995.

Fausett, L., "Fundamentals of Neural Networks Architectures, Algorithms, and Applications," Prentice Hall, Englewood Cliffs, N.J., 1994.

Flanagan, M. J. and Hiltner, D. W., 1993, "Calibration of a Transonic 5-Hole Probe for a Multi-Element Airfoil Cascade Facility," AIAA-93-2471, 29th Joint Propulsion Conference and Exhibit, Monterey, California.

Franke, M. E. and Pletcher, J. H., 1985, "Response of an External Transducer for Measuring Dynamic Pressure in Hydraulic Lines," ISA Paper #85-108, pp. 51-58.

Franke, M. E., "Dynamic Pressure Measurements in Pneumatic Lines," ISA Paper #86-0106, pp. 57-63.

Franke, M. E. and Chepren, W. P., 1987, "Flow Effects on Dynamic Pressure Measurements," ISA Paper #87-0207, pp. 73-77.

Freeman, J.A. and Skapura, D.M., "Neural Networks Algorithms, Applications and Programming Techniques," Addison-Wesley, 1992.

Fuchs, H.V., "Measurement of Pressure Fluctuations within Subsonic Turbulent Jets," *J. of Sound and Vibration*, Vol. 22, No. 3, 1972, pp. 361-378.

Gallington, R. W., "Measurements of Very Large Flow Angles with Non-Nulling Seven-Hole Probe," Aeronautic Digest - Spring/Summer 1980 , USAFA-TR-80-17, USAF Academy.

Gerner, A. A. and Maurer, C. L., 1981, "Calibration of Seven-Hole Probes Suitable for High Angles in Subsonic Compressible Flows," United States Air Force Academy (USAFA) -TR-81-4.

Gerner, A. and Sisson, G., 1981, "Seven-Hole Probe Data Acquisition System," USAFA-TN-81-8.

Gettelman, C. C. and Krause, L. N., 1951, "Characteristics of a Wedge with Various Holder Configurations for Static-Pressure Measurements in Subsonic Gas Streams," NACA RM E51G09.

George, W.K., Beuther, P.D. and Arndt, R.E.A., "Pressure spectra in turbulent free shear flows," *J. Fluid Mech.*, Vol. 148, 1984, pp. 155-191.

Giess, P. A., Rehder, H. J. and Kost, F., 2000, "A New Test Facility for Probe Calibration – Offering Independent Variation of Mach and Reynolds Number," Proceeding of the XVth Bi-Annual Symposium on Measuring Techniques in Transonic and Supersonic Flow in Cascades and Turbomachines, Firenze.

Gizzi, W. P. and Gyarmathy, G., 1998, "Correction of Time-Dependent Aerodynamic Measurement Errors of Fast-Response Probes," XIVth Symposium on Measuring Techniques for Transonic and Supersonic Flows in Cascades and Turbomachines.

Gonsalez, J. C. and Arrington, E. A., 1999, "Five-Hole Flow Angle Probe Calibration for the NASA Glenn Icing Research Tunnel," NASA CR-1999-202330.

Gossweiler, C.R., Kupferschmied, K. and Gyarmathy, G., "On Fast-Response Probes: Part 1- Technology, Calibration and Application to Turbomachinery," *presented at the International Gas Turbine and Aeroengine Cogress and Exposition,* The Hague, Netherlands, June, 1994.

Hagan, M., Demuth, H. and Beale, M., "Neural Network Design," PWS Publishing Company, Boston, Mass., 1996.

Hamming, R. W., 1973, Numerical Methods for Scientists and Engineers," McGraw-Hill, New York.

Hassoun, M.H., "Fundamentals of Artificial Neural Networks" The MIT Press, Mass., 1995.

Helmholtz, H., 1885, "On the Sensations of Tone," Dover Publications, New York.

Hemke, P. E., 1927, "The Measurement of Pressure Through Tubes in Pressure Distribution Tests," NACA Report 270, pp. 301-311.

Hoang, H. T., "The Hemisphere-Cylinder at an Angle of Attack," Ph.D. Dissertation, Department of Engineering Mechanics, Virginia Polytechnic Institute, Dec. 1991.

Holman, J. P., 1994, "Experimental Methods for Engineers," 6th ed. McGraw-Hill, New York.

Holmes, J. D. and Lewis, R. E., 1987, "Optimization of Dynamic Pressure Measurement Systems. II. Parallel Tube Manifold Systems," Journal of Wind Engineering and Industrial Aerodynamics, 25, pp. 275-290.

Hougen, J. O., Martin, O. R. and Walsh, R. A., 1963, "Dynamics of Pneumatic Transmission Lines," Control Engineering, pp. 114-117.

Houtman, E.M. and Bannink, W.J., "The Calibration and Measuring Procedure of a Five-Hole Hemispherical Head Probe in Compressible Flow," Report LR-585, Delft University of Technology, April 1989.

Humm, H. J., Gizzi, W. P., Gyarmathy, G., "Dynamic Response of Aerodynamic Probes in Fluctuating 3D Flows," Proceeding of the 12th Symposium on Measuring Techniques for Transonic and Supersonic Flows in Cascades and Turbomachines, Academies of Sciences of the Czech Republic, Prague 1994.

Humm, H.J., Gossweiler, C.R. and Gyarmathy, G., "On Fast-Response Probes: Aerodynamic Probe Design Studies," presented at the International Gas Turbine and Aeroengine Cogress and Exposition, The Hague, Netherlands, June, 1994.

Huston, W. B., 1946 "Accuracy of Airspeed Measurements and Flight Calibration Procedures," NACA TR 919, pp. 499-534.

Iberall, A. S., " Attenuation of Oscillatory Pressure in Instrumentation Lines," RP2115, National Bureau of Standards, Volume 45, July 1950, pp 85-108.

Johansen, E. S., Rediniotis, O. K., Jones, G., "The Compressible Calibration of Miniature Multi-Hole Probes," Journal of Fluids Engineering, March 2001, pp 128-139.

Jiang, Y. C. Tai, K. Walsh, T. Tsao, G. W. Lee and C. H. Ho, "A Flexible MEMS Technology and Its First Application to Shear Stress Sensor Array," Proceedings of 9th IEEE MEMS Workshop, Nagoya, Japan, 1997, pp. 465-470.

Johansen, E. S., Rediniotis, O. K. and Jones, G., 2001, "The Compressible Calibration of Miniature Multi-Hole Probes," JFE, Vol. 123, pp. 128-138.

Johnson, G. H. and Reed, L. S., 1985, "Seven Hole Probe in Shear Flow," AIAA-85-0076, 23rd Aerospace Sciences Meeting, Reno, Nevada.

Kalvesten, E., L. Smith, L. Tenerz and G. Stemme, "The First Surface Micromachined Pressure Sensor for Cardiovascular Pressure Measurements," *IEEE MEMS'98*, Heideberg, Germany, 1998. pp. 574-579.

Karam, J. T. and Franke M. E., 1967, "The Frequency Response of Pneumatic Lines," Journal of Basic Engineering, pp. 371-378.

Kerrebrock, J.L., et al., "A Miniature High Frequency Sphere Probe," *Proceedings of ASME Symposium on Measurement Methods in Rotating Components of Turbomachinery*, editors B. Lakshminarayana and P. Runstadler, ASME 1980, pp. 91-98.

Kinser, R.E. and Rediniotis, O.K., "Development of A Nearly-Omni-Directional, Three Component Velocity Measurement Pressure Probe," AIAA Paper No. 96-0037, 34th AIAA Aerospace Sciences Meeting, Reno, Nevada, January 1996.

Kjelgaard, S.O., "Theoretical Derivation and Calibration Technique of a Hemispherical-Tiped, Five-Hole Probe", NASA Technical Memorandum 4047, 1988.

Kline, S. J. and McClintock, F. A., 1953, "Describing Uncertainties in Single-Sample Experiments," ASME Mechanical Engineering, Vol. **75**, pp. 3-8.

Kovasznay, L. S. G., et al., "Instantaneous Pressure Distribution Around a Sphere in Unsteady Flow," Journal of Fluids Engineering, December 1982, pp 497-502.

Kovasznay, L. S. G. and Chih-Ming, H., 1975, "Static Pressure Rise in Acoustically Driven Cavities," AIAA Journal, **13**, pp. 1403-1404.

Krause, L. K. and Dudzinski, T. J., 1969, "Flow Direction Measurement with Fixed Position Probes in Subsonic Flow over a Range of Reynolds Number," Proceedings for 15th International Aerospace Symposium, Las Vegas, Nevada.

Landweber, L., "The Axially Symmetric Potential Flow About Elongated Bodies of Revolution, "Rep. Taylor Model Basin, Washington, No. 761, 1951.

Larson, T. J., Whitmore, S. A., Ehernberger, L. J., Johnson, J. B. and Siemers, P. M., "Qualitative Evaluation of a Flush Aft data System at Transonic Speeds and High Angles of Attack," NASA TP-271 6, 1987.

Larson, T. J., Moes, T. R. and Siemers, P. M., "Wind Tunnel Investigation of a Flush Airdata System at Mach Numbers From 0.7 to 1.4," NASA TM-101697, 1990.

Lin, L., W. Yun, H-C Chu and M. Chiao, "Surface Micromachined Diaphragm Pressure Sensors with Optimized Piezoresistive Sensing Resistors," *IEEE TENCON'95*, Hong Kong, 1995, pp. 24-27.

Lisec, T., M. Kreutzer and B. Wagner, "Surface Micromachined Piezoresistive Pressure Sensors with Step-Type Bent and Flat Membrane Structures," *IEEE Trans. Electr. Dev.*, Vol. 43, No. 9, Sept. 1996, pp. 1547-1552.

Liu, J., *Integrated Micro Devices for Small Scale Gaseous Flow Study*, Ph.D. Thesis, California Institute of Technology, 1995.

Loehrke, R. I. and Nagib H. M., 1972, "Experiments on Management of Free-Stream Turbulence," AGARD-R-598.

Lotz, I., "Calculation of Potential Flow Past Airship Bodies in Yaw," NACA TM 675, Washington, July, 1932.

Maskell, E. C., "Flow Separation in Three Dimensions," R.A.E. Rept. 2565, Nov. 1955.

Matsunaga, S., Ishibashi, H., and Nishi, M., "Measurement of Instantaneous Pressure and Velocity in Nonsteady Three-Dimensional Water Flow by Means of a Combined Five-Hole Probe," *Transaction of the AME J. of Fluid Engineering*, Vol. 102, 1980, pp. 196-202.

Meade, A. J., and Schiff, L. B., "Experimental Study of Three Dimensional Separated Flow Surrounding a Hemisphere-Cylinder at Incidence," AIAA Paper 87-2492-CP, Aug. 1987.

Meier, H. U., and Kreplin, H. P., "Experimental Investigations of Boundary Layer Transition and Separation on a Body of Revolution," Z. Flugwiss Weltraumforschung, Vol. 4, 1980, pp. 65-71.

Moffat, R.J., "Contributions to the Theory of Single-Sample Uncertainty Analysis," Transactions of the ASME, Vol. 104, June 1982.

Munk, M. M., "Airship Theory," NACA Repts., 184 and 191, 1923/24.

Naughton, J.W., Cattafesta III, L.N., and Settles, G.S., "Miniature Fast-Response Five-Hole Conical Probe for Supersonic Flowfield Measurements," *AIAA J.*, Vol. 31, No. 3, 1993, pp. 453-458.

Ng, W.F. and Popernack, Jr., T.G., "Combination Probe for Hi-Frequency Unsteady Aerodynamic Measurements," *IEEE Transactions on Aerospace and Electronic Systems*, Vol. 24, No.1, 1988, pp. 76-84.

Nichols, N. B., 1962, "The Linear Properties of Pneumatic Transmission Lines," ISA Transactions 1, pp. 5-14.

Ohman, L. H., 1995, "Torque and Thrust From Five-Hole Pressure Probe Measurements in the near Slipstream of a Propeller in Compressible Flow," NRC Canada, IAR-AN-81.

Ohman, L. H. and Nguyen, V. D., 1993, Applications of the Five-Hole Probe Technique for Flow Field Surveys at the Institute for Aerospace Research," Presented at the AGARD Meeting on Wall Interference, Support Interference and Flow Field Measurements, pp. 4.1-4.11.

Ostowari, C. and Wentz, W. H., 1983, "Modified Calibration Technique of a Five-Hole Probe for High Flow Angles," Experiments in Fluids **1**, pp. 166-168.

Paniagua, G. and Denos, R., 2000, "Numerical Compensation in the Time Domain of Pressure Sensors," VKI RP 2000-59, Proceedings of the 15th Symposium on Measuring Techniques for Transonic and Supersonic Flow in Cascades and Turbomachines, Firenze, Italy.

Payne, F. M., Ng, T. T. and Nelson, R. C., 1989, "Seven Hole Probe Measurement of Leading Edge Vortex Flows," Experiments in Fluids **7**, pp. 1-8.

Rayleigh, J. W. S., 1894, "The Theory of Sound," Dover Publications, New York.

Rediniotis, O. K., Klute, S. M., Hoang, N. T. and Telionis, D. P., "Pitching-up Motions of a Delta Wing." AIAA Journal, Vol. 32, April 1994, pp. 716-725.

Rediniotis, O. K., " The Transient Development of Vortices Over a Delta Wing," Doctoral Dissertation, VPI & SU, October 1992.

Rediniotis, O. K., Hoang, N. T., and Telionis, D. P., "The Seven-Hole Probe: Its Calibration and Use." (invited paper) Forum on Instructional Fluid Dynamics Experiments, Vol. 152, June 1993, pp. 21-26.

Rediniotis, O.K. and Chrysanthakopoulos, G., "A Wide-Range, High-Accuracy Neural/Fuzzy Calibration Technique for Flow-Diagnostics Instrumentation," AIAA Paper No 95-0020, 33rd Aerospace Sciences Meeting, Reno, Nevada, Jan. 1995.

Rediniotis, O.K. and Chrisanthakopoulos, G., "A Wide-Range, High-Accuracy Neural/Fuzzy Calibration Technique for Flow-Diagnostics Instrumentation," _Journal of Fluids Engineering_, Vol. 120, No. 1, pp. 95-101, March 1998.

Rediniotis, O.K., Johansen, E., Tsao, T., Seifert, A. and Pack, L., "MEMS-Based Probes for Velocity and Pressure Measurements in Unsteady and Turbulent Flowfields," AIAA Paper No. 99-521, 37th Aerospace Science Meeting and Exhibit, January 1999, Reno, Nevada.

Rediniotis, O. K. and Pathak, M. M., "A Simple Technique for Frequency Response Enhancement of Miniature Pressure Probes," _AIAA Journal_, Vol. 37, No. 7, pp. 897-899, July 1999.

Rediniotis, O. K. and Kinser, R. E., 1998, "Development of a Nearly Omnidirectional Velocity Measurement Pressure Probe," AIAA Journal, Vol. 36, No. 10, pp. 1854-1860.

Rediniotis, O. K. and Vijayagopal, R., 1999, "Miniature Multihole Pressure Probes and Their Neural-Network-Based Calibration," AIAA Journal, Vol. **37**, No. 6, pp. 666-674.

Reed, L., Mattingly, J. D. and Jonas, F. M., 1984, "The Seven-Hole Probe," USAFA-TN-84-9.

Reichert, B. A. and Wendt, B. J., 1994, "A New Algorithm for Five-Hole Probe Calibration, Data Reduction, and Uncertainty Analysis," NASA TM 106458.

Rohloff, T., J., "Development and Evaluation of Neural Network Flush Airdata Sensing Systems," Ph.D. Dissertation, University of California Los Angeles, Department of Mechanical Engineering, May 1998.

Rousso, M. D. and F. D. Kochendorfer, 1951, "Velocity and Temperature Fields in Circular Jet Expanding from Chocked Nozzle into Quiescent Air," NACA RM E51F18.

Shepherd, I. C., 1981, "A Four Hole Pressure Probe for Fluid Flow Measurements in Three Dimensions," JFE, Vo. **103**, pp. 590-594.

Scharrer, G. L. and Lilley, D. G., 1984, "Five-Hole Probe Measurements of Swirl, Confinement and Nozzle Effects on Confined Turbulent Flow," AIAA-84-1605, 17th Fluid Dynamics, Plasma Dynamics and Laser Conference, Snowmass, Colorado.

Schlichting, H., "Boundary-Layer Theory," McGraw-Hill Book Company, New York, Seventh Edition, 1979.

Schreck, S. J., Faller, W. E., and Luttges, M. W., "Neural Network Prediction of Three-Dimensional Unsteady Separated Flow Fields," AIAA Paper No. 93-3426-CP, Monterey, CA, August 1993.

Schreck, S. J. and Faller, "Encoding of Three-Dimensional Unsteady Separated Flow Field Dynamics in Neural Network Architectures," AIAA Paper No. 95-0103, Reno, Nevada, January 1995.

Schubauer, G. B., Spangenberg, W. G. and Klebanoff, P. S., 1948, "Aerodynamic Characteristics of Damping Screens," NACA TN 2001.

Scutte, P. C., Cate, K. H. and Young, S. D., 1985, "A Dynamic Pressure Calibration Standard," ISA Paper #85-0110.

Senoo, Y., Kita, Y. and Ookuma, K., "Measurement of Two-Dimensional Periodic Flow With a Cobra Probe," *Transactions of the AME J. of Fluid Engineering*, 1973, pp. 295-300.

Siddon, T.E., "On the Response of Pressure Measuring Instrumentation in Unsteady Flow," Univ. of Toronto Inst. Aerospace Rep. 136, 1969.

Sinclair, A. R. and Robins, A. W., 1952, "A Method for the Determination of the Time Lag in Pressure Measuring Systems Incorporating Capillaries," NACA TN 2793.

Strunk, R. D., 1971, "Frequency Response of Fluid Lines With Nonlinear Boundary Conditions," Journal of Basic Engineering, pp. 365-372.

Taback, I., 1949, "The Response of Pressure Measuring Systems to Oscillating Pressures," NACA TN 1819.

Takahashi, T. T., 1997, "Measurement of Air Flow Characteristics Using Seven-Hole Cone Probes," NASA TM 112194.

Tamigniaux, T. L. B. and Oats, G. C., 1985, "An Experimental Investigation of the Effect of a Nearby Solid Surface on a Five-Hole Pressure Probe," AIAA-85-0334, 23rd Aerospace Sciences Meeting, Reno, Nevada.

Tijdeman, H., 1969, "Remarks on the Frequency Response of Pneumatic Lines," Journal of Basic Engineering, pp. 325-327.

Traub, L. W., "Prediction of Tunnel Wall Upwash For Delta Wings Including Vortex Breakdown Effects," *The Aeronautical Journal*, Vol. 103, No. 1021, 1999, pp. 139-142.

Traub, L. W., "Prediction of Vortex Breakdown and Longitudinal Characteristics of Swept Slender Planforms," *Journal of Aircraft*, Vol. 34, No. 3, 1997, pp. 353-359.

Traub, L. W., "Prediction of Delta Wing Leading Edge Vortex Circulation and Lift-Curve Slope," *Journal of Aircraft*, Vol. 34, No. 3, 1997, pp. 450-452.

Traub, L. W., "A Theoretical and Experimental Investigation of Biplane Delta Wings," *Journal of Aircraft*, Vol. 38, No. 3, 2001, pp.

Treiber, M., Kupferschmied, P. and Gyarmathy, G., Proc. 14th Symposium on Measuring Techniques for Transonic and Supersonic Flows in Cascades and Turbomachines, Limerick, Ireland.

Vandrey, F., "A Method for Calculating the Pressure Distribution of a Body of Revolution Moving in a Circular Path Through a Perfect Incompressible Fluid," A.R.C. R&M 3139, Dec. 1953.

Wenger, C. and Devenport, W., 1998, "A Seven-Hole Pressure Probe Measurement System and Calibration Method Utilizing Error Tables," AIAA Paper No. 98-0202, 36th AIAA Aerospace Sciences Meeting, Reno, Nevada.

Whitmore, S. A, Davis, R. J. and Fife, J. M., "In-Flight Demonstration of a Real-Time Flush Airdata Sensing System," AIAA Journal of Aircraft, Vol. 33, Number 5, pp. 970-977, September-October 1996.

Whitmore, S. A., Cobleigh, B. R. and Haering, E. A., "Design and Calibration of the X-33 Flush Airdata Sensing System," NASA TM 1998-206540, January 1998.

Whitmore, S. A., Heeg, J., Larson, T. J., Ehernberger, L. J., Hagen, F. W. and DeLeo, R. V., 1987, "High-Angle-of-Attack Pneumatic Lag and Upwash Corrections for a Hemispherical Flow Direction Sensor," NASA TM 86790.

Whitmore, S. A., 1988, "Formulation of a General Technique for Predicting Pneumatic Attenuation Errors in Airborne Pressure Sensing Devices," NASA TM 100430.

Whitmore, S. A., Lindsey, W. T., Curry, R. E. and Gilyard, G. B., 1990, "Experimental Characterization of the Effects of Pneumatic Tubing on Unsteady Pressure Measurements," NASA TM 4171.

Whitmore, S. A. and Leondes, C. T., 1990, "Compensating for Pneumatic Distortion in Pressure Sensing Devices," NASA TM 101716.

Whitmore, S. A. and Moes, T. R., 1991, "The Effects of Pressure Sensor Acoustics on Airdata Derived From a High-Angle-of-Attack Flush Airdata Sensing (HI-FADS) System," NASA TM 101736.

Whitmore, S. A. and Leondes, C. T., 1991, "Pneumatic Distortion Compensation for Aircraft Surface Pressure Sensing Devices," AIAA J. Aircraft, 28, pp. 828-836.

Whitmore, S. A., Petersen, B. J. and Scott, D. D., 1996, "A Dynamic Response Model for Pressure Sensors in Continuum and High Knudsen Number Flows with Large Temperature Gradients," NASA TM 4728.

Wildhack, W. A., 1937, "Pressure Drop in Tubes in Aircraft Instrument Installations," NACA TR 593.

Ying, S. X., Schiff, L. B., and Steger, J. L., "A Numerical Study of Three Dimensional Separated Flow Past a Hemisphere Cylinder," AIAA Paper 87-1207, June, 1987.

Zeiger, M. D. and Schaeffler, N. W., 2001, "Correcting Multi-Hole Probe Alignment Bias Errors Post Calibration," AIAA-2001-0900, 39th Aerospace Sciences Meeting and Exhibit, Reno, Nevada.

Zeiger, M. D. and Chalmeta, L. P., 1998, "Tip Geometry Effects on Calibration and Performance of Seven-Hole Probes," AIAA-98-2810, 29th Fluid Dynamics Conference, Albuquerque, New Mexico.

Zilliac, G.G., "Modeling, Calibration, and Error Analysis of Seven-Hole Pressure Probes," Experiments in Fluids, Vol. 14, pp. 104-120, 1993.

Zilliac, G.G., "Calibration of Seven-Hole Probes For Use in Fluid Flows With Large Angularity," NASA TM 102200, December 1989.

# 18. PUBLICATIONS RESULTING FROM THIS WORK

Rediniotis, O. K. and Vijayagopal, R., "Miniature Multi-Hole Pressure Probes and Their Neural-Network-Based Calibration," *AIAA Journal*, Vol. 37, No. 6, pp. 666-674, June 1999.

Rediniotis, O. K. and Pathak, M. M., "A Simple Technique for Frequency Response Enhancement of Miniature Pressure Probes," *AIAA Journal*, Vol. 37, No. 7, pp. 897-899, July 1999.

Rediniotis, O. K., Johansen, E. S. and Jones, G., "The Compressible Calibration of Miniature Multi-Hole Probes," *Journal of Fluids Engineering*. Vol. 123, pp. 128-138, March 2001.

Traub, L. W. and Rediniotis, O. K., "Theoretical Prediction of the Pressure Distribution on a Hemisphere-Cylinder," *Journal of Aircraft* (in press).

Johansen, E. and Rediniotis, O.K., "Development of an Unsteady Flow Facility for the Calibration of High-Frequency-Response Multi-Hole Probes," *AIAA Journal* (in review).

Johansen, E. and Rediniotis, O.K., "Unsteady Calibration of Miniature Multi-Hole Probes," *AIAA Journal* (in preparation).

Allen, R. Traub, L. Johansen, E., Rediniotis, O. K. and Tsao, T. "A MEMS-Based Five-Sensor Probe." AIAA Paper No. 2000-0621, 38th Aerospace Science Meeting and Exhibit, January 2000, Reno, Nevada.

Rediniotis, O.K., Johansen, E., Tsao, T., Seifert, A. and Pack, L., "MEMS-Based Probes for Velocity and Pressure Measurements in Unsteady and Turbulent Flowfields," AIAA Paper No. 99-521, 37th Aerospace Science Meeting and Exhibit, January 1999, Reno, Nevada.

# APPENDIX: SUCCESS STORIES

# OUR PROBES AND THE X-34
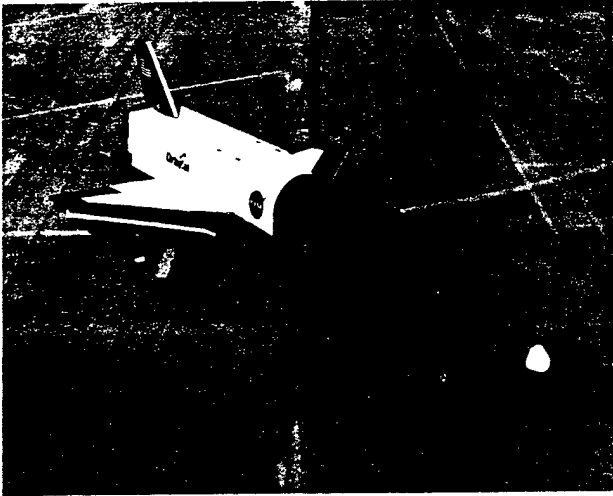


One of our customers, Orbital Sciences Corporation of Dulles, Virginia, is the primary NASA contractor for the X-34 flight vehicle. The X-34, a single-engine rocket plane, will fly itself using onboard computers. The vehicle is approximately 58 feet long, 28 feet wide at wing tip and 11 feet tall from the bottom of the fuselage to the top of the tail.

The X-34 launches from an L-1011 airliner and reaches altitudes of up to 250,000 feet and travel up to eight times faster than the speed of sound.
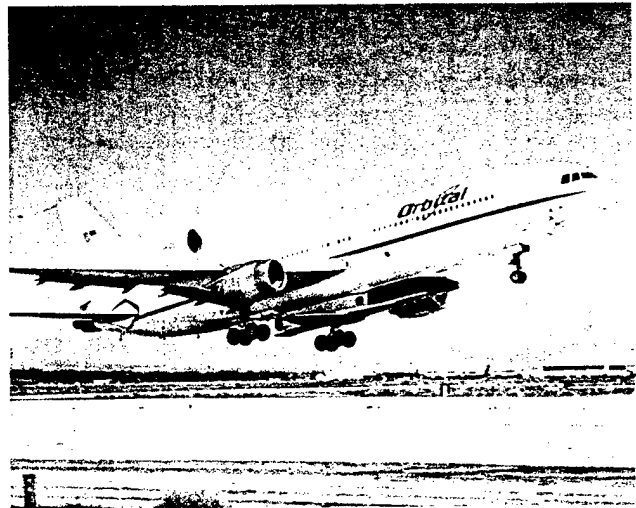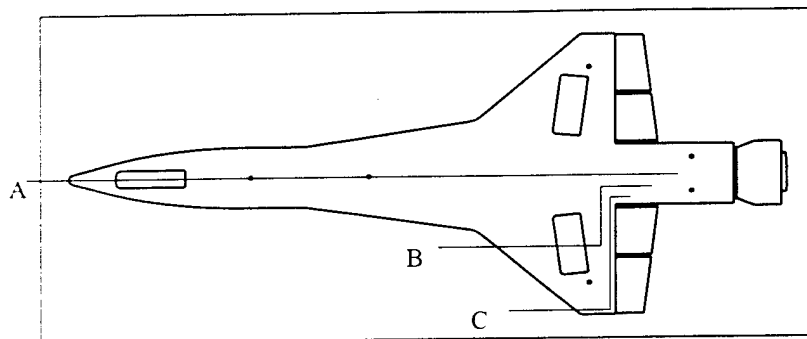
Orbital has been utilizing our line of seven-hole probes beginning with the wind tunnel testing of the X-34. Orbital tested a 1/30 scale model of the X-34 and the L-1011 in the wind tunnel of Calspan Corp. The X-34 model was equipped with three custom designed seven-hole probes, one in the nose and two on the wing, as shown in the figure above (probes labeled A, B and C). Three-dimensional velocity data was sampled from the probes as the X-34 model was moved away from the L-1011 model, simulating the drop tests, scheduled to be conducted later.

In addition to the wind tunnel tests, Orbital also utilized a set of seven-hole probes on the full-scale drop test model. Three probes were again used in the same locations as the wind tunnel model. For these tests, the X-34 will be mounted underneath the L-1011 and flown on "captive-carry" flights to allow the Federal Aviation Administration to approve modifications to the L-1011.
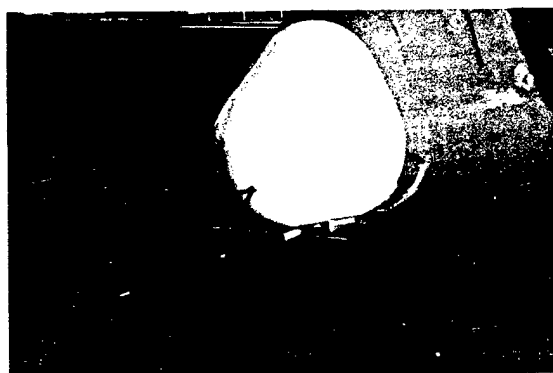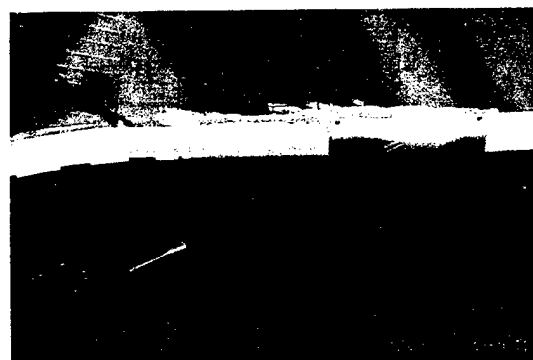




When powered flights begin for X-34, the demonstrator will be carried aloft and separate from the L-1011 before igniting its rocket engine. Following the powered portion of flight, the un-piloted X-34 will land horizontally, initially on a dry lakebed and eventually on a runway. **The pictures above and to the left show our probes installed on the wing and nose of the full-scale aircraft, respectively.**

201

# OUR PROBES HELP NASA
# AND BOEING STUDY THE AERODYNAMICS OF HIGH-LIFT
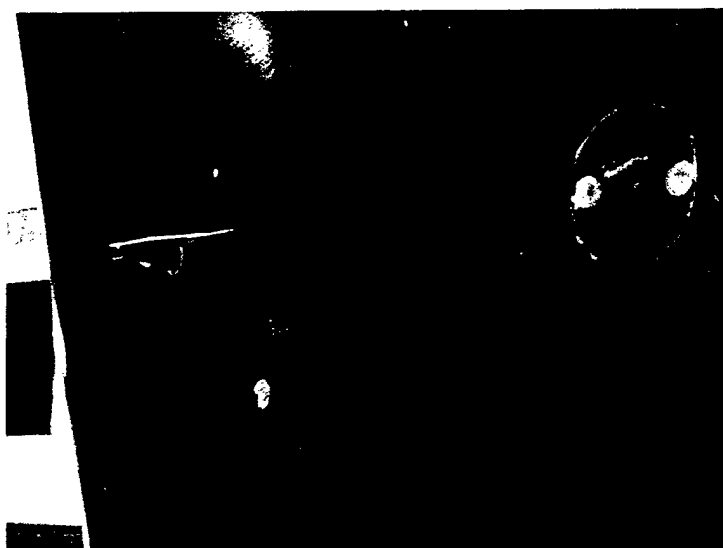# CONFIGURATIONS



*We joined NASA Langley, the Boeing Company and Aeroprobe Corp. in an effort to design and study novel high-lift wing configurations. The configuration to be tested was a 20% scale airliner wing, as shown in the figure on the left, installed in the test section of the 14'x22' tunnel of NASA Langley.*

*Four miniature 7-hole probes were designed and built. They were subsequently calibrated at the NASA Langley Flow Modeling and Control Branch. The four miniature 7-hole probes were identical and their design is illustrated in the figure below. It is worth-noticing that the probe tip diameter was only 0.065". The back of the probe was formed into a bullet-shape afterbody to minimize unsteady vortex-shedding effects. Each one of the ports on the probe tip communicates, through internal tubing and a 90-degree elbow, with one of the stainless steel connecting tubes.*

**0.065**        **0.25**

**0.750**      **1.500**      **0.500**

**2.875**

**Connecting Tubes**
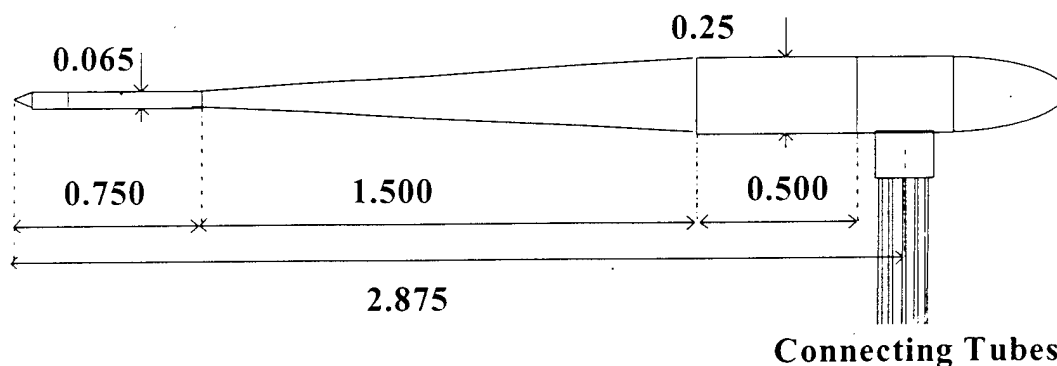
*All probes were calibrated at the NASA LaRC Probe Calibration Tunnel (PCT). This facility is a variable density pressure tunnel that can independently control Mach number, Reynolds number, and total temperature. The four probes were calibrated at Mach numbers ranging from 0.1 to 0.8, in increments of 0.1, and at free-stream total pressure of 17, 32 and 60 psi which yielded a Reynolds number (per unit length) range from $2.5 \cdot 10^6 m^{-1}$ to $52 \cdot 10^6 m^{-1}$. Angles can be predicted to within 0.6 degrees with 99 % confidence and velocity magnitudes can be predicted to within 1.0 % also with 99 % confidence, while the corresponding uncertainties (standard deviation of the error distribution) are less than 0.2 degrees in angle prediction and less than 0.35% in velocity magnitude prediction.*

*The figure above shows one of the probes installed on the wing.*

# Our Probes Used in DOE's Renewable Energy Research

DOE's National Renewable Energy Laboratory (NREL) is planning to test a 10-meter diameter research wind turbine in the world's largest wind tunnel. The test will use NASA's 24.4 by 36.6 meter (80' by 120') wind tunnel. The tunnel is part of the National Full-Scale Aerodynamics Complex (NFAC) at the NASA Ames Research Center in Moffett Field, (Silicon Valley) California and is primarily used for determining low- and medium-speed aerodynamic characteristics of full-scale aircraft and rotorcraft. The tunnel is powered by six 18,000-hp fans that produce test section wind velocities up to 50 m/s (115 mph).

The NREL "Unsteady Aerodynamics" research wind turbine is extensively instrumented to measure structural loads and aerodynamic responses of a rotating airfoil. We fabricated five 7-hole probes and installed them on one of the blades, as shown in the figure below. The probes are installed on special booms mounted on the blade leading edge and rotate with the blade. The probes provide measurements on the flow magnitude and direction, as seen by the blade. The turbine will be tested in the tunnel in a 2-bladed, fixed-pitch (stall-controlled) configuration. It will be operated at constant RPM with the rotor oriented upwind or downwind of the tower, and the hub in either rigid or damped-teetered configurations. An extensive range of pitch angles, pitch motions, yaw positions, and wind velocities are planned. NREL researchers focused wind tunnel test objectives to meet recommendations of an international science panel of wind turbine aerodynamics experts.
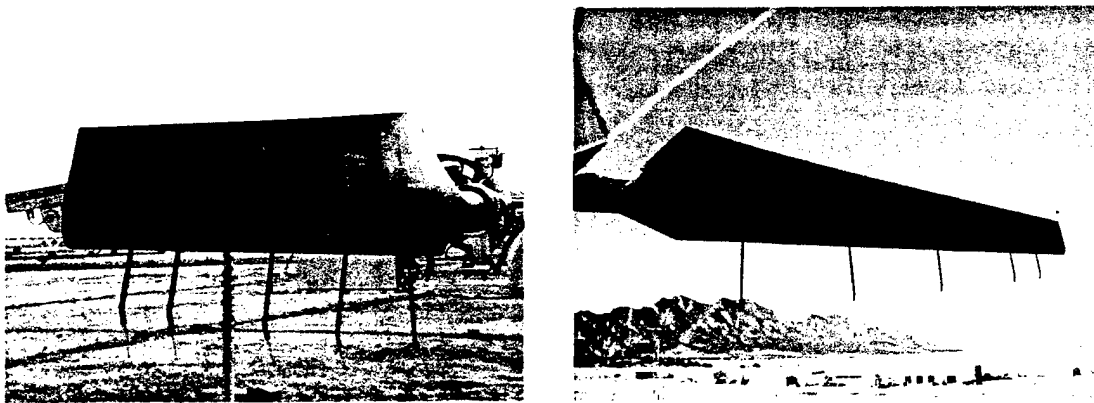


The five 7-hole probes were installed on one of the turbine blades to measure the flow magnitude and direction, as seen by the blade.

The NREL research turbine has been field-tested in various configurations since 1989 at DOE's National Wind Technology Center (NWTC) located near Boulder, Colorado. It has been operated in outdoor atmospheric turbulent wind conditions up to 31 m/s (70 mph), and has been exposed to winds above 65 m/s (145 mph) with the rotor parked. The figure below illustrates one of those test, during which, amongst else, probe data was acquired and flow visualization was performed. The probes can be seen installed at the leading edge of the top (black) blade.

Test data have been made available to the research community through International Energy Agency Annex XIV and Annex XVIII. Reports summarizing results of the atmospheric turbine tests have demonstrated the extremely complex dynamic nature of the typical wind turbine operating environment. Highly turbulent wind and sheared inflow conditions are major factors that contribute to the complexity.

*Testing in a controlled wind tunnel environment will* eliminate these factors, and resulting data will provide information from which a significant portion of the complex inflow-induced operating environment is removed. This will enable researchers to isolate and characterize specific dynamic stall responses and 3-D rotational effects under benign steady-state operating conditions. Resulting data are needed to improve and validate enhanced engineering models for designing and analyzing advanced wind energy machines. A three-week wind-tunnel test period is scheduled to take place in the first half of 2000. Pictures from the rig setup procedures in the tunnel are shown in the figures below. Close inspection reveals the probes mounted on the black blade.
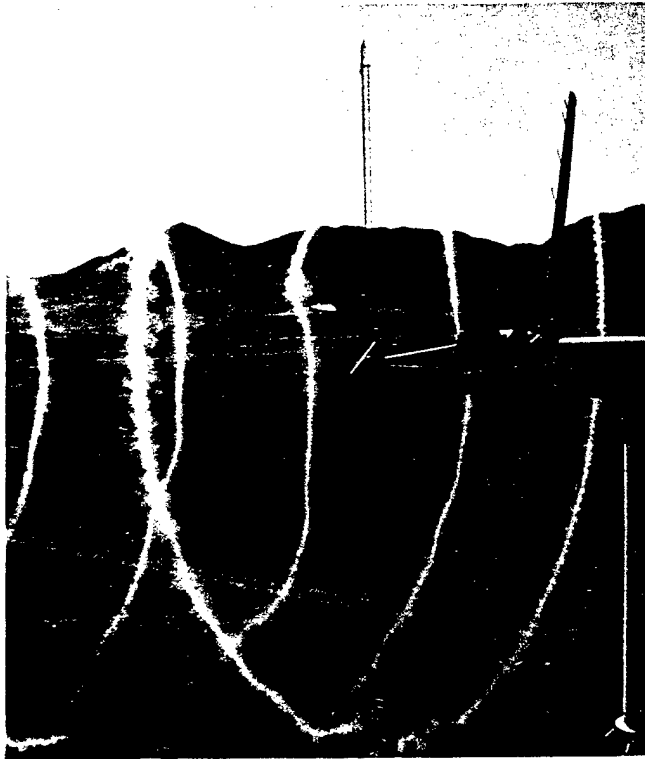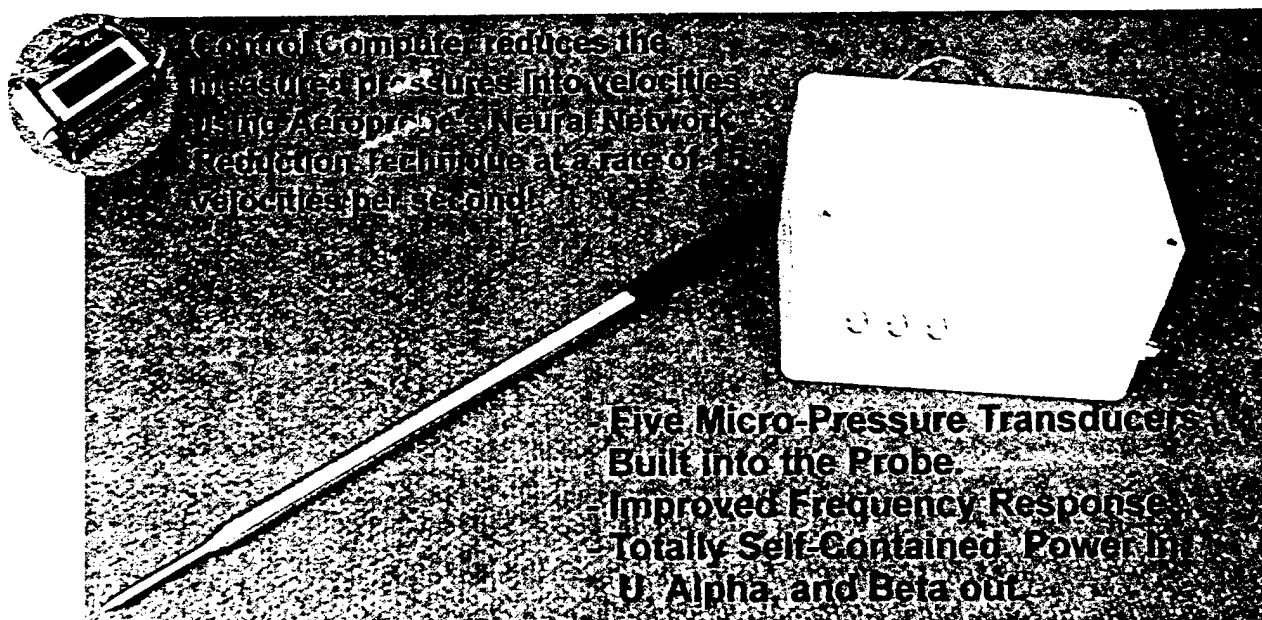


The probes were installed at the leading edge of one of the blades (top, black blade) and used during turbine field tests.
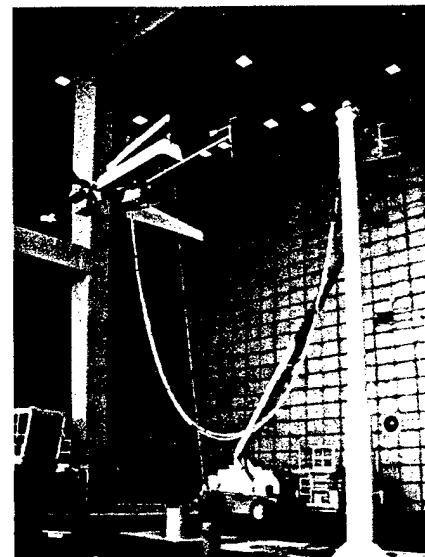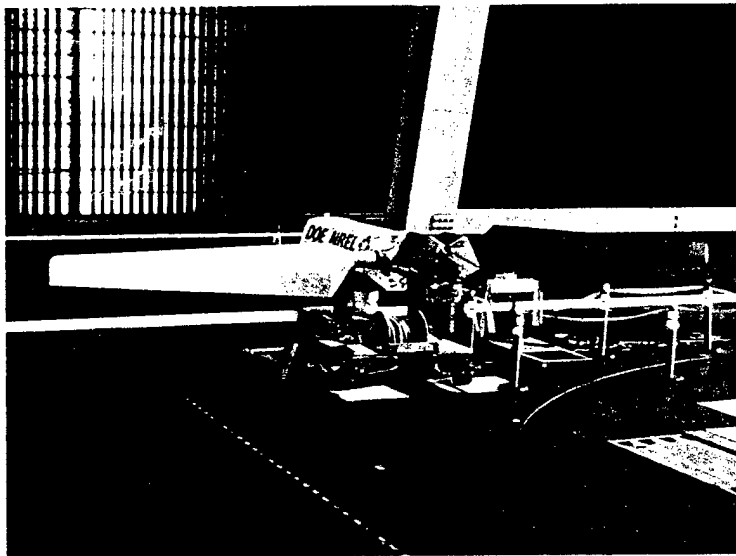


The turbine rig is in the process of being set-up for tests at the NASA Ames 80'x120' wind tunnel. Close inspection reveals the probes mounted on the black blade (left picture).

# Embedded Transducer Probe Technology



Control Computer reduces the
measured pressures into velocities
using Aeroprobe's Neural Network
Reduction Technique at a rate of 15
velocities per second.

Five Micro-Pressure Transducers
Built into the Probe.
Improved Frequency Response.
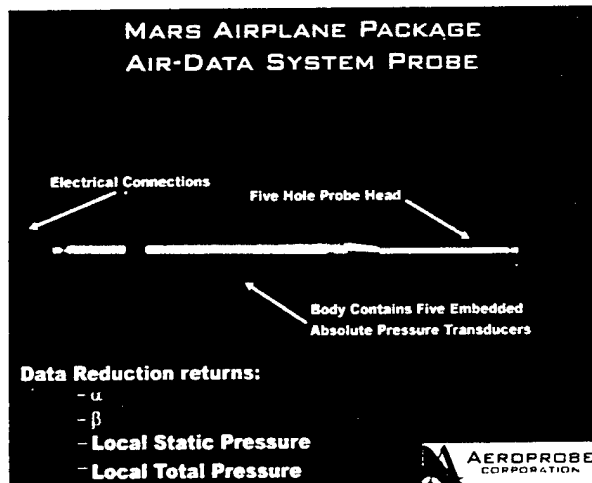Totally Self-Contained. Power In,
U, Alpha, and Beta out.

*Our embedded transducer probes bring all of the innovations that we have brought to the instrumentation community to the unmanned aerial vehicle (UAV) market.*

- *State of the Art Calibration*
- *Neural Network-Based Pressure-to-Velocity reduction*
- *Seven years of multi-hole probe construction experience*

*The embedded transducer probe features a self-contained control computer, which acquires the voltages from the transducers and then reduces the pressures to velocity components, on-line. The control computer uses very little power requiring just 12 volts DC. Outputs from the computer are in the form of voltages, which are scaled to a predetermined range. These voltages can be hooked directly into your flight data system and represent the airspeed U, angle of attack, $\alpha$, and yaw angle, $\beta$.*

Our embedded transducer probe technology is also available without the control computer unit for use in laboratory situations. Embedding the transducers within the probe body greatly increases the frequency response of the probe. This makes the embedded transducer probe an excellent instrumentation choice for cases where the measurement of all three velocity components, static and dynamic pressure is required with a high frequency response. We have designed and fabricated probes with frequency response as high as 100Khz.



"Bullet" shape tip houses 5 miniature Kulite

## MARS AIRPLANE PACKAGE AIR-DATA SYSTEM PROBE

Electrical Connections

Five Hole Probe Head

Body Contains Five Embedded Absolute Pressure Transducers

**Data Reduction returns:**
- u
- β
- **Local Static Pressure**
- **Local Total Pressure**

AEROPROBE CORPORATION

The figure above shows a close-up picture of a hemispherical-tip five-sensor embedded transducer probe we recently designed and fabricated for one of our customers, General Electric. The stringent probe design specifications included, amongst else:

- Frequency response of at least 20Khz
- Operating temperatures as high as 400°F
- Small enough size to fit between the stages of a range of different turbine engines, where flow measurements were desired

The "bullet" shape tip measures ¼" in diameter and ½" in length and houses 5 miniature Kulite pressure transducers.

To coincide with and celebrate the 100th anniversary of the Wright Brothers' historic first powered flight, NASA has planned an ambitious mission to the red planet that features the deployment of an autonomous aircraft to survey Mars from the air. One of the vendors that NASA selected to submit proposals for this project was Aurora Flight Science Corporation of Manassas, Virginia. The air data system had to be capable of measuring the angle-of-attack and side-slip of the aircraft and the absolute dynamic and static pressure. The outputs are to be recorded as part of the mission's scientific data and used for aircraft control. We were able to adapt our current embedded transducer technology to the air data system, overcoming the technical difficulties of the harsh conditions in the Martian atmosphere, which is over 100 time less dense than that of Earth's and the temperature goes through wild swings of over 100°C. All of these objectives were met along with the need for the final package to weigh less than 100 grams.
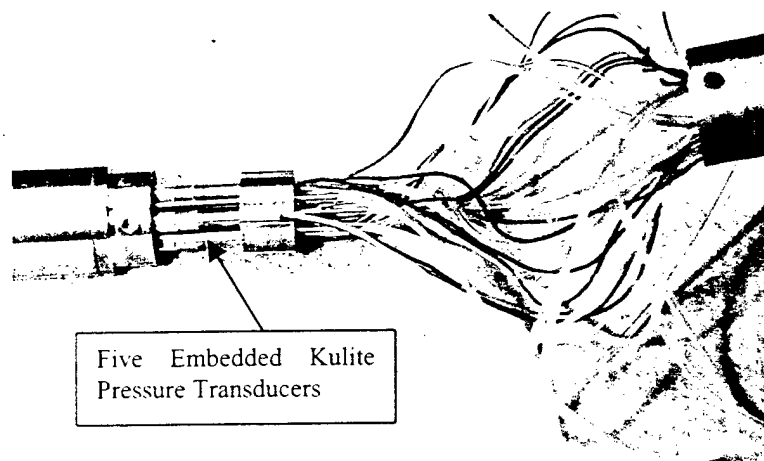
# GRYOGENIC Embedded KULITE PROBE
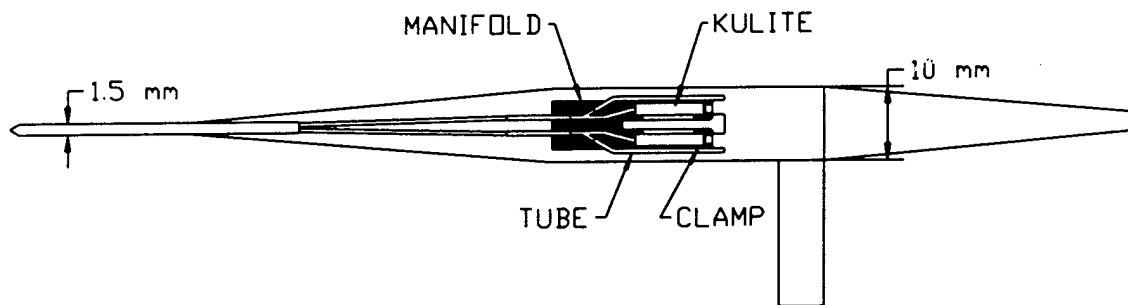


To achieve physics-based flow modeling as well as validate control approaches in flow control applications, high-accuracy flow diagnostics instrumentation is necessary. So far, no instrument was available that could provide simultaneous information on the three components of velocity, the static and total pressure at a measurement point, especially in a cryogenic wind-tunnel environment. The objective was to develop such an instrument that can provide such information in complex, unsteady flows, especially in high Ma, high Re cryogenic conditions.
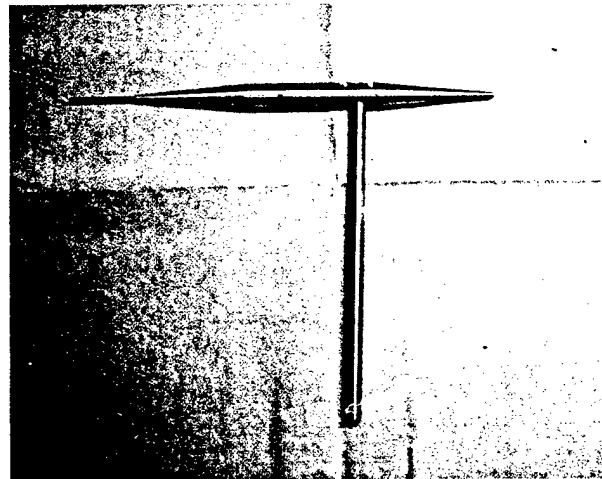
The instrument was developed for the NASA Langley Flow Modeling and Control Branch and was used in separation control experiments over wings in realistic flow conditions at the cryogenic wind tunnel at NASA Langley. A schematic of the probe dimensions and structure is shown above, as well a picture of the completed probe. The frequency response of the probe was 1Khz and could operate at temperatures as low as 180 °K.

*The figure on the left shows a picture of the internal probe structure, illustrating details of the Kulite transducer housing scheme inside the probe.*

Five Embedded Kulite Pressure Transducers

*The probe was used in wind-tunnel experiments of Active Control of Shock-Induced Separation (lead by Seifert & Pack at NASA Langley). The wing model used is illustrated in the figure below and was called the "Hump" model. The cryogenic tunnel conditions allowed the achievement of high Reynolds and Mach numbers (M=0.2-0.75) at relatively modest velocity magnitudes.*

*The experiment was designed to access the effectiveness of tangential oscillatory blowing excitation (introduced between the green and pink strips in the figure) in reducing or eliminating shock-induced separation. The function of the probe (shown in the schematic mounted downstream of the trailing edge) was to study the dynamic velocity and pressure effects. Very successful separation control was demonstrated which opens new horizons in the use of thicker (t/c=20-25%), more efficient airfoils as well as the introduction of new techniques for fast control of forces and moments on*



*a wing. The probe data also provided a database for CFD and Control tools validation.*